

**EVALUATION OF DRILLING PERFORMANCE AND PENETRATION  
MECHANISMS USING SEISMIC WHILE DRILLING AND ACOUSTIC EMISSION  
METHODS**

by

© Yingjian Xiao

A Dissertation submitted to the

School of Graduate Studies

in partial fulfillment of the requirements for the degree of

**Doctor of Philosophy**

**Faculty of Engineering and Applied Science**

Memorial University of Newfoundland

**September 2017**

St. John's

Newfoundland and Labrador

## **ABSTRACT**

In oil and gas industry, drilling provides the path to exploit underground resources. Increasing rate of penetration (ROP) is one of the goal of drilling engineers to build this path. This dissertation focuses on study of a novel drilling technique, i.e. passive Vibration Assisted Rotary Drilling (pVARD) technique, and characterization of drilling mechanisms in comparison to the other two widely used drilling techniques, i.e. rotary drilling and rotary-percussion drilling (RPD). In terms of the fundamental differences between drill bit vibrations from three drilling techniques, seismic while drilling (SWD) and acoustic emission (AE) technologies are used to study drill bit sources and corresponding drilling mechanisms.

First, geomechanics response of synthetic rock is studied using AE technique based on standard confined compressive strength (CCS) tests. This research aims to compare synthetic to natural rock in terms of deformation properties and provides support for the following drill-off test (DOT).

Second, pVARD tool drillings are conducted in comparison to rotary drilling both in laboratory and field tests using AE and SWD techniques, respectively. In laboratory, AE signal energy and cutting size distribution are correlated to polycrystalline diamond compact (PDC) bit drilling performance. Results show that micro crack is generated from drag bit shearing action and the higher AE energy, coarser cuttings and higher ROP are

obtained. In field test, surface wave energy and frequency bandwidth are correlated to drill bit vibration and drilling performance.

Third, laboratory active vibration DOTs are conducted to study the penetration mechanisms from a diamond coring bit using AE technique. Spectral and energy analysis of the AE signals indicate that the higher ROP and larger cutting size are correlated with a higher AE energy and a lower AE frequency, indicating larger fractures are being created to generate the larger size of cuttings.

Fourth, rotary-percussion drilling sources are studied by two field experiments on weak shales and hard arkose using SWD technique. Characterization of these sources consist of spectral analysis and mean power study, along with field measurements of the source radiation patterns. In addition, polarization analysis is conducted on P-waves recorded at surface geophones for understanding the particle motions.

## ACKNOWLEDGEMENTS

I would like to express my gratitude to my supervisor Dr. Stephen D. Butt and my supervisory committee Dr. Charles Hurich and Dr. John Molgaard, for their expert guidance, patience and supports throughout this research work. I gratefully acknowledge their technical expertise, critical thinking, and valuable comments on publications and dissertation.

I would also like to thank Atlantic Canada Opportunity Agency (AIF contract number: 781-2636-1920044), involving Husky Energy, Suncor Energy and Research and Development Corporation (RDC) of Newfoundland and Labrador, for funding this research over the past four years. I would like to acknowledge the financial support provided by the School of Graduate Studies at Memorial University. In addition, I acknowledge the financial support from Anaconda Mining Co. through Mitacs-Accelerate Graduate Internship.

During this research, I would give my appreciation to all group members who give me help in Drilling Technology Laboratory. Specifically, thanks will be given to Farid Arvani for help in building AE system, Zhen Zhang, Hongyuan Qiu, Igor Kyzym, Rosana Reyes, and Yuanchi Tian for helps in experiments, Shawn Organ and David Snook for helps in technical support, Dr. Sharon Deemer for help in seismic data processing.

Last but not least, I am grateful to my wife Xiaoying Song who always gives me patience and encourages whenever challenges are encountered.



1.4.1	Drilling techniques .....	8
1.4.1.1	Rotary drilling	8
1.4.1.2	Rotary-percussion drilling	10
1.4.1.3	pVARD drilling	13
1.4.2	Bit vibration and bit-rock interaction .....	15
1.4.3	Seismic While Drilling .....	17
1.4.3.1	Introduction	17
1.4.3.2	Use of drill bit signal as seismic source	19
1.4.3.3	SWD sources in rotary drilling, rotary-percussion drilling and pVARD drilling	20
1.4.3.4	Wave radiation patterns at drill bit sources	24
1.4.3.5	Polarization analysis	28
1.4.4	Acoustic emission.....	29
1.4.4.1	Introduction	29
1.4.4.2	Rock deformation and failure	32
1.4.4.3	Drilling using AE technique	33
1.4.5	Cutting size and drilling performance .....	34
1.5	References .....	36
Chapter 2 Micro-Seismic Evaluation of Fracturing in Cores during Triaxial Compression		
	Tests .....	51
2.1	Co-authorship Statement.....	51
2.2	Abstract .....	52
2.3	Introduction .....	53

2.4	Experimental Setup.....	53
2.4.1	Axial loading frame.....	53
2.4.2	Monitoring acoustic emission.....	54
2.4.3	Test materials.....	55
2.4.4	Overall workflow.....	56
2.5	Results.....	57
2.5.1	Single acoustic emission.....	57
2.5.2	Single test inspection.....	58
2.5.3	Dominant frequency and source energy.....	61
2.5.4	Source location and failure observation.....	63
2.6	Conclusions.....	65
2.7	Acknowledgements.....	66
2.8	References.....	66
Chapter 3 Micro-Seismic Monitoring of PDC Bit Drilling Performance during Vibration Assisted Rotational Drilling.....		
69		
3.1	Co-authorship Statement.....	69
3.2	Abstract.....	70
3.3	Introduction.....	71
3.4	Experimental Setup.....	72
3.4.1	Test materials.....	73
3.4.2	Small drilling simulator.....	73
3.4.3	Monitoring acoustic emission.....	74
3.4.4	Cutting analysis overview.....	76

3.5	Results.....	77
3.5.1	Review of drilling conditions .....	77
3.5.2	Rock penetration characterization .....	78
3.5.3	Cutting analysis results .....	80
3.5.4	Acoustic emission results .....	84
3.5.5	Acoustic emission and ROP .....	87
3.6	Discussion and Conclusions.....	88
3.7	Acknowledgements.....	88
3.8	References.....	89
Chapter 4 A Novel Method for Assessment of Rock-Bit Interaction and Drilling Performance Using Elastic Waves Propagated by the Drilling System .....		
4.1	Co-authorship Statement.....	92
4.2	Abstract .....	93
4.3	Introduction .....	95
4.4	Methodology .....	98
4.4.1	Experimental methods .....	98
4.4.2	Surface wave as a monitor of drilling performance .....	103
4.5	Properties of the Rocks .....	104
4.6	Data Acquisition and Processing .....	105
4.6.1	Data acquisition .....	105
4.6.2	Seismic data processing.....	107
4.6.3	Bit vibration data collection and analysis.....	112
4.7	Data Analysis and Interpretation.....	114

4.7.1 Rigid drilling on red shale .....	115
4.7.2 pVARD and rigid drilling on red shale .....	121
4.7.3 pVARD and rigid drilling on grey shale .....	129
4.8 Discussion and Conclusions.....	133
4.9 Acknowledgements.....	135
4.10 References.....	135
Chapter 5 Investigation of Active Vibration Drilling Using Acoustic Emissions and Cuttings Size Analysis .....	140
5.1 Co-authorship Statement.....	140
5.2 Abstract.....	141
5.3 Introduction.....	142
5.4 Methodology .....	145
5.4.1 Experimental method.....	145
5.4.2 Testing plan .....	150
5.5 Data Acquisition and Processing .....	151
5.6 Data Analysis and Interpretation.....	157
5.6.1 Drilling performance and vibration .....	157
5.6.2 Acoustic emission analysis.....	158
5.6.3 Cutting size distribution.....	162
5.6.3.1 Particle size distribution (PSD)	162
5.6.3.2 Mean particle size	164
5.6.4 Correlation of ROP to AE energy and cutting size .....	167
5.7 Discussion and Conclusion .....	167

5.8	Acknowledgements.....	167
5.9	Abbreviations.....	168
5.10	References.....	169
Chapter 6 Characterization of Rotary-Percussion Drilling as a Seismic While Drilling		
	Source.....	174
6.1	Co-authorship Statement.....	174
6.2	Abstract.....	175
6.3	Introduction.....	176
6.4	Methodology.....	179
6.4.1	Field experiments.....	180
6.4.2	Red Bridge Road quarry experiment.....	181
6.4.3	Collier Point experiment.....	185
6.5	Data Processing.....	189
6.5.1	Seismic data from the Red Bridge Road experiment.....	189
6.5.2	Seismic data from the Collier Point experiment.....	191
6.5.2.1	Hydrophone data for cross-hole survey.....	192
6.5.2.2	The 3C geophone seismic data.....	194
6.6	Data Analysis and Interpretation.....	195
6.6.1	Characterization of the rotary-percussion drilling source.....	195
6.6.2	Radiation pattern of drill-bit source.....	199
6.6.2.1	Energy radiation within vertical plane.....	199
6.6.2.2	Energy radiation within horizontal plane.....	202
6.6.3	Polarization analysis.....	204

6.6.4	Deviation of horizontal components of P-wave polarizations from source-receiver azimuths .....	211
6.7	Conclusions .....	214
6.8	Acknowledgements .....	215
6.9	References .....	216
Chapter 7	Concluding Remarks .....	221
7.1	Summary .....	221
7.2	Concluding Remarks .....	221
7.3	Dissertation Highlights and Contributions .....	225
7.3.1	Rock failure mechanisms and acoustic emission .....	225
7.3.2	Characterization of bit vibration and bit-rock interaction .....	225
7.3.3	Evaluation of drilling performance and penetration mechanisms .....	227
7.4	Recommendations for Future Work .....	227
Appendix 1	Processing of AE Signals Using Matlab® Codes .....	229
A1.1	Main Function .....	229
A1.2	Function “readSignal” .....	232
A1.3	Function “averageSignal” .....	236
A1.4	Function “processSignal” .....	236
Appendix 2	Calculation of Bit Vibrations from Sensor Sub Data .....	241
A2.1	Methodology .....	241
A2.2	References .....	242

## List of Tables

Table 2.1: Inputs for monitoring acoustic emission.....	55
Table 2.2: Loading plan for triaxial compression test and CCS results.....	56
Table 3.1: Scheme for drill-off test with AE detection.....	74
Table 3.2: Inputs for monitoring acoustic emission.....	75
Table 4.1: Geomechanics and ultrasonic properties of the shale formations oriented perpendicular to bedding.....	105
Table 4.2: Drill-off test parameters for the seismic-while-drilling experiments .....	114
Table 5.1: Geomechanics and ultrasonic properties of the drilling sample material .....	146
Table 5.2: Inputs for monitoring acoustic emission.....	150
Table 6.1: Geomechanics and ultrasonic properties of rocks, in which red shale properties are in reference to Rana et al.....	181
Table 6.2: Seismic sources generated by rotary-percussion drilling and other bit sources .....	196

## List of Figures

Figure 1.1: Sketch of rotary drilling process modified from Bourgoyne et al.....	9
Figure 1.2: Bassinger percusslon tool (from Guarin et al.).....	12
Figure 1.3: (a) Demonstration of pVARD drilling; (b) Laboratory scale pVARD tool. Modified from Rana et al.....	15
Figure 1.4: Drill string vibrations (from Schlumberger Ltd.).....	16
Figure 1.5: Basic concept of seismic while drilling (from Poletto and Miranda).....	18
Figure 1.6: Roller tooth indention and gouging action are demonstrated on left column; Measured cone teeth forces in right column: (a) cone outer row, (b) cone inner row, (c) particular of outer row, (d) particular of inner row which is modified from Sheppard and Lesage .....	22
Figure 1.7: (a) Lobed pattern of one tricone bit; Vibration forces from modeling when (a) average vertical force $F_m = \text{WOB}$ and (b) maximum force $F_{\max} = 2\text{WOB}$ , (c) downhole real data. Modified from Poletto and Miranda.....	22
Figure 1.8: (a) Forces applied on single PDC cutter; (b) Wear flat area. Modified after Guyen Minh Duc et al.....	23
Figure 1.9: Source radiation and wave amplitudes in solid medium radiated from a cylinder hole wall subjected to (a) vertical shearing stress, (b) radial stress and (c) torsional shearing stress. Modified from Heelan .....	26
Figure 1.10: Available elastic waves in drilling, i.e. head wave, direct arrival, rig-related arrival as surface wave (from Rector and Hardage) .....	27

Figure 1.11: (A) Two components signals at a 3C geophone; (B) Corresponding hodogram from the time window 209-220 ms with a polarization angle oriented to the maximum energy direction, which is modified after DiSiena et al.....	29
Figure 1.12: Two acoustic technologies used to study geological structure: sonic technology (left) and AE technology (right) (after Hardy).....	30
Figure 1.13: Two types of AE signals: (a) burst and (b) continuous (after Ríos-Soberanis) .....	31
Figure 1.14 Typical AE signal frequency ranges (after Hardy).....	32
Figure 1.15: Stress-strain diagram showing the deformation process of rock (after Martin) .....	33
Figure 2.1: Strength test apparatus with the Hoek triaxial cell (left) and working schematic (right) .....	54
Figure 2.2: Tested concrete cores (low, medium and high strength).....	56
Figure 2.3: Flow chart of CCS test with monitoring acoustic emissions.....	57
Figure 2.4: One burst event from top sensor (upper) and bottom sensor (lower) detected from the high strength material with 4 MPa confining pressure.....	58
Figure 2.5: Mechanical and acoustic responses of low strength cores with acoustic properties comparison from both sensors .....	59
Figure 2.6: Mechanical and acoustic responses of medium strength cores with acoustic properties comparison from both sensors .....	60
Figure 2.7: Mechanical and acoustic responses of high strength cores with acoustic properties comparison from both sensors .....	61

Figure 2.8: DF versus time for low, medium and high strength cores under confining pressure of 2 MPa (upper) and 4 MPa (lower). Linear fit was provided for each group of scattered points.....	62
Figure 2.9: AE energy versus dominant frequency for low, medium and high strength cores under confining pressure of 2 MPa (upper) and 4 MPa (lower). Linear fit was provided for each group of scattered points.....	63
Figure 2.10: One dimensional acoustic source distribution versus test time for low, medium and high strength cores. Vertical axes were scaled to actual core heights.....	64
Figure 2.11: Post failure illustration for low, medium and high strength cores under confining pressure of 2 MPa.....	65
Figure 3.1: Generic view of small drilling simulator (left) and cutting collection and acoustic emission setup (right).....	72
Figure 3.2: Top view of p-sensors distribution around synthetic concrete cylinder.....	75
Figure 3.3: Flow chart for monitoring acoustic emissions .....	76
Figure 3.4: Rigid drilling when WOB = 100.0 kg. PDC bit penetrates around 20 mm on medium strength concrete (upper left) and axial vibration magnitude varies with time (upper right). Vibration is converted from time domain to frequency domain (Lower).....	77
Figure 3.5: Laboratory rate of penetration (ROP) versus WOB under three different compliance settings .....	78
Figure 3.6: ROP is normalized to 300 RPM situation for eliminating the effect of different rotary speed (upper) and actual rotary speed normalized to 300 RPM (lower).....	79
Figure 3.7: Particle-size distribution from drilling with rigid compliance (upper), medium compliance (middle) and strong compliant setting (lower) .....	80

Figure 3.8: Particle-size distribution from different WOB .....	82
Figure 3.9: Particles obtained from drilling when WOB=234.6 kg at strong compliance setting, whose size ranges from 850 to 2000 micron (upper) and from 420 to 590 micron (lower).....	84
Figure 3.10: Single acoustic emission from rigid drilling when WOB=100.0 kg (upper) and spectrogram (lower) .....	85
Figure 3.11: Average event energy (upper) and event rate (number of triggered events per second, lower) from the trigger channel .....	86
Figure 3.12: Average event energy versus ROP under three different compliant settings	87
Figure 4.1: Spread of 1C geophones array (20) with three seismic source boreholes in Greenslades Construction Quarry of east Newfoundland (based on Google map) .....	99
Figure 4.2: Cross section of A-A' showing the rock formation penetrated based on analysis of drill cuttings sampled while drilling.....	100
Figure 4.3: Onsite view of seismic while drilling at Greenslades Construction Quarry with (a): overview of drill site with in-line geometry of geophones; (b): 1C geophone; (c): front view of drill rig showing the drilling bottom-hole assembly, modified from Rana et al. ....	102
Figure 4.4: Demonstration of direct wave and surface wave generated from rig-ground interaction, which was modified from Rector and Hardage .....	104
Figure 4.5: 3D Geometry of 1C geophone array with regarding to the three boreholes (looking north) .....	106
Figure 4.6: Sample seismic data cross correlated on channel #20. In borehole 2 from 79.2 to 85.3 m, red shale was drilled by a hammer bit and a PDC bit with the pVARD tool.	

Every twenty traces were assembled in one group recorded by 20 geophones. The space between traces is 5 m. No scaling was applied .....	108
Figure 4.7: Assembly of cross correlated traces from channel #3 in borehole 2. Drilling depths ranged from 0 to 91.4 m. Trace was individually scaled at its peak amplitude	109
Figure 4.8: Sample frequency spectrum for surface wave traces recorded at channel #3 when drill rig was on with no drilling.....	110
Figure 4.9: Demonstration of eight frequency bandwidths for surface wave traces recorded from 8 DOTs, which are divided into two drillings, i.e. the pVARD tool (T1-T4) and rigid (T5-T8) .....	111
Figure 4.10: Sensor package was coaxially located inside the downhole SensorSub. Accelerometers were collaboratively used in obtaining accelerations for bit vibration modified from Gao.....	112
Figure 4.11: Bit vibration was interpreted as three accelerations. Red shale was drilled with one PDC bit from 69.3 to 93.8 m in borehole 1 .....	113
Figure 4.12: Red shale was drilled from 69.3 to 93.8 m in borehole 1. Results were shown as ROP and vibration accelerations (top), surface wave energies from multiple channels (bottom).....	116
Figure 4.13: Five frequency bandwidths corresponded five WOBs of rigid drilling from channel #1, when red shale was drilled from 69.3 to 93.8 m in borehole 1 .....	117
Figure 4.14: Five frequency bandwidths corresponded five WOBs of rigid drilling from channel #3, when red shale was drilled from 69.3 to 93.8 m in borehole 1 .....	118
Figure 4.15: Five frequency bandwidths corresponded five WOBs of rigid drilling from channel #7, when red shale was drilled from 69.3 to 93.8 m in borehole 1 .....	119

Figure 4.16: Five frequency bandwidths corresponded five WOBs of rigid drilling from channel #10, when red shale was drilled from 69.3 to 93.8 m in borehole 1 .....	120
Figure 4.17: Five frequency bandwidths corresponded five WOBs of rigid drilling from channel #13, when red shale was drilled from 69.3 to 93.8 m in borehole 1 .....	121
Figure 4.18: Red shale was drilled from 82.3 to 106.0 m in borehole 2. Results were shown as ROP, and surface wave energy comparison for the pVARD tool and rigid drillings .....	122
Figure 4.19: Four frequency bandwidths corresponded four WOBs for the pVARD tool and rigid drillings from channel #1, when red shale was drilled from 82.3 to 106.0 m in borehole 2.....	124
Figure 4.20: Four frequency bandwidths corresponded four WOBs for the pVARD tool and rigid drillings from channel #3, when red shale was drilled from 82.3 to 106.0 m in borehole 2.....	125
Figure 4.21: Four frequency bandwidths corresponded four WOBs for the pVARD tool and rigid drillings from channel #5, when red shale was drilled from 82.3 to 106.0 m in borehole 2.....	126
Figure 4.22: Four frequency bandwidths corresponded four WOBs for the pVARD tool and rigid drillings from channel #7, when red shale was drilled from 82.3 to 106.0 m in borehole 2.....	127
Figure 4.23: Four frequency bandwidths corresponded four WOBs for the pVARD tool and rigid drillings from channel #10, when red shale was drilled from 82.3 to 106.0 m in borehole 2.....	128

Figure 4.24: Four frequency bandwidths corresponded four WOBs for the pVARD tool and rigid drillings from channel #13, when red shale was drilled from 82.3 to 106.0 m in borehole 2.....	129
Figure 4.25: Grey shale was drilled from 54.5 to 60.0 m in borehole 3. Results were shown as ROP, and surface wave energy comparison for the pVARD tool and rigid drillings .....	130
Figure 4.26: Four frequency bandwidths corresponded four WOBs for the pVARD tool and rigid drillings from channel #7, when grey shale was drilled from 54.5 to 60.0 m in borehole 3.....	131
Figure 4.27: Four frequency bandwidths corresponded four WOBs for the pVARD tool and rigid drillings from channel #10, when grey shale was drilled from 54.5 to 60.0 m in borehole 3.....	132
Figure 4.28: Four frequency bandwidths corresponded four WOBs for the pVARD tool and rigid drillings from channel #13, when grey shale was drilled from 54.5 to 60.0 m in borehole 3.....	133
Figure 5.1: Schematic diagram for conducting DOTs using a small drilling simulator at the Memorial University of Newfoundland. A DOT is conducted on a concrete cylinder, which is firmly mounted to the vibration table .....	148
Figure 5.2: Schematic view of a diamond coring bit drilling: (a) drilling parameters for a six-segment diamond bit; (b) penetration process of a single segment; (c) two-segment diamond bit used in this paper. This is modified after Karakus and Perez.....	149
Figure 5.3: Overview of the DOT setup (a) with a concrete cylinder for mounting AE transducers; (b) the laser sensor attached to the stationary rig frame .....	149

- Figure 5.4: A sample DOT is synchronized with the displacement of the vibrating table (a) at vibration L1 and WOB=95.3 kg, from which an analysis window of vibration (b) and the corresponding frequency spectrum (c) are obtained. The peak frequency of 60 Hz represents the working frequency of the vibrating table..... 153
- Figure 5.5: A sample AE signal (a) with its frequency spectrum (b) indicating a peak frequency of 133 kHz and a spectral centroid of 264 kHz at vibration L1 and WOB=95.3 kg. The spectral centroid is calculated based on a frequency range of 0 and 1 MHz.. 154
- Figure 5.6: Four waveforms of a single event are recorded by four AE sensors from passive drilling at WOB=106.5 Kg. Each waveform is shown in left panel and peak frequency and spectral centroid are shown in right panel..... 155
- Figure 5.7: A sample DOT with synchronized vibration (a) and synchronized AE count and average energy (b) at vibration L1 and WOB=95.3 kg. The time at 0 second shows the start of the DOT ..... 156
- Figure 5.8: An assembly of both ROP (a) and the corresponding vibration level (b) are in correlation to WOB. ROP is positively correlated with WOB ..... 157
- Figure 5.9: Peak frequency distribution is in correlation to WOB at drilling with settings of passive, vibrations L1 and L2. An arithmetic average of peak frequencies is obtained based on fifteen events at each WOB. Peak frequency is found to decrease with increasing WOB..... 159
- Figure 5.10: Spectral centroid varies with respect to WOB for the three drilling settings. Spectral centroids decrease with increasing WOB ..... 160

Figure 5.11: Average energy of AEs is in positive correlation to (a) WOB and (b) ROP for all DOTs using three settings of passive, vibrations L1 and L2. Bit vibration enhances the AE average energy .....	161
Figure 5.12: PSD charts for all DOTs using the three settings, i.e. passive, vibrations L1 and L2. Cutting is coarser when the PSD curve shifts to the right for each drilling setting .....	163
Figure 5.13: Demonstration of mean particle sizes for three increasing WOBs using the RR diagram, modified from Brezani and Zelenak. Mean particle size is obtained as the mesh size at 36.79% retained .....	166
Figure 5.14: Mean particle size is positively correlated to WOB for DOTs using the three settings. Coarser cutting is obtained with the increase in WOB .....	166
Figure 6.1: Spread of 1C geophones array (20) with three seismic source boreholes in Red Bridge Road quarry of eastern Newfoundland and Labrador of Canada.....	182
Figure 6.2: Cross section of A-A' showing the rock formation penetrated based on analysis of cuttings circulated from bottom hole.....	183
Figure 6.3: (a) Overview of drill site with in-line geometry of geophones; (b) 1C geophone; (c) Front view of the drill rig modified from Rana et al. ....	184
Figure 6.4: Top view of 3C geophones (12) spread around two source boreholes in Collier Point barite mine at eastern Newfoundland and Labrador of Canada .....	186
Figure 6.5: Cross section of B-B' showing the rock formation penetrated based on analysis of cuttings.....	187
Figure 6.6: (a) Onsite seismic while drilling (facing south); (b) 3C geophone with horizontal in-line component facing borehole 2; (c) hydrophone.....	188

- Figure 6.7: Sample seismic data cross-correlated on channel #20. No scaling (a) is compared with scaling at individual peak amplitude (b). In borehole 2 from 79.2 to 85.3 m depth, seismic sources are obtained from one rotary-percussion drilling (RPD) and one conventional drilling with a polycrystalline diamond compact (PDC) bit. Every twenty traces are assembled in one group recorded by 20 geophones..... 190
- Figure 6.8: Cross-correlated records from channel #3 in borehole 2. One rotary-percussion drilling starts from surface and is followed by one conventional drilling with a polycrystalline diamond compact bit to 91.4 m depth. Trace is individually scaled at its peak amplitude ..... 191
- Figure 6.9: Illustration of cross-hole survey on hammer bit source with in-line spread of hydrophones ..... 192
- Figure 6.10: Sample seismogram of P-waves received by hydrophones. The polarities have been reversed from trace #11 to #21 for consistency. The drill-bit source depth is apparently located between trace #10 and #11 ..... 193
- Figure 6.11: Seismogram received on vertical component of 3C geophones. Varying arrival times and amplitudes result from varying source-receiver distance and the geometric divergence ..... 195
- Figure 6.12: Frequency spectra of rotary-percussion drilling SV waves vary with different rock strengths: i.e. grey and red shales from the Red Bridge Road experiment, and arkose from the Collier Point experiment. Source-receiver distance for three rotary-percussion drilling sources is 79 m. Increase of rock strength increases peak frequency and widens bandwidth..... 198

- Figure 6.13: Mean power of rotary-percussion drilling and conventional drillings, i.e. roller-cone bit and polycrystalline diamond compact bit, in terms of surface waves from (a) grey shale and (b) red shale. The magnitude of sources from rotary-percussion drilling is higher than polycrystalline diamond compact bit in three orders in grey shale, and is higher than polycrystalline diamond compact and roller-cone bits in two orders in red shale ..... 198
- Figure 6.14: Measured amplitude distribution of P-waves within the vertical plane along with energy radiations from theoretical (a) axial bit vibration and (b) lateral bit vibration. Measured amplitude distribution partially confirms the theoretical predication for axial bit vibration. An additional lateral vibration is indicated by the new horizontal energy lobe (b) ..... 201
- Figure 6.15: Measured amplitude distribution of P-waves within the horizontal plane. Five groups of geophones are distributed as even as possible around borehole #2 (polar center), with redundant measurements for every group showing an arithmetic average (cycle) and errors ..... 203
- Figure 6.16: Orientation of 3C geophone showing three orthogonal components. The orientation of H-I component follows the source-receiver azimuth ..... 205
- Figure 6.17: Hodograms for P-waves recorded at the azimuth of  $32.8^\circ$  from multiple depths of sources. The azimuths are relative to the direction away from the source. Each row refers to an event covering two hodograms in column (a) and (b). Blue lines show hodograms of P-waves at specific time windows. Black arrows show the vectors for particle motion directions..... 207

- Figure 6.18: Hodograms for P-waves recorded at varying azimuths of geophones from a common source depth of 17.1 m. The azimuths are relative to the direction away from the source. Each row refers to an event covering two hodograms in column (a) and (b). Blue lines show hodograms of P-waves at specific time windows. Black arrows show the vectors for particle motion directions .....209
- Figure 6.19: Calculated polarization angles from hodograms of P-waves recorded at 11 geophones (except geophone #12) from the six depths of sources. Polarization angles are rotated counterclockwise from the H-I orientations. Radii represent planar distance of source-geophone in meters.....211
- Figure 6.20: Polarization angles from six sources of depths from 17.1 to 45.3 m recorded by a single geophone. Particle motions deviate the H-I orientations showing the H-I components are not in exact consistence with the source-receiver azimuths. Radii represent planar distance of source-geophone in meters .....214

## **List of Symbols, Nomenclature or Abbreviations**

1C	One-Component (geophone)
3C	Three-Component (geophone)
AE	Acoustic Emission
ASTM	American Society for Testing and Materials
BHA	Bottom-Hole-Assembly
BHP	Bottom-Hole-Pressure
BPSD	Bar Particle Size Distribution
CCS	Confined Compressive Strength
DAQ	Data Acquisition
DEM	Distinct Element Model
DF	Dominant Frequency
DOC	Depth-Of-Cut
DOT	Drill-Off Test
DTL	Drilling Technology Laboratory
FFID	Field File Identification Number
FFT	Fast Fourier Transform
FLAC3D	Fast Lagrangian Analysis of Continua 3D
H-I	Horizontal In-Line
H-O	Horizontal Out-Of-Line
IADC	International Association of Drilling Contractors
LVDT	Linear Variable Differential Transformer

NDT	Non-Destructive Testing
PAC	Physical Acoustics Corporation
PDC	Polycrystalline Diamond Compact (bit)
PFC2D	Particle Flow Code 2D
PLI	Point Load Index
PSD	Particle Size Distribution
pVARD	passive Vibration Assisted Rotary Drilling
P-wave	Primary or Pressure Wave
RBR	Red Bridge Road
RC	Roller Cone (bit)
RDC	Research and Development Corporation
RMS	Root Mean Square
ROP	Rate of Penetration
RPD	Rotary-Percussion Drilling
RPM	Revolutions-Per-Minute
RR	Rosin-Rammler
RRSB	Rosin-Rammler-Sperling-Bennett
RVSP	Reverse Vertical Seismic Profile
SDS	Small Drilling Simulator
SH	Shear wave Horizontally polarized
SNPA	Societe Nationale des Petroles D'Aquitaine
SV	Shear wave Vertically polarized

S-wave	Secondary or shear wave
SWD	Seismic While Drilling
T-D	Time-Depth
TOB	Torque-On-Bit
UCS	Unconfined Compressive Strength
V	Vertical (geophone component)
VSP	Vertical Seismic Profile
WOB	Weight-On-Bit

## **List of Appendices**

Appendix 1	Processing of AE Signals Using Matlab® Codes .....	229
Appendix 2	Calculation of Bit Vibrations from Sensor Sub Data.....	241

## **Chapter 1 Introduction and Overview**

### **1.1 Introduction**

Drilling is essential to exploration of oil and gas, especially for deep formation resources. Increasing the rate of penetration (ROP) has been of major interest for drilling communities in the oil and gas industry, and over the last century technologies have been developed to achieve this target. These technologies have widely employed natural bit vibration or incorporated extra vibration into drilling. There are three types of drilling technologies: 1) Rotary drilling is driven by a rotary table and kelly system, in which natural bit vibration is generated during a drill-off test (DOT); 2) Rotary-percussion drilling (RPD) was first proposed in 1902 by adding percussive blows to the conventional rotary drilling for the purpose of significantly improving the ROP. This type of drilling uses active vibrating forces applied on a drill bit and is widely used in blast hole drilling in hard rock mining; 3) A novel drilling tool, referred to here as a passive Vibration Assisted Rotary Drilling (pVARD) tool, has been designed and fabricated at the Drilling Technology Laboratory of Memorial University of Newfoundland, Canada. A pVARD tool mounted behind a drill bit is designed to incorporate a particular compliance from a group of springs, and possibly also mass and damping. It is chosen so that natural vibration occurring at the bit face during rotation of the drill bit is of a direction, frequency and magnitude, which is intended to increase the ROP without enhancing wear/damage to the bit. This tool consists of an inner hollow shaft and an outer shell, between which relative motions occur. One group of springs and dampening rubbers included in the inner shaft absorb and convert natural bit

vibrations to axial displacement. This pVARD technology, incorporating spring compliance into the drill string, improves bit-rock interaction and increases ROP. This tool passively employs natural bit vibration and shows promising improvement in drilling performance from both laboratory and field tests.

The main focus of this thesis is a study of seismic while drilling (SWD) or acoustic emission (AE) technologies as a feasible and indirect way of studying the drilling mechanism in all three modes of drilling.

## **1.2 Statement of the Problem**

The pVARD tool has not been tested before and thus is a compelling technology to study. As described before, compliance components are included in the pVARD tool which makes pVARD drilling distinct from rotary drilling and RPD. Initial laboratory and field tests show that pVARD technology is promising compared to rotary drilling. Some empirical relations have been proposed to describe ROP related parameters such as: weight-on-bit (WOB), rotary speed, and rock strength, which is designated as ‘The Perfect-Cleaning Theory’ [1,2]. A Distinct Element Model (DEM) numerically simulated the cutting process of a polycrystalline diamond compact (PDC) bit in both rotary drilling and RPD [3]. However, a study is required of the root cause of the increase of ROP and drilling mechanism in rotary drilling, pVARD, and RPD. This includes the following:

1) Measurement of bit vibration is essential for understanding the bit-rock interaction and the bit drilling mechanism. For rotary and pVARD drillings, bit vibration is measured by accelerometers mounted on drill strings. In the pVARD tool, multiple springs are stacked, providing compliance for the whole drill string, but the final bit vibration has never been determined. In RPD, strong and high frequency of hammer blowing makes it difficult to directly measure bit vibration. An alternative way is to characterize seismic waves radiated from bit-rock interaction.

2) Seismic waves and acoustic emissions that radiate from bit-rock interaction correlate with bit vibration modes and drilling mechanisms. The drilling industry greatly benefits from studying the characteristics of seismic waves while drilling. This facilitates the chance of predicting formations about to be encountered. This also provides indications of drill bit condition. Limited research has been conducted to correlate seismic radiation to drilling mechanism and drilling performance.

3) Seismic source radiation from bit-rock interaction has been comprehensively studied both in theory and practice. Based on axial and torsional motions of a drill bit, seismic wave energies from single modes of motion and a combination of modes of motions have been theoretically calculated and observed in some experiments. However, radiated seismic wave energy distribution for hard rock drilling has not yet been reported. Elastic wave velocities are greater when rock strength is stronger. Also, seismic source energies could dramatically vary on different rock types.

### **1.3 Research Plan and Objectives**

The objective of this thesis is to uncover drilling mechanisms for rotary, pVARD and RPD using SWD or AE technologies. In this way, drilling performance and drilling conditions are assessed from DOTs. This research was conducted at Memorial University of Newfoundland and divided into the following five projects.

#### **1.3.1 Micro-seismic evaluation of fracturing in cores during triaxial compression**

##### **tests**

This project aimed to provide a geotechnical evaluation of synthetic rock using AE technology. The purpose of studying synthetic rock is to confirm that this synthetic rock is comparable to natural rock for the following DOTs. In the Drilling Technology Laboratory, synthetic rock is casted using fine aggregate and Portland cement and specimens are cored as the standard NQ size, i.e. a standard “Q” wireline bit size. Standard confined compressive strength (CCS) tests are conducted on these cores with two AE transducers, one mounted at each end. Received AE events are used to investigate the deformation process of core samples. Acoustic properties of these events are interpreted as emission rate, cumulative event number, event energy and dominant frequency (DF). Core cracks were visually shown and cracking mechanism was determined to be a shearing type. A comparison was conducted on three groups of core samples with different strengths. In this manner, AE technology provides a way to characterize real-time deformation process in rock.

### **1.3.2 Micro-seismic monitoring of PDC bit drilling performance during vibration assisted rotational drilling**

This project evaluated drilling performance and drilling mechanism using AE technology on rotary and pVARD drillings. In the Drilling Technology Laboratory, a two-cutter PDC bit was mounted on a laboratory-scale drill rig, along with four AE transducers for real time monitoring. Rotary speed was kept constant for all DOTs. Drilling cuttings were also collected for each test and a particle size distribution chart was obtained. A ROP was obtained for every WOB, and a corresponding AE energy level was obtained.

ROP was correlated with AE energy and the size distribution of cuttings. There was an increase of ROP from pVARD drilling compared to that from rotary drilling.

### **1.3.3 A novel method for assessment of rock-bit interaction and drilling performance using elastic waves propagated by the drilling system**

This project studied drilling performance and drilling mechanisms using SWD technology. Field DOTs were conducted using both rotary and pVARD drilling. Bit vibration was measured for each test by one sensor sub downhole of the ground. An array of one-component (1C) geophones measured seismic waves. Those seismic waves were studied by characteristics such as frequency spectrum and amplitude.

ROP was correlated with the bit vibration level which also affected seismic wave characteristics. In this way, drilling performance can be indirectly studied using seismic analysis. Compared to rotary drilling, the improvement in drilling performance from pVARD drilling was also studied regarding these characteristics.

### **1.3.4 Investigation of active vibration drilling using acoustic emissions and cuttings**

#### **size analysis**

This project used AE technology to study penetration mechanisms and bit-rock interaction in active vibration DOTs. In the Drilling Technology Laboratory, active bit vibration was indirectly provided by one external electromagnetic vibrating table for the purpose of studying the effect on ROP. One impregnated diamond coring bit is mounted on a laboratory-scale drill rig, along with four AE transducers for real time monitoring. Vibration displacement of the rock sample was measured by one laser sensor attached to the stationary rig frame. Rotary speed was kept constant for all DOTs. Drilling cuttings were also collected for each test and a particle size distribution chart was obtained. The three drilling settings were comprised of 60 Hz vibration with two amplitudes, and one passive drilling setting, i.e. there was no vibration source.

Changes in ROP were correlated with changes in AE energy and the size distribution of cuttings. There was an increase of ROP from RPD compared to that from rotary drilling. This was studied in relation to corresponding AE energies and size distribution of cuttings. The spectral analysis was conducted on recorded AE signals and spectral characteristics

were used to correlate crack sizes. A comparison was conducted on ROPs from drilling using varying vibration settings.

### **1.3.5 Characterization of rotary-percussion drilling as a seismic while drilling**

#### **source**

This project was a comprehensive evaluation of the RPD source using SWD technology. Three objectives are described: 1) A study was conducted on frequency spectra of seismic waves from RPD in response to rock strength. A comparison was done on mean powers of seismic waves from RPD and that from conventional drilling using a PDC bit and a roller cone bit; 2) A measurement was conducted on P-wave energy radiation patterns from a hard arkose using both cross-hole survey hydrophones and surface 3C geophones. These geophones included three orthogonal components, i.e. vertical (V), horizontal in-line (H-I) and out-of-line (H-O); 3) A calculation was finished on P-wave particle motion directions of seismic waves recorded by 3C geophones. In addition, polarization analysis is conducted on P-waves recorded at surface geophones for understanding the particle motions.

## **1.4 Literature Review**

This section is a detailed literature review of drilling as a seismic source and introduction to SWD and AE technologies. First, three different drilling technologies are introduced, especially the newly developed pVARD technology. Second, drill bit vibration is analyzed, as bit-rock interaction is the source of seismic radiation. Third, SWD technology

applications are introduced, along with a comparison of seismic sources from three types of drilling. Then, AE technology applications are introduced. Finally, drill cutting size analysis is introduced which provides another way of studying drilling mechanisms and drilling performance.

## **1.4.1 Drilling techniques**

### ***1.4.1.1 Rotary drilling***

As the most widely used drilling technique to date, rotary drilling largely contributes to exploration and production in the oil and gas industry. The rotary drilling process is demonstrated in Figure 1.1. The key components for rotary drilling are the combination of a rotary table and a kelly. A drill pipe is connected to the kelly which is driven by the rotary table, and torque is transferred from the surface down the drill pipe to a drill bit. Weight is applied on the drill bit which is designated as WOB and rock is cracked by the bit-rock interaction. Drilling mud, circulating from the mud tank, is elevated in pressure by the mud pump travelling through the inner hole of drill pipe to the bit, through the nozzle of the bit and up through the annulus between drill pipe and wellbore back to the mud tank. Thus, drilling cuttings are taken by drilling mud circulating through annulus from bottom to surface and the bottom hole is cleaned, which makes the drilling smooth [2].

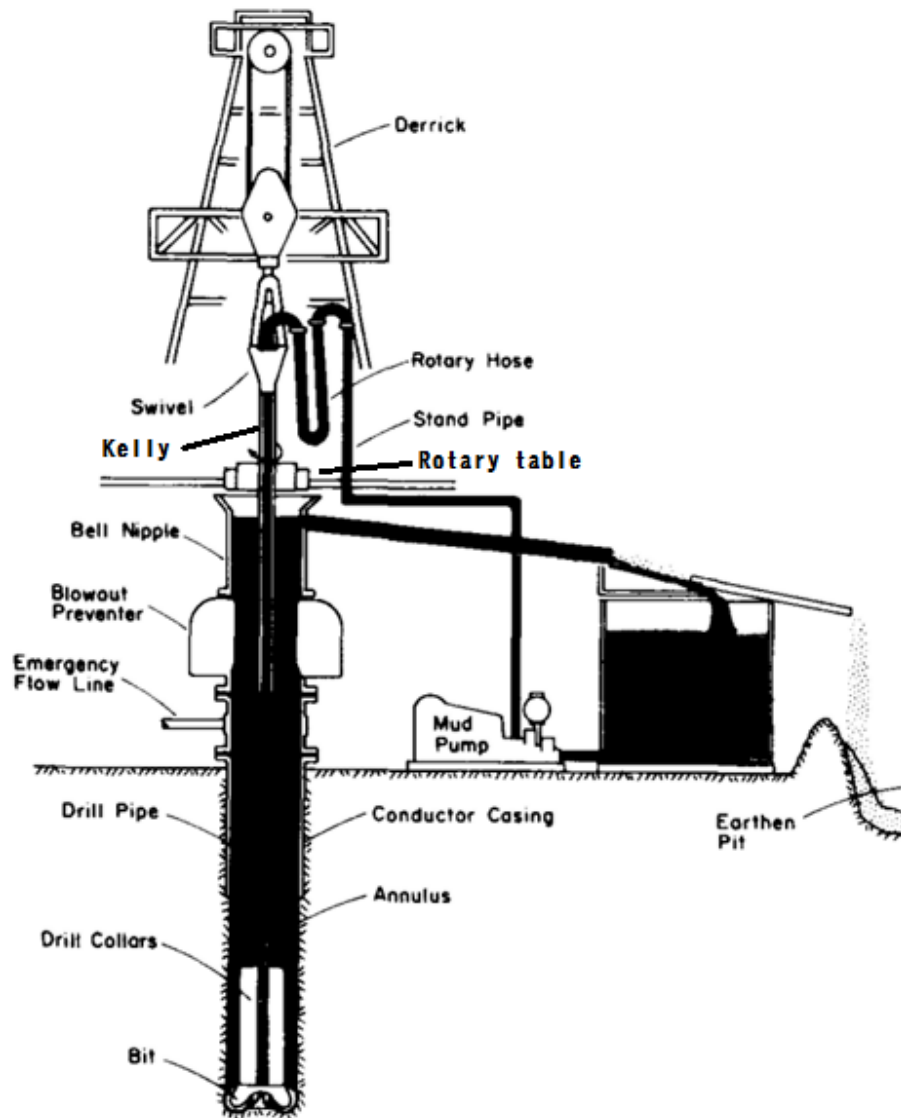


Figure 1.1: Sketch of rotary drilling process modified from Bourgoyne et al. [2]

ROP, or drilling performance, is a key parameter to evaluate the whole drilling process. Increasing ROP has been a goal to be achieved by drilling communities. An empirical relation was proposed by other researchers to describe ROP related factors such as rotary speed, rock strength, WOB, and bit diameter, known as ‘The Perfect-Cleaning Theory’ [1]. This theory is based on the assumption that bottom-hole cuttings are immediately cleaned

after they are generated. In fact, this empirical relation is not perfect as other drilling parameters are not included such as bottom-hole-pressure (BHP), flow rate, and cutting cleaning efficiency. In this manner, another empirical relation has been developed considering both initial chip formation and a cutting removal process. This is known as ‘The Imperfect-Cleaning Theory’, i.e. the bit nozzle hydraulic force and fluid viscosity are added to demonstrate cutting removal [4].

Extensive research has been conducted regarding the effect of BHP, flow rate and cutting cleaning efficiency on drilling performance. In laboratory drilling tests with a single-diamond bit, an elevated BHP tends to inhibit the removal of crushed cuttings which makes new penetration harder. An increase of BHP decreases the volume of cut and ROP [5]. Numerical simulations have also been conducted to study the effect of BHP on the rock cutting process using a Particle Flow Code (PFC2D) model. Under a constant rotary speed, simulation results indicate that ROP decreases in proportion to the logarithm of BHP [6]. The effect of flow rate on drilling performance has been investigated in high velocity jet DOTs. Flow rate is increased when other drilling conditions remain constant. The ROP was increased with the increase of flow rate to its maximum value, and thereafter the ROP decreased [7]. Drilling fluid largely functions in drilling processes and one of its most important roles is cleaning the bottom hole to ensure a smooth bit penetration process [2].

#### ***1.4.1.2 Rotary-percussion drilling***

In 1902, an RPD was first proposed by adding percussive blows to a rotary drilling as a means to improve ROP [8]. Since then, RPD has evolved into one of the most efficient

drilling methods using both top-hammer and down-the-hole hammer configurations. In particular, it is used to rapidly penetrate hard igneous and metamorphic rocks in the mining and construction industries. A percussion tool or hammer is demonstrated in Figure 1.2, and the mechanism is described as follows. First, in position 'A', both a hammer piston and control sleeve are located at the top position of one stroke when the control sleeve spring is extended to its maximum displacement. Then, mud circulation inside the percussion tool is shut off and a high mud pressure is instantaneously built up above the tool. This drives the hammer piston down as shown in position 'B'. Finally, in position 'C', the hammer piston strikes an anvil and corresponding kinematic energy is transferred through the anvil to a drill bit, causing percussive blows to the rock. Thereafter, the hammer piston returns from the bottom due to the rebound of the anvil and the contraction of the hammer spring, until the piston reaches the position 'A'. A full stroke is then finished by a control of the sleeve spring, hammer spring and momentary shut off of fluid circulation.

In the 1950s, RPD was further developed as a resonant sonic technology by applying high-frequency and continuous forces on drill bits, which was extensively tested to successfully increase bit cutting efficiency and improve drilling performance [9]. A percussion tool can be used in both onshore and offshore drillings [10].

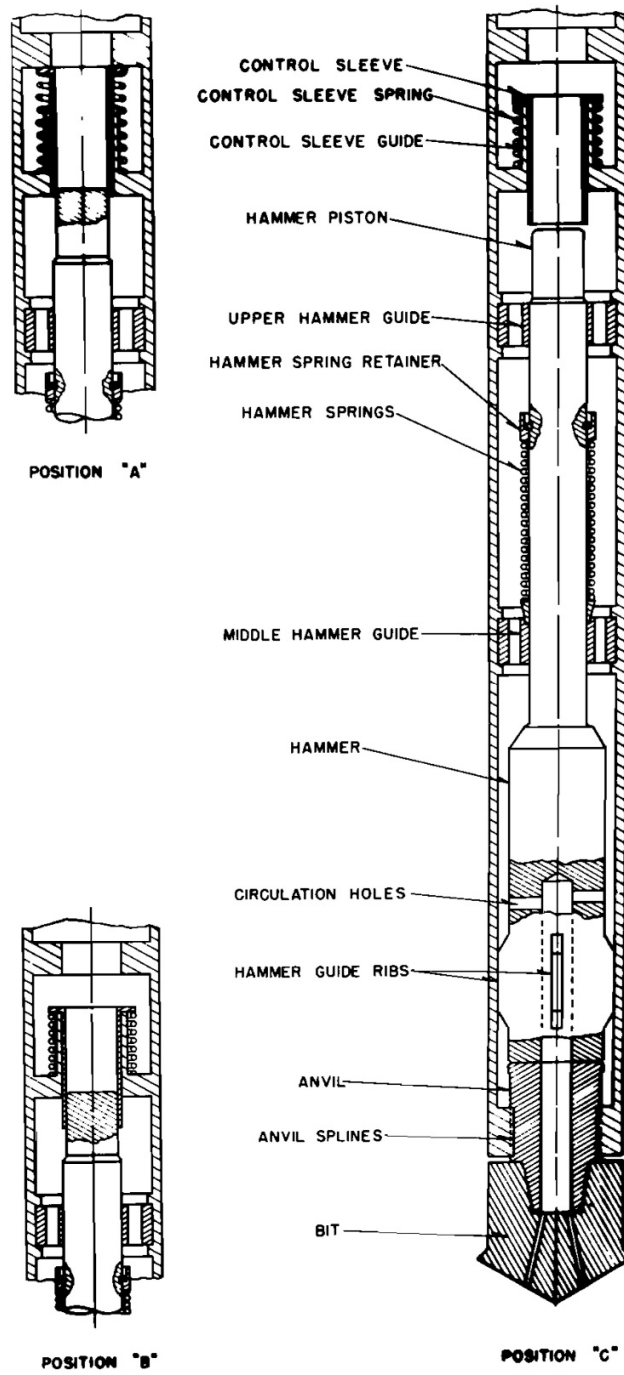


Figure 1.2: Bassinger percussor tool (from Guarin et al. [8])

RPD takes the advantage over rotary drilling by promoting rock failure and dramatically increasing ROP. In RPD, rock fails due to a high frequency of dynamic loads from a drill bit instead of crushing from a stationary force as in rotary drilling. A Fast Lagrangian Analysis of Continua 3D (FLAC3D) model numerically simulated RPD and showed rock failure as aggressive tensile failure due to wave reflection, as well as compressive failure and rock fatigue due to cyclic loading [11]. In this way, the ROP is commonly reported to be higher than that from rotary drilling. In the testing of a percussion tool modified by J.A Wanamaker, it was found that in comparison to rotary drilling, ROP was elevated by 48% and bit life was extended by 120% [12]. Under the same conditions of WOB and rotary speed, RPD was reported to be 7.3 times faster than conventional rotary drilling [13].

Hammers are classified into two types according to the medium used to drive the hammer piston, i.e. hydraulic and pneumatic. A fluid hammer was first applied in the 1990s; thereafter improvement of hammers consisted of changes to hammer design, performance and reliability [14]. Hydraulic hammers have been used to conduct drilling in hard rock formations. Air hammers are limited by penetration depth [13]. Challenges exist when hard rock formations are interbedded with softer and fractured formations. A novel drilling solution was proposed to combine drag bit, percussive hammer and high-pressure fluid jet, known as “Jet Assisted Rotary-Percussion Hammer” [15].

#### ***1.4.1.3 pVARD drilling***

As previously described, RPD and resonant sonic drilling have been successfully applied to rapid drilling in hard rocks, soils and similar unconsolidated materials respectively.

However, for various reasons, neither percussive nor resonant sonic drilling technology is suited for oil and gas drilling in sedimentary formations where well control must be maintained to prevent kicks and blowouts. At the Drilling Technology Laboratory of Memorial University of Newfoundland, one group investigated the possibilities of using natural bit vibration to improve drilling performance for rotary drilling. By drilling with a PDC bit and adding dampening rubbers beneath rock specimens in combination with pulse cavitation, the dampening compliance enhanced the oscillatory bit-rock interaction and resulted in improved cutting efficiency and overall ROP [16]. Thereafter, the idea was further developed to incorporate axial compliance directly into a drill string which also improved ROP. These concepts were progressively investigated, refined and incorporated in both laboratory- and field-scale versions of the pVARD tool, which demonstrated improved ROP under both sets of conditions [17,18].

This pVARD tool (Figure 1.3) consists of an inner hollow shaft and an outer shell, between which relative motions occur. One group of springs and dampening rubbers are included on the inner shaft absorbing and converting natural bit vibrations to axial displacement. This tool is placed above a drill bit adding compliance to the whole drill string. An increase was reported on the bit-rock contact time per revolution and ROP compared to rotary drilling in both laboratory and field tests [17]. The pVARD drilling differs from RPD because natural bit vibration is passively utilized rather than providing active bit vibration.

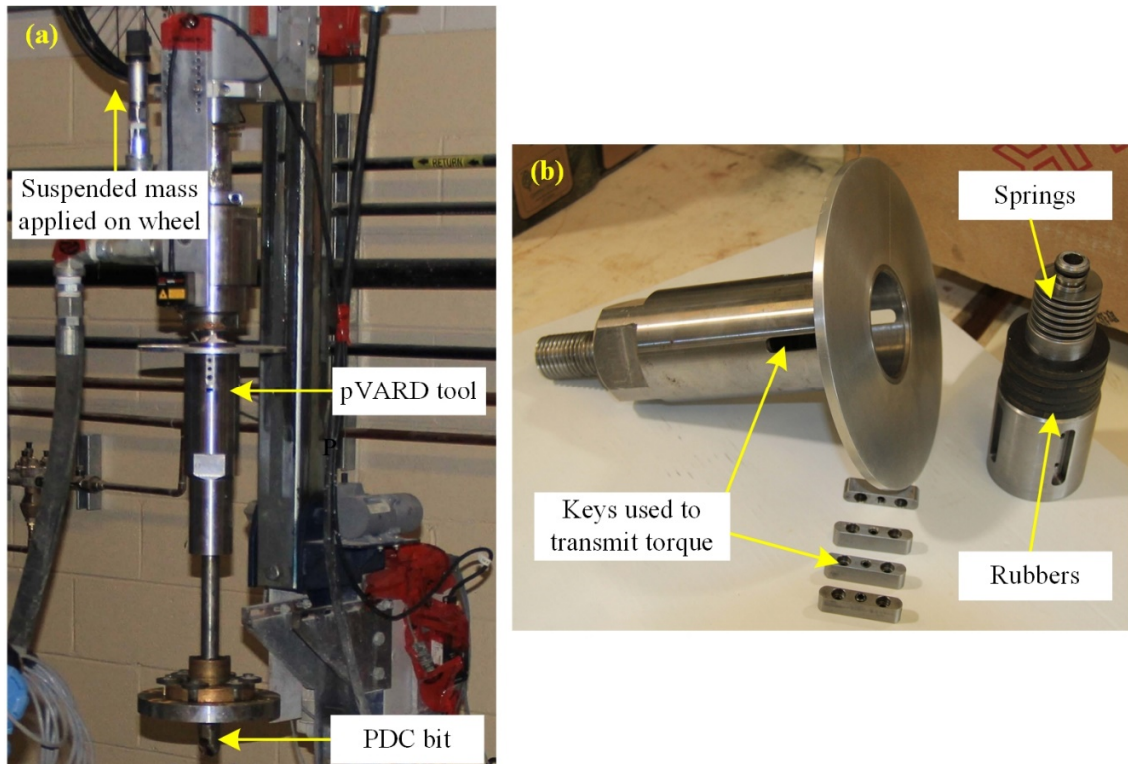


Figure 1.3: (a) Demonstration of pVARD drilling; (b) Laboratory scale pVARD tool. Modified from Rana et al. [17]

#### 1.4.2 Bit vibration and bit-rock interaction

In drilling engineering, drill string vibrations can be considered in terms of axial, lateral and torsional vibrations [19], which are illustrated in Figure 1.4. Axial vibration causes bit bounce. Torsional vibration indicates irregular torsion of the downhole drill string and the stick/slip phenomenon can be observed. Lateral vibration is the most destructive and can cause a strong shock of drill string on the borehole wall. As the drill bit is connected to the drill string, the drill bit vibrates accordingly.

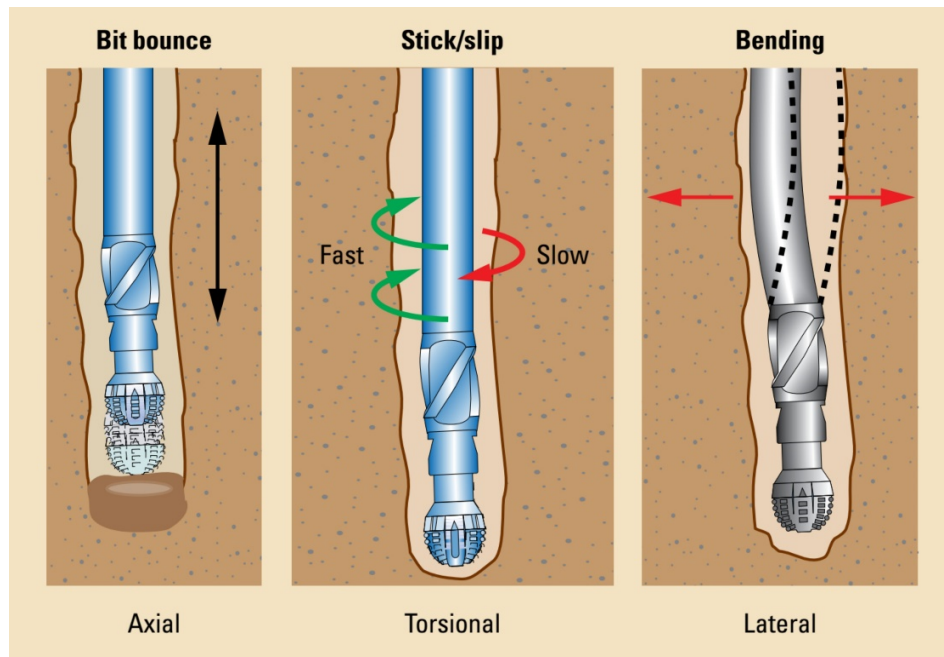


Figure 1.4: Drill string vibrations (from Schlumberger Ltd. [19])

Drilling performance is strongly influenced by bit motions and bit-rock interaction. This has been extensively studied using roller cone and PDC bits. Theoretical models have been developed to study forces applied to roller cone bits as well as the correlation to ROP and drilling conditions [e.g. 20,21]. Empirical relations have been proposed to correlate drag forces on a single-cutter PDC bit to rock type, depth-of-cut (DOC) and bit wear state [e.g. 22]. Some researchers have reported on bit-rock interactions through measurement and evaluation of the three modes of drill string vibrations (i.e. axial, lateral and torsional) recognizing that these drill string vibrations are excited by bit-rock interactions [23]. For example, a numerical study of coupled axial and torsional vibrations identified the root cause of self-excited vibration as the delay in axial position of the bit, during the bit-rock interaction [24]. These bit vibrations were experimentally measured as accelerations with a down-hole sensor sub [25]; interpretation of the acceleration data was used to correlate

bit vibrations to drilling conditions such as: rock type and WOB [26]. In laboratory tests, axial bit vibration generated from the pVARD tool was recorded by a laser sensor, showing that the vibration largely contributed to improving drilling performance [17,18], and peaks in the frequencies of axial bit vibrations were found around the angular velocity and its multiples [23].

### **1.4.3 Seismic While Drilling**

#### ***1.4.3.1 Introduction***

The Seismic While Drilling (SWD) method uses the noise or pulse generated during the bit-rock interaction as a seismic source, which is detected by geophones located at the surface. Figure 1.5 is a schematic overview of the SWD method. This is contrary to the conventional borehole seismic method, in which geophones are lowered down into a borehole receiving seismic waves radiated from sources placed at the surface. This seismic data is used to identify reflections caused by the geological structures and to give information on properties about drilled and to-be-drilled rocks, which is known as the conventional Vertical Seismic Profile (VSP). In this way, the term Reverse VSP (RVSP) is used to indicate a SWD method, in which the seismic source is located in a borehole and receivers are at surface [27].

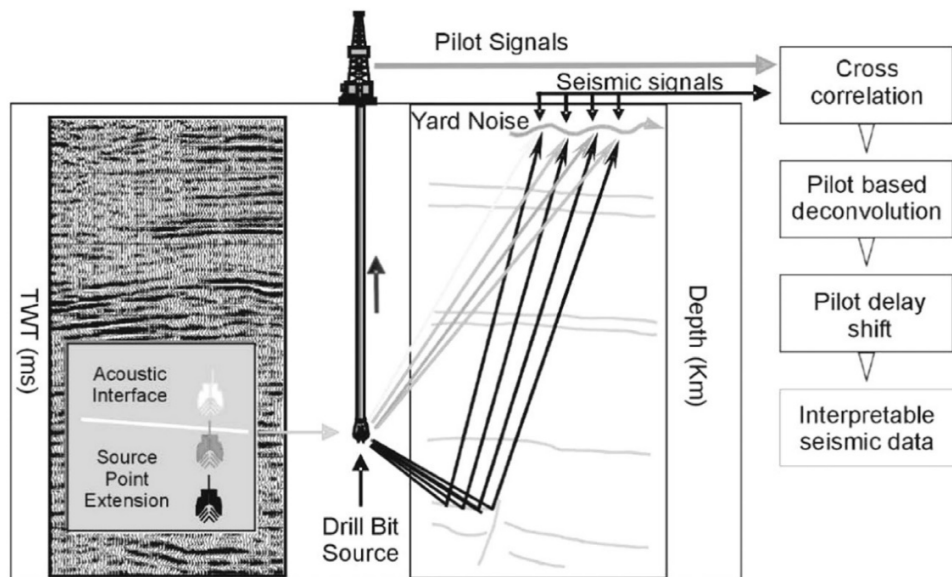


Figure 1.5: Basic concept of seismic while drilling (from Poletto and Miranda [27])

The history of SWD technology dates back to the 1930s. In 1936, a cable tool drilling, an early form of percussive drilling (without rotation), was first proposed to generate discrete signals received by ground geophones, for the purpose of monitoring drill bit location without interrupting normal drilling activities [28]. Unfortunately, this technique failed to mature when rotary drilling became the norm [29]. In 1968, the stiffness of rock was investigated by a geologist from the French Institute of Petroleum (IFP) by exploiting drill bit signals [30]. SWD was intensively studied during the 1980s and 1990s [31]. In 1988, seismic data was recorded from a drill bit and was correlated to the signal recorded by an accelerometer at the top of a drill string. This cross-correlation technique was patented by Societe Nationale Elf Aquitaine, Paris, France [32]. In 1999, BP and Schlumberger built tools to test techniques for seismic measurements while drilling at the Rocky Mountain Oilfield Test Center [33].

#### ***1.4.3.2 Use of drill bit signal as seismic source***

The use of SWD technology has largely expanded its original purpose from locating the drill bit position to others applications. They include positioning the drill bit, real-drill-time imaging ahead of the bit, guiding the bit to a target, and predicting overpressure intervals ahead of the bit etc. [31]. Early studies focused on locating drill bit positions. In 1977, a bit position monitoring method was patented to obtain a precise bit position based on differences in arrival times of seismic signals recorded at ground geophones. For reference, a motion sensor (commonly called a 'pilot sensor') was attached on the drilling apparatus to record signals arriving directly along the drill pipe. Discrete elastic waves were generated when the drill bit was raised and suddenly released to impact the bottom-hole [34]. In 1984, a new method of determining drill bit positions was patented by analyzing coherent drill bit signals. During drilling, the bit-rock interaction generated seismic signals recorded by a group of geophones. First, a bit location was assumed. Then, a signal received by a geophone was time shifted by the time of elastic wave travelling from the assumed bit location to this geophone. Furthermore, the rest of the signals were time shifted by an appropriate time from this bit location to a specific geophone. Finally, the coherency about this bit location was determined by adding or multiplying those time shifted waveforms. This procedure was repeated on multiple possible bit locations. The drill bit position was precisely determined by the highest coherency [35]. After that, a method of cross correlation was used, i.e. continuous seismic signals were correlated based on a reference geophone at top of the drill string. Seismic signals were obtained from offshore SWD surveys using the TOMEX® SWD system (Baker Atlas). A time-depth (T-D) curve was obtained to continuously monitor drill bit position [36].

The drilling community has expressed great interest in using SWD technology to study the bit-rock interaction and drilling conditions. The spectral content analysis is a frequently used method for analyzing properties of rocks drilled and drill bit conditions. In 1972, the Société nationale des pétroles d'Aquitaine (SNPA) developed a dynamic model for estimating the vibration state along a drill string based on the longitudinal vibration theory. The vibration originated from the bit-rock interaction based on a tricone bit. In this way, this technology allows us to predict rock properties, especially the hardness by means of measuring the vibration state at the kelly [37]. In 1990, frequency peaks of bit accelerations recorded from laboratory drillings shifted with varying wear state of a roller cone bit teeth as defined by the International Association of Drilling Contractors (IADC). Thus, the signature of bit vibration provided a way of predicting bit wear states [38]. From a field test, frequency spectra of seismic signals showed a relation to bit geometries of both coring bits and roller cone bits, i.e. seismic frequency peaks were at multiples of the blades of bits [39]. In addition, frequency spectra from RPD sources showed relationships between specific frequency bands to varying drilling conditions [40], bit types [41] and rock types [42].

#### ***1.4.3.3 SWD sources in rotary drilling, rotary-percussion drilling and pVARD drilling***

For the purpose of SWD, seismic sources in the three drillings differ due to differences in both bit vibration and bit-rock interaction. For rotary drilling, roller cone bits and PDC bits are most widely used. Characteristics of seismic waves from them will be described in the following two paragraphs. RPD sources will also be detailed due to its wide application in

mining drilling. Seismic radiation generated in the pVARD drilling has not been studied before, but the bit vibration level is more comparable to that of rotary drilling, than to that of RPD.

A roller cone bit (e.g. tricone) mainly works through an indentation and gouging mechanism during drilling. When a roller cone bit interacts with a hard rock formation, axial vibration mainly comes from two aspects: the high frequency vibration caused by teeth indentation and the low frequency vibration caused by the lobed pattern. Figure 1.6 shows the tooth indentation of a roller cone along with samples of teeth forces measured from experiments. Periodic forces indicate a periodic vibration from the indentation of roller cone teeth. Figure 1.7 shows three lobes of a tricone bit along with three samples of bit forces. The combination of two periodic vibrations generates a new periodic vibration. Those periodic forces from the lobed pattern show a lower frequency of vibration than that from the tooth indentation. Every tooth of the roller cone bit generates a percussive pulse and each pulse can be regarded as wideband [43]. Downhole measurements have shown that axial and torsional vibrations are largely quasi-random due to the unevenness of formation strength and random breakage process [44]. In this way, the spectrum of seismic waves radiated from a roller cone bit becomes wideband, which makes it ideal as a seismic source [27].

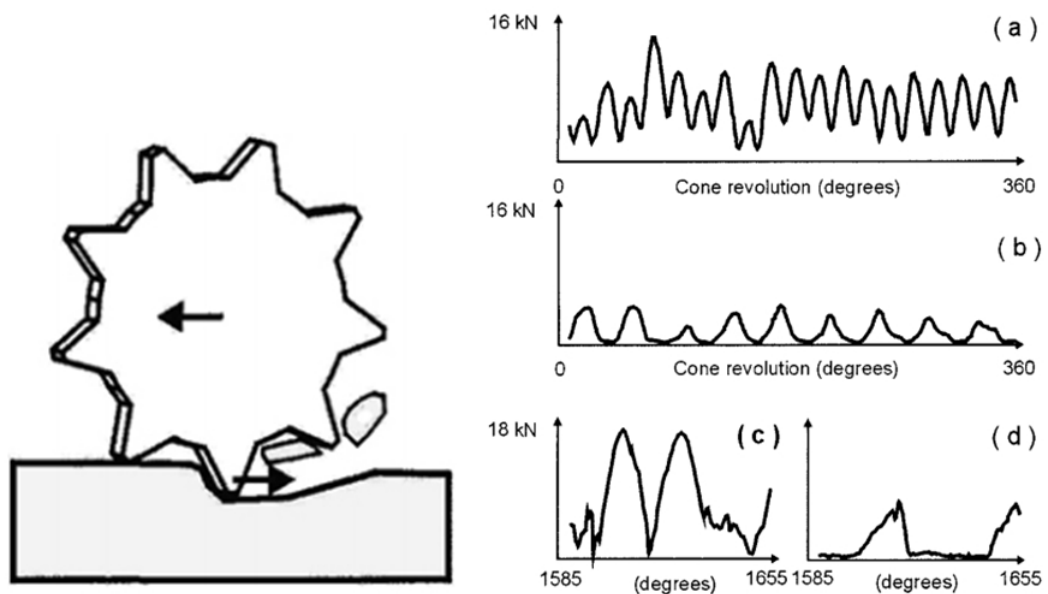


Figure 1.6: Roller tooth indentation and gouging action are demonstrated on left column; Measured cone teeth forces in right column: (a) cone outer row, (b) cone inner row, (c) particular of outer row, (d) particular of inner row which is modified from Sheppard and Lesage [21]

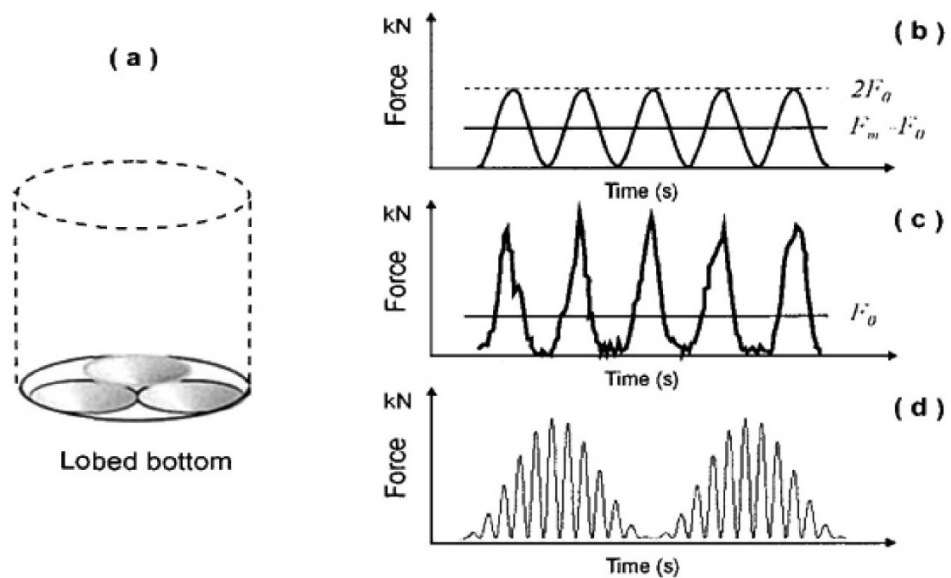


Figure 1.7: (a) Lobed pattern of one tricone bit; Vibration forces from modeling when (a) average vertical force  $F_m = \text{WOB}$  and (b) maximum force  $F_{\max} = 2\text{WOB}$ , (c) downhole real data. Modified from Poletto and Miranda [27]

A PDC bit has cutting and grinding mechanisms. Figure 1.8 shows a force analysis for a cutter on a multi-cutter PDC bit. In the cutting action, a concentration zone of high compressive stresses occurs before the cutter with a certain clearance angle in (a) while (b) shows a cutter with zero clearance angle. This compression zone exists in the direction of the resultant force, and a high tensile stress zone exists around the cutter edges. In the grinding action, tensile stresses exist behind the cutter and compressive stresses occur ahead of it. In this manner, it is found that forces on cutters are usually constant. This penetration mechanism differs from that of a roller cone bit which incorporates both percussive and gouging actions. In comparison of the roller cone bit drilling, seismic waves radiated from the PDC bit drilling are lower in magnitude. This shows that PDC bits are less favorable than roller cone bits for SWD purposes [27].

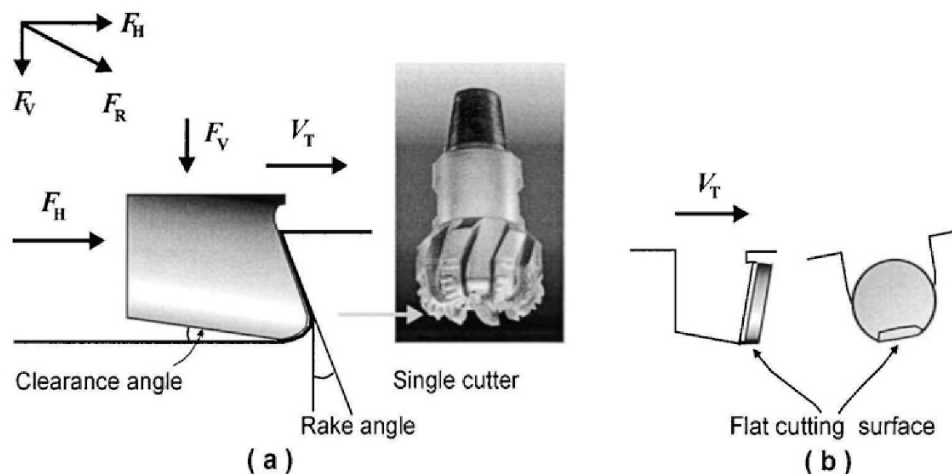


Figure 1.8: (a) Forces applied on single PDC cutter; (b) Wear flat area. Modified after Guyen Minh Duc et al. [45]

The RPD drilling is ideal for SWD analysis due to a high magnitude and wideband frequency spectrum of seismic waves radiated from its percussive action. Some

applications (see below) show RPD a great potential for SWD purposes. In an RPD test, frequency spectra and energy levels of RPD sources were successfully correlated to varying percussion rates [40]. A new Rotary-Percussion Sounding System (RPSS) monitored drilling parameters in an RPD drilling. These parameters were successfully used to estimate the strength of in-situ rock. Applications of this system showed that RPD was a potential for SWD due to its high density and broad frequency spectrum in recorded seismic waves [46,47]. In hard rock environments, a reverse circulation percussion drilling provided stronger and wider band seismic sources than most standard active sources [41]. RPD drilling in simulated lunar rocks in the laboratory has been performed to assist lunar exploration [42].

Generally, the seismic source from a roller cone bit is wideband, and higher in magnitude than that from a PDC bit. RPD source is wideband with strong magnitude. Both roller cone bit sources and RPD sources are more favorable for SWD drilling purposes than PDC bit sources.

#### ***1.4.3.4 Wave radiation patterns at drill bit sources***

The geotechnical and engineering communities have expressed a great interest in the study of radiation patterns of drill-bit seismic sources. For the simplified situation of a homogeneous and isotropic medium, the source radiation from a single force has been theoretically studied. A mathematical model of radiation has been proposed when three types of stresses are applied at one cylindrical hole which is embedded in an infinite solid medium (Figure 1.9). The radiated waves were interpreted as P-waves and S-waves. The

latter waves can be vertically polarized SV, or horizontally polarized SH. P-wave amplitude was maximized parallel to the stress direction and minimized perpendicular to the stress direction [48]. Another theoretical model calculated the radiation patterns of P-wave and SV wave under a harmonic vertical force applied to an infinite, homogeneous, and isotropic medium. These patterns resembled that under a single force [49,50]. In realistic situations, inhomogeneity and anisotropy of a medium significantly complicate the radiation pattern. A theoretical model was proposed to study source radiation patterns in a finely stratified medium with randomly distributed elastic parameters. The radiation patterns significantly differed from those calculated in an isotropic and homogeneous medium [51].

Field measurements of radiation patterns from drillings have shown a good agreement with the theoretical radiation patterns. In a roller cone bit drilling (Figure 1.10), measurements of P-wave amplitudes decreased with increasing angles which are measured relative to the direction of axial drill-tooth impact. SV wave amplitudes were reported higher than that for SH wave. These measurements confirmed the theoretical radiation patterns [52,53]. In another field cross-hole survey, SV wave amplitudes were measured for different depths in a tricone bit drilling. Measurements were analogous to the theoretical SV wave radiation patterns [54].

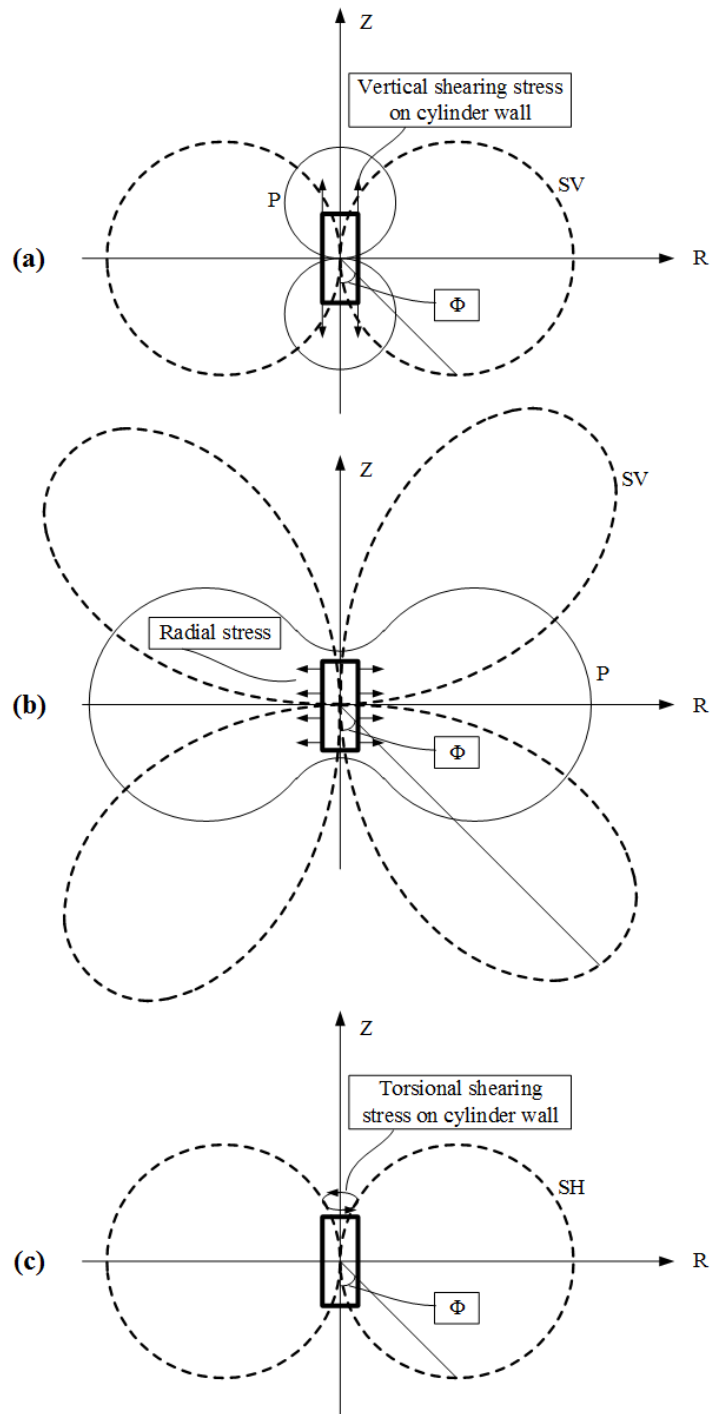


Figure 1.9: Source radiation and wave amplitudes in solid medium radiated from a cylinder hole wall subjected to (a) vertical shearing stress, (b) radial stress and (c) torsional shearing stress. Modified from Heelan [48]

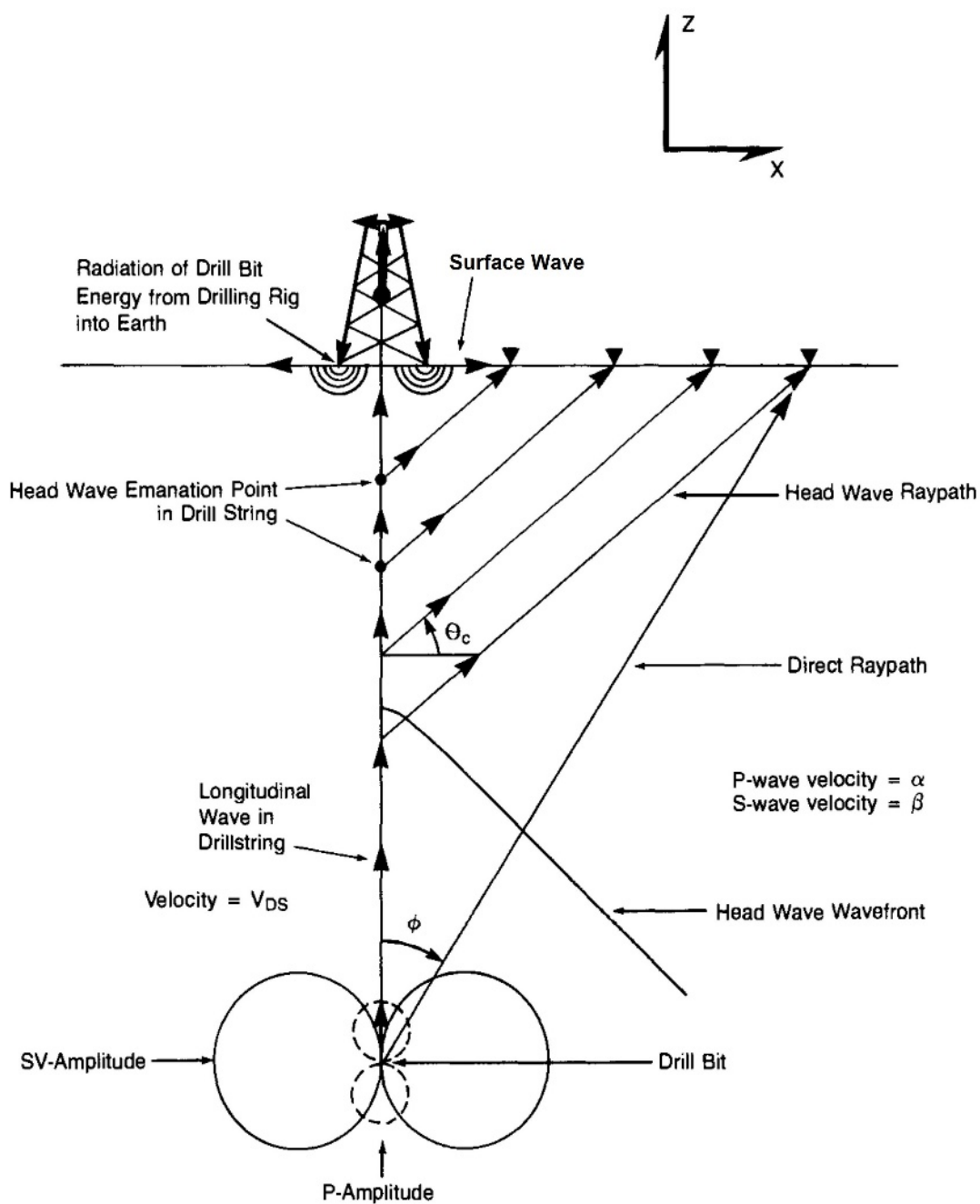


Figure 1.10: Available elastic waves in drilling, i.e. head wave, direct arrival, rig-related arrival as surface wave (from Rector and Hardage [53])

#### ***1.4.3.5 Polarization analysis***

The purpose of polarization analysis is to determine the actual particle motion (displacement) direction of seismic waves. In this manner, the true wave motion can be understood. A particle motion direction is calculated by the following procedures. First, the original components of a hodogram, i.e. a cross-plot of seismic wave amplitudes recorded by two components, are projected to a new coordinates system which is rotated within that plane. Second, the power of projected components are calculated. Third, the maximum power is found from all rotated coordinates; the angle of rotation for the maximum value is then taken as the polarization angle and the corresponding direction is defined as the particle motion direction [55]. In Figure 1.11, the two original components are projected to a new coordinate X'-Y' and the corresponding energy is calculated for the angle of rotation. The direction with the maximum power, i.e. at the rotation angle of  $\theta_{max}$  is defined as the polarization direction. The polarization analysis has been used to investigate polarization angles. In a roller cone bit drilling, 3C geophones recorded seismic waves. It was found that polarization angles were in correlation with varying azimuths and offsets of these geophones [56]. Seismic event types (P-refracted, converted shear, ground roll) were discriminated by comparing polarization angles, which were highly correlated to the source-geophone geometry. This correlation has been successfully used to confirm the actual geophone orientation [57].

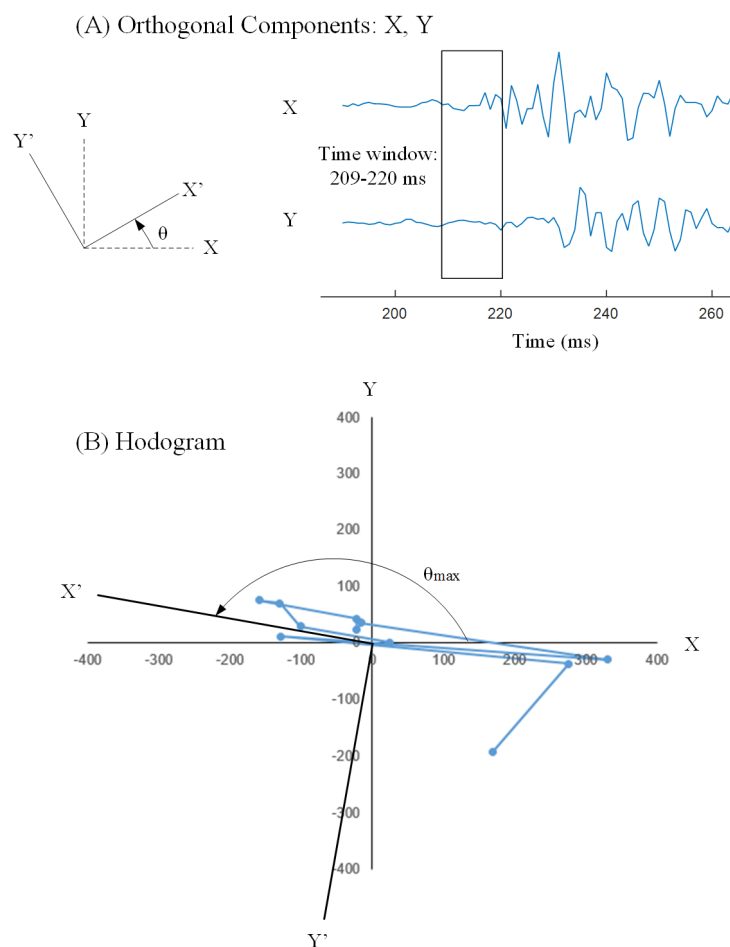


Figure 1.11: (A) Two components signals at a 3C geophone; (B) Corresponding hodogram from the time window 209-220 ms with a polarization angle oriented to the maximum energy direction, which is modified after DiSiena et al. [55]

## 1.4.4 Acoustic emission

### 1.4.4.1 Introduction

There are commonly two acoustic technologies used in the geotechnical area: sonic technology and AE technology. Figure 1.12 demonstrates basic principles of the two acoustic technologies. Sonic technology utilizes two transducers: one transmitter which generates mechanical signals, and one receiver which monitors signals as transmitted

through a geological structure. AE technology uses one transducer (or receiver) to passively monitor self-generated signals within this structure [58]. In the early 1940s, the sonic technology was utilized by two researchers from the U.S. Bureau of Mines (USBM) to study underground mining. Rock bursts and mine failures were predicted by a success in recording micro-level ‘sounds’ when a transmitter was turned off [59,60]. The utilization of AE technology was generally regarded as starting in the late 1940s from the work conducted by Kaiser on metals [61]. During the 1950s and 1960s, AE monitoring was concentrated on studying underground mining [62,63], and tunnel roof safety [64,65]. After the 1970s, numerous laboratory AE studies were conducted on the failures in physical models of pressured cavities [66], an estimation of in-situ stress [67,68], the creep behavior of rock salt [69,70], the phenomenon of hydraulic fracturing [71], and the mechanical deformation behavior of rock [72,73].

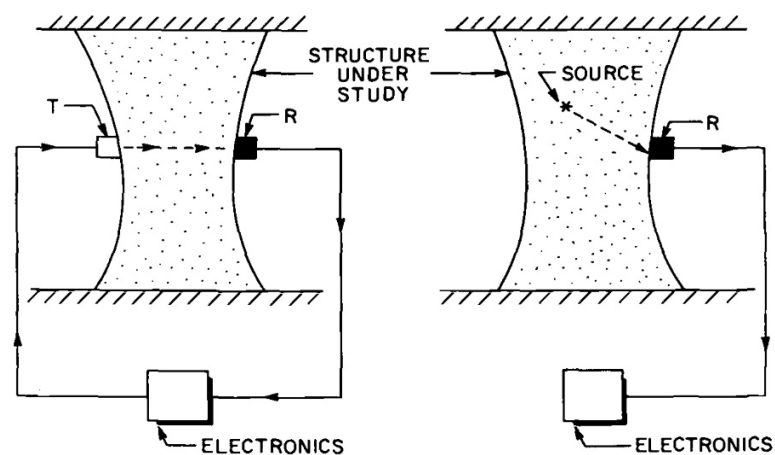


Figure 1.12: Two acoustic technologies used to study geological structure: sonic technology (left) and AE technology (right) (after Hardy [58])

There are two types of signals received by AE transducers: burst and continuous signals (Figure 1.13). A burst of signal is commonly correlated to a short time crack or deformation

such as crack initiation. It is readily identified because the beginning and end are easily recognized. While, this situation does not apply to a continuous signal which is related to external noises [74]. Burst signal amplitudes are significantly larger than that of both background noises and continuous signals. A high frequency is commonly found in a continuous signal [75]. The frequency distribution of an AE signal depends on a source and the distance between the source and a receiver. Figure 1.14 shows the typical frequency ranges of AE signals and application areas. AE signals were observed with frequencies lower than 1 Hz in the field; they were also reported to be of high frequencies more than 500 kHz in laboratory [58].

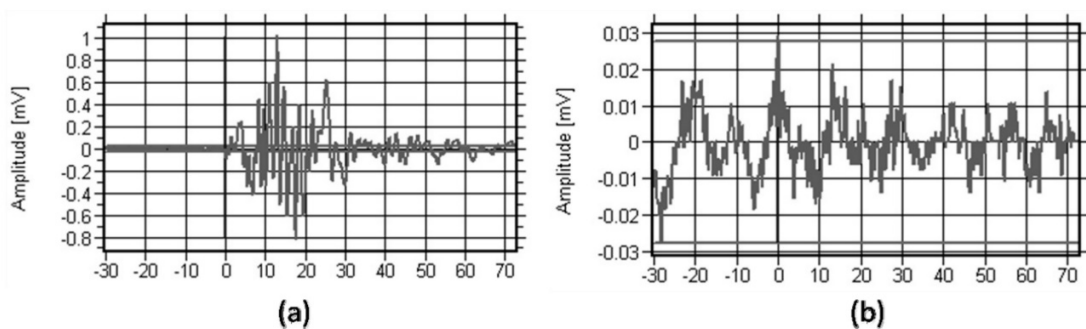


Figure 1.13: Two types of AE signals: (a) burst and (b) continuous (after Ríos-Soberanis [74])

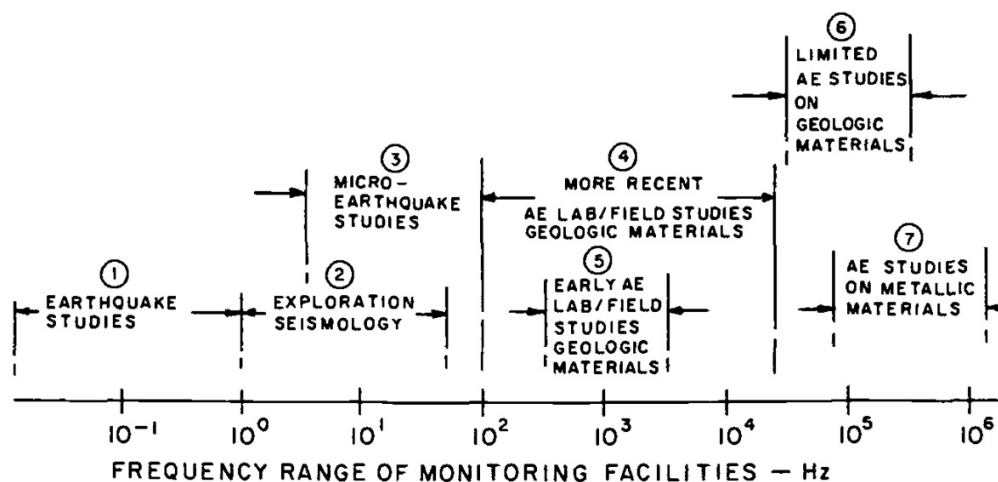


Figure 1.14 Typical AE signal frequency ranges (after Hardy [58])

#### 1.4.4.2 Rock deformation and failure

In geotechnical testing, piezoelectric transducers are commonly used in the study of rock deformation and fracturing processes. In a laboratory test, four different deformation stages were identified from a standard strength test on rock samples under triaxial stresses (Figure 1.15). AE transducers were commonly put on both top and bottom ends of rock specimens to monitor the whole deformation process until rock failure [73,76,77]. A sequence of burst of signals were commonly recorded and some AE parameters were interpreted such as DF, energy, hit rate, and cumulative AE count. The cumulative count dramatically increased when a new crack initiated at the end of elastic deformation stage II. AE source locations were commonly calculated to track the crack propagation to map failures in one dimension [78], two dimensions [79], and three dimensions [80]. In addition, numerical models have simulated the seismicity of the rock deformation and failure [81,82].

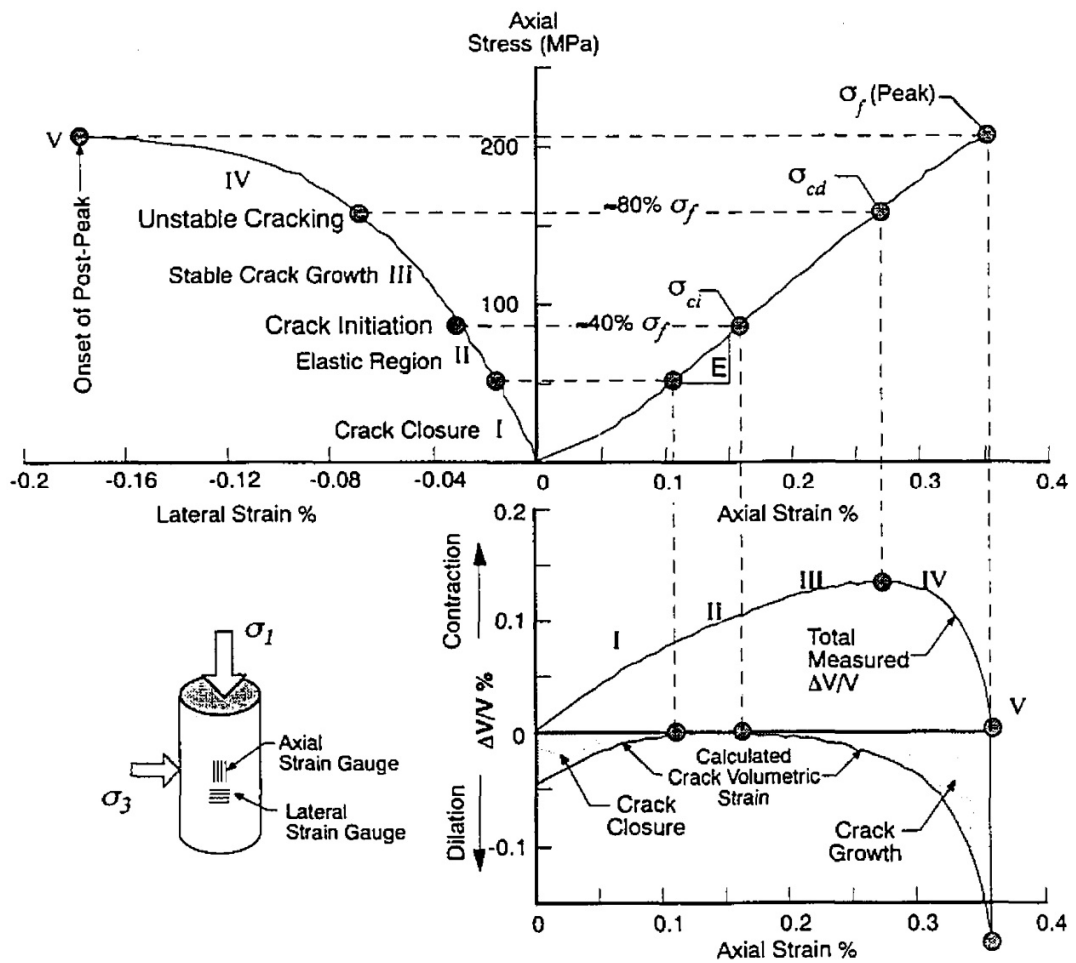


Figure 1.15: Stress-strain diagram showing the deformation process of rock (after Martin [83])

#### 1.4.4.3 Drilling using AE technique

In the drilling area, most studies refer to SWD technique, while some uses of AE technique are relevant to geotechnical drilling. AE studies on drilling commonly concentrate on the study of coal exploitation due to a high risk of exposure to dust illness. In a drilling test on coal samples, a single-cutter bit was used under varying advance rates. AE signals were monitored. Their characteristics were successfully correlated to size and shape distributions

of coal cuttings, and bit wear states [84,85]. Drill bit wear states were reflected significantly by AE characteristics [86,87]. For the drilling with a impregnated diamond bit, the dominant bit action consisted of cutting and friction processes [88], and the processes were investigated by monitoring AE signals. From the experimental results, AE signal amplitudes were used to show the change of DOC [89].

#### 1.4.5 Cutting size and drilling performance

The particle size is of great importance for studying characteristics of rock debris in the geotechnical area. In 1933, a particle size distribution (PSD) function was first proposed from a sieving analysis on powdered coal, known as the Rosin-Rammler (RR) model [90], or Rosin-Rammler-Sperling-Bennett (RRSB) model [91]. Later, this model was widely used to describe the PSD of powders of various types and sizes, and was specifically suited to representing powders from operations such as grinding, milling, and crushing [92]. This two-parameter model is described in Equation 1.1.

$$R(d) = 100 \exp\left[-\left(\frac{d}{d_m}\right)^n\right] \quad (1.1)$$

$R(d)$  = retained weight fraction or cumulative weight percent (%);  $d$  = particle size or mesh size ( $\mu\text{m}$ );  $d_m$  = mean particle size ( $\mu\text{m}$ ); and  $n$  = measure of the spread of particle sizes distribution parameter. Calculations of the two parameters are commonly done by linear regression of data represented as  $\{ \log[-\log(\text{cumulative percentage oversize})] \}$  versus  $[\log(\text{retaining powder sieve size})]$ . This linear regression is facilitated by a routine use of

Matlab® codes, in which 36.79% of cumulative percentage oversize corresponds to a sieve size, i.e. mean particle size [93].

A PSD is commonly obtained from a sieving test, which is one of the major methods used to physically divide a collection of cuttings into sub-classes. Separated fractions are retained by test sieves with apertures allowing cuttings undersize to pass through, and then weighted. Principles of the selection of test sieves, operations, and reporting of results are detailed in a book [91]. An operational standard from American Society for Testing and Materials (ASTM) governs sieving in the range from 75  $\mu\text{m}$  to 75 mm [94]. For particles finer than 75  $\mu\text{m}$ , a sedimentation method using the hydrometer is recommended to quantitatively calculate soil particle sizes [95]. The PSD can be presented by three ways: tabular listing fraction of specific size, mathematical expression using formulae, and graphical means. The typical way is to express PSD as a normal-logarithmic relationship. A new bar particle size distribution (BPSD) diagram was proposed to be more directly compare different size ranges of cutting particles [96].

In drilling, ROP has been previously correlated to the cutting size. Extensive drilling tests showed a positive relation between ROP and the cutting size, i.e. the higher the penetration rate, the higher magnitude of the mean particle size in a diamond core bit drilling [97,98], RPD [99] and a PDC bit drilling [96]. Limitations of those research works are a lack of direct measurement of crack related energy, to facilitate the interpretation of the mechanism of higher ROP. Although AE technology has been used in studying the bit advance rate and corresponding cutting size distribution with a single-cutter bit in the lab [84,85], drillings

in real world are more complicated due to multiple drag cutters and varying drill bits such as roller cone and hammer.

## 1.5 References

1. Maurer WC. The perfect-cleaning theory of rotary drilling. *J Petrol Technol.* 1962;14(11):1270-1274. doi:10.2118/408-PA
2. Bourgoyne AT Jr, Millheim KK, Chenevert ME, Young FS Jr. *Applied Drilling Engineering*. Richardson, TX: Society of Petroleum Engineers; 1991.
3. Mozaffari M. *Development and Characterization of Portland Cement-Based Synthetic Rock Materials* [master's thesis]. St. John's, Canada: Memorial University of Newfoundland; 2013.
4. Warren TM. Penetration rate performance of roller cone bits. *SPE Drill Eng.* 1987;2(1):9-18. doi:10.2118/13259-PA
5. Garner NE. Cutting action of a single diamond under simulated borehole conditions. *J Petrol Technol.* 1967;19(7):937-942. doi: 10.2118/1701-PA
6. Akbari B, Butt SD, Munaswamy K, Arvani F. Dynamic single PDC cutter rock drilling modeling and simulations focusing on rate of penetration using distinct element method. Paper presented at: 45th US Rock Mechanics / Geomechanics Symposium; June 26-29, 2011; San Francisco, CA

7. Khorshidian H, Butt SD, Arvani F. Influence of high velocity jet on drilling performance of PDC bit under pressurized condition. Paper presented at: 48th U.S. Rock Mechanics/Geomechanics Symposium; June 1-4, 2014; Minneapolis, MN.
8. Guarin PL, Arnold HE, Harpst WE, Davis EE. Rotary percussion drilling. Paper presented at: Twenty-ninth API Annual Meeting; November 1949; Chicago, IL.
9. Volk BW, McLellan GW, Moak DJ, Lerch RE, Thompson KM, Barrow JC. ResonantSonic drilling: history, progress, and advances in environmental restoration programs. International Atomic Energy Agency.
10. US Department of Energy. Russian drilling technology studies. <http://www.netl.doe.gov/kmd/CDs/Disk36/Man1.pdf>.
11. Han G, Bruno M, Dusseault MB. Dynamically modelling rock failure in percussion drilling. Paper presented at: The 40th U.S. Symposium on Rock Mechanics; June 25-29, 2005; Anchorage, AK.
12. Samuel GR. Percussion drilling...is it a lost technique? a review. Paper presented at: Permian Basin Oil and Gas Recovery Conference; March 27-29, 1996; Midland, TX.
13. Melamed Y, Kiselev A, Gelfgat M, Dreesen D, Blacic J. Hydraulic hammer drilling technology: developments and capabilities. *J. Energy Resour Technol.* 1999;122(1):1-7. doi:10.1115/1.483154

14. Han G, Bruno MS. Percussion drilling: from lab tests to dynamic modeling. Paper presented at: International Oil & Gas Conference and Exhibition in China; December 5-7, 2006; Beijing, China.
15. Pixton DS; Novatek Inc. Development and testing of a jet assisted polycrystalline diamond drilling bit: phase II development efforts.
16. Babapour S, Butt SD. Investigation of enhancing drill cuttings cleaning and penetration rate using cavitating pressure pulses. Paper presented at: The 48th U.S. Rock Mechanics/Geomechanics Symposium; June 1-4, 2014; Minneapolis, MN.
17. Rana PS, Abugharara AN, Butt SD, Molgaard J. Experimental evaluation of passive-Vibration Assisted Rotary Drilling (p-VARD) tool to enhance drilling performance. Paper presented at: The 49th U.S. Rock Mechanics/Geomechanics Symposium; June 28-July 1, 2015; San Francisco, CA.
18. Xiao Y, Zhong J, Hurich C, Butt SD. Micro-seismic monitoring of PDC bit drilling performance during vibration assisted rotational drilling. Paper presented at: The 49th U.S. Rock Mechanics/Geomechanics Symposium; June 28-July 1, 2015; San Francisco, CA.
19. Schlumberger Ltd. Drillstring vibrations and vibration modeling. [https://www.slb.com/~media/Files/drilling/brochures/drilling\\_opt/drillstring\\_vib\\_br.pdf](https://www.slb.com/~media/Files/drilling/brochures/drilling_opt/drillstring_vib_br.pdf).
20. Biggs MD, Cheatham JB. Theoretical forces for prescribed motion of a roller bit. *Soc Petrol Eng J.* 1969;9(04):473-481. doi:10.2118/2391-PA

21. Sheppard MC, Lesage M. The forces at the teeth of a drilling rollercone bit: theory and experiment. Paper presented at: SPE Annual Technical Conference and Exhibition; October 2-5, 1988; Houston, TX.
22. Glowka DA. Use of single-cutter data in the analysis of PDC bit designs: part 1 - development of a PDC cutting force model. *J Petrol Technol.* 1989;41(8):797-849. doi:10.2118/15619-PA
23. Reyes R. *Bit-Rock Interaction in Rotary Drilling: Numerical and Experimental Study* [master's thesis]. St. John's, Canada: Memorial University of Newfoundland; 2017.
24. Richard T, Germy C, Detournay E. Self-excited stick-slip oscillations of drill bits. *C R Mecanique.* 2004;332(8):619-626. doi:10.1016/j.crme.2004.01.016
25. Gao Q. *Development of Laboratory and Field Drilling Tools to Measure Bit Operating Conditions and Drill String Motions* [master's thesis]. St. John's, Canada: Memorial University of Newfoundland; 2014.
26. Rahman R. *Development and Interpretation of Downhole Data from Downhole Vibration Monitoring Tool* [master's thesis]. St. John's, Canada: Memorial University of Newfoundland; 2015.
27. Poletto FB, Miranda F. *Seismic While Drilling: Fundamentals of Drill-Bit Seismic for Exploration.* Oxford, UK: Elsevier Ltd; 2004.

28. Weatherby BB, inventor; Geophysical Res Corp, assignee. Method of making sub-surface determinations. US patent 2,062,151. November 24, 1936.
29. Meehan R, Miller D, Haldorsen J, Kamata M, Underhill B. Rekindling interest in seismic while drilling. *Oilfield Rev.* 1993;5(1):4-13.
30. Naville C, Serbutoviez S, Throo A, Vincké O, Cecconi F. Seismic while drilling (SWD) techniques with downhole measurements, introduced by IFP and its partners in 1990-2000. *Oil Gas Sci Technol - Rev IFP.* 2004;59(4):371-403. doi:10.2516/ogst:2004027
31. Hardage B. Seismic-while-drilling: techniques using the drill bit as the seismic source. AAPG Search and Discovery website. <http://www.searchanddiscovery.com/documents/2009/40411hardage/index.htm>.
32. Staron P, Arens G, Gros P, inventors; Societe Nationale Elf Aquitaine, assignee. Method of instantaneous acoustic logging within a wellbore. US patent 4,718,048. January 5, 1988.
33. Anchliya A. A review of seismic while drilling (SWD) techniques: a journey from 1986 to 2005. Paper presented at: SPE Europec/EAGE Annual Conference and Exhibition; June 12-15, 2006; Vienna, Austria.
34. Bailey JR, inventor; Senturion Sciences Inc, assignee. Continuous bit positioning system. US patent 4,003,017. January 11, 1977.

35. Katz LJ, inventor; Katz Lewis J, assignee. Method and system for seismic continuous bit positioning. US patent 4,460,059. July 17, 1984.
36. Rector JW, Weiss DS. Real-time drill-bit VSP from an offshore platform. Paper presented at: 1989 SEG Annual Meeting; October 29-November 2, 1989; Dallas, TX.
37. Lutz J, Quichaud C, Raynaud M, Raynal J, Mucklero JA, Gstalder S. Instantaneous logging based on a dynamic theory of drilling. *J Petrol Technol.* 1972;24(06):750-758. doi:10.2118/3604-PA
38. Jardine SI, Lesage ML, McCann DP. Estimating tooth wear from roller cone bit vibration. Paper presented at: SPE/IADC Drilling Conference; February 27-March 2, 1990; Houston, TX.
39. Gradl C, Eustes AW, Thonhauser G. An analysis of noise characteristics of drill bits. Paper presented at: The 2008 SPE Annual Technical Conference and Exhibition; September 21-24, 2008; Denver, CO.
40. Yokota T, Onishi K, Karasawa H, Ohno T, Ota A, Kaneko T. Seismic while drilling: basic experiments using a percussion drill as an energy source. *Explor Geophys.* 2004;35(4):255-259. doi: 10.1071/EG04255
41. Sun B, Bóna A, Zhou B, van de Werken M. A comparison of radiated energy from diamond-impregnated coring and reverse-circulation percussion drilling methods in hard-rock environments. *Geophysics.* 2015;80(4):K13-K23. doi:10.1190/geo2014-0344.1

42. Poletto F, Magnani P, Gelmi R, et al. Seismic while drilling ( SWD) methodology in support to moon subsurface stratigraphy investigations. *Acta Astronaut.* 2015;110:99-114.
43. Hardage BA. *Crosswell Seismology and Reverse VSP*. London, UK: Geophysical Press; 1992.
44. Skaugen E. The effects of quasi-random drill bit vibrations upon drillstring dynamic behavior. Paper presented at: SPE Annual Technical Conference and Exhibition; September 27-30, 1987; Dallas, TX.
45. Guyen Minh Duc N, Cholet H, Tricot P. Stress concentration induced in elastic rocks under a diamond bit tooth. Paper presented at: Fall Meeting of the Society of Petroleum Engineers of AIME; October 8-11, 1972; San Antonio, TX.
46. Chitty DE, Blouin SE, Zimmer VL, Thompson PH, Tremba EL. Rotary percussion sounding system for in situ rock mass characterization. Paper presented at: The 40th U.S. Symposium on Rock Mechanics; June 25-29, 2005; Anchorage, AK.
47. Reppert PM. Seismic while drilling (SWD) with a rotary percussive sounding system (RPSS). *J Environ Eng Geophys.* 2013;18(3):169-182. doi:10.2113/JEEG18.3.169
48. Heelan PA. Radiation from cylindrical source of finite length. *Geophysics.* 1953;18(3):685-696. doi:10.1190/1.1437923

49. Gangi A. *A Theoretical Study of the Radiation Patterns of a Tunnel-Boring Machine (Infinite Medium)*. Vicksburg, MS: U.S. Army Engineer Waterways Experiment Station; 1987. Technical Report GL-87-20.
50. Poletto F. Energy balance of a drill-bit seismic source, part 1: rotary energy and radiation properties. *Geophysics*. 2005;70(2):T13-28. doi:10.1190/1.1897038
51. Carcione JM, Carrion PM. 3-D radiation pattern of the drilling bit source in finely stratified media. *Geophys Res Lett*. 1992;19(7):717-720. doi:10.1029/92GL00543
52. Rector JW. *Utilization of Drill Bit Vibrations as a Downhole Seismic Source* [dissertation]. Stanford, CA: Stanford University; 1990.
53. Rector JW, Hardage BA. Radiation pattern and seismic waves generated by a working roller-cone drill bit. *Geophysics*. 1992;57(10):1319-1333. doi:10.1190/1.9781560801580
54. Aleotti L, Poletto F, Miranda F, Corubolo P, Abramo F, Craglietto A. Seismic while-drilling technology: use and analysis of the drill-bit seismic source in a cross-hole survey. *Geophys Prospect*. 1999;47(1):25-39. doi:10.1046/j.1365-2478.1999.00113.x
55. DiSiena JP, Gaiser JE, Corrigan D. Horizontal components and shear wave analysis of three-component VSP data. In: Toksoz, N, Stewart RR, eds. *Vertical Seismic Profiling - Part B: Advanced Concepts*. London, UK: Geophysical Press; 1984:177-188.
56. Guevara SE, Stewart RR. *Multicomponent Seismic Polarization Analysis*. Calgary, Canada: CREWES; 1998. CREWES Research Report Volume 10.

57. Guevara SE, Stewart RR. *Source-Geophone Azimuth from 3-C Seismic Polarization*. Calgary, Canada: CREWES; 2000. CREWES Research Report Volume 12.
58. Hardy HR Jr. Applications of acoustic emission techniques to rock and rock structures: a state-of-the-art review. In: Drnevich VP, Gary RE, eds. *Acoustic Emissions in Geotechnical Engineering Practice*. West Conshohocken, PA: American Society for Testing and Materials; 1981:4-92.
59. Obert L. *Use of Subaudible Noises for Prediction of Rock Bursts*. Washington, D.C.: U.S. Department of the Interior, Bureau of Mines; 1941. Report of Investigations 3555.
60. Obert L, Duvall W. *Use of Subaudible Noises for Prediction of Rock Bursts, Part II*. Washington, D.C.: U.S. Department of the Interior, Bureau of Mines; 1942. Report of Investigations 3654.
61. Kaiser J. *An Investigation into the Occurrence of Noises in Tensile Tests or a Study of Acoustic Phenomena in Tensile Tests* [dissertation]. Munich, Germany: Technical University of Munich; 1950.
62. Merrill RH. *Design of Underground Mine Openings, Oil Shale Mine, Rifle, Colorado*. Washington, D.C.: U.S. Department of the Interior, Bureau of Mines; 1954. Report of Investigations 5089.

63. Buchheim W. Geophysical methods for the study of rock pressure in coal and potash salt mining. Paper presented at: International Strata Control Congress; October 14-16, 1958; Leipzig, Germany.
64. Crandell FJ. Determination of incipient roof failures in rock tunnels by micro-seismic detection. *J Boston Soc Civ Eng.* 1955:39-54.
65. Beard FD. Microseismic forecasting of excavation failures. *Civ Eng.* 1962;32(5):50-51.
66. Khair AW. *Failure Criteria Applicable to Pressurized Cavities in Geologic Materials under in-situ Stress Conditions* [dissertation]. State College, PA: Pennsylvania State University; 1972.
67. Hayashi M, Kanagawa T, Hibino S, Motozima M, Kitahara Y. Detection of anisotropic geo-stresses trying by acoustic emission, and non-linear rock mechanics on large excavating caverns. Paper presented at: 4th ISRM Congress; September 2-8, 1979; Montreux, Switzerland.
68. Li Y, Qiao L, Sui ZL. In-situ stress measurement based on acoustic emission in combination with core orientation techniques. Paper presented at: International Symposium on In-Situ Rock Stress; August 25-27, 2010; Beijing, China.
69. Hardy HR. Basic studies associated with the design of salt caverns for the storage of pressurized fluids. Paper presented at: ISRM International Symposium; May 26-28, 1982; Aachen, Germany.

70. Zhang C, Liang W, Xu S, Yu Y. Experimental study of the acoustic emission characteristics of salt rock under uniaxial compression. Paper presented at: ISRM SINOROCK 2013; June 18-20, 2013; Shanghai, China.
71. Solberg P, Lockner D, Byerlee JD. Hydraulic fracturing in granite under geothermal conditions. *Int J Rock Mech Min Sci & Geomech Abstr.* 1980;17(1):25-33. doi: 10.1016/0148-9062(80)90003-0
72. Lockner DA, Byerlee JD, Kuksenko V, Ponomarev A, Sidorin A. Quasi-static fault growth and shear fracture energy in granite. *Nature.* 1991;350:39-42. doi:10.1038/350039a0
73. Butt SD, Calder PN. Experimental procedures to measure volumetric changes and microseismic activity during triaxial compression tests. *Int J Rock Mech Min Sci & Geomech Abstr.* 1998;35(2):249-254. doi:10.1016/S0148-9062(97)00325-2
74. Ríos-Soberanis CR. Acoustic emission technique, an overview as a characterization tool in materials science. *J Appl Res Technol.* 2011;9(3):367-379.
75. Baranov VM, Kudryavtsev EM, Sarychev GA, Schavelin VM. *Acoustic Emission in Friction.* Oxford, UK: Elsevier BV; 2007.
76. Lockner D. The role of acoustic-emission in the study of rock fracture. *Int J Rock Mech Min Sci.* 1993;30(7):883-899. doi:10.1016/0148-9062(93)90041-B

77. Keshavarz M, Pellet FL, Hosseini KA. Comparing the effectiveness of energy and hit rate parameters of acoustic emission for prediction of rock failure. Paper presented at: ISRM International Symposium on Rock Mechanics - SINOROCK; May 19-22, 2009; The University of Hongkong, China.
78. Lockner D, Byerlee JD. Hydrofracture in weber sandstone at high confining pressure and differential stress. *J Geophys Res.* 1977;82(14):2018-2026. doi:10.1029/JB082i014p02018
79. Fortin J, Stanchits S, Dresen G, Gueguen Y. Acoustic emissions monitoring during inelastic deformation of porous sandstone: comparison of three modes of deformation. *Pure Appl Geophys.* 2009;166(5):823-841. doi:10.1007/s00024-009-0479-0
80. Damani A, Sharma A, Sondergeld C, Rai C. Mapping of hydraulic fractures under triaxial stress conditions in laboratory experiments using acoustic emissions. Paper presented at: SPE Annual Technical Conference and Exhibition; October 8-10, 2012; San Antonio, TX.
81. Tang C, Kaiser PK, Yang G. Numerical simulation of seismicity in rock failure. Paper presented at: 2nd North American Rock Mechanics Symposium; June 19-21, 1996; Montreal, Quebec, Canada.
82. Cai M, Kaiser PK, Tasaka Y, Kurose H, Minami M, Maejima T. Numerical simulation of acoustic emission in large-scale underground excavations. Paper presented at: The 42nd U.S. Rock Mechanics Symposium; June 29-July 2, 2008; San Francisco, CA.

83. Martin CD. *The Strength of Massive Lac du Bonnet Granite around Underground Openings* [dissertation]. Winnipeg, Canada: University of Manitoba; 1993.
84. Hardy HR, Shen HW, Kimble EJ. Laboratory studies of acoustic emission during coal cutting. Paper presented at: The 13th International Modal Analysis Conference; February 13-16, 1995; Nashville, TN.
85. Shen HW, Hardy HR, Khair AW. Laboratory study of acoustic emission and particle size distribution during rotary cutting. *Int J Rock Mech Min Sci.* 1997;34(3-4):121.e1-121.e16. doi:10.1016/S1365-1609(97)00247-5
86. Sun X. A study of acoustic emission in drilling applications. Paper presented at: The 37th U.S. Symposium on Rock Mechanics; June 7-9, 1999; Vail, CO.
87. Ferrari G, Gómez MP. Correlation between acoustic emission, thrust and tool wear in drilling. *Procedia Mater Sci.* 2015;8:693-701. doi:10.1016/j.mspro.2015.04.126
88. Mostofi M. *Drilling Response of Impregnated Diamond Bits: Modelling and Experimental Investigations* [dissertation]. Perth, Australia: Curtin University; 2014.
89. Karakus M, Perez S. Acoustic emission analysis for rock-bit interactions in impregnated diamond core drilling. *Int J Rock Mech Min Sci.* 2014;68(2014):36-43. doi:10.1016/j.ijrmms.2014.02.009
90. Rosin P, Rammler E. The laws governing the fineness of powdered coal. *J Inst Fuel.* 1933;7:29-36.

91. Merkus HG. *Particle Size Measurements: Fundamentals, Practice, Quality*. Dordrecht, Netherlands: Springer; 2009.
92. Djamarani KM, Clark IM. Characterization of particle size based on fine and coarse fractions. *Powder Technol.* 1997;93(2):101-108. doi:10.1016/S0032-5910(97)03233-6
93. Brezani I, Zelenak F. Improving the effectivity of work with rosin-rammler diagram by using MATLAB GUI tool. *Acta Montan Slovaca.* 2010;15(2):152-157.
94. ASTM International. ASTM D6913, standard test methods for particle-size distribution (gradation) of soils using sieve analysis.
95. ASTM International. ASTM D422, standard test method for particle-size analysis of soils.
96. R Reyes R, Kyzym I, Rana PS, Butt SD, Molgaard J. Cuttings analysis for rotary drilling penetration mechanisms and performance evaluation. Paper presented at: The 49th U.S. Rock Mechanics/Geomechanics Symposium; June 28-July 1, 2015; San Francisco, CA.
97. Pfleider E, Blake RL. Research on the cutting action of the diamond drill bit. *Min Eng.* 1953;5:187-195.
98. Ersoy A, Waller MD. Drilling detritus and the operating parameters of thermally stable PDC core bits. *Int J Rock Mech Min Sci & Geomech Abstr.* 1997;34(7):1109-1123. doi:10.1016/S1365-1609(97)90203-3

99. Altindag R. Estimation of penetration rate in percussive drilling by means o coarseness index and mean particle size. *Rock Mech Rock Eng.* 2003;36(4):323-332. doi:10.1007/s00603-003-0002-3

## **Chapter 2 Micro-Seismic Evaluation of Fracturing in Cores during Triaxial Compression Tests**

Yingjian Xiao <sup>a</sup>, PhD candidate

Abdelsalam Abugharara <sup>a</sup>, PhD candidate

Stephen D. Butt <sup>a</sup>, Professor

<sup>a</sup> Drilling Technology Laboratory, Memorial University of Newfoundland, St. John's, NL, Canada A1B 3X5

This chapter is based on the objective defined in section 1.3.1 and was presented at the International Symposium of the Society of Core Analysts held in St. John's Newfoundland and Labrador, Canada, 16-21 August, 2015.

### **2.1 Co-authorship Statement**

The contributions of this collaborative work are described in the following five parts. 1) Identification of research topic and design of experiments are contributed by Yingjian Xiao and Abdelsalam Abugharara. 2) Preparation of cores, construction of acoustic emission testing system (hardware and software), and measurement configurations are solely contributed by Yingjian Xiao. Practical conduction of triaxial compression tests are cooperated by Yingjian Xiao and Abdelsalam Abugharara. 3) Post processing and data analysis are solely contributed by Yingjian Xiao. 4) Manuscript preparation are solely

contributed by Yingjian Xiao. 5) Dr. Butt supervises the whole experiment and provides technical knowledge and reviews the manuscript.

## **2.2 Abstract**

This study is an evaluation of rock cracking and failure by means of laboratory standard strength tests and real time micro-seismic or acoustic emission (AE) monitoring. Three groups of rock-like materials were cast using fine aggregate and Portland cement, out of which standard test specimens were cored. Confined compressive strength (CCS) tests were conducted on those cores while two non-destructive testing (NDT) sensors were placed in end platens used to compress the core. Conventional rock mechanics results were obtained such as stress-strain response. Hundreds of micro-seismic events were recorded in the process of rock deformation and especially when the core failed. Seismic data processing indicated the synchronization of event occurrence rate with correlated material deformation. Also, micro-seismic properties were analyzed such as dominant frequency (DF), event energy and cumulative AE counts. Event energy was found closely related to the peak amplitude of seismic waves. Under the same confining pressure, DF was prone to decrease with increase of deformation until the core failed. This correlated with the higher AE event rate when deformation increased. High strength material tended to generate higher DF than that of low strength material. For the same strength material, increasing confining pressure played different roles on the dominant frequency. Finally, AE event occurrence locations were determined along the core length which was compared with the observation of core surface cracks.

## **2.3 Introduction**

Micro-seismic events or AE are the elastic waves produced when rock undergoes internal change, such as micro-crack initiation and propagation. Piezoelectric transducers are commonly employed in detecting and monitoring micro-crack propagation [1]. As an alternative way to ‘see’ micro-crack initiation and propagation, AE detection was applied in triaxial compression tests to monitor the whole deformation process [2]. Some AE parameters such as DF, event energy and cumulative AE counts are related to the different deformation stages [3,4]. AE events were located in hydraulic fracturing researches [5-7]. Numerical simulation was used to simulate the deformation process and predict the failure [8,9]. Crack type was also classified based on detected acoustic emissions for failure prediction [10-13].

## **2.4 Experimental Setup**

Monitoring AE during the CCS test was scheduled. The CCS tests were conducted using a servo-controlled axial loading frame and a Hoek triaxial pressure cell. AE were recorded using a two-sensor AE system.

### **2.4.1 Axial loading frame**

During the CCS test, axial load was applied by the Instron load frame (Figure 2.1). The maximum loading could be 250 kN. By setting the loading rate of 1 mm/min, displacement and load were recorded until the core specimen failed. The core was put into the Hoek triaxial cell and specific confining pressure was loaded by a manually operated pump.

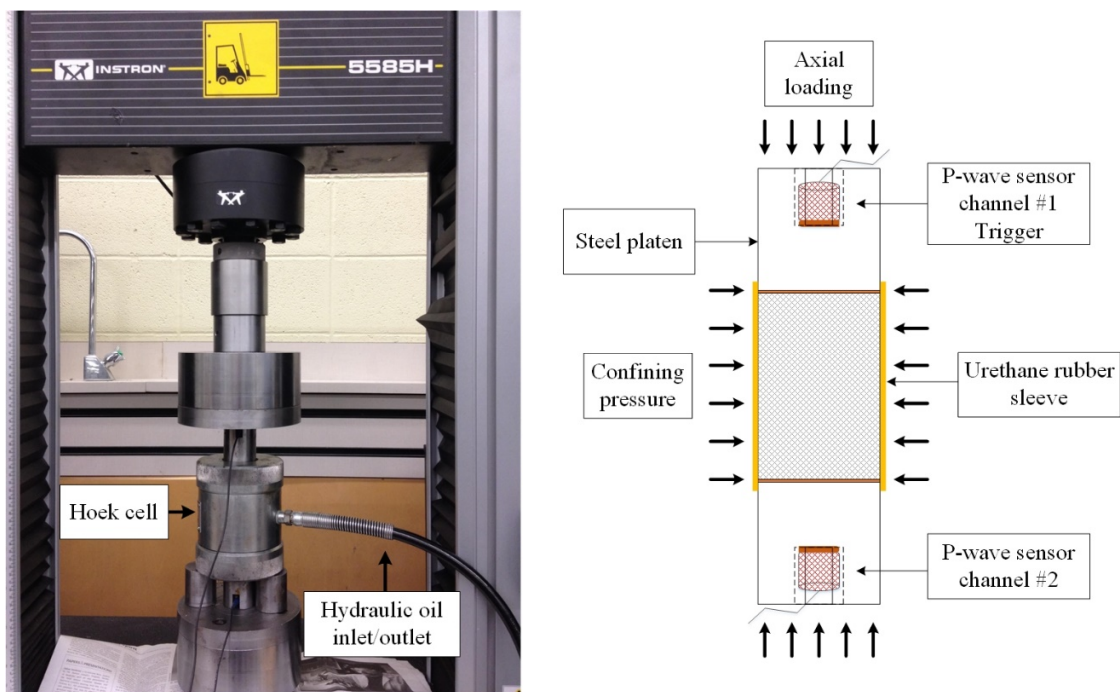


Figure 2.1: Strength test apparatus with the Hoek triaxial cell (left) and working schematic (right)

#### 2.4.2 Monitoring acoustic emission

Two Panametrics P-wave sensors were placed into steel platens on both ends of core specimens (Figure 2.1). Sponge material was put between the sensors and the loading frame for complete contact assurance and P-wave couplant was put between the steel platens and core ends and between sensors and steel platens to make better signal transmittal. The central frequency of the P-wave sensors was 1.14 MHz with working bandwidth of from

0.65 to 1.63 MHz at -6dB attenuation. Two 2/4/6 preamplifiers from Physical Acoustics Corporation (PAC) were utilized and the gain was selected to be 40dB. Two customized power supply adapters were connected to the preamplifiers with output voltage of 20 volt. The DAQ system was comprised of GaGe CompuScope 8280 eight-channel board and its included DAQ software. The trigger sensor was always located on the top of cores. Inputs for AE detection are listed in Table 2.1.

Table 2.1: Inputs for monitoring acoustic emission

Sampling frequency	P-wave sensors #	Gain	Peak-peak input	Trigger level
10 MHz	2	40 dB	10 V	0.15 V

### 2.4.3 Test materials

Three groups of rock-like materials were used with UCS (0 confining pressure) at 20, 55.5 and 87.5 MPa, designated as low, medium and high strengths (L, M and H) in Figure 2.2. These materials were made of fine aggregate, Portland cement and water. This type of rock-like materials has been used in all previous lab tests in this project based on the ability of the reproducibility. Such tests were performed to study the drill-ability including AE. In this paper, AE tests were conducted to investigate the deformation and cracking properties which were valuable for future bit-rock interaction investigation, but petroleum cores were not involved. Standard NQ cores were drilled with core diameter of 47.6 mm and the minimum ratio of height to diameter was 2:1. All the coring process and requirements were done in accordance to ASTM D4543 [14]. Averaged core dimensions and the loading plan are given in Table 2.2. To be consistent with the investigation of rock-like material's

properties and mechanical response, confining pressures were chosen in accordance to previous rock characterization tests.



Figure 2.2: Tested concrete cores (low, medium and high strength)

Table 2.2: Loading plan for triaxial compression test and CCS results

Core #	Length (mm)	Diameter (mm)	P-wave velocity (m/s)	Confining pressure (MPa)	CCS (MPa)
L1	111.64	47.23	4304.0	2	33.90
L2	105.04	47.22	4304.0	4	41.48
M1	100.79	47.38	4785.4	2	59.84
M2	103.47	47.18	4785.4	4	75.36
H1	108.39	47.43	4710.4	2	105.65
H2	104.88	47.51	4710.4	4	116.11

#### 2.4.4 Overall workflow

The overall flow chart for this test is shown in Figure 2.3. Acoustic emission signals from cracking were automatically detected and saved to the AE computer disk. At the same time,

CCS test was being conducted and the stress and strain data were recorded into the other computer. Both the computers were synchronized before each test began.

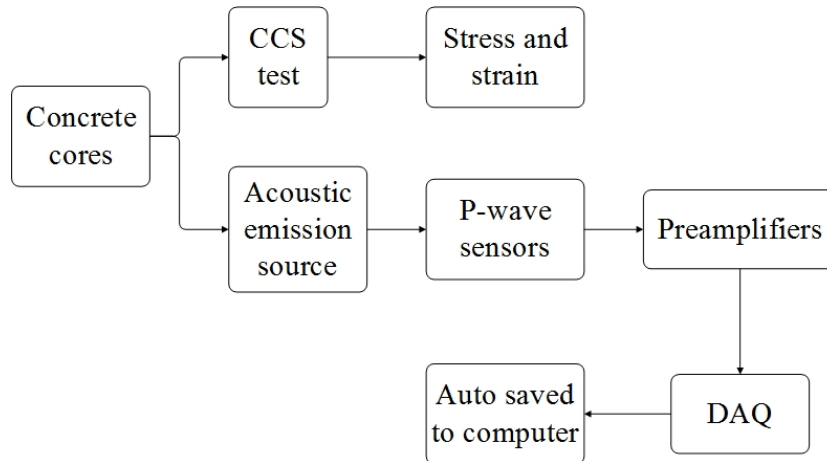


Figure 2.3: Flow chart of CCS test with monitoring acoustic emissions

## 2.5 Results

The CCS tests [15] were conducted with the results in Table 2.2 and acoustic responses were also obtained. Analysis of AE signals resulted in characteristics such as DF, event energy, peak amplitude, cumulative AE number. AE event location is calculated from the relative difference of arrival times and P-wave velocity. The whole processing is facilitated by Matlab® codes demonstrated in Appendix 1.

### 2.5.1 Single acoustic emission

Figure 2.4 shows a single event from a CCS test. The top sensor was always set as the trigger channel and two bursts of signals were captured at both sensors. The different first

arrival time demonstrated that the AE source located closer to the top sensor. AE parameters were calculated based on methodology previously developed [3].

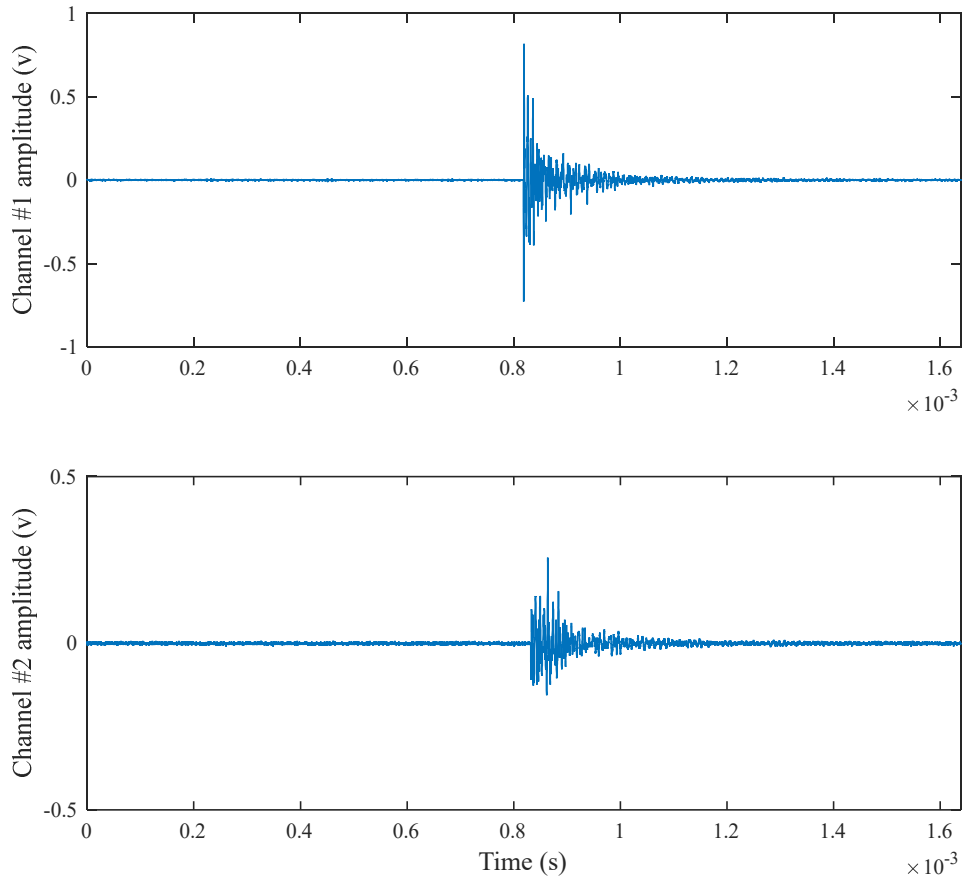


Figure 2.4: One burst event from top sensor (upper) and bottom sensor (lower) detected from the high strength material with 4 MPa confining pressure

### 2.5.2 Single test inspection

AE event locations were determined and only those from inside the cores were kept. The mechanical response and acoustic properties of low, medium and high strength cores were plotted together for comparison from Figure 2.5 to Figure 2.7. Stress and cumulative AE counts were plotted on the same time base. Few AE events were detected during the linear

elastic response. AE events initiated at the end of the linear loading sections and the number increased within non-linear ductile deformation section. This is explained by the initiation of micro-cracks and micro-crack connection. AE rate dramatically increased before and after the core failed. This was due to the micro-crack propagation and crack nucleation that was continuously generated. Event energy and peak amplitude were also investigated from both sensors. Event energy was found closely correlated with peak amplitude. And energy from both sensors correlated with each other. This indicated that a single channel of signals could be used for AE analysis. For medium strength cores, limited AE events were detected due to less capability of signal transmittal between core surfaces and sensors.

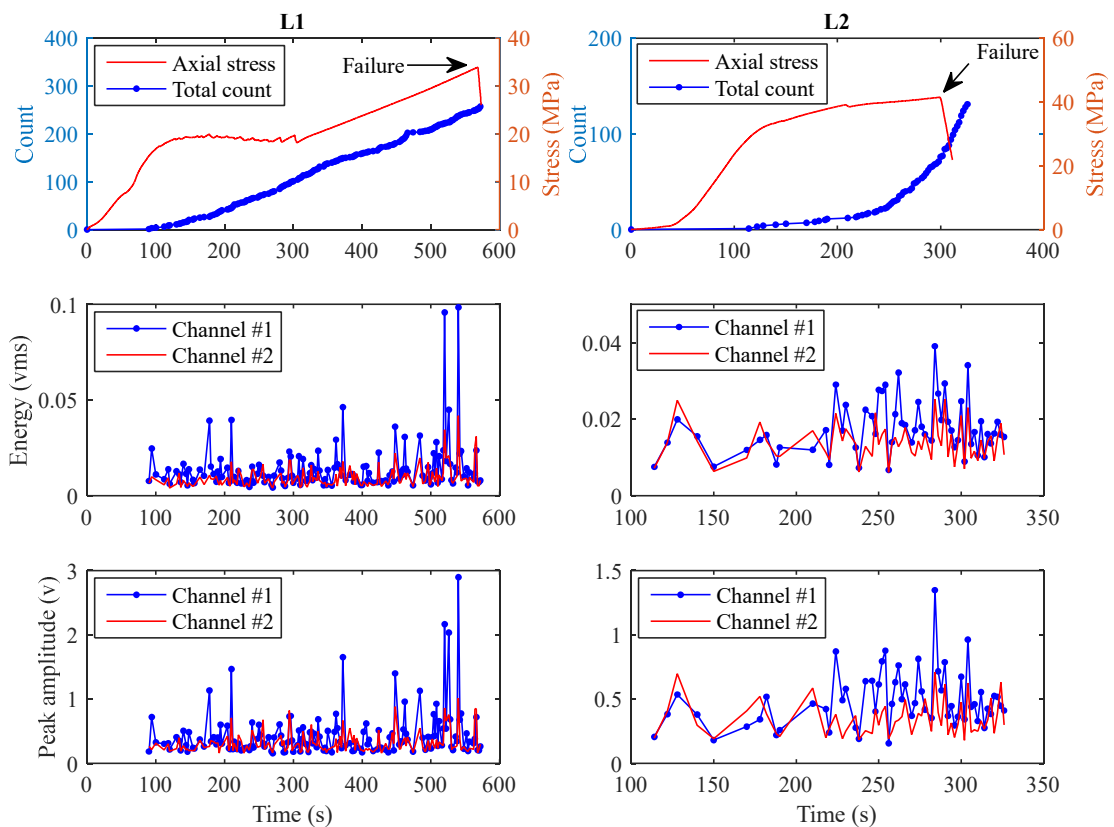


Figure 2.5: Mechanical and acoustic responses of low strength cores with acoustic properties comparison from both sensors

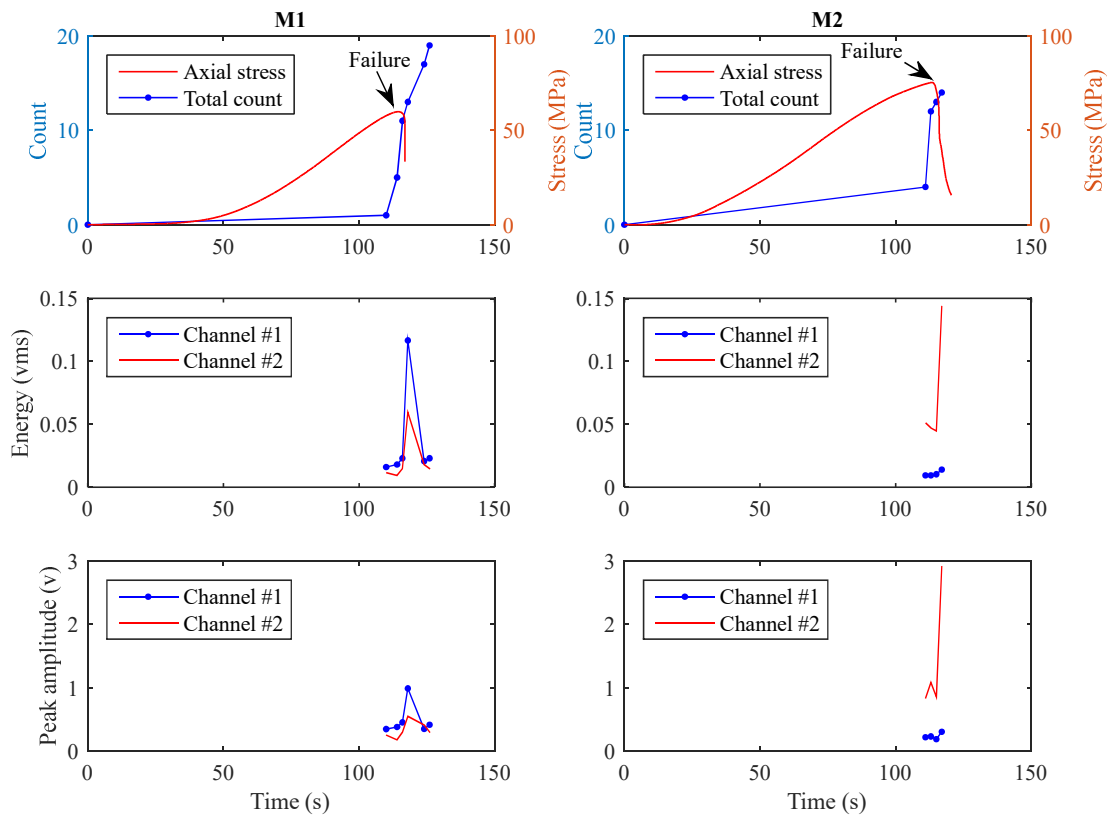


Figure 2.6: Mechanical and acoustic responses of medium strength cores with acoustic properties comparison from both sensors

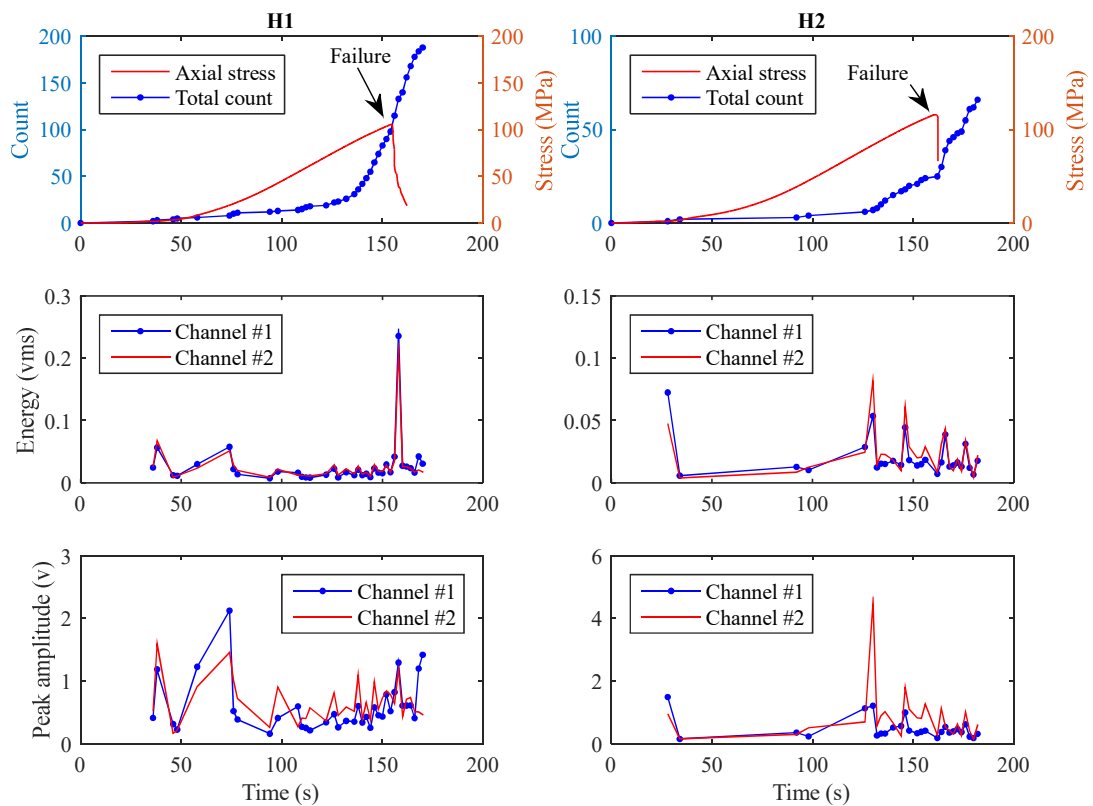


Figure 2.7: Mechanical and acoustic responses of high strength cores with acoustic properties comparison from both sensors

### 2.5.3 Dominant frequency and source energy

DF and AE event energy of signals from the top trigger sensor were compared for all tests in Figure 2.8 and Figure 2.9, separately. Linear fit was plotted for each group of scattered points to the test time. Under the same confining pressure, DF tends to decrease with the increase of core deformation. For the low strength material, DF stays constant during the rock deformation process.

AE event energy generally decreases with increased DF under the same confining pressure. An exception exists that event energy increases with increased DF for the medium strength material under the confining pressure of 2 MPa.

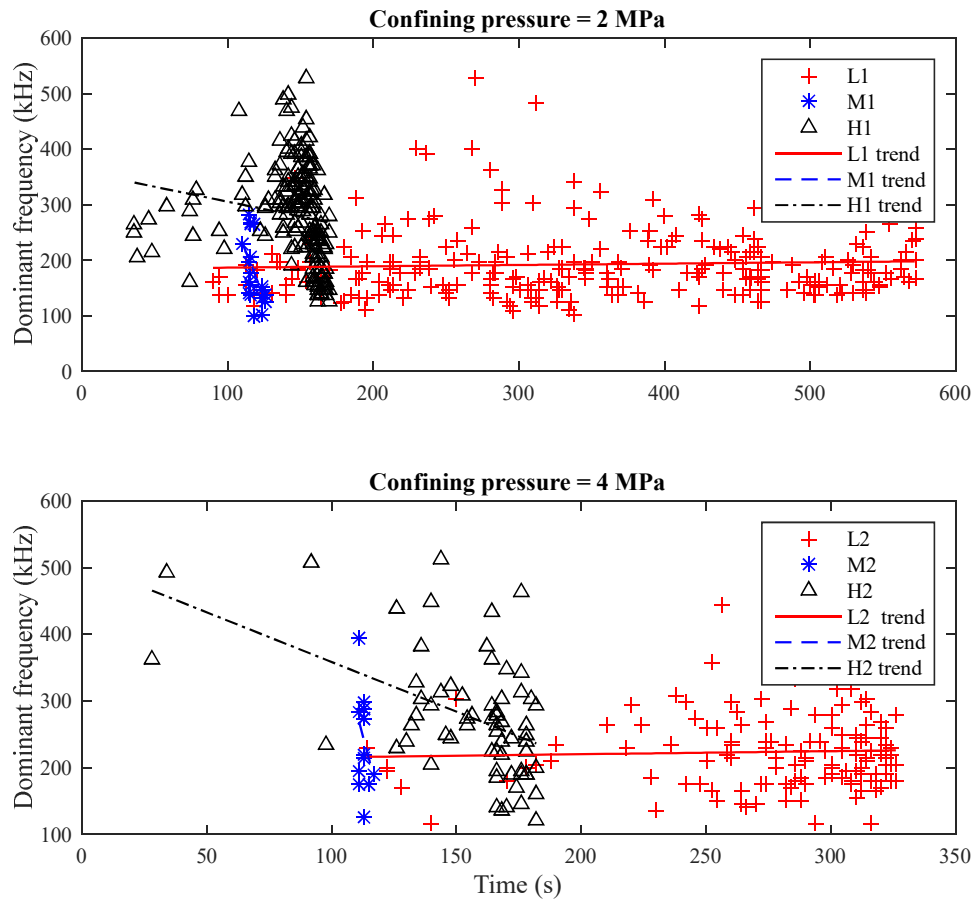


Figure 2.8: DF versus time for low, medium and high strength cores under confining pressure of 2 MPa (upper) and 4 MPa (lower). Linear fit was provided for each group of scattered points

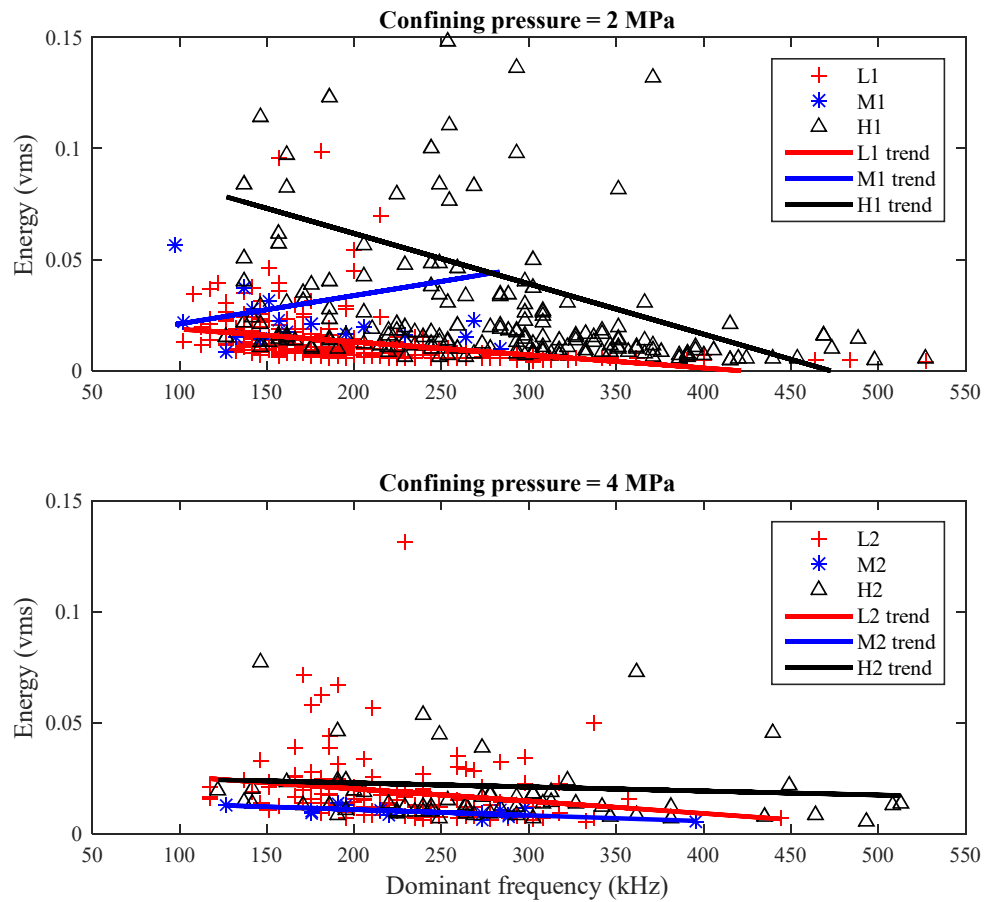


Figure 2.9: AE energy versus dominant frequency for low, medium and high strength cores under confining pressure of 2 MPa (upper) and 4 MPa (lower). Linear fit was provided for each group of scattered points

#### 2.5.4 Source location and failure observation

The AE source location was obtained and plotted versus the test time in Figure 2.10. The vertical axes are scaled to the actual core lengths. The above AE distribution characteristics or cracks were observed from the post failure demonstration in Figure 2.11. For low strength material, the majority of AE events were located in the upper half of the core under both confining pressures. This coincides with the observed results in Figure 2.11. For medium strength material, there was limited number of AE sources due to lack of good

sensor contact. For high strength material, AE sources were distributed more uniformly along the length of the core.

The cores failed due to shear cracking and macroscopic cracks propagate along all the length of the cores. Cracks mainly distributed along one portion of core length for low strength material, which was possibly due to unevenly distributed axial stress.

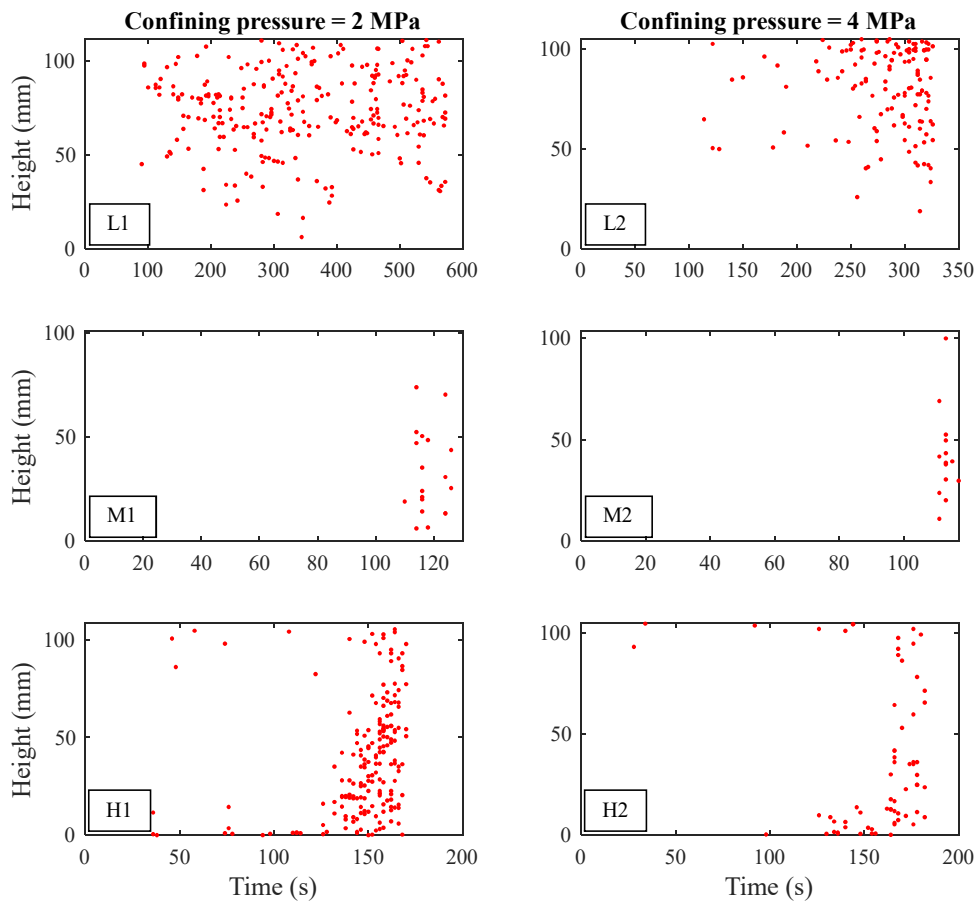


Figure 2.10: One dimensional acoustic source distribution versus test time for low, medium and high strength cores. Vertical axes were scaled to actual core heights

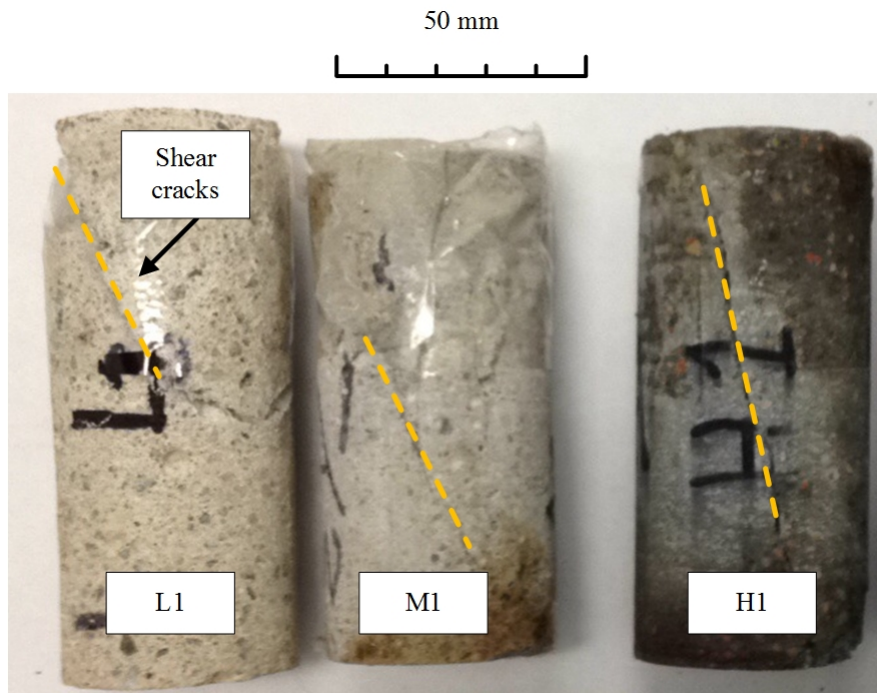


Figure 2.11: Post failure illustration for low, medium and high strength cores under confining pressure of 2 MPa

## 2.6 Conclusions

- 1) AE provides one feasible technique of characterizing rock deformation and failure in the laboratory. AE event rates correlate with the rock failure.
- 2) AE event DF tends to decrease with increased deformation. Also, event energy tends to decrease with increased dominant frequency. There is no evident relationship between DF and CCS.
- 3) AE source location was plotted versus time along the length of the cores. For low strength cores, AE sources were mainly distributed on one end which was observed in the

failed specimens. For medium strength and high strength cores, AE sources were more uniformly distributed along the core length.

## 2.7 Acknowledgements

The research was conducted at Drilling Technology Laboratory of Memorial University of Newfoundland and funded by Atlantic Canada Opportunity Agency (AIF contract number: 781-2636-1920044), involving Husky Energy, Suncor Energy and Research and Development Corporation (RDC) of Newfoundland and Labrador. The authors give appreciation to Zhen Zhang for preparing concrete cores. Many thanks will be given to Farid Arvani for helping constructing the whole acoustic emission system.

## 2.8 References

1. Hardy HR Jr. Applications of acoustic emission techniques to rock and rock structures: a state-of-the-art review. In: Drnevich VP, Gary RE, eds. *Acoustic Emissions in Geotechnical Engineering Practice*. West Conshohocken, PA: American Society for Testing and Materials; 1981:4-92.
2. Lockner D. The role of acoustic-emission in the study of rock fracture. *Int J Rock Mech Min Sci*. 1993;30(7):883-899. doi:10.1016/0148-9062(93)90041-B

3. Butt SD, Calder PN. Experimental procedures to measure volumetric changes and microseismic activity during triaxial compression tests. *Int J Rock Mech Min Sci & Geomech Abstr.* 1998;35(2):249-254. doi:10.1016/S0148-9062(97)00325-2
4. Keshavarz M, Pellet FL, Hosseini KA. Comparing the effectiveness of energy and hit rate parameters of acoustic emission for prediction of rock failure. Paper presented at: ISRM International Symposium on Rock Mechanics - SINOROCK; May 19-22, 2009; The University of Hongkong, China.
5. Damani A, Sharma A, Sondergeld C, Rai C. Mapping of hydraulic fractures under triaxial stress conditions in laboratory experiments using acoustic emissions. Paper presented at: SPE Annual Technical Conference and Exhibition; October 8-10, 2012; San Antonio, TX.
6. Chitrala Y, Sondergeld CH, Rai C. Microseismic studies of hydraulic fracture evolution at different pumping rates. Paper presented at: SPE Americas Unconventional Resources Conference; June 5-7, 2012; Pittsburgh, PA.
7. Fortin J, Stanchits S, Dresen G, Gueguen Y. Acoustic emissions monitoring during inelastic deformation of porous sandstone: comparison of three modes of deformation. *Pure Appl Geophys.* 2009;166(5):823-841. doi:10.1007/s00024-009-0479-0
8. Cai M, Kaiser PK, Tasaka Y, Kurose H, Minami M, Maejima T. Numerical simulation of acoustic emission in large-scale underground excavations. Paper presented at: The 42nd U.S. Rock Mechanics Symposium; June 29-July 2, 2008; San Francisco, CA.

9. Tang C, Kaiser PK, Yang G. Numerical simulation of seismicity in rock failure. Paper presented at: 2nd North American Rock Mechanics Symposium; June 19-21, 1996; Montreal, Quebec, Canada.
10. Zang AR, Wagner FC, Stanchits S, Dresen G, Andresen R, Haidekker MA. Source analysis of acoustic emissions in Aue granite cores under symmetric and asymmetric compressive loads. *Geophys J Int.* 1998;135(3):1113-1130. doi:10.1046/j.1365-246X.1998.00706.x
11. Aggelis DG. Classification of cracking mode in concrete by acoustic emission parameters. *Mech Res Commun.* 2011;38(3):153-157. doi:10.1016/j.mechrescom.2011.03.007
12. Ohno K, Ohtsu M. Crack classification in concrete based on acoustic emission. *Constr Build Mater.* 2010;24(12):2339-2346. doi:10.1016/j.conbuildmat.2010.05.004
13. Chow TM. *Concurrent Ultrasonic Tomography and Acoustic Emission in Solid Materials* [dissertation]. Kingston, Canada: Queen's University; 1992.
14. ASTM International. ASTM D4543, standard practices for preparing rock core as cylindrical test specimens and verifying conformance to dimensional and shape tolerances.
15. ASTM International. ASTM D7012, standard test method for compressive strength and elastic moduli of intact rock core specimens under varying states of stress and temperatures.

## **Chapter 3 Micro-Seismic Monitoring of PDC Bit Drilling Performance during Vibration Assisted Rotational Drilling**

Yingjian Xiao <sup>a</sup>, PhD candidate

Jinghan Zhong <sup>a</sup>, Graduate Student

Charles Hurich <sup>b</sup>, Associate Professor

Stephen D. Butt <sup>a</sup>, Professor

<sup>a</sup> Drilling Technology Laboratory, Memorial University of Newfoundland, St. John's,  
NL, Canada A1B 3X5

<sup>b</sup> Department of Earth Sciences, Memorial University of Newfoundland, St. John's, NL,  
Canada A1B 3X5

This chapter is based on the objective defined in section 1.3.2 and was presented at the at the 49th US Rock Mechanics/Geomechanics Symposium held in San Francisco, CA, USA, 28 June-1 July 2015.

### **3.1 Co-authorship Statement**

The contributions of this collaborative work are described in the following five parts. 1) Identification of research topic and design of experiments are solely contributed by Yingjian Xiao. 2) Preparation of cores, construction of acoustic emission testing system (hardware and software), and measurement configurations are solely contributed by

Yingjian Xiao. Practical conduction of drill-off tests are cooperated by Yingjian Xiao and Jinghan Zhong. 3) Post processing and data analysis are solely contributed by Yingjian Xiao. 4) Manuscript preparation are solely contributed by Yingjian Xiao. 5) Dr. Hurich and Dr. Butt supervise the whole experiment and provide technical knowledge and review the manuscript.

### **3.2 Abstract**

This study is an evaluation of the feasibility of real-time drilling performance monitoring using a near-bit AE detection tool in drilling with PDC drag bits under laboratory conditions to investigate an improved drilling performance with a new Vibration Assisted Rotational Drilling tool. This paper focuses on calibrating the micro-seismic response to rock failure mechanisms, improved Rate of Penetration (ROP) and cutting particle-size distribution. Concrete cylinders with comparable properties to natural rock were fabricated in the laboratory. Drill-Off Tests (DOT) were conducted under rigid and compliant drilling with a two-cutter PDC bit. Simultaneously, micro-crack Acoustic Emissions (AE) from the bit-rock interaction process were monitored by four symmetrically mounted Non-Destructive Testing (NDT) sensors. The fracture characteristics were investigated by analyzing acoustic events in terms of event occurrence rate, and average event energy. Analysis from the DOT indicates that some factors are correlated with improved drilling performance, including particle-size distribution, vibration compliance setting and acoustic emission. A stronger vibration compliance setting increases ROP by increasing cutting depth per revolution and bigger cuttings are generated. Higher average event energy

corresponds to bigger cracking when cracking event rate increases. All of this has contributed to our understanding of the mechanisms of improved drilling performance.

### **3.3 Introduction**

One of the major problems for field drilling engineers is how to drill to target formations fast and safely. In drilling subsurface formations a vertical oscillation generator was found to increase penetration rate [1] and this early stage of oscillation vibrator drilling was called ResonantSonic Drilling. After that, both surface and offshore mechanical vibrator were introduced [2]. Vertical vibration applied to a bit leads to variation of WOB. A new vibration tool developed in the Drilling Technology Laboratory (DTL) at Memorial University was tested for improving ROP [3,4]. Laboratory tests have shown that controlled amplitude and frequencies of vibration were available from this vibration tool. This tool was tested to influence drilling efficiency and rate of penetration.

Micro seismic events, or acoustic emission (AE), are the elastic waves produced when rock undergoes internal change, such as micro crack initialization and propagation. In non-destructive testing (NDT), piezoelectric transducers are commonly employed in detecting and monitoring micro crack propagation. As an alternative way to ‘see’ micro crack initiation and propagation, AE detection has been applied in triaxial compression tests to monitor the whole deformation process [5,6]. Some AE parameters such as dominant frequency, event energy and cumulative emission counts are related to the different deformation stages. Numerical models from Particle Flow Code (PFC2D) has been used to

simulate UCS tests to predict rock failure [7]. In this PFC2D model of tri-axial compression tests, the number of cracks was taken as the hit number. In addition, AE detection is commonly used in hydraulic fracturing (HF) researches. In a physical model, high pressurized fluid was injected to cylindrical rocks to simulate hydraulic fracturing processes. The AE technique was used to characterize crack initiation and propagation [8].

### 3.4 Experimental Setup

Acoustic emissions were monitored during drill-off tests and cuttings were also collected. DOT utilized a small drilling simulator which has been used before [9]. Modification was made to this drilling system to monitor acoustic emissions and collect cuttings. The drilling system is shown in Figure 3.1.

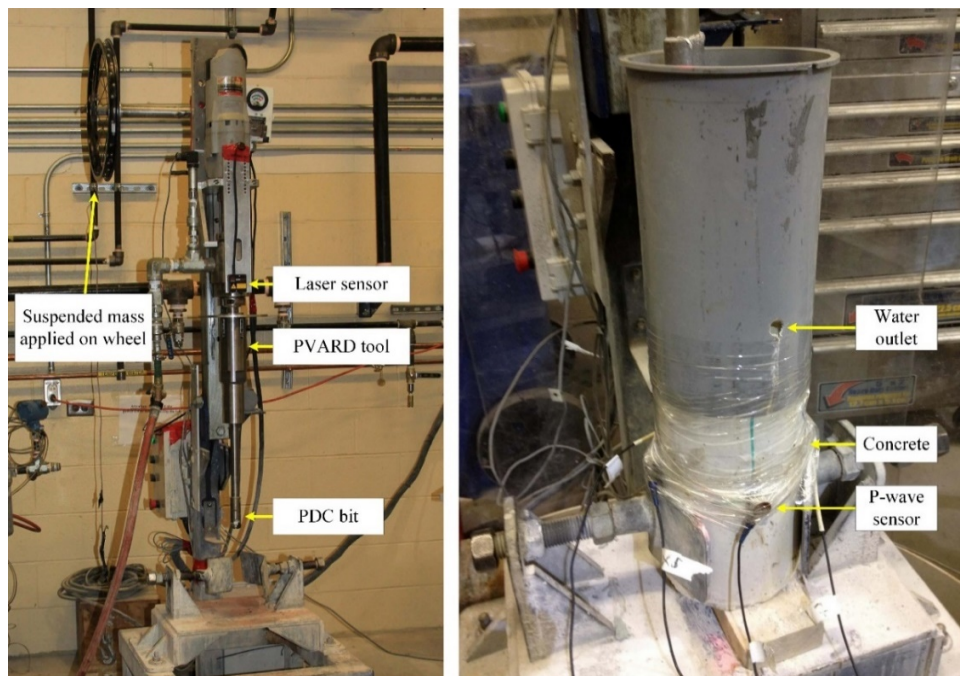


Figure 3.1: Generic view of small drilling simulator (left) and cutting collection and acoustic emission setup (right)

### **3.4.1 Test materials**

The drill-off tests were conducted on one synthetic concrete with the unconfined compressive strength (UCS) of about 40 MPa. This concrete was made of aggregate, cement, and water with the mass ratio of 4:1:0.6. The dimensions of the concrete cylinders were 4 inch outer diameter by 6 inch height. One test sample was required for each variation in drilling parameters. Before the test, portions of the cylindrical surfaces are ground to flat for attachment of acoustic emission sensors.

### **3.4.2 Small drilling simulator**

The atmospheric drilling is simulated by one small drilling simulator (Figure 3.1). WOB is applied by a mass suspended on a wheel and torque by motor acting through gears. There are two settings for the rotary speed, 300 RPM and 600 RPM. In the paper, only tests at 300 RPM are reported. A constant flow rate of tap water is used for bottom-hole cleaning.

A two-cutter PDC bit with an outer diameter of 35 mm was used. A laser sensor was attached on the moving part of the rig which can measure the bit vibration within a working amplitude range of 20 mm.

A pVARD vibration tool is applied on the top of drill string with two compliance settings labeled medium and strong compliance [10]. The compliant section converts bit vibration into the axial displacement. And the damping part absorbs harmful vibrations for the sake

of preventing the drill-string from damage. In this paper, three different settings of compliance are utilized. The proposed scheme for each compliance setting of drill-off test is listed in Table 3.1.

Table 3.1: Scheme for drill-off test with AE detection

Compliance setting	Rated rotary speed (RPM)	Flow rate (US gpm)	Depth for each run (mm)
Rigid	300	0.68	~15
Medium	300	0.68	~15
Strong	300	0.68	~15

### 3.4.3 Monitoring acoustic emission

Four Panametrics P-wave sensors were placed symmetrically around the cylindrical concrete samples (Figure 3.2). Shear wave couplant was put between sensor and concrete surfaces to optimize signal transmission. The central frequency of P-wave sensors was 1.14 MHz with working bandwidth of from 0.65 to 1.63 MHz at -6dB attenuation. From the frequency spectrum calibration report, the wide range of bandwidth guarantees reliable signals obtained from concrete even if the dominant frequency of signal is not located exactly inside the best working bandwidth. Four PAC 2/4/6 preamplifiers were utilized and gain selection of 20dB is applied in the laboratory drilling tests. Four customized power supply adapters are connected to these preamplifiers with output voltage of 20 volt. The DAQ system was comprised of GaGe CompuScope 8280 eight-channel board and its included DAQ software. The on-board memory of 128 MB allows to save up to 250

triggered events per channel to the computer disk. The trigger sensor was always put closest to the drilling source.

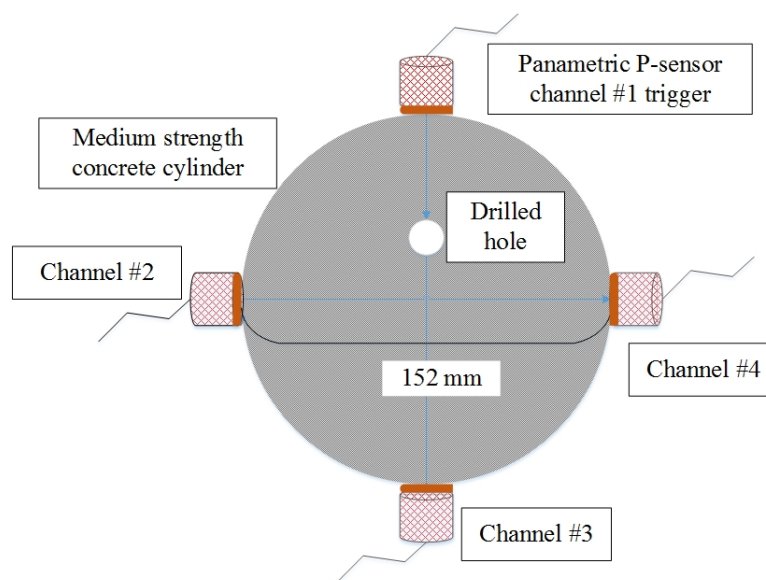


Figure 3.2: Top view of p-sensors distribution around synthetic concrete cylinder

The overall working flow chart for monitoring acoustic emissions is displayed in Figure 3.3. All signals are automatically saved to computer disk when all settings are set well before each run of test. All settings for acoustic emissions detection are displayed in Table 3.2.

Table 3.2: Inputs for monitoring acoustic emission

Sampling frequency	P-wave sensors #	Gain	Peak-peak input	Trigger level
10 MHz	4	20 dB	10 V	0.05

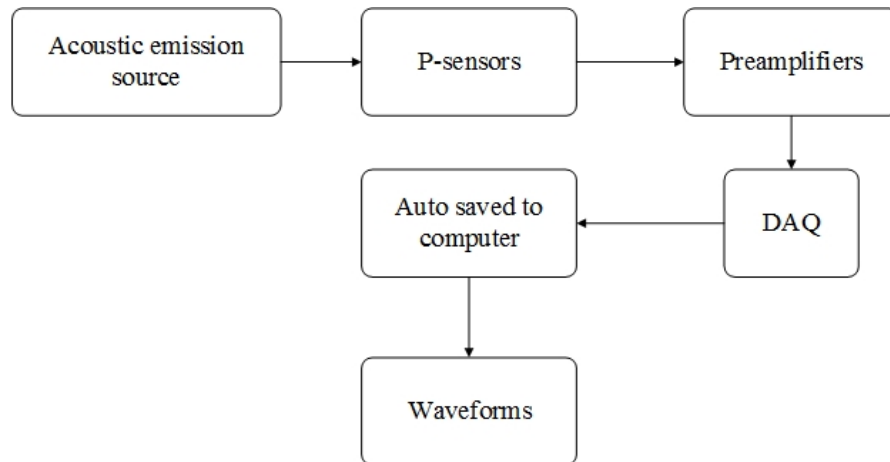


Figure 3.3: Flow chart for monitoring acoustic emissions

#### 3.4.4 Cutting analysis overview

For each run of drill-off test, all cuttings were collected from the fluid flow outlet. The concrete top surface was sufficiently cleaned for next run of test. Following ASTM standard D6913–04 [11] and cutting analysis procedure from researchers in DTL [12], collected cuttings were fully dried and different range of cutting size was analyzed with sieves with apertures 2000, 850, 630, 590, 420, 300, 160, 75, and 37 micron. The smallest size of cutting was assumed to be 10 micron which was convenient for calculating particle-size distribution.

For smaller size of cuttings than 37 micron, no more sieve analysis was done due to the small amount of mass. Furthermore, cutting size analysis whose sizes were smaller than 37 micron could be done with hydrometers [13].

### 3.5 Results

During the drill-off tests, drilling related and acoustic emission data were monitored and saved automatically. Drilling performance parameters included penetration depth, duration, WOB, flow rate, bit vibration magnitude. Synchronized acoustic emission data obtained included trigger time, events, event number. During each test, cuttings were collected which were used to characterize drilling performance.

#### 3.5.1 Review of drilling conditions

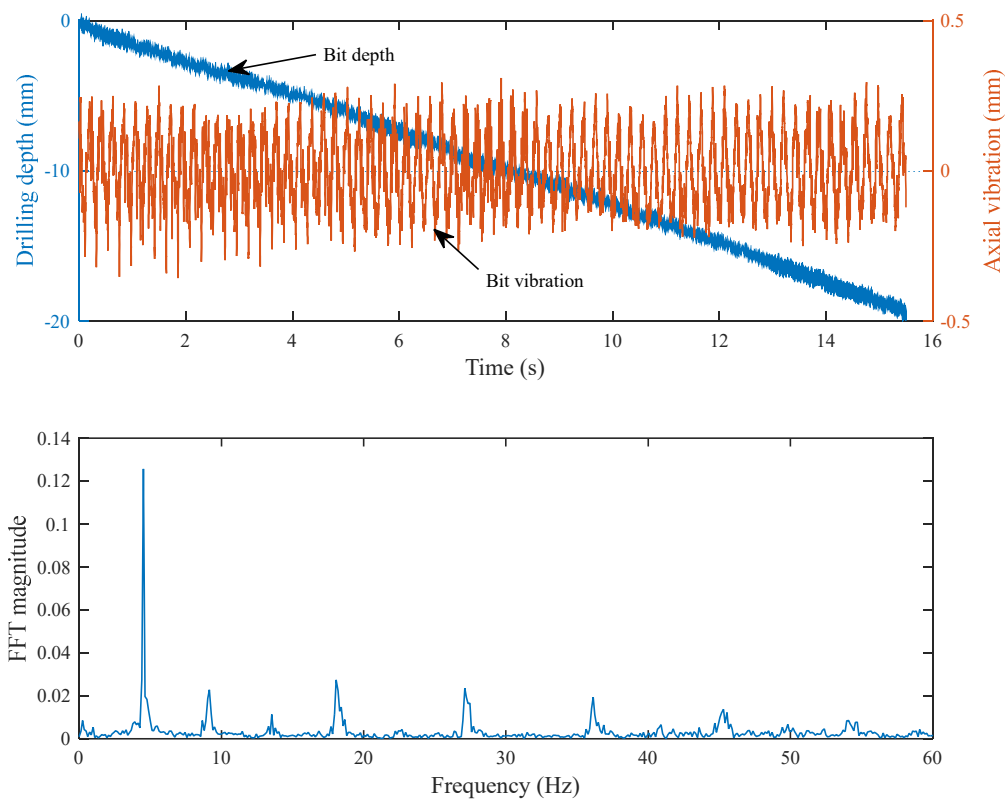


Figure 3.4: Rigid drilling when WOB = 100.0 kg. PDC bit penetrates around 20 mm on medium strength concrete (upper left) and axial vibration magnitude varies with time (upper right). Vibration is converted from time domain to frequency domain (Lower)

Drill-off tests were conducted on the medium strength concrete with rated rotary speed of 300 RPM. Figure 3.4 shows an example of the penetration time and depth. By converting axial vibration magnitude from time domain to frequency domain, the dominant frequency was found to be 4.5 Hz. Processing of AE parameters are finished by Matlab® codes which are accessible from Appendix 1.

### 3.5.2 Rock penetration characterization

Under laboratory conditions, a series of WOB was confirmed from 100.0 to 234.6 kg. Resultant ROPs were shown in Figure 3.5. From this figure, ROP increases with increasing WOB for each setting. For the high WOB situation, the penetration rate with the strong compliance setting was the highest while the penetration rate under rigid setting was the lowest. The intersection of the curves for rigid and medium compliance settings indicates that there is little difference in penetration rate under low WOB situations.

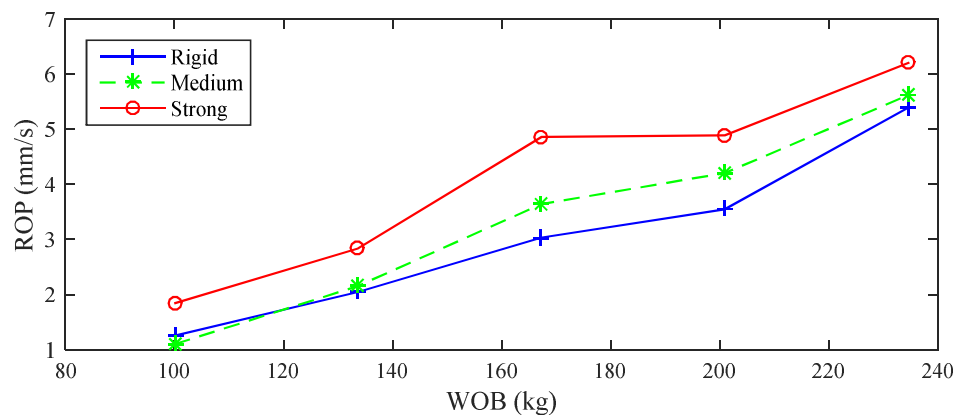


Figure 3.5: Laboratory rate of penetration (ROP) versus WOB under three different compliance settings

To eliminate the effect of rotary speed on penetration rate, both rate of penetration and rotary speed were normalized to 300 RPM. Normalized ROP was obtained from the actual ROP multiplied by the ratio of the rated rotary speed over the actual one. The normalized rotary speed was the ratio of the actual rotary speed over the rated one. Normalized results are shown in Figure 3.6. The rotary speed decreases with increased WOB and corresponding drag force on PDC bit cutter increases. The normalized ROP is higher than actual ROP for all WOB situations due to the slight decrease of rotary speed from the rated one.

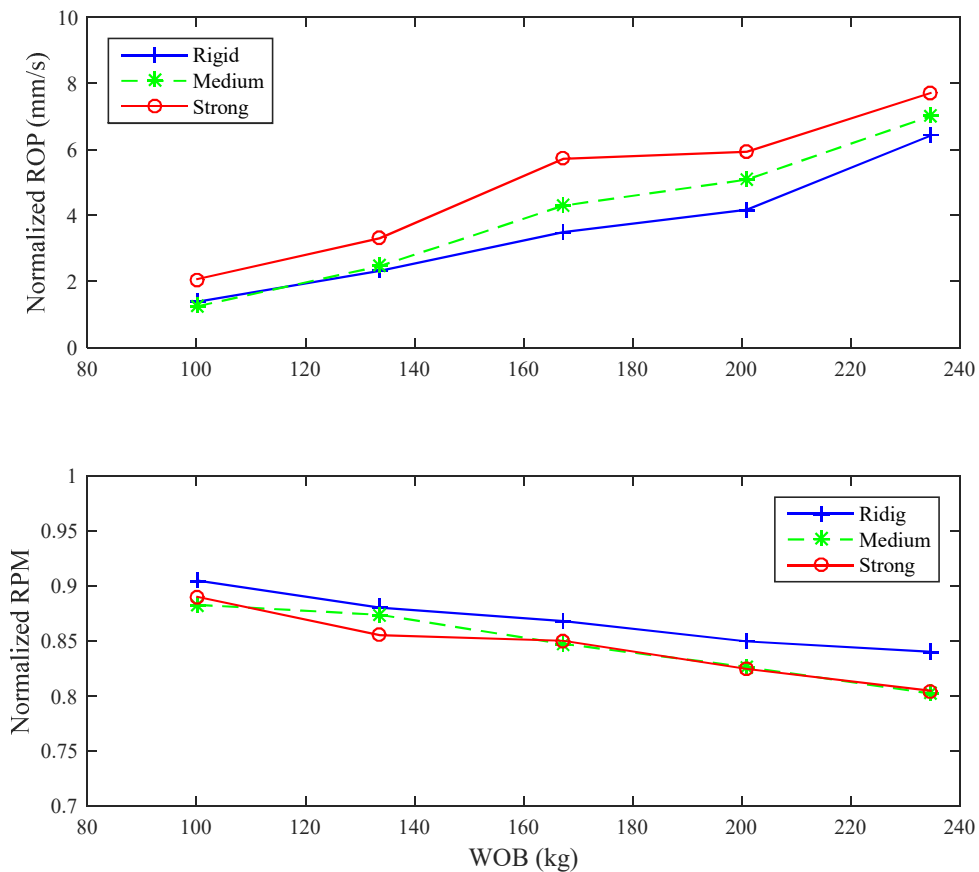


Figure 3.6: ROP is normalized to 300 RPM situation for eliminating the effect of different rotary speed (upper) and actual rotary speed normalized to 300 RPM (lower)

### 3.5.3 Cutting analysis results

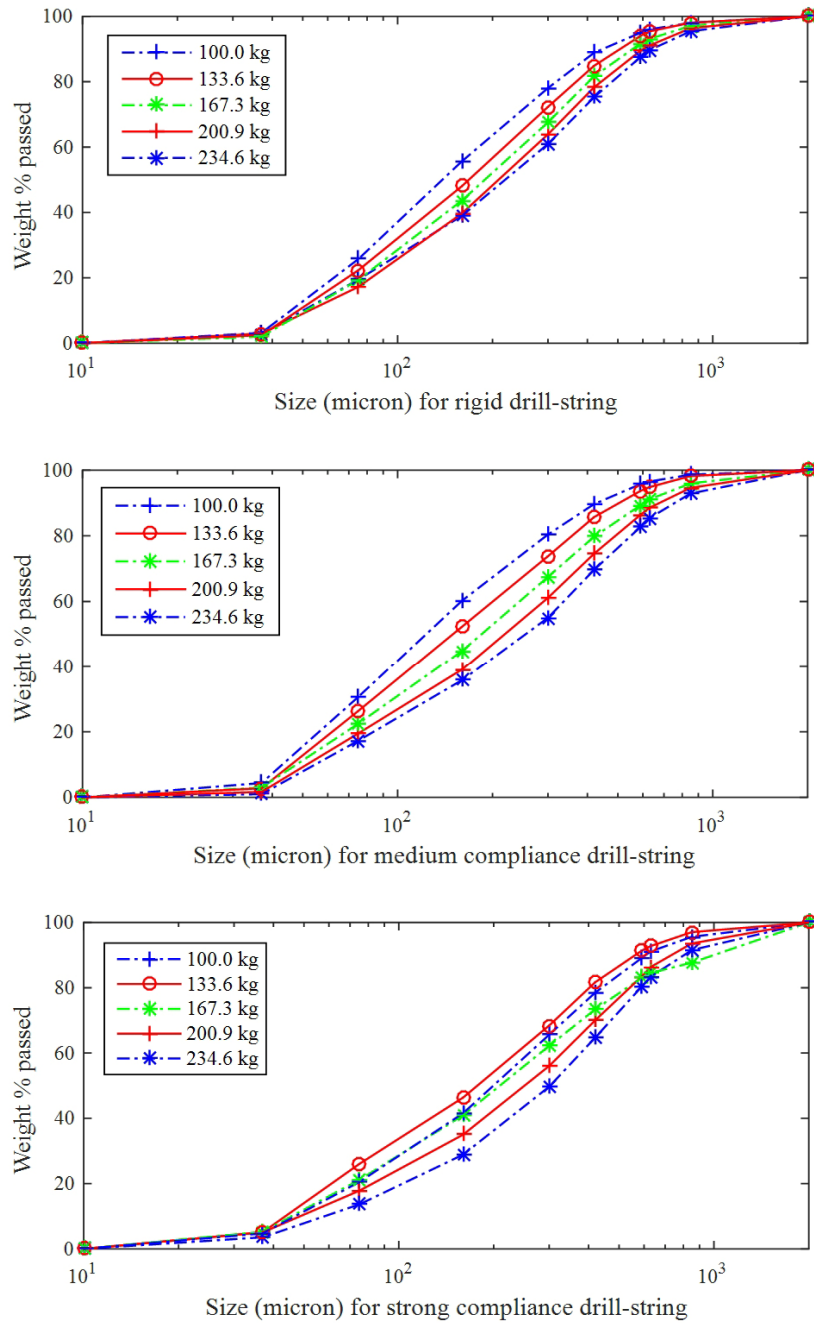


Figure 3.7: Particle-size distribution from drilling with rigid compliance (upper), medium compliance (middle) and strong compliant setting (lower)

Particle-size distribution charts are obtained for three different drilling settings in Figure 3.7 in ranges from 10 micron to 2 millimeters. The vertical axis stands for the cumulative percentage that cuttings are less than indicated size. For any indicated sieve size, the lower the cumulative percentage, the higher percentage of cuttings are left in sieves. For any cumulative percentage, the higher of the size indicates bigger cuttings are obtained.

From Figure 3.7, cuttings size is generally bigger with increasing of WOB for all rigid, medium and strong compliance settings. There is exemption on drilling with strong compliance setting. Cutting size with WOB of 100.0 kg is bigger than that with WOB of 133.6 kg. The general trend indicates that higher WOB tends to generate bigger cutting size.

Cutting size is also investigated for three compliance settings under the same WOB in Figure 3.8. In these figures, cutting size distribution is investigated for all applied five WOBs. For lower WOB situations such as 100.0 and 133.6 kg, strong compliance setting tends to generate bigger cuttings while rigid compliance setting generates bigger cutting than medium compliance. For larger WOB situations, stronger compliance settings tends to generate bigger cuttings.

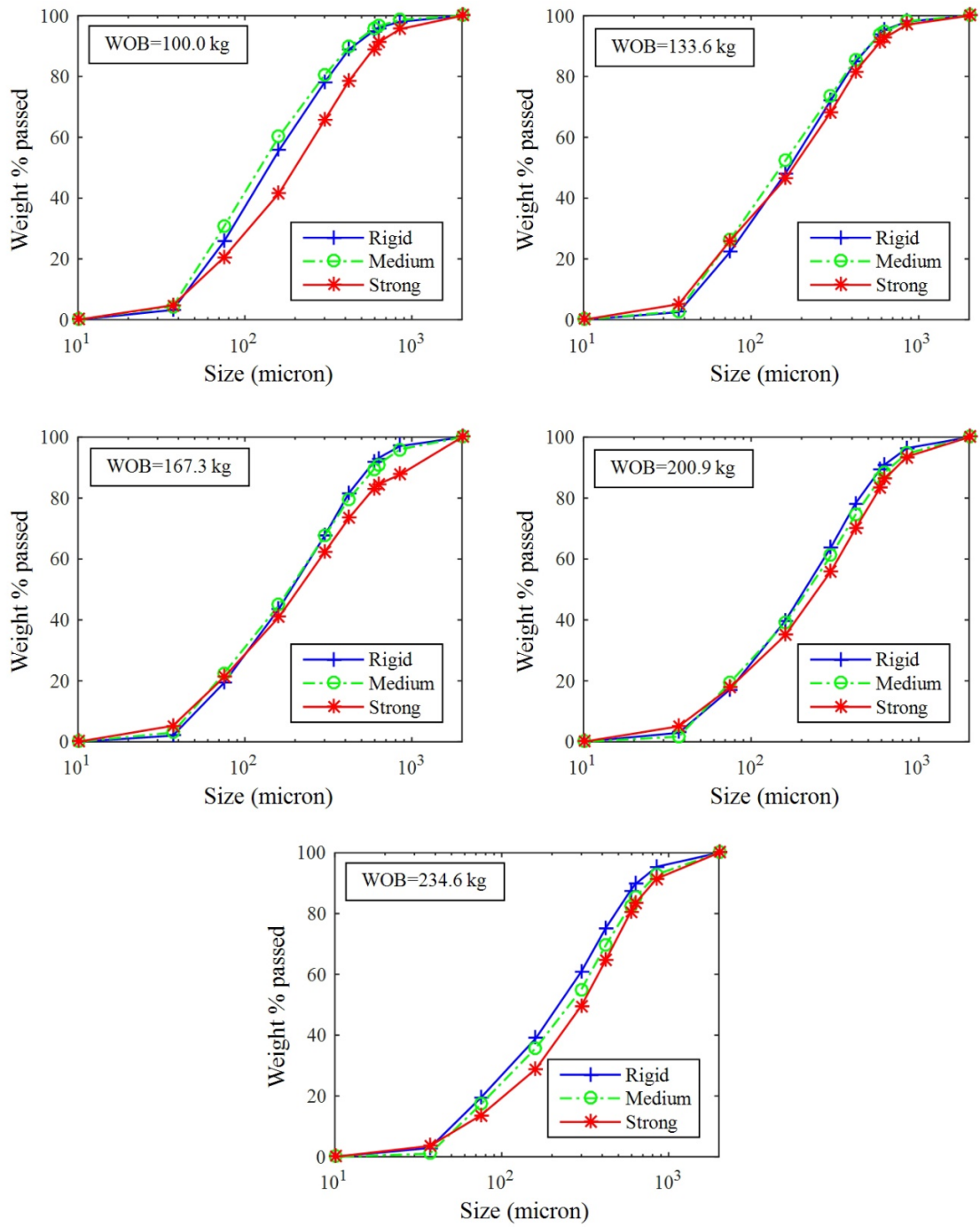


Figure 3.8: Particle-size distribution from different WOB

The dependence of the cutting size distribution on compliance setting is explained as follows. The compliance system gives different response to different axial force, i.e. WOB. The compliance system absorbs and converts the bit motion into axial displacement with little effectiveness at low WOB. And it works with higher effectiveness at higher WOB. This is observed and justified from the comparison of size distribution when WOBs are at the level of no higher than and higher than 133.6 kg. An obvious role of different compliance on cutting size distribution was observed when WOB is above 133.6 kg.

Cutting size was analyzed with a microscope at 16 X magnification. Some of the magnified cuttings were identified in Figure 3.9. Cutting particles are comprised of aggregates such as siliceous siltstone and volcanic rocks, and concrete clump containing smaller aggregates. From these figures, particles sharpness decreases from large size to smaller cutting size. This indicates that bigger cuttings are re-grounded when bottom hole cleaning is not perfect.

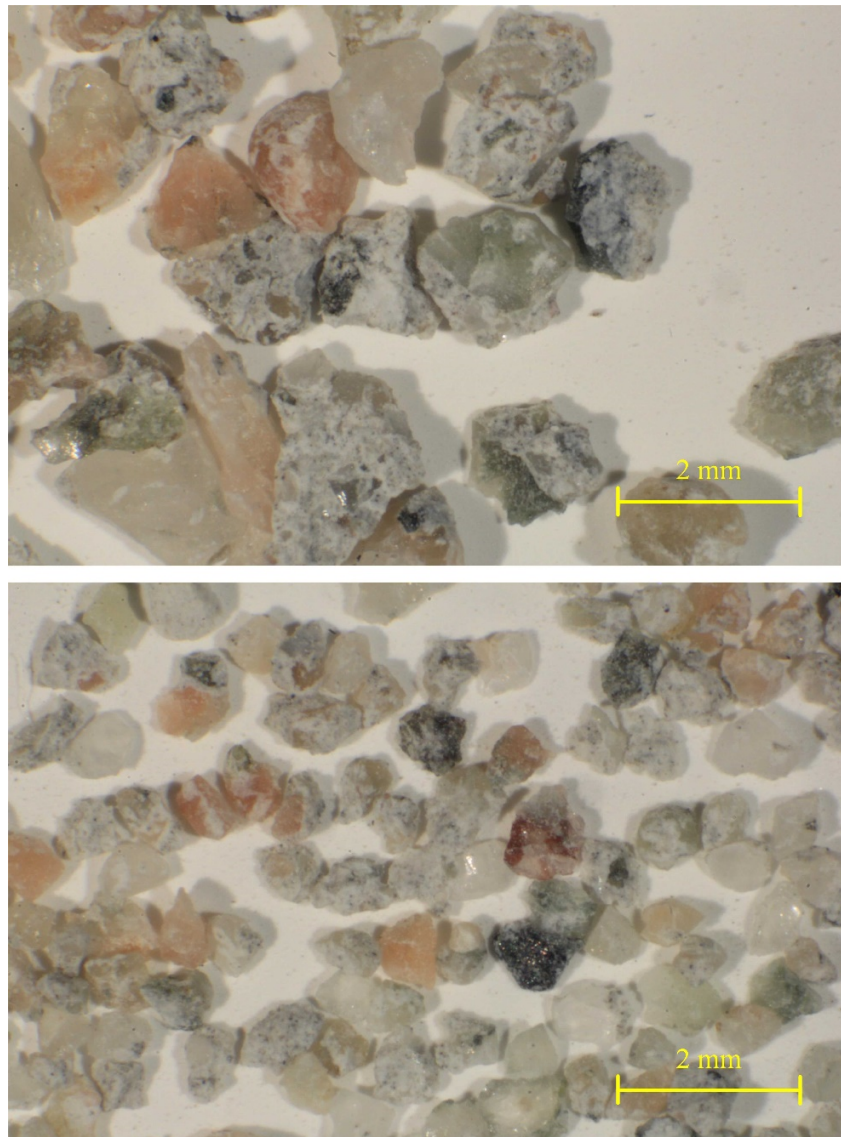


Figure 3.9: Particles obtained from drilling when WOB=234.6 kg at strong compliance setting, whose size ranges from 850 to 2000 micron (upper) and from 420 to 590 micron (lower)

#### 3.5.4 Acoustic emission results

Acoustic emission events were recorded during each run of drill-off test. A typical signal and its spectrogram analysis are displayed in Figure 3.10. The waveform shows transient

fluctuations of emissions power with respect to a background level. Each waveform lasts 1.6384 millisecond and comprises of 16384 points. The spectral content of the transient signals ranges from 50 to 300 kilo Hertz. Considering the drilling process, acoustic emission signal is comprised of rock cracking, system noise, drill rig vibration, etc. The cracking signal will not be solely extracted from the continuous waveform in this paper.

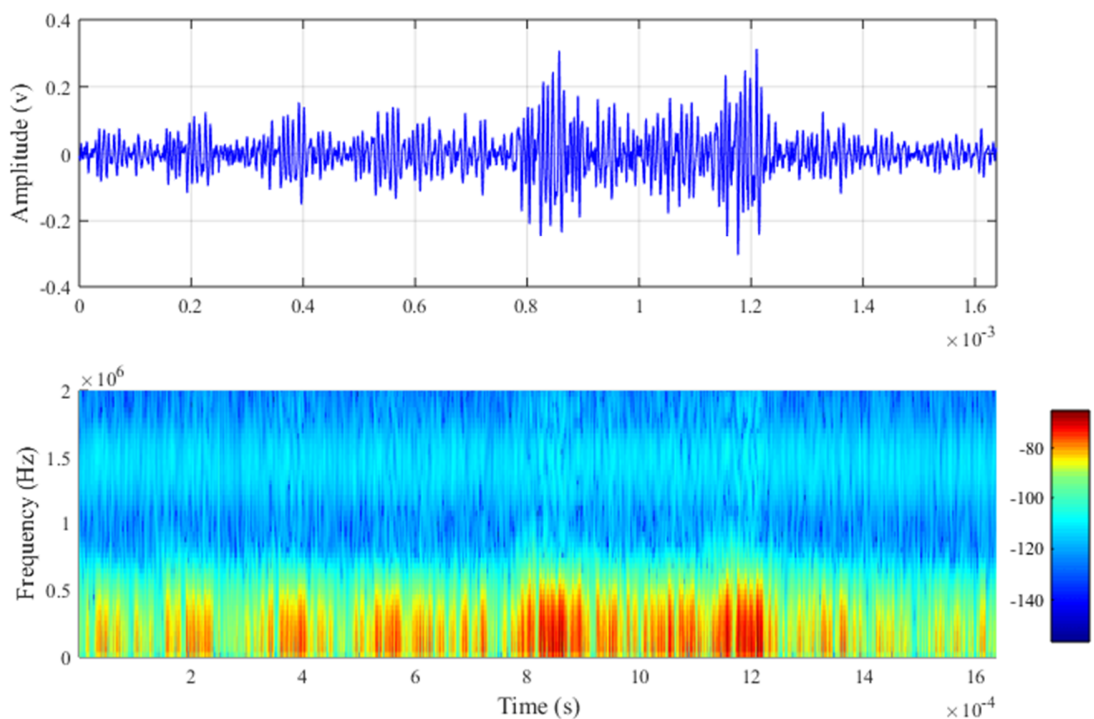


Figure 3.10: Single acoustic emission from rigid drilling when WOB=100.0 kg (upper) and spectrogram (lower)

The acoustic emission event rate is calculated based on cumulative number of triggered events during a typical time window within each run of drill-off test. Also, the corresponding event energy is integrated from the event waveform on the time domain [5]. Then, the average event energy is obtained from this drilling window (demonstrated in

Figure 3.4). Both event rate and average energy for the trigger channel are shown in Figure 3.11.

The average event energy increases with increase of WOB for all three compliance settings, and event rate slightly increases. Under the same WOB, the average event energy of rigid compliance setting is the largest and smallest magnitude of event energy is emitted from strong compliance drilling. The reason is that higher rate of events are generated in strong compliance settings than that in rigid setting.

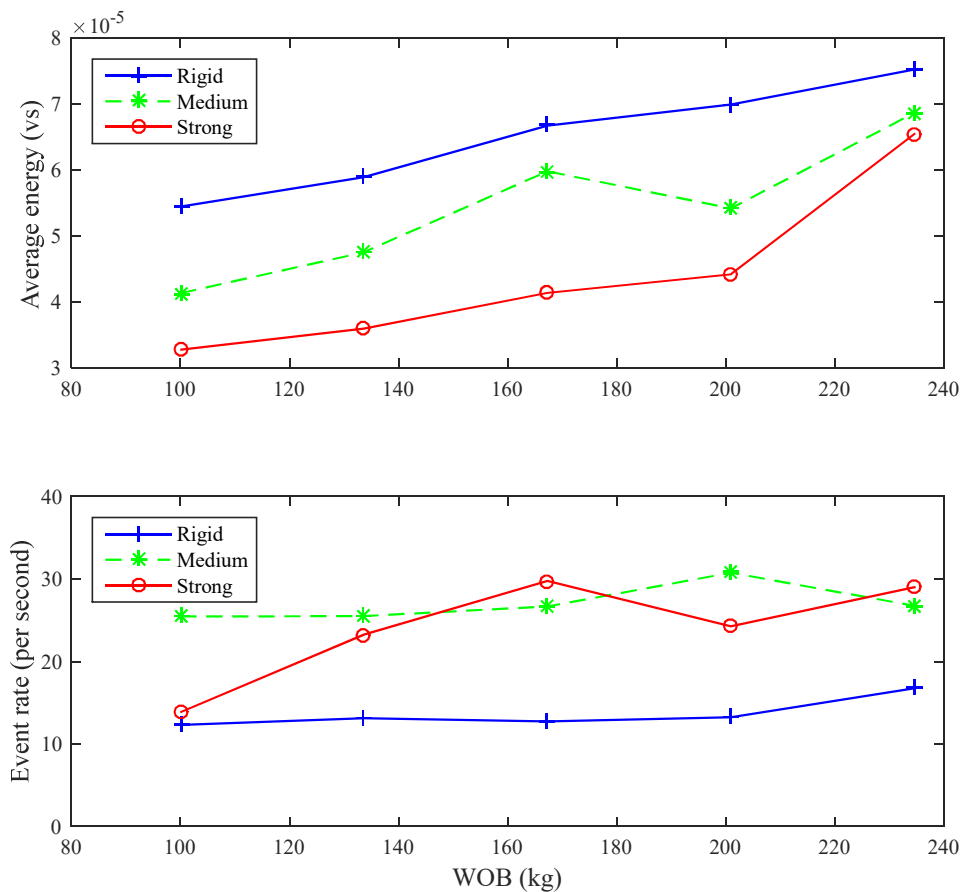


Figure 3.11: Average event energy (upper) and event rate (number of triggered events per second, lower) from the trigger channel

### 3.5.5 Acoustic emission and ROP

Some conclusions can be obtained by comparing the event rate and average event energy in Figure 3.12. With increasing ROP, the average event energy increases for all the three different complicate setting. This correlates with the previous cutting size distribution results. Bigger size of cutting is generated with increase of ROP. In this way, higher average event energy correlates with bigger size of cutting, or in other words, larger crack surfaces during the drilling process.

Under the same ROP, the highest average event energy occurs in the rigid complicate setting while the lowest average event energy occurs at the strong complicate setting. The higher average event energy mainly originates from a lower event rate generated with less compliant setting as shown in Figure 3.11.

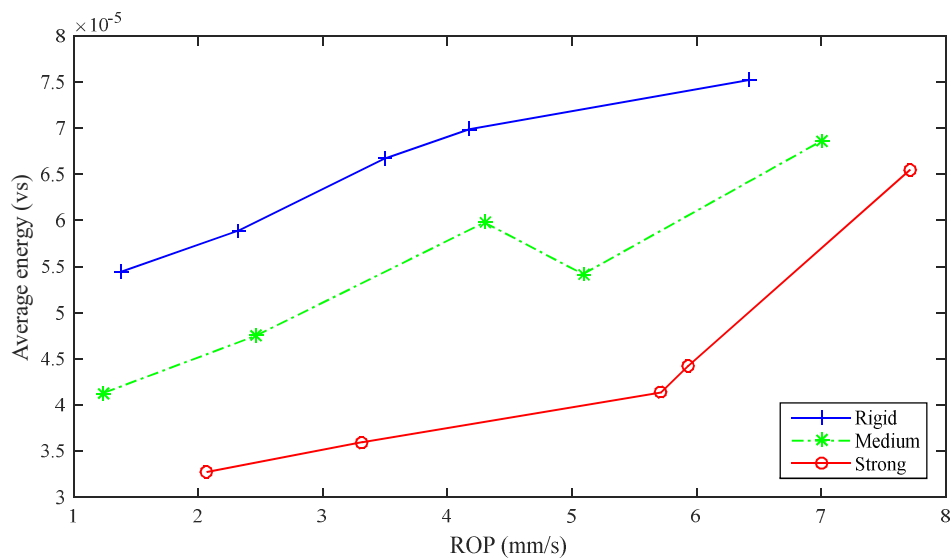


Figure 3.12: Average event energy versus ROP under three different compliant settings

### **3.6 Discussion and Conclusions**

1) Rate of penetration increases with increase of applied WOB. A stronger compliance setting helps to improve drilling performance compared to rigid drilling setting.

2) Cutting size distribution correlates with improved rate of penetration. The higher the WOB, the higher the cutting size. Also, a stronger compliance setting drilling increases ROP by increasing cutting size for each size range.

3) A higher average event energy correlates with higher ROP with increase of WOB, which corresponds to bigger cutting size and higher event rate.

4) Under the same WOB condition, average event energy is reversely correlated to compliance setting. Stronger compliance tends to generate lower average event energy due to higher event rate.

5) The future work of interest is the frequency content within the acoustic signal.

### **3.7 Acknowledgements**

The research was conducted at Drilling Technology Laboratory of Memorial University of Newfoundland and funded by Atlantic Canada Opportunity Agency (AIF contract number:

781-2636-1920044), involving Husky Energy, Suncor Energy and Research and Development Corporation (RDC) of Newfoundland and Labrador. Also, the authors give appreciation to Hongyuan Qiu and Abdelsalam Abugharara for helping the experiments. Many thanks will be given to Farid Arvani for helping constructing the whole acoustic emission system, and Igor Kyzym, Rosana Reyes, Yuanchi Tian and Shawn Organ for technical help in cutting analysis. Great appreciation to Dr. John Molgaard for reviewing paper draft and giving precious suggestions.

### 3.8 References

1. Volk BW, McLellan GW, Moak DJ, Lerch RE, Thompson KM, Barrow JC. ResonantSonic drilling: history, progress, and advances in environmental restoration programs. International Atomic Energy Agency. [http://www.iaea.org/inis/collection/NCLCollectionStore/\\_Public/25/040/25040388.pdf](http://www.iaea.org/inis/collection/NCLCollectionStore/_Public/25/040/25040388.pdf).
2. US Department of Energy. Russian drilling technology studies. <http://www.netl.doe.gov/kmd/CDs/Disk36/Man1.pdf>.
3. Li H. *Experimental Investigation of the Rate of Penetration of Vibration Assisted Rotary Drilling* [master's thesis]. St. John's, Canada: Memorial University of Newfoundland; 2011.
4. Khorshidian H. *Phenomena Affecting Penetration Mechanisms of Polycrystalline Diamond Compact Bits* [master's thesis]. St. John's, Canada: Memorial University of Newfoundland; 2012.

5. Butt SD, Calder PN. Experimental procedures to measure volumetric changes and microseismic activity during triaxial compression tests. *Int J Rock Mech Min Sci & Geomech Abstr.* 1998;35(2):249-254. doi:10.1016/S0148-9062(97)00325-2
6. Keshavarz M, Pellet FL, Hosseini KA. Comparing the effectiveness of energy and hit rate parameters of acoustic emission for prediction of rock failure. Paper presented at: ISRM International Symposium on Rock Mechanics - SINOROCK; May 19-22, 2009; The University of Hongkong, China.
7. Cai M, Kaiser PK, Tasaka Y, Kurose H, Minami M, Maejima T. Numerical simulation of acoustic emission in large-scale underground excavations. Paper presented at: The 42nd U.S. Rock Mechanics Symposium; June 29-July 2, 2008; San Francisco, CA.
8. Damani A, Sharma A, Sondergeld C, Rai C. Mapping of hydraulic fractures under triaxial stress conditions in laboratory experiments using acoustic emissions. Paper presented at: SPE Annual Technical Conference and Exhibition; October 8-10, 2012; San Antonio, TX.
9. Khorshidian H, Butt SD, Arvani F. Influence of high velocity jet on drilling performance of PDC bit under pressurized condition. Paper presented at: 48th U.S. Rock Mechanics/Geomechanics Symposium; June 1-4, 2014; Minneapolis, MN.
10. Rana PS, Abugharara AN, Butt SD, Molgaard J. Experimental evaluation of passive-Vibration Assisted Rotary Drilling (p-VARD) tool to enhance drilling performance. Paper

presented at: The 49th U.S. Rock Mechanics/Geomechanics Symposium; June 28-July 1, 2015; San Francisco, CA.

11. ASTM International. ASTM D6913, standard test methods for particle-size distribution (gradation) of soils using sieve analysis.

12. Reyes R, Kyzym I, Rana PS, Butt SD, Molgaard J. Cuttings analysis for rotary drilling penetration mechanisms and performance evaluation. Paper presented at: The 49th U.S. Rock Mechanics/Geomechanics Symposium; June 28-July 1, 2015; San Francisco, CA.

13. ASTM International. ASTM D422, standard test method for particle-size analysis of soils.

## **Chapter 4 A Novel Method for Assessment of Rock-Bit Interaction and Drilling Performance Using Elastic Waves Propagated by the Drilling System**

Yingjian Xiao <sup>a</sup>, PhD candidate

Charles Hurich <sup>b</sup>, Associate Professor

Stephen D. Butt <sup>a</sup>, Professor

<sup>a</sup> Drilling Technology Laboratory, Memorial University of Newfoundland, St. John's, NL, Canada A1B 3X5

<sup>b</sup> Department of Earth Sciences, Memorial University of Newfoundland, St. John's, NL, Canada A1B 3X5

This chapter is based on the objective defined in section 1.3.3 and was submitted as a research paper to the International Journal of Rock Mechanics and Mining Sciences on February 2017 and is currently under review.

### **4.1 Co-authorship Statement**

The contributions of this collaborative work are described in the following four parts. 1) Identification of research topic and design of experiments are contributed by Yingjian Xiao, Dr. Hurich and Dr. Butt. 2) Dr. Hurich is in charge of the field seismic survey and Yingjian

Xiao is one of the three members. Yingjian Xiao is responsible of coordinating drilling testing and seismic survey. 3) Yingjian Xiao analyzes data and prepare the manuscript. 4) Dr. Hurich and Dr. Butt provide technical knowledge and review the manuscript.

## **4.2 Abstract**

A novel passive Vibration Assisted Rotary Drilling (pVARD) tool was designed and tested to improve drilling performance or rate of penetration (ROP) both in laboratory and field trials. This paper focuses on characterizing drilling performance by means of seismic while drilling (SWD) method and bit vibration analysis. The field scale pVARD tool was applied in drill-off test (DOT) with an array of geophones (1C) spread along drill site. Rotary drilling using a PDC bit was conducted and bit-rock interaction acted as the seismic source for reverse vertical seismic profile (RVSP). The surface wave was selected for characterizing drilling performance due to limited body waves observed during the experiment. The frequency spectra of the surface waves were determined which provided two effective seismic parameters: surface wave energy and frequency bandwidth for drilling performance analysis. These spectra varied in response to variation in drilling conditions, i.e. weight on bit (WOB), pVARD tool use and configuration, and rock type. Bit vibration was assessed by means of vibration accelerations measured with one downhole SensorSub. The whole available data used for characterizing drilling performance included WOB, bit vibration accelerations, seismic energy and frequency bandwidth and rock type. Three groups of DOT tests were conducted: 1) conventional

drilling in red shale, 2) pVARD drilling and conventional drilling in red shale, and 3) pVARD drilling and conventional drilling in grey shale.

Surface waves were used to indirectly characterize drill bit-rock interaction and drill-bit source. From reported RVSP analysis, observed surface waves were shown to be generated by rig-ground interaction coupled to the longitudinal wave travelling along the drill string to the drill rig. In this way, bit-rock interaction or drilling performance was indirectly characterized by the SWD method. Seismic energy and frequency bandwidth was closely correlated with bit vibration and drilling performance when WOB varied.

Analysis of the data shows that the seismic energy and frequency bandwidth decreased with increase of drilling performance. This is explained as more energy being partitioned for improved drilling performance with less energy partitioned to longitudinal wave and rig-ground motion. This phenomenon existed for both conventional drilling and pVARD tool drilling, independent of rock type. For comparable WOB, seismic energy and frequency bandwidth varied in response to drilling with or without pVARD tool, from which the pVARD tool mechanism was further investigated. The SWD method was successfully applied in studying drill-bit interaction and improved drilling performance from pVARD tool. This method is promising for characterizing real-time drilling in future.

**Keywords:** Vibration drilling tool; seismic while drilling; surface wave; frequency bandwidth; bit-rock interaction, drilling performance.

### 4.3 Introduction

A novel drilling tool, the passive Vibration Assisted Rotary Drilling (pVARD) tool, was designed and fabricated at Memorial University of Newfoundland, Canada. Field tests of this tool showed significant increase in rate of penetration (ROP) [1]. However, the relationship between the enhancement mechanism and bit-rock interaction is the subject of ongoing research. The goal of this paper is to characterize drilling performance and bit-rock interaction using seismic while drilling (SWD) as one component of this ongoing work. SWD is a passive seismic recording method using the interaction of the drill-bit and the formation to generate seismic waves that are recorded by surface geophones. Drill-off tests (DOT) are drilling experiments where drilling parameters are systematically varied and the impact on ROP is measured. Varied parameters for the DOTs in this investigation include weight-on-bit (WOB), rotary speed, rock type (i.e. stronger red shale and softer grey shale) and use of and configuration of the pVARD tool. This paper discusses two DOTs in red shale and 1 DOT in grey shale, both comparing conventional drilling and pVARD drilling. Comprehensive assessment is based on drilling data, seismic data, and bit vibration data recorded using a downhole SensorSub.

Improving ROP has been of paramount interest for drilling communities in oil and gas industry and technologies have been developed for achieving this target over the last century. Of all the technologies, utilization of natural bit vibration or addition of extra bit vibration on drill bit is one of the most effective and widely used. In 1902, rotary-percussion drilling was first proposed by adding percussive blows to the conventional rotary drilling

as a means to improve ROP [2]. Since then, rotary-percussion drilling has evolved into one of the most efficient drilling methods using both top-hammer and down-the-hole hammer configuration, in particular, for rapidly penetrating hard igneous and metamorphic rocks in the mining and construction industries. In the 1950s, resonant sonic technology was developed which applies sub-percussive axial vibrations to the bit to successfully increase bit cutting efficiency and improve drilling performance [3]. This technology has evolved into sonic drilling, which is widely used for rapid drilling in soils and similar unconsolidated materials. However, for various reasons, neither drilling technology is suited for oil and gas drilling in sedimentary formations where well control must be maintained to prevent kicks and blowouts. At the Drilling Technology Laboratory of Memorial University of Newfoundland, one group of drilling experts investigated the possibilities of using natural bit vibration to improving drilling performance for otherwise conventional rotary drilling. By drilling with one polycrystalline diamond compact (PDC) bit and adding dampening elements beneath rock specimens in combination to one pulse cavitation drilling tool, the dampening compliance enhanced the oscillatory bit-rock interaction and resulted in improved cutting efficiency and overall drilling ROP [4]. After this, the idea was further developed to incorporate axial compliance directly into the drill string which also improved drilling ROP. These concepts were progressively investigated and refined and incorporated in both laboratory and field scale versions of the pVARD tool, which demonstrated improved ROP under both laboratory and field conditions [5,6]. One set of pVARD field trials formed the basis of the investigation reported in this paper.

Drilling performance is strongly influenced by bit motions and bit-rock interaction which has extensively studied on widely used bits such as roller cone and PDC bits. Theoretical models have been developed to assess forces applied in roller cone bits and the correlation to ROP and drilling conditions [e.g. 7,8]. Empirical relations were proposed to correlate drag forces on one single-cutter PDC bit to rock type, depth-of-cut (DOC) and bit wear state [e.g. 9]. Some researchers have reported on bit-rock interactions through measurement and evaluation of the three modes of drill string vibrations (i.e. axial, lateral and torsional) recognizing that these drill string vibrations are excited by bit-rock interactions [10]. For example, one numerical study of coupled axial and torsional vibrations showed the root cause of self-excited vibration as the delay in axial position of the bit, during the drag bit-rock interaction [11]. These bit vibrations were experimentally measured as accelerations with one down-hole SensorSub [12], and the acceleration data interpretation were used to correlate bit vibrations to drilling conditions such as rock type and WOB [13]. In the laboratory tests, axial bit vibration generated from the pVARD tool was recorded by a laser probe, showing the vibration played a great role in improving drilling performance [5,6], and frequency peaks of axial bit vibrations were found around the angular velocity and its multiples [10].

Seismic while drilling was intensively studied during the 1980s and 1990s [14]. This technology had many applications such as positioning the drill-bit, real-drill-time imaging ahead of bit, guiding the bit to a target, predicting overpressure intervals ahead of bit. Of all the applications, characterization of bit rock interaction and drilling performance using SWD method was of greatest interest in the current discussion: spectral content analysis of

a radiated source is a frequently used method which helps to better understand drill bit conditions. For example, from accelerometers attached to the rig recording roller cone bit drilling source, frequency peaks showed the relationship to formation characteristics [15] and bit wear state [16]. Frequency peaks of the seismic sources showed the relation to bit geometries of both coring bit and roller cone bit [17]. Frequency spectra from rotary-percussion drilling sources showed relationship between specific band to drilling conditions [18], bit types [19] and rock type [20].

## **4.4 Methodology**

### **4.4.1 Experimental methods**

Three shallow boreholes were drilled in September 2014 for testing the pVARD tool protocol at Greenslades Construction Quarry of eastern Newfoundland and Labrador, Canada (Figure 4.1). The SWD method utilized drill-bit rock interaction as a seismic source monitored by an array of 1C geophones (20) which were in-line spread. The space between geophones is 5 m. Three boreholes were drilled with an offset of approximately 7 m. The lithology of underground formations by cross section A-A' is shown in Figure 4.2. The lithologic section is composed of the Manuels River Formation of the Harcourt Group which is black to dark grey shale with thin beds of grey limestone which is labelled as grey shale in this investigation. This formation is underlain by the Chamberlain's Brook Formation of the Adeyton Group defined as green to grey shales with some red mudstones

and shales, and is labelled as red shale [21]. This lithology cross section was confirmed by analysing drill cuttings circulated back to surface.



Figure 4.1: Spread of 1C geophones array (20) with three seismic source boreholes in Greenslades Construction Quarry of east Newfoundland (based on Google map)

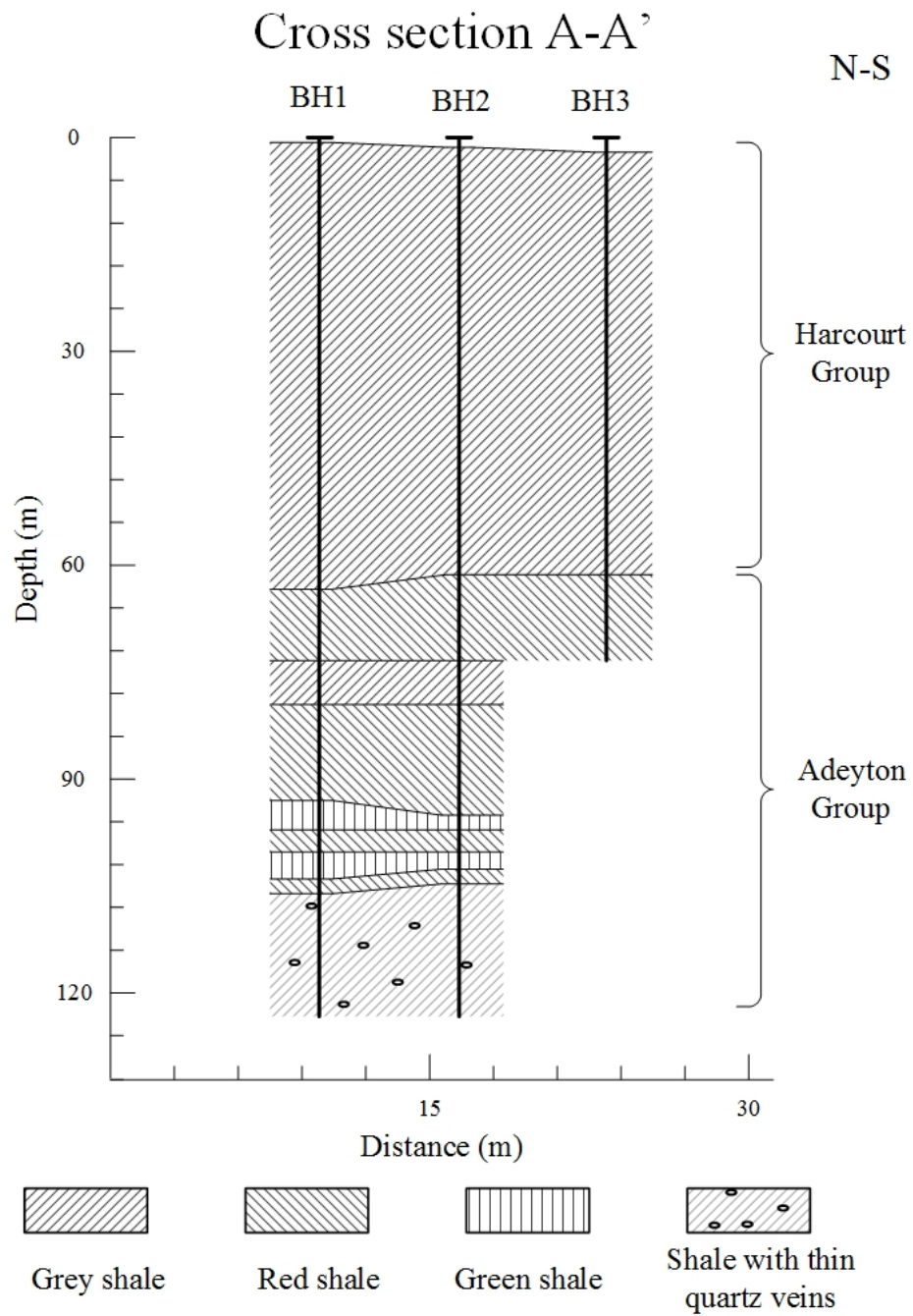


Figure 4.2: Cross section of A-A' showing the rock formation penetrated based on analysis of drill cuttings sampled while drilling

SWD recording took place during the drilling tests to evaluate if SWD data could be used to characterize rotary drilling performance. The drill rig used was an Ingersoll Rand T3W rig (Figure 4.3). The pVARD tool was installed above the downhole sensor-sub which was used to measure bit rotations and multi-axis accelerations. The pVARD tool utilized a series of springs and dampening material to modulate axial compliance which was shown to improve drilling performance [5]. A rotary-percussion hammer bit was used to penetrate the upper formations to the trial depths, followed by drilling using PDC and roller cone bits and with and without the pVARD tool. In this paper, the 152 mm PDC bit was used as the only bit for investigating drilling performance. A linear array of geophones at the surface was deployed as is typical in the reverse vertical seismic profile (RVSP) method.

Drilling parameters were obtained from the drill rig, i.e. WOB, rotary speed, drilling depth and duration. Those parameters remained constant for each three meters drilling interval. The drilling rotary speed was nominally set to 100 revolutions-per-minute (rpm) but this fluctuated with WOB and the precise measurement of ROP was computed as DOC per revolution. To facilitate comparison with familiar values, this measurement was then normalized to ROP at 100 rpm. Water was used for circulating cuttings. Circulation flow, jet nozzle configuration and pressure drop across the bit were varied and optimized at the start of the field trials and then kept constant for the remainder of the trials. The effect of bottom-hole-pressure (BHP) on ROP was neglected due to the small variation in BHP over the depth range of the trials.

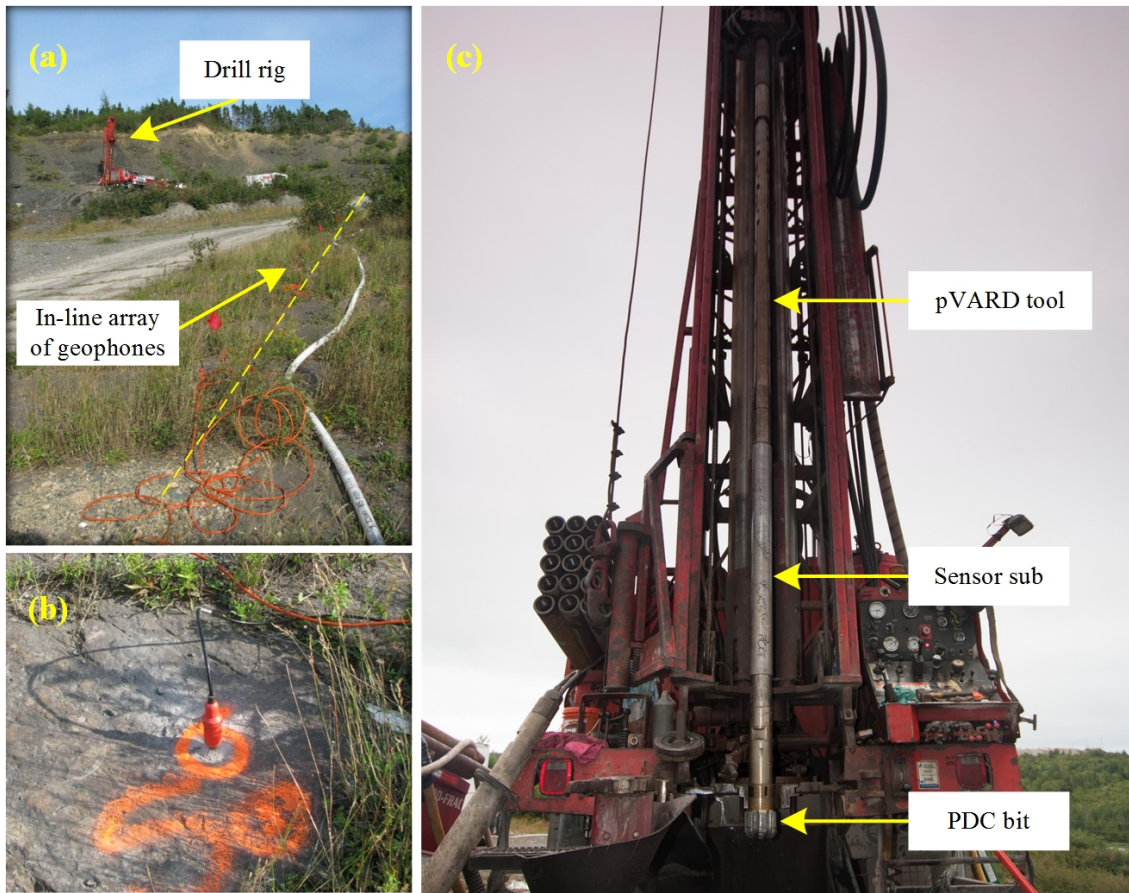


Figure 4.3: Onsite view of seismic while drilling at Greenslades Construction Quarry with (a): overview of drill site with in-line geometry of geophones; (b): 1C geophone; (c): front view of drill rig showing the drilling bottom-hole assembly, modified from Rana et al. [5]

Excluding bit vibration, the drilling parameters that most significantly influenced ROP were WOB, rotary speed and rock type which effected ROP by means of rock strength. The relationship between WOB, rotary speed and rock strength is addressed by Maurer as the “Perfect-Cleaning Theory” and is expressed mathematically in Equation (1) [22,23].

$$R = \frac{K}{S^2} \left[ \frac{W}{d_b} - \frac{W_0}{d_b} \right]^2 N \quad (1)$$

Where

$R$  = rate of penetration,

$K$  = constant of proportionality,

$S$  = compressive strength of rock,

$W$  = weight on bit,

$W_0$  = threshold weight on bit, i.e. the minimum weight on bit to start effective penetration,

$d_b$  = bit diameter,

$N$  = rotary speed.

The other important factors that caused variation of ROP were bit vibration and bit-rock interaction [5,6] which are detailed in the bit vibration and drilling performance analysis presented in this paper.

#### **4.4.2 Surface wave as a monitor of drilling performance**

Surface wave have been observed in SWD experiments while drilling using roller cone bits [24]. This indicates that not only direct waves but surface waves might be used to monitor drilling performance if the surface waves are at least in part generated by longitudinal vibrations in the drill string coupled with the drill rig [24]. To explicitly clarify this phenomenon, surface wave and body wave travel paths are shown in Figure 4.4. A portion of bit-rock interaction energy is transmitted through the drill string as a longitudinal wave. When the longitudinal waves interact with the drill rig, they modify the surface waves generated by the drill rig. In this way, observation of the modified surface waves can be

used to characterize the drill bit source by way of characterizing rig motion which is closely related to drill bit motion.

In this research, both surface and body waves were confirmed in rotary-percussion hammer bit drilling, while only surface waves were observed from PDC bit drilling. Thus the surface wave was utilized to characterize the drill-bit source.

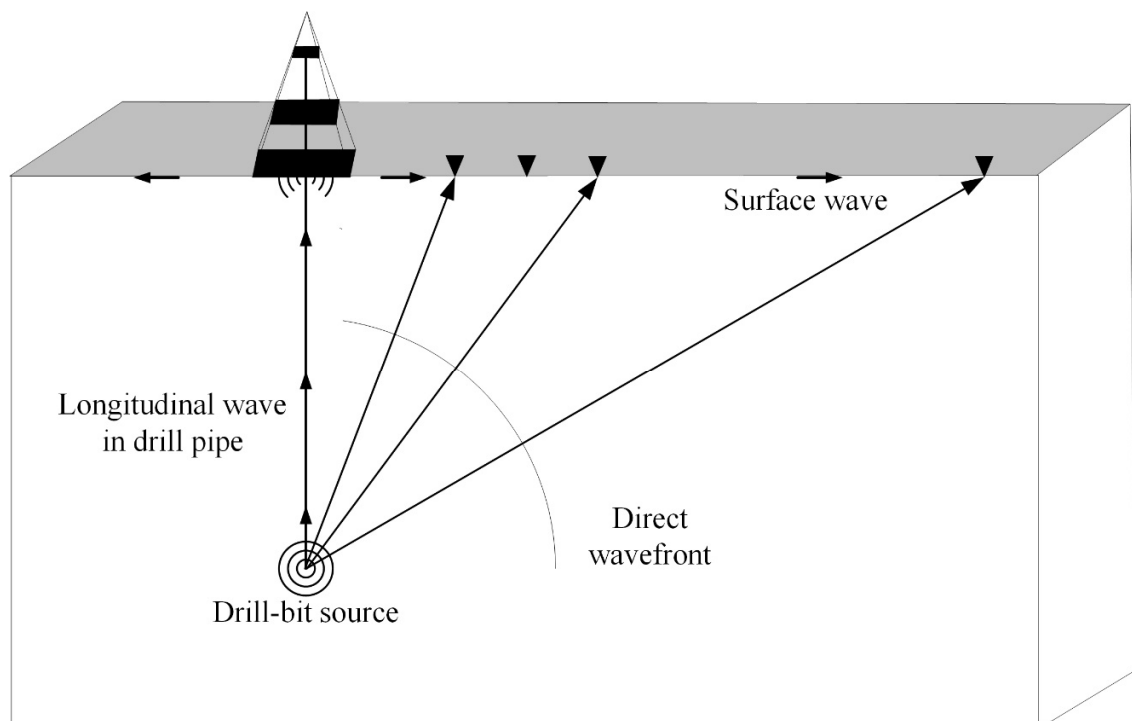


Figure 4.4: Demonstration of direct wave and surface wave generated from rig-ground interaction, which was modified from Rector and Hardage [24]

#### 4.5 Properties of the Rocks

The geomechanics and ultrasonic properties of the shales are essential for understanding the DOTs, elastic wave propagation and SWD. Outcrop blocks for the relevant lithologies

were obtained in an adjacent quarry. Then, geomechanics and ultrasonic tests were conducted on these rocks at Drilling Technology Laboratory. Table 4.1 shows test results. Results of red shale were reported by other researchers [5]. The unconfined compressive strength (UCS) was measured by the point load index method [25] and ultrasonic velocities were measured by the ultrasonic testing method [26]. From these results, it is evident that the red shale was comparatively stronger and more competent than the grey shale, and that the drilling trails were conducted in low to medium strength formations.

Table 4.1: Geomechanics and ultrasonic properties of the shale formations oriented perpendicular to bedding

	UCS (MPa)	Density (kg/m <sup>3</sup> )	P-wave velocity (m/s)	S-wave velocity (m/s)
Red shale	56.0	2760.0	5154.0	3767.0
Grey shale	32.3	2579.7	3394.9	2693.5

## 4.6 Data Acquisition and Processing

### 4.6.1 Data acquisition

Figure 4.5 shows the 3D geometry of the array of 1C geophones with respect to the drill-bit source for three boreholes whose depths were precisely shown in Figure 4.2. Onsite geophone array could be visualized in Figure 4.3. The dip of the ground surface was approximately 18° based on geophone GPS coordinates. Seismic signals were continuously recorded for 30 s with sampling frequency of 1000 Hz and multiple 30 s recordings were obtained for each 3 m run of the DOTs.

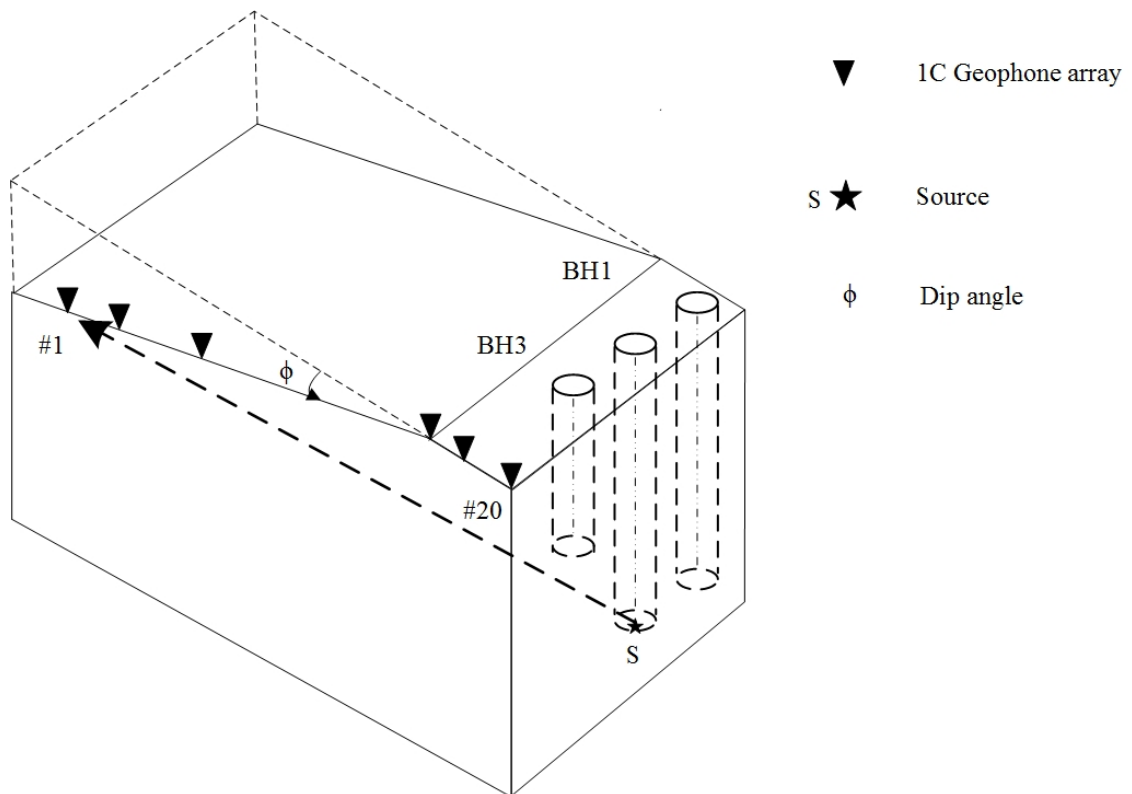


Figure 4.5: 3D Geometry of 1C geophone array with regarding to the three boreholes (looking north)

Based on the objective of studying drilling performance of the pVARD tool using SWD, the plan for conducting the DOTs is listed as follows:

- 1) Characterization of rigid drilling in red shale,
- 2) Comparison of pVARD tool and rigid drilling in red shale,
- 3) Comparison of pVARD tool and rigid drilling in grey shale.

#### 4.6.2 Seismic data processing

Raw seismic data were processed using the GEDCO Vista 2D/3D Seismic Data Processing package. The processing workflow sequentially included notch filtering to remove 60 Hz noise, spiking deconvolution, and then cross correlation with the reference channel #20. Channel #20 was selected as the reference channel because it was the closest geophone to the drill rig. In Figure 4.6, sample cross correlated seismic data are shown from Borehole 2. Twenty traces were grouped as one drill-bit source and apparent difference of amplitude were shown between hammer bit drilling and PDC bit with pVARD tool drilling.

In Figure 4.7, seismic data are assembled into a RSVP by assembling traces from the same geophone at different bit depths. Hammer bit drilling was followed by PDC bit drilling with the pVARD tool. From the arrival time and apparent velocity, the vertically polarized shear wave (SV) was identified. In the RSVP, the SV wave arrival time decreases as drilling depth increases due to the time shift introduced by the correlation with the reference channel. Seismic wave frequency spectra have been demonstrated to be useful to characterize drilling parameters [18]. However, because we did not reliably observe the body waves (SV) with all of the drill bits used, we chose to use the surface wave to characterize drilling performance.

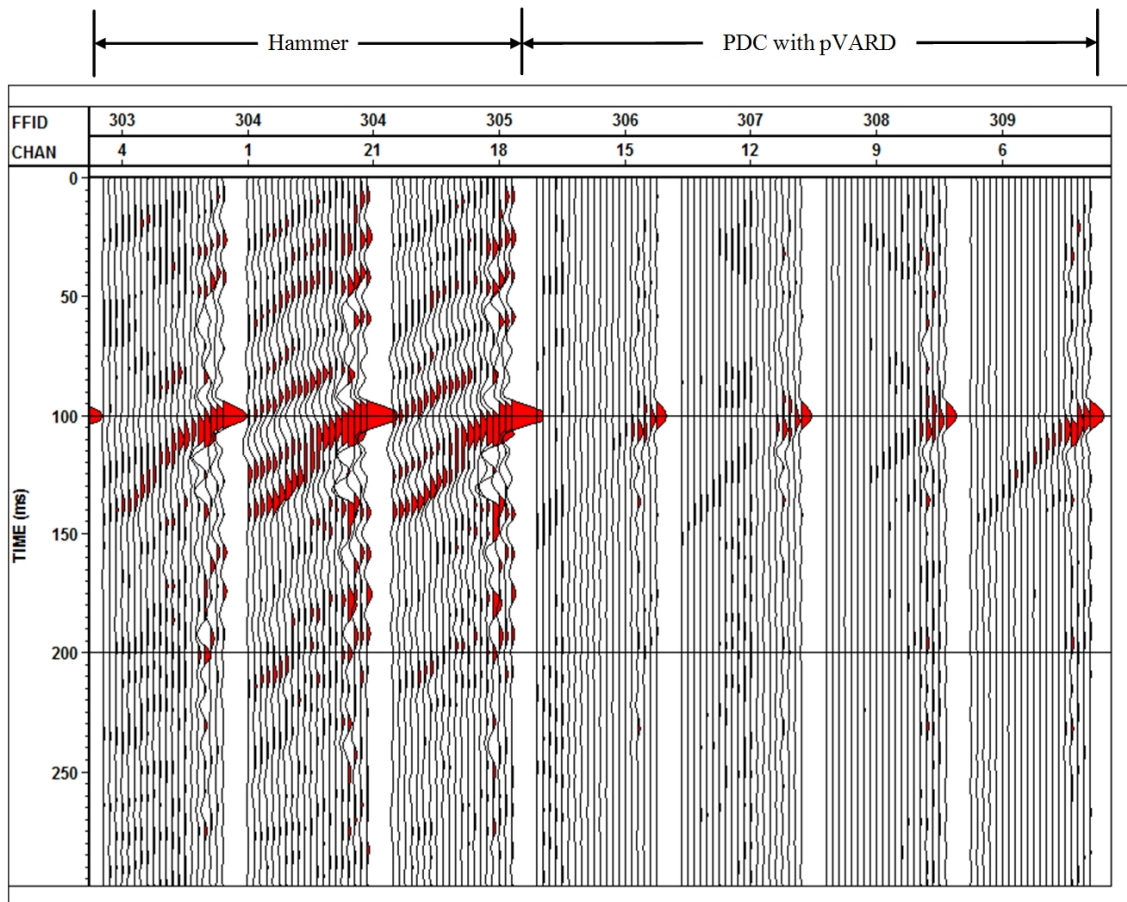


Figure 4.6: Sample seismic data cross correlated on channel #20. In borehole 2 from 79.2 to 85.3 m, red shale was drilled by a hammer bit and a PDC bit with the pVARD tool. Every twenty traces were assembled in one group recorded by 20 geophones. The space between traces is 5 m. No scaling was applied

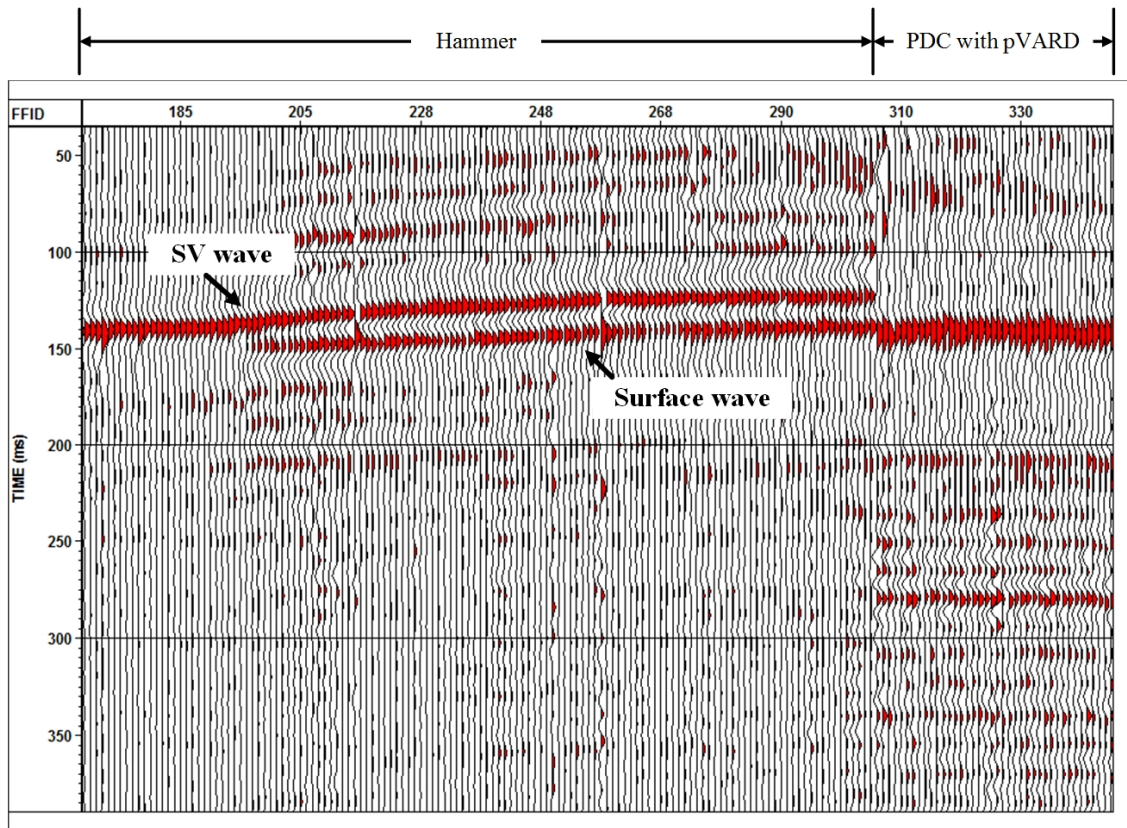


Figure 4.7: Assembly of cross correlated traces from channel #3 in borehole 2. Drilling depths ranged from 0 to 91.4 m. Trace was individually scaled at its peak amplitude

Figure 4.8 shows the frequency spectra recorded when there was no drilling. This is essentially the background noise when there is no penetration with the bit and therefore no bit-rock interaction and the associated drilling modified surface waves. Figure 4.9 provides example surface wave frequency spectra recorded while drilling using the same color bar scale for surface wave magnitude as for Figure 4.8. The narrower frequency spectrum for the background noise confirms that there is less rig motion when not drilling and that the bit-rock interaction while drilling modified the surface waves radiated from the drill rig. In Figure 4.9, the frequency spectra for eight separate DOT drilling experiments are given, representing 4 increasing WOBS with the pVARD tool (labelled as T1 through T4) and 4

increasing WOBs without the pVARD tool, i.e. rigid or conventional drilling (labelled as T5 through T8). For these specific frequency spectra, it can be observed that i) the frequency bandwidth of the surface waves decreases with increasing WOB, and ii) the surface wave amplitudes for pVARD drilling are higher than for rigid drilling. This confirms that the different drilling parameters used for the DOTs generates surface waves with distinct frequency and amplitude spectra.

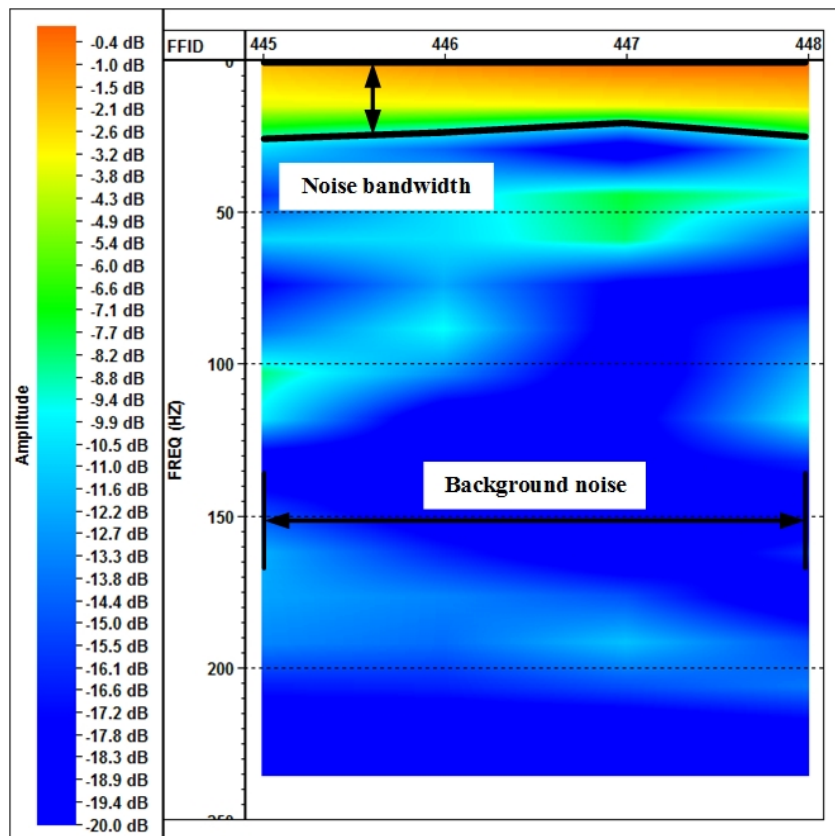


Figure 4.8: Sample frequency spectrum for surface wave traces recorded at channel #3 when drill rig was on with no drilling

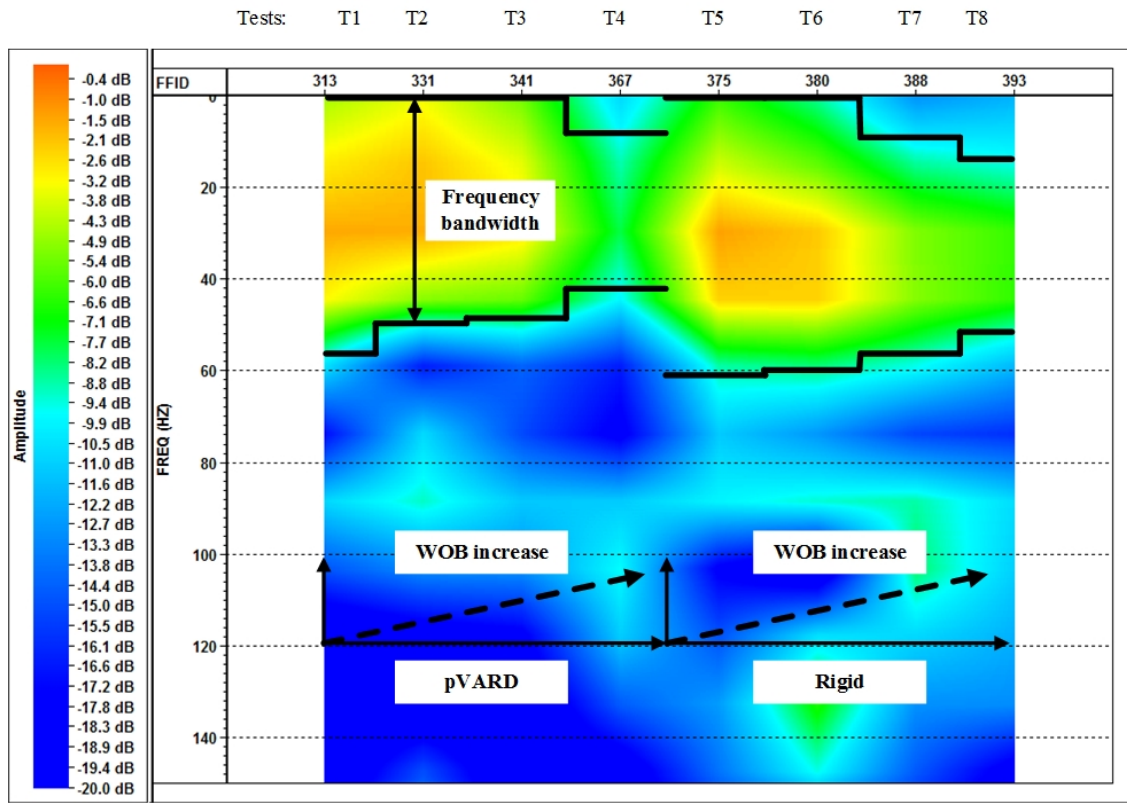


Figure 4.9: Demonstration of eight frequency bandwidths for surface wave traces recorded from 8 DOTs, which are divided into two drillings, i.e. the pVARD tool (T1-T4) and rigid (T5-T8)

In addition to frequency spectrum, the energy level was also an effective means to quantitatively characterize drill-bit source. In this paper, surface wave amplitude level was obtained by means of root mean square (RMS) method [27], which was accessible by a workflow in Halliburton SeisSpace/ProMAX 2D package. This value was used to characterize the surface wave energy level.

### 4.6.3 Bit vibration data collection and analysis

There were generally three types of drill string vibration in rotary drilling, i.e. axial, lateral and torsional vibrations [10]. In this research, they were evaluated by accelerations in axial, lateral and torsional directions, respectively, using the downhole SensorSub which was mounted behind the PDC bit in the drilling Bottom-Hole-Assembly (BHA) for measuring near-bit accelerations and rotation (Figure 4.3). The SensorSub used four triaxial accelerometers and a magnetometer (Figure 4.10), from which the near-bit axial, lateral and torsional accelerations were calculated [12]. The calculation procedure is demonstrated in Appendix 2. Accelerations were further processed using the RMS method which provided a measure of magnitude of a signal [27].

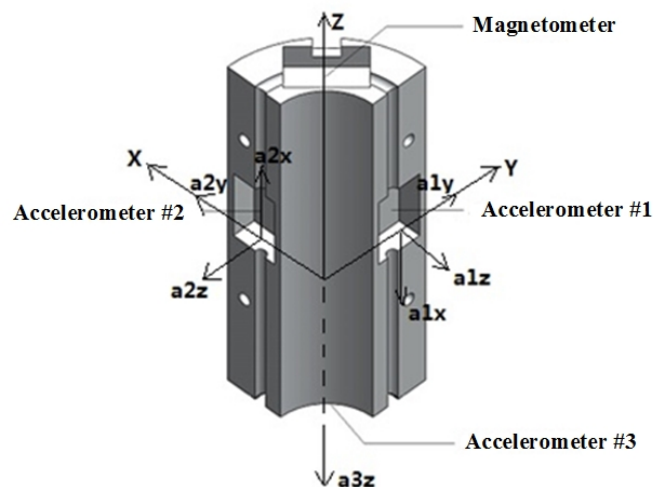


Figure 4.10: Sensor package was coaxially located inside the downhole SensorSub. Accelerometers were collaboratively used in obtaining accelerations for bit vibration modified from Gao [12]

In Figure 4.11, bit vibration levels are related to corresponding WOB when drilling was conducted in borehole 1 red shale from 69.3 to 93.8 m. Acceleration was normalized to

rotary speed of 100 rpm for comparison. Torsional vibration resulted from angular velocity change of drill string which played less role than axial and lateral vibrations and thus not investigated for the following research. Bit vibration levels in both axial and lateral directions generally decreased with the increase of WOB applied on the PDC bit. An exception is noted when WOB was the lowest, however, this is reasonable because when axial load increased the amplitude of bit natural vibration decreased. Axial vibration level remained the lowest compared to other vibrations while it was comparable to the lateral vibration level. These results were visually verified from field observations on drill string vibration on the ground. Torsional vibration or “stick-slip” of drill-string was commonly observed using the PDC bit by the driller, while axial and lateral vibration were not apparently observed.

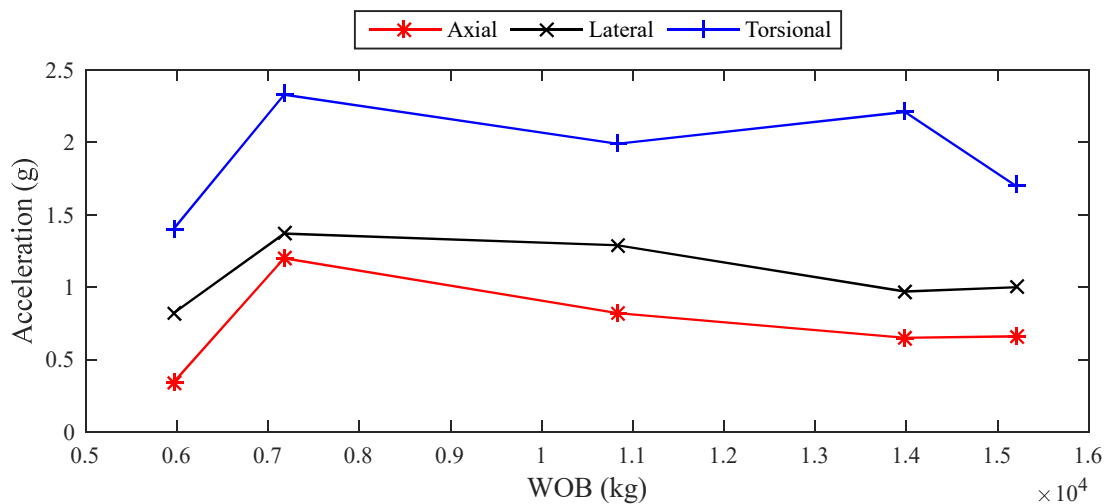


Figure 4.11: Bit vibration was interpreted as three accelerations. Red shale was drilled with one PDC bit from 69.3 to 93.8 m in borehole 1

#### 4.7 Data Analysis and Interpretation

In Table 4.2, three groups of seismic while drilling tests were conducted in three different boreholes. Rock type remained the same for each group, within the group drilling settings varied. The drilling setting was designated as rigid indicating the pVARD tool was not present. The setting of pVARD tool springs was set as V12000 which meant working load of 12,000 pounds for the tool springs at quarter deflection [1]. For every setting of drilling, increasing WOBs were applied and corresponding seismic events were recorded and distinguished by field file identification number (FFID). Representative seismic records were selected for processing. ROP and bit vibration data were finally normalized to 100 rpm for comparison.

Table 4.2: Drill-off test parameters for the seismic-while-drilling experiments

Borehole	Rock	Drilling setting	WOB (kg)	Seismic events FFID
1	Red shale	Rigid	5959.8	74,75
			7177.5	87,88,89
			10830	96,97
			13982	64,65
			15200	67
2	Red shale	pVARD	6047.6	313
			7265.3	330,331
			8482.9	341,342,343
			8816.3	367
2	Red shale	Rigid	6574.1	373,374,375
			6591.7	380,381,382,383
			6609.2	387,388
			7756.6	393
3	Grey shale	pVARD	5328.1	560
			6475.6	562
			7622.9	564,565

			9935.4	567
			5415.9	569
3	Grey shale	Rigid	6580.9	570,572
			7745.8	574
			8910.8	575

#### 4.7.1 Rigid drilling on red shale

In borehole 1, the red shale was drilled with rigid setting from 69.3 to 93.8 m depth. Available data include WOB, ROP, rotary speed, seismic signals, and bit vibrations.

In Figure 4.12, normalized ROP is plotted versus WOB and corresponding axial and lateral acceleration. RMS of surface wave amplitude is interpreted as the energy from different drilling depths received by five different geophones. From Figure 4.13 to Figure 4.17, frequency spectra were obtained on five depths at selected channels #1, #3, #7, #10 and #13. Every black window represents one drilling condition of WOB.

From the drilling performance (Figure 4.12), ROP generally increases with the increase of WOB, which confirms Maurer's "Perfect bottom-hole cleaning theory" [22]. The maximum ROP was not determined to be the optimum drilling performance under the present drilling conditions due to lack of sufficient post-peak experiments. Corresponding axial and lateral vibration magnitudes decreased which showed bit vibration was depressed due to increase in WOB. Surface wave energies from all channels decreased. Simultaneously from the frequency spectra, frequency bandwidth of specific energy level (above -8.8 dB), i.e. black window height decreased.

Due to transmission of energy from drill bit through drill pipe to rig (Figure 4.4), drill bit energy was partitioned to rig-ground interaction and rig arrival or surface wave was obtained [24]. Based on this, decrease of surface wave energy and frequency bandwidth resulted from lower magnitude and less variation of rig-ground motion. A reasonable presumption is that less drill bit energy was partitioned to generate surface wave while more energy was used in bit penetration, when WOB is increased.

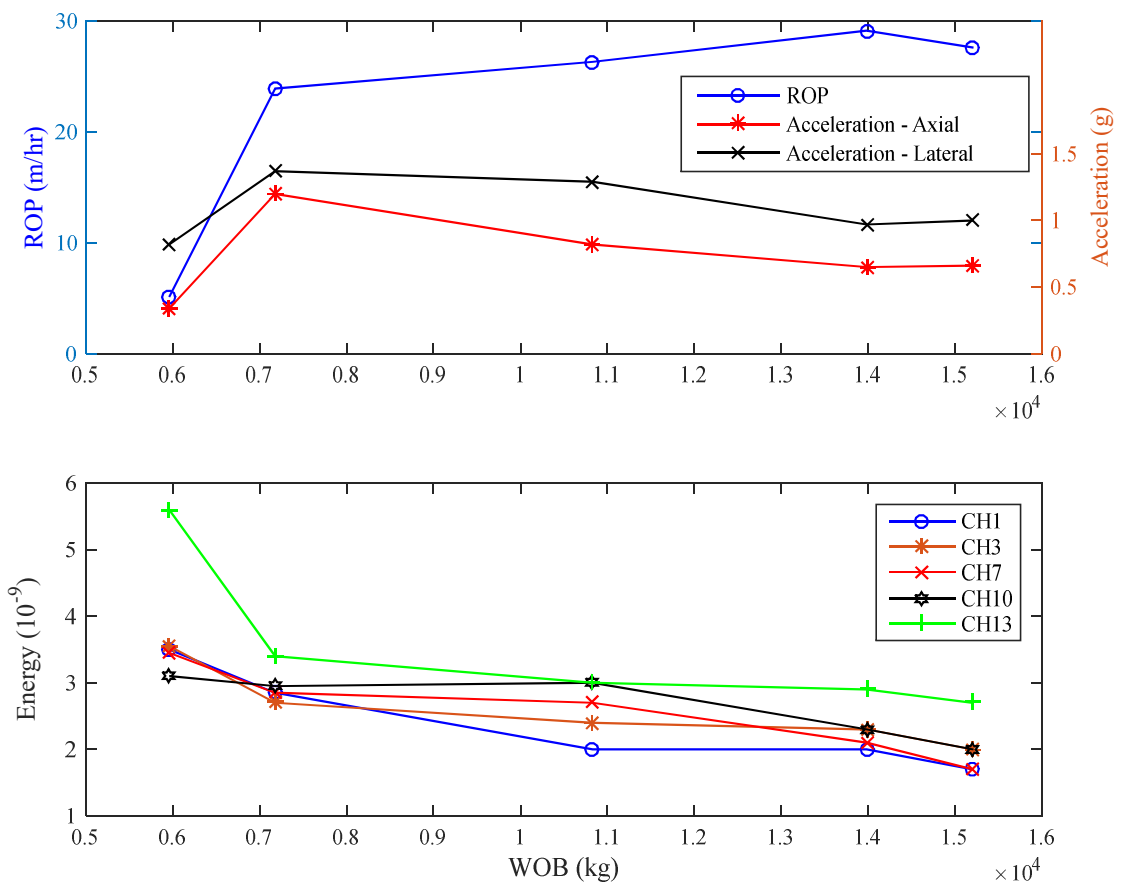


Figure 4.12: Red shale was drilled from 69.3 to 93.8 m in borehole 1. Results were shown as ROP and vibration accelerations (top), surface wave energies from multiple channels (bottom)

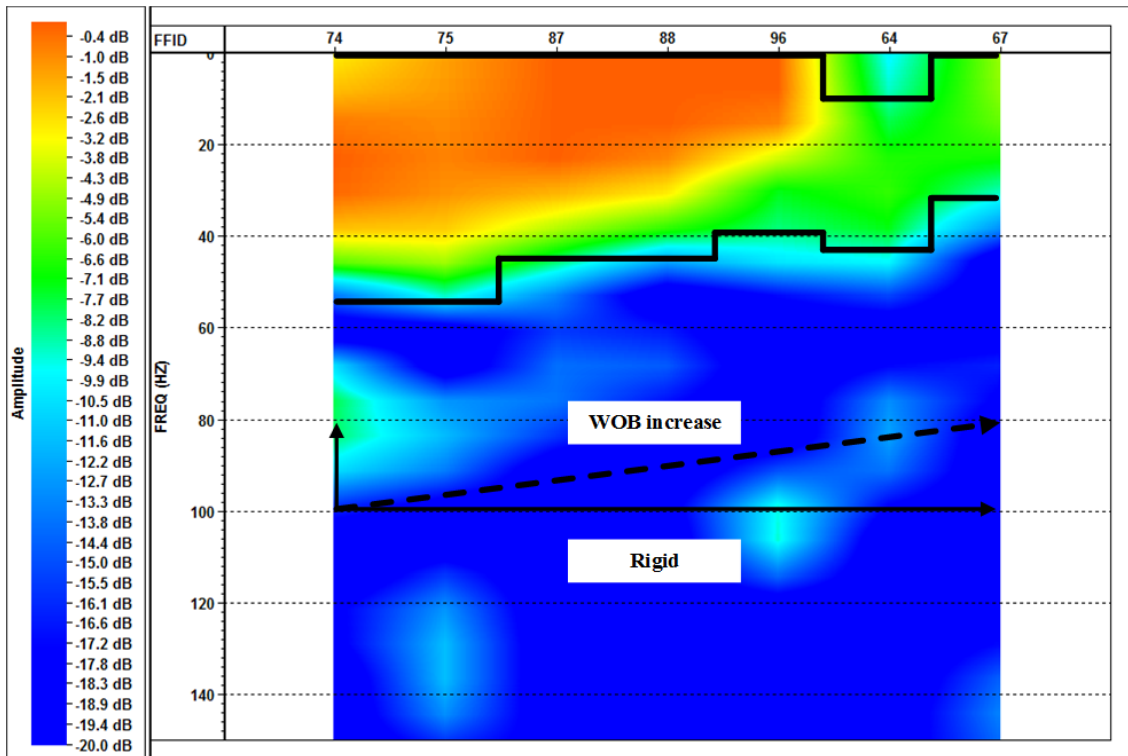


Figure 4.13: Five frequency bandwidths corresponded five WOBs of rigid drilling from channel #1, when red shale was drilled from 69.3 to 93.8 m in borehole 1

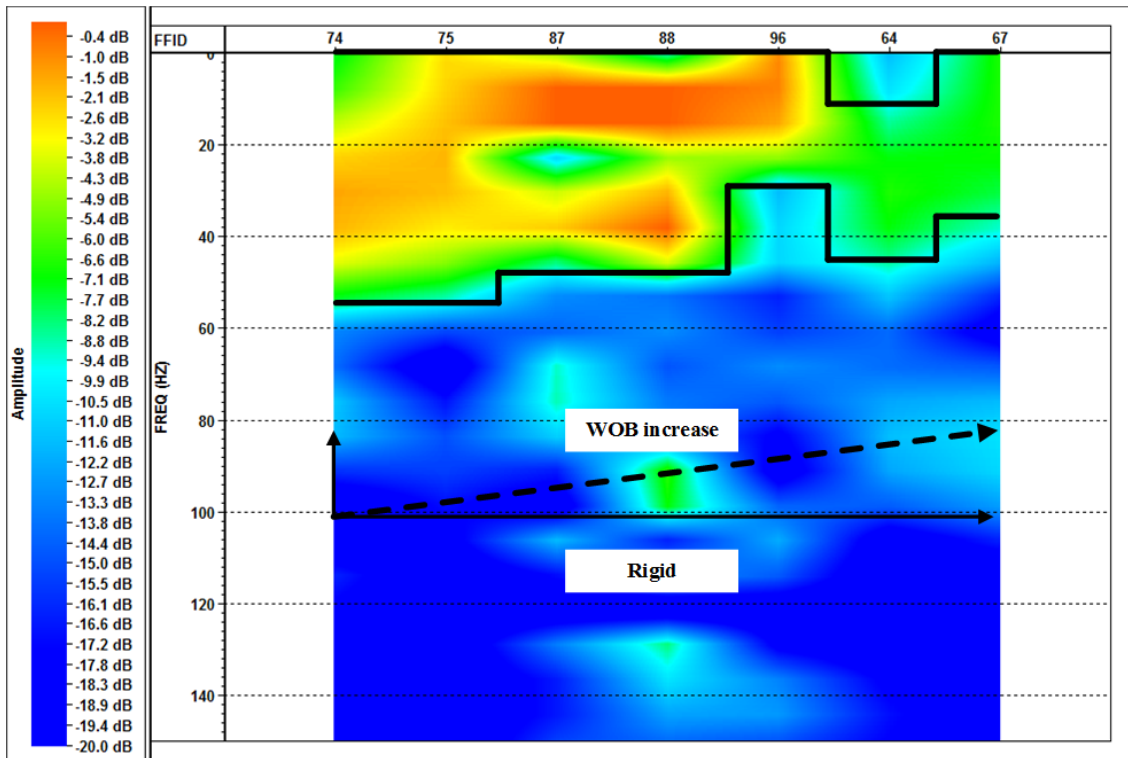


Figure 4.14: Five frequency bandwidths corresponded five WOBs of rigid drilling from channel #3, when red shale was drilled from 69.3 to 93.8 m in borehole 1

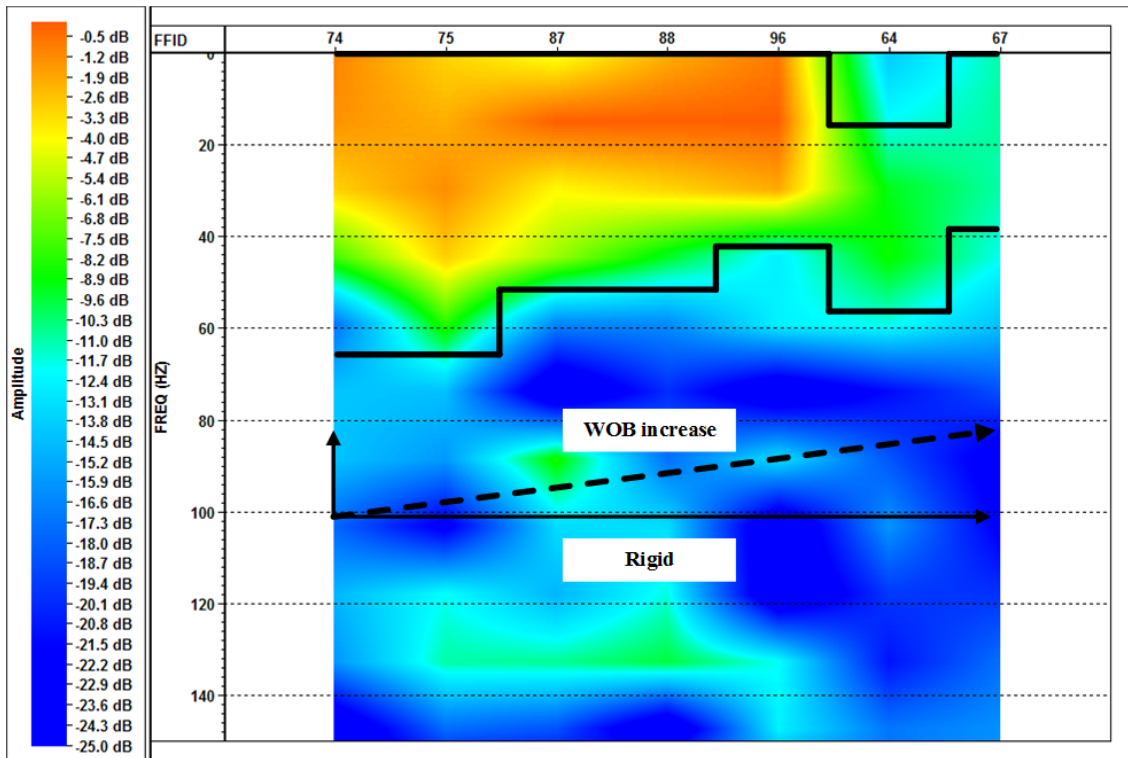


Figure 4.15: Five frequency bandwidths corresponded five WOBs of rigid drilling from channel #7, when red shale was drilled from 69.3 to 93.8 m in borehole 1

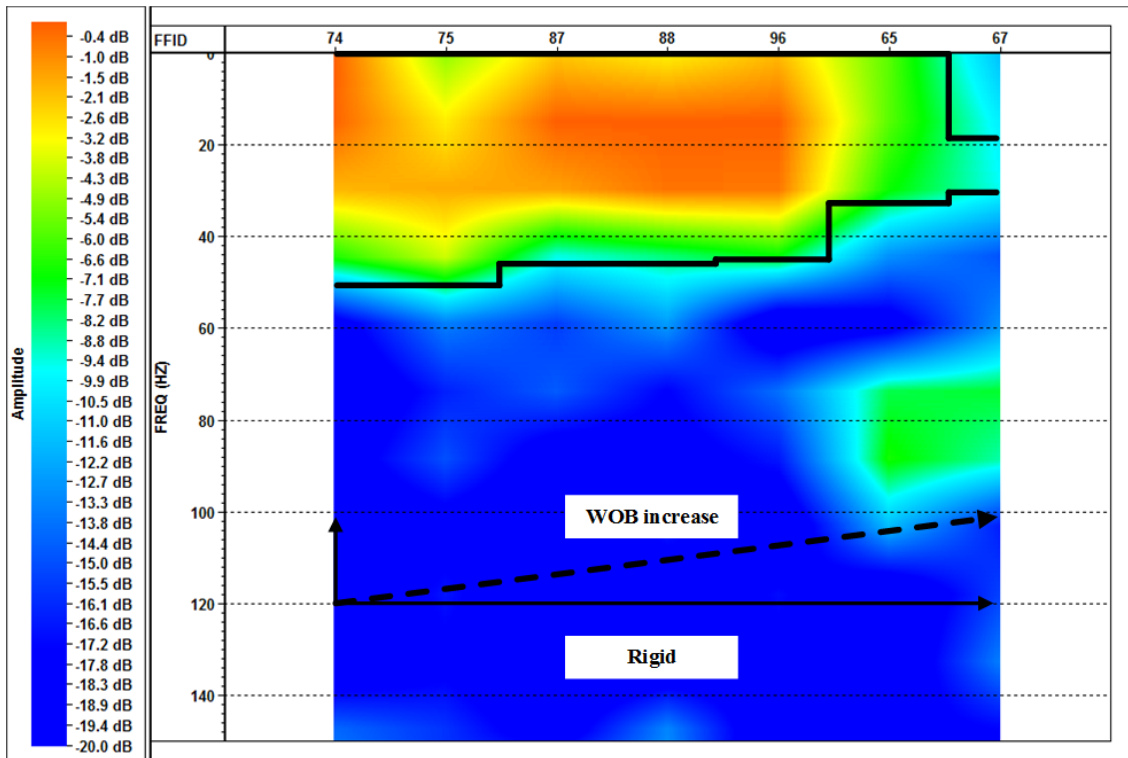


Figure 4.16: Five frequency bandwidths corresponded five WOBs of rigid drilling from channel #10, when red shale was drilled from 69.3 to 93.8 m in borehole 1

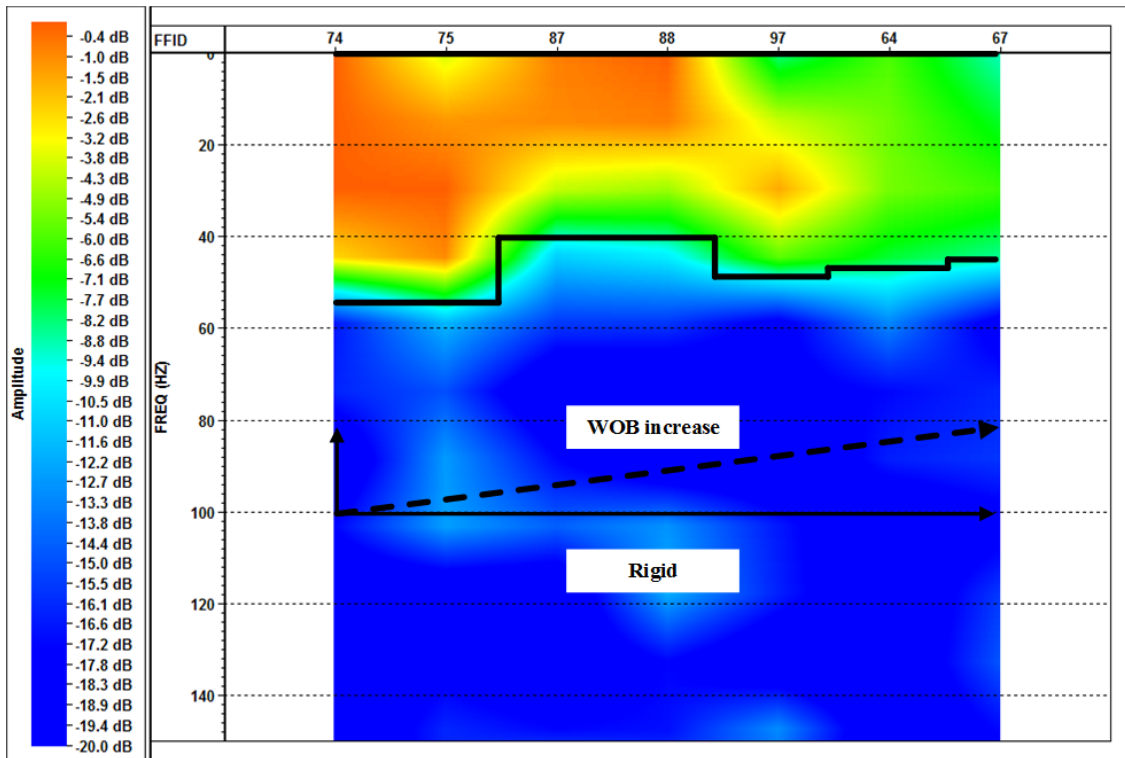


Figure 4.17: Five frequency bandwidths corresponded five WOBs of rigid drilling from channel #13, when red shale was drilled from 69.3 to 93.8 m in borehole 1

#### 4.7.2 pVARD and rigid drilling on red shale

In borehole 2, red shale was drilled with rigid setting from 103.6 to 106.0 m depth and drilled with pVARD tool from 82.3 to 103.6 m depth. Available data include WOB, ROP, rotary speed, seismic signals, while bit vibration data are not available.

In Figure 4.18, normalized ROP was plotted versus WOB. Surface wave energy was interpreted from different drilling depth received by six different geophones. From Figure 4.19 to Figure 4.24, frequency spectra were obtained on four depths for each setting at selected channels #1, #3, #5, #7, #10 and #13.

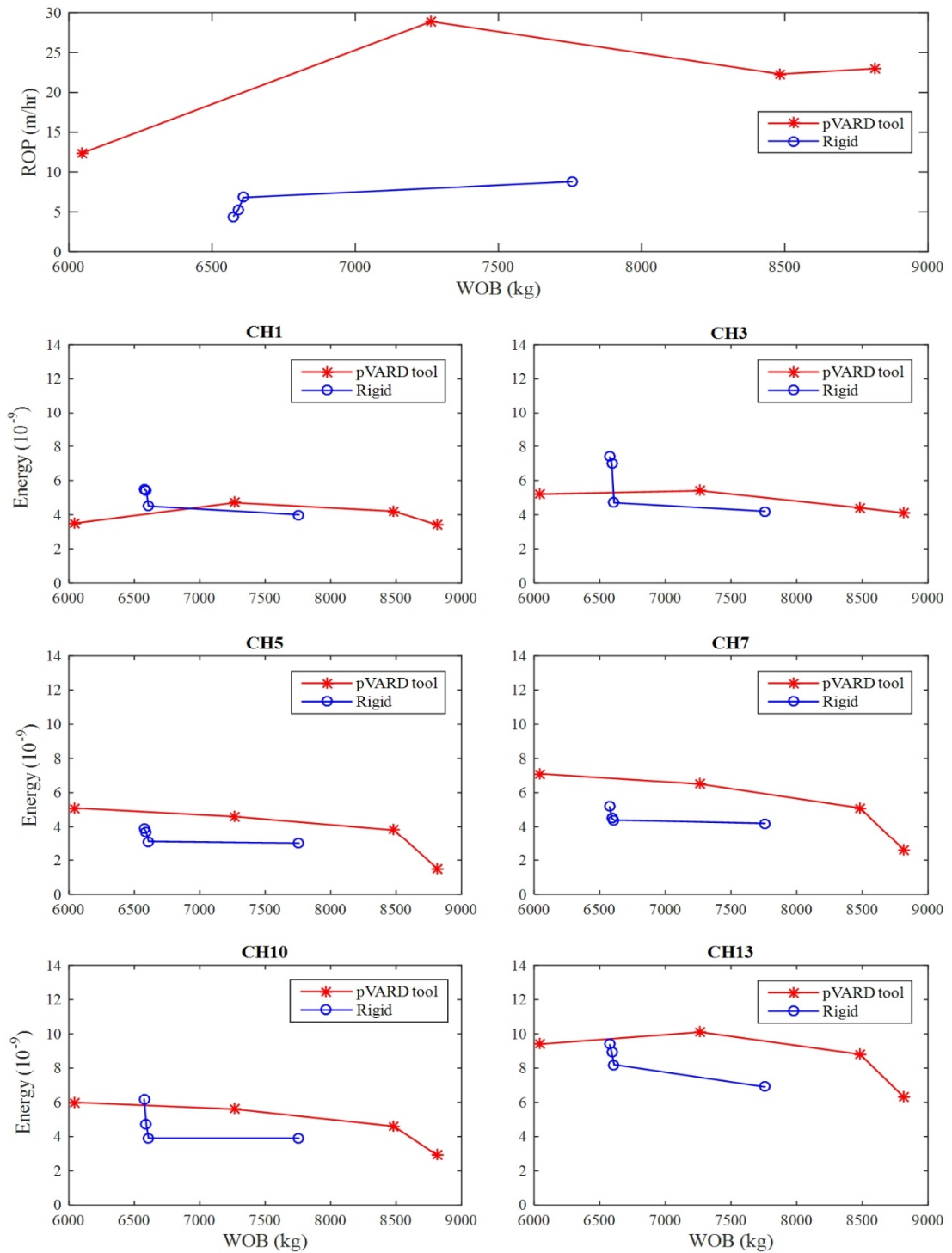


Figure 4.18: Red shale was drilled from 82.3 to 106.0 m in borehole 2. Results were shown as ROP, and surface wave energy comparison for the pVARD tool and rigid drillings

From the drilling performance, ROP generally increased with the increase of WOB for both means of drillings, while surface wave energies decreased. Simultaneously from the frequency spectrum, seismic frequency bandwidth of specific energy level (0 to -8.8 dB) decreased. This confirmed that the decrease of surface wave energy and frequency bandwidth from rig motion was due to increase of bit energy partition into bit penetration from increase of WOB. Rig-ground interaction was weakened in magnitude and motion variation.

Furthermore, ROP increased with the pVARD tool compared to rigid drilling. For comparable WOB, the pVARD tool provided higher level of surface wave energy resulting from higher magnitude of rig-ground interaction. This phenomenon can be explained in terms of the pVARD tool mechanism. The pVARD tool improved drilling performance by means of increasing bit-rock contact time per every cycle of axial vibration period, thus rocks were more easily cracked which was confirmed in the laboratory experiments [6]. This function of imposing the bit on rock for a longer time with the pVARD tool made the whole drill string more compliant than the rigid case. In this way, the higher magnitude of rig motion was generated from additional compliance of drill string. The frequency bandwidths of the pVARD and rigid drillings were comparable.

Finally, increase of WOB resulted in improved ROP by more energy partition into bit penetration, and less energy partition to rig-ground motion transmitted through the drill string causing less surface wave energy and frequency bandwidth. For comparable WOB, drill string compliance made more bit energy partition into bit penetration and increased

ROP by increasing bit-rock contact time, and intensified the rig-ground interaction resulting in higher magnitude of surface wave.

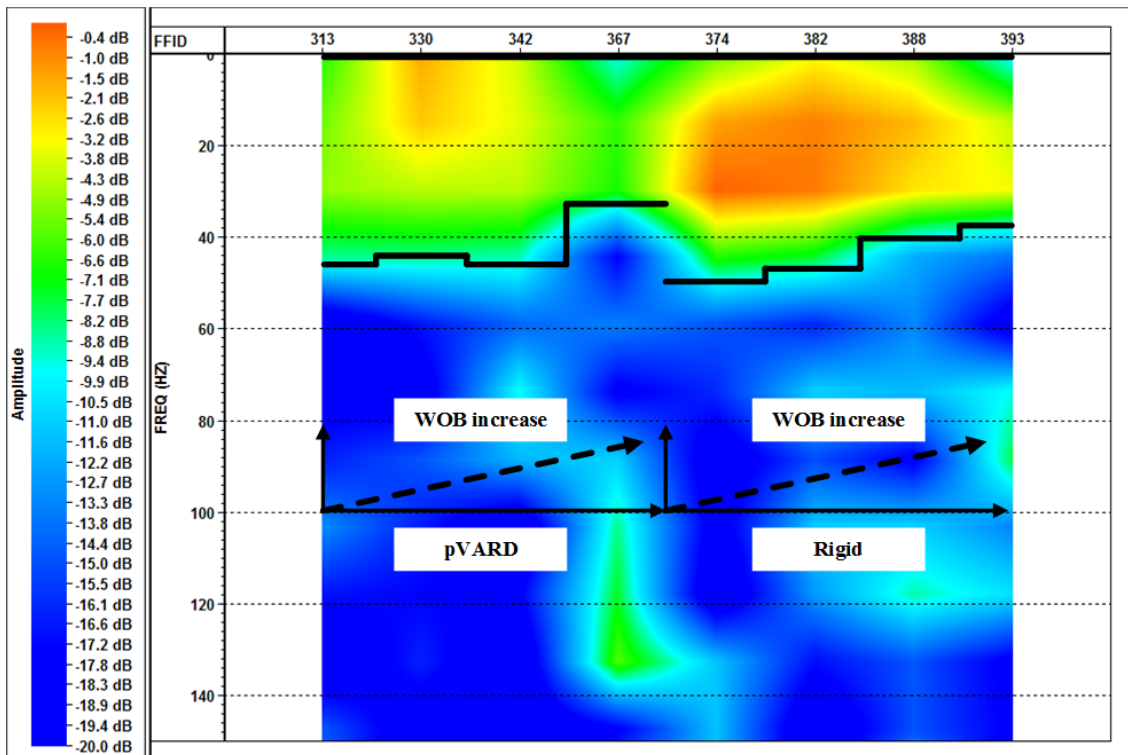


Figure 4.19: Four frequency bandwidths corresponded four WOBs for the pVARD tool and rigid drillings from channel #1, when red shale was drilled from 82.3 to 106.0 m in borehole 2

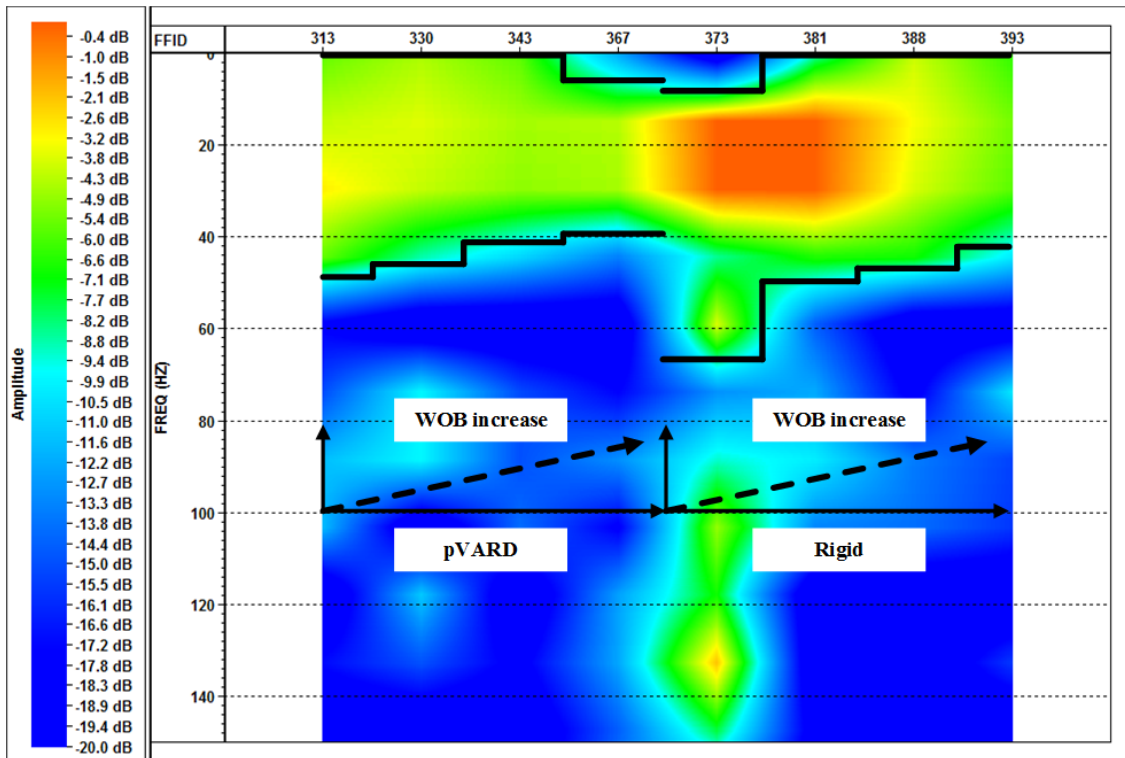


Figure 4.20: Four frequency bandwidths corresponded four WOBs for the pVARD tool and rigid drillings from channel #3, when red shale was drilled from 82.3 to 106.0 m in borehole 2

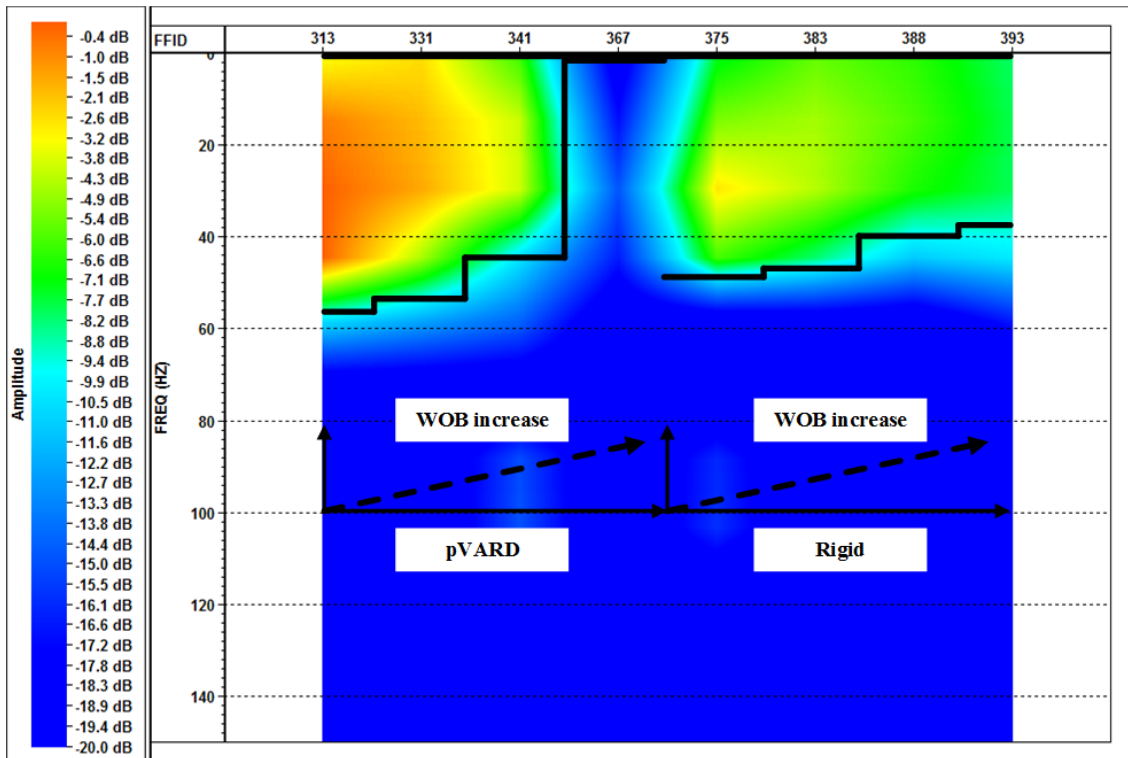


Figure 4.21: Four frequency bandwidths corresponded four WOBs for the pVARD tool and rigid drillings from channel #5, when red shale was drilled from 82.3 to 106.0 m in borehole 2

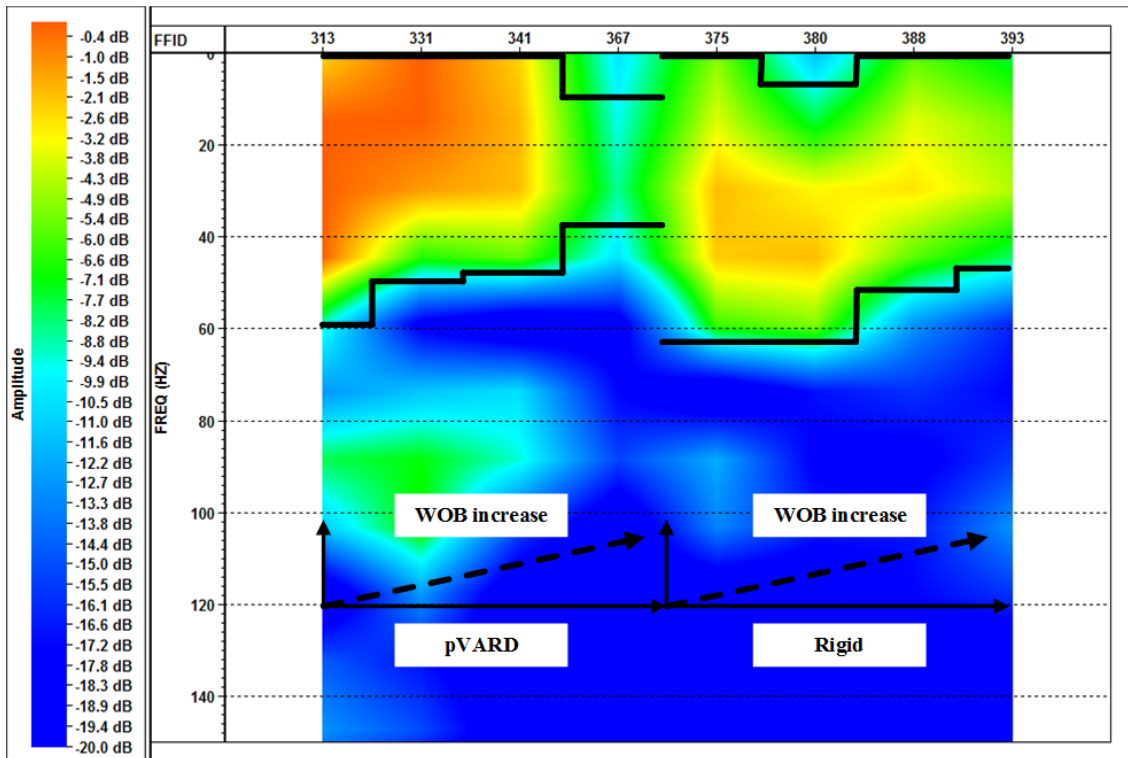


Figure 4.22: Four frequency bandwidths corresponded four WOBs for the pVARD tool and rigid drillings from channel #7, when red shale was drilled from 82.3 to 106.0 m in borehole 2

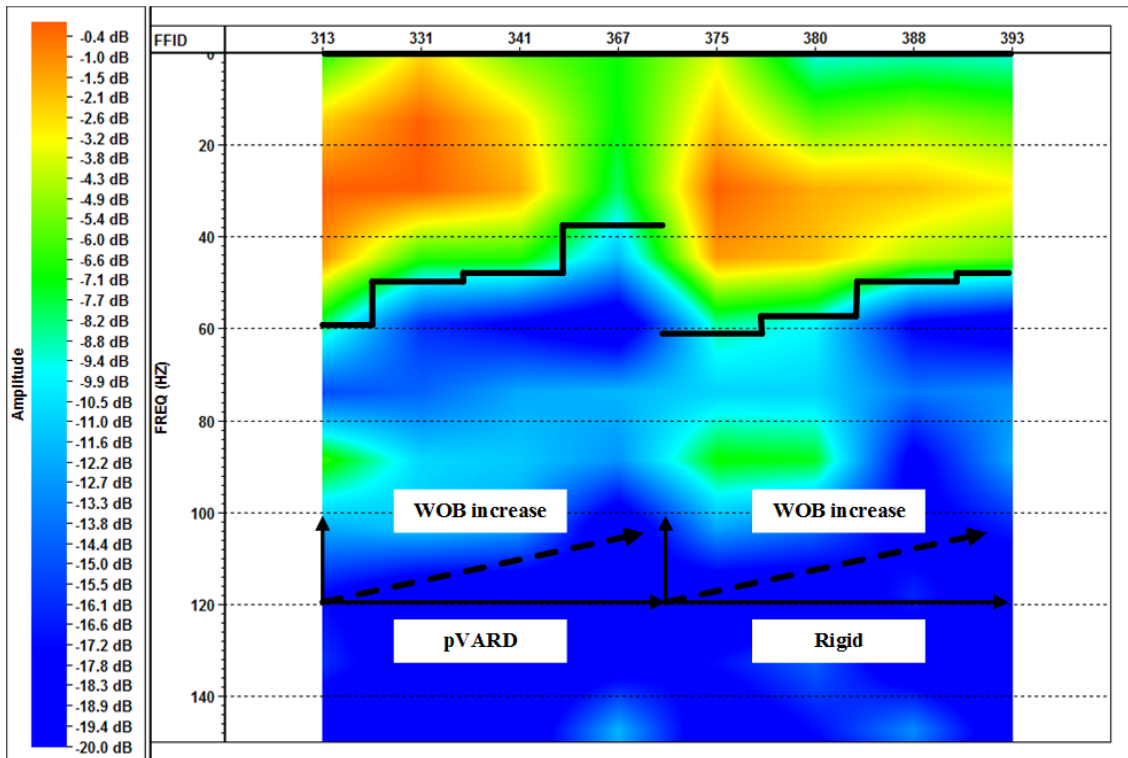


Figure 4.23: Four frequency bandwidths corresponded four WOBs for the pVARD tool and rigid drillings from channel #10, when red shale was drilled from 82.3 to 106.0 m in borehole 2

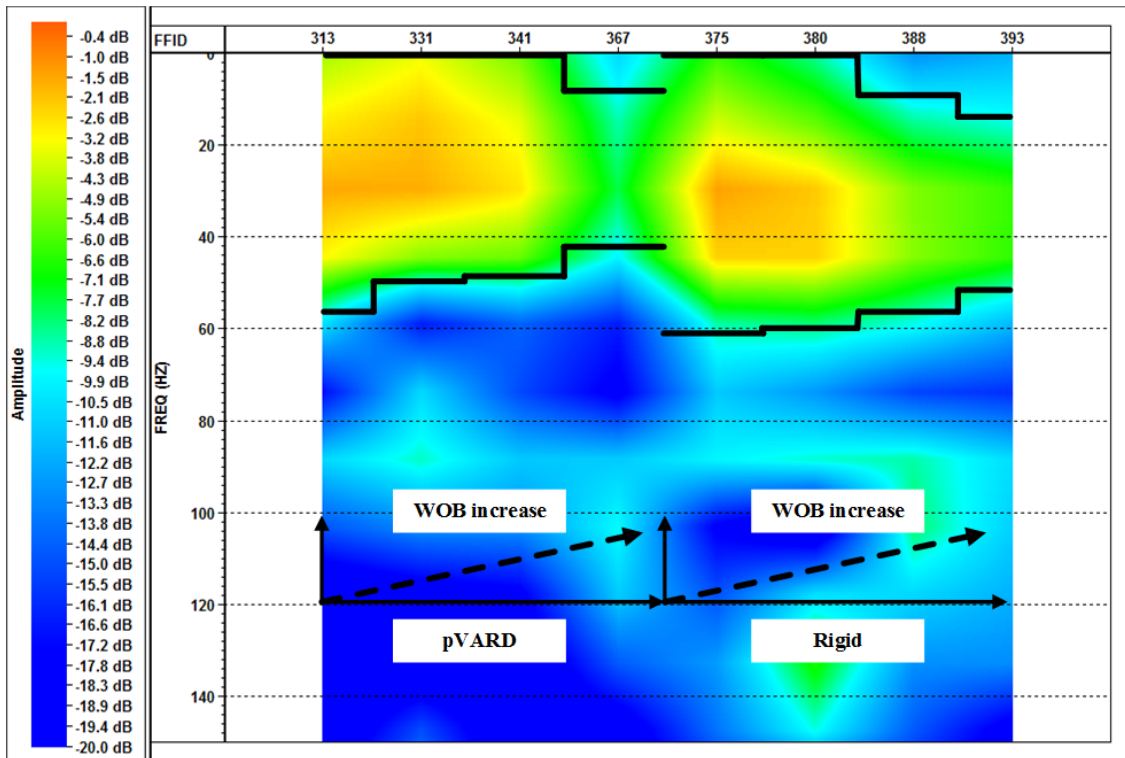


Figure 4.24: Four frequency bandwidths corresponded four WOBs for the pVARD tool and rigid drillings from channel #13, when red shale was drilled from 82.3 to 106.0 m in borehole 2

### 4.7.3 pVARD and rigid drilling on grey shale

In borehole 3, grey shale was drilled with conventional setting from 57.5 to 60.0 m depth, and drilled with the pVARD tool from 54.5 to 57.5 m depth. Available data include WOB, ROP, rotary speed, seismic signals, while bit vibration data are not available.

In Figure 4.25, normalized ROP is plotted versus WOB. Surface wave energy is interpreted from different drilling depths received by three different geophones. From Figure 4.26 to Figure 4.28, frequency spectra were obtained on four depths for each setting at selected

channels #7, #10 and #13. The energy level was set from 0 to -15 dB for the optimum demonstration based on the received surface wave energy.

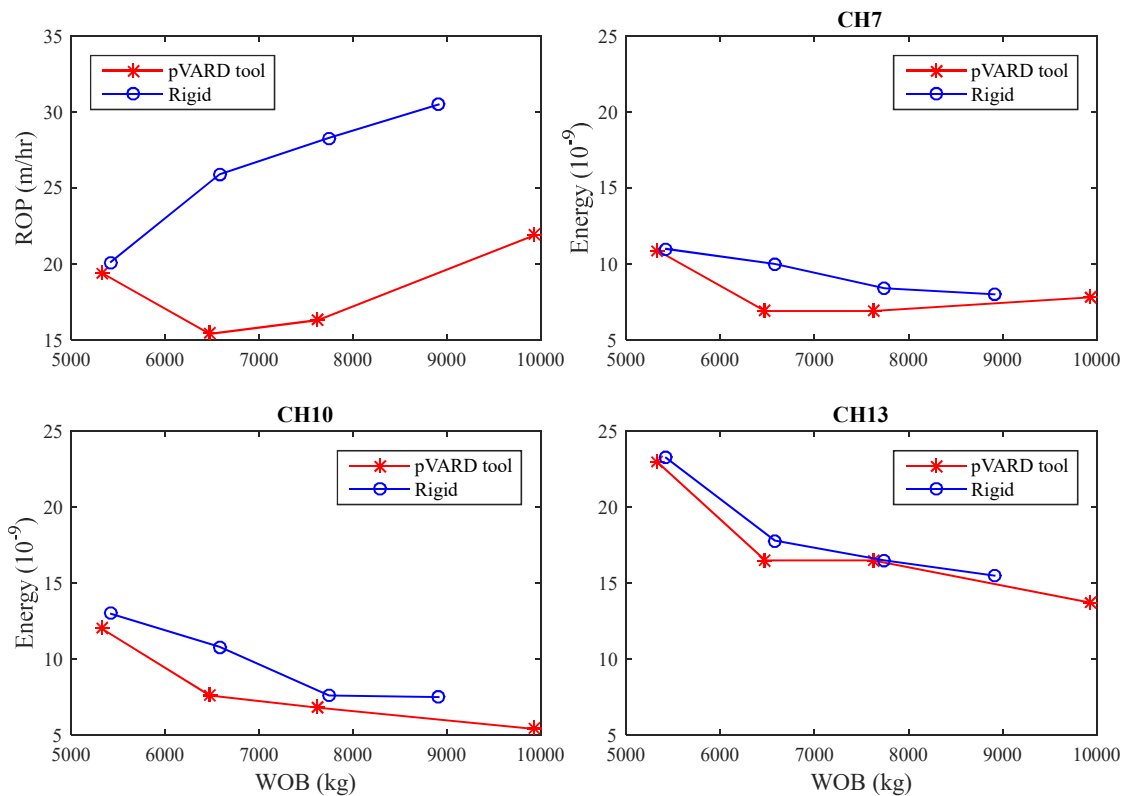


Figure 4.25: Grey shale was drilled from 54.5 to 60.0 m in borehole 3. Results were shown as ROP, and surface wave energy comparison for the pVARD tool and rigid drillings

From the drilling performance (Figure 4.25), ROP generally increased with the increase of WOB for both means of drillings, while surface wave energies decreased. Simultaneously from seismic spectra, the seismic frequency bandwidth of specific energy level (above -6.6 dB) decreased. This again confirmed that less energy was partitioned from drill bit source to the rig and rig-ground interaction was weakened.

Furthermore, ROP was lower with the pVARD tool than rigid drilling which was in contrast with drilling on red shale. For comparable WOB, the pVARD tool provided a narrower frequency bandwidth and lower surface wave energy compared to rigid drilling. This showed that rig-ground interaction was weakened in magnitude and vibration content, when less drill bit energy was partitioned into drilling penetration. The analysis indicated that more drill bit energy was partitioned to drill string which was actually absorbed by the pVARD tool in terms of compliance. The pVARD drilling here differed from that previously stated and the only difference was strength of rock. This setting of the pVARD tool did not improve drilling performance in weaker grey shale. The pVARD tool hindered effective drilling in softer grey shale indicating the limitation of this tool to drilling in soft rock.

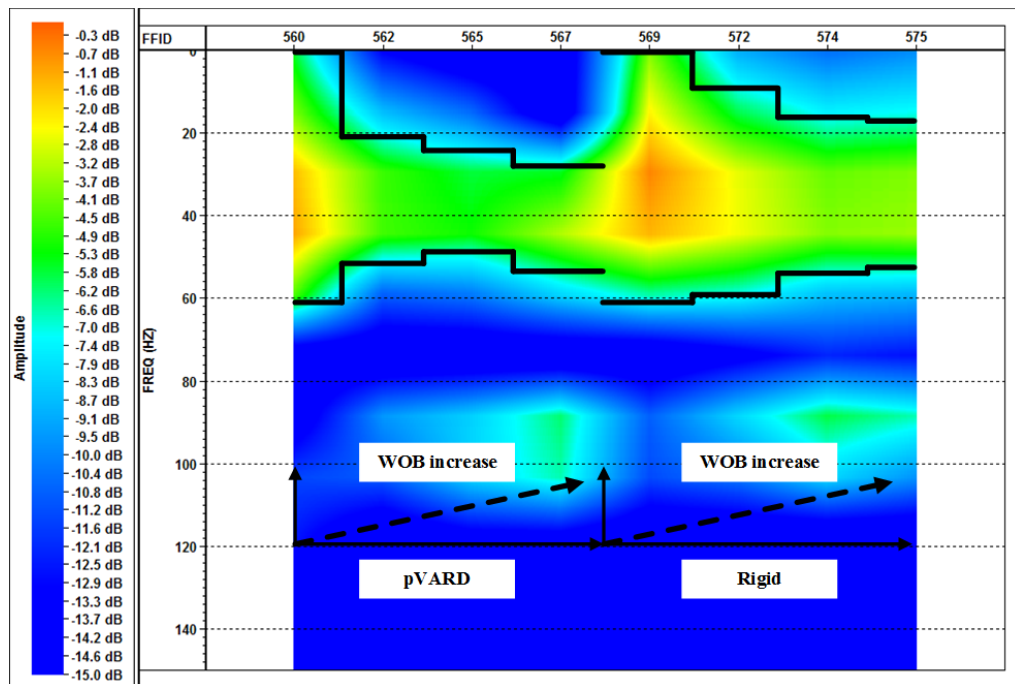


Figure 4.26: Four frequency bandwidths corresponded four WOBs for the pVARD tool and rigid drillings from channel #7, when grey shale was drilled from 54.5 to 60.0 m in borehole 3

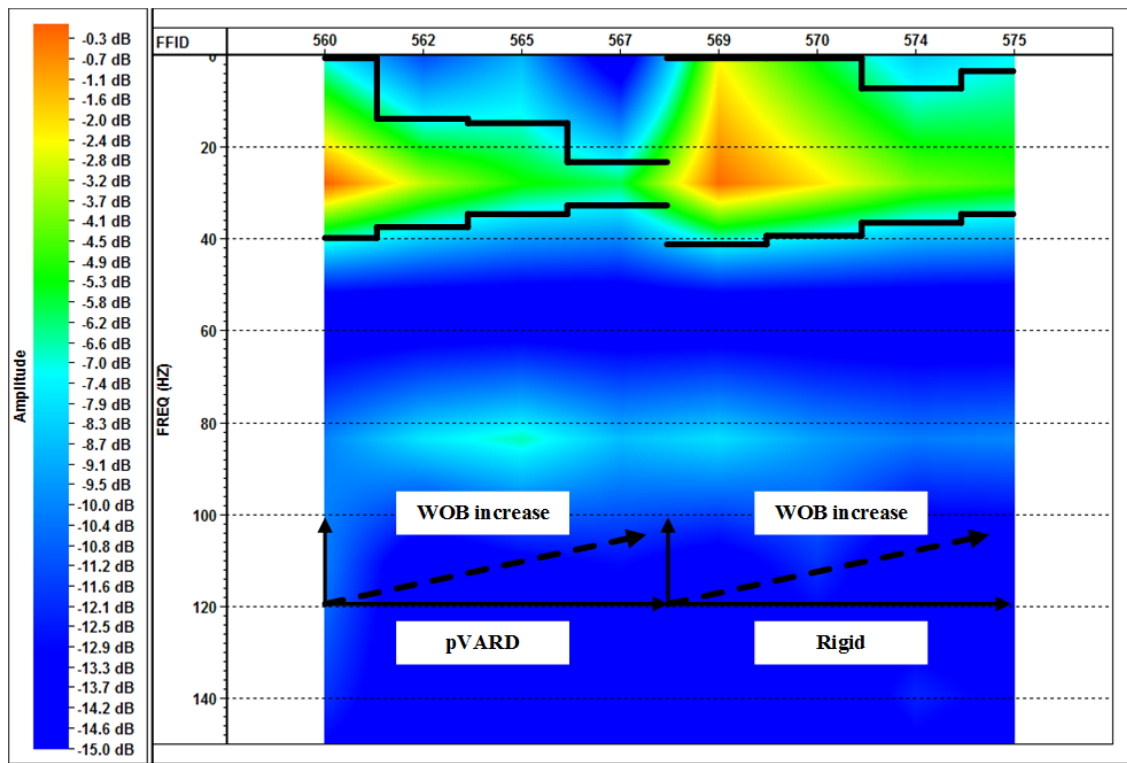


Figure 4.27: Four frequency bandwidths corresponded four WOBs for the pVARD tool and rigid drillings from channel #10, when grey shale was drilled from 54.5 to 60.0 m in borehole 3

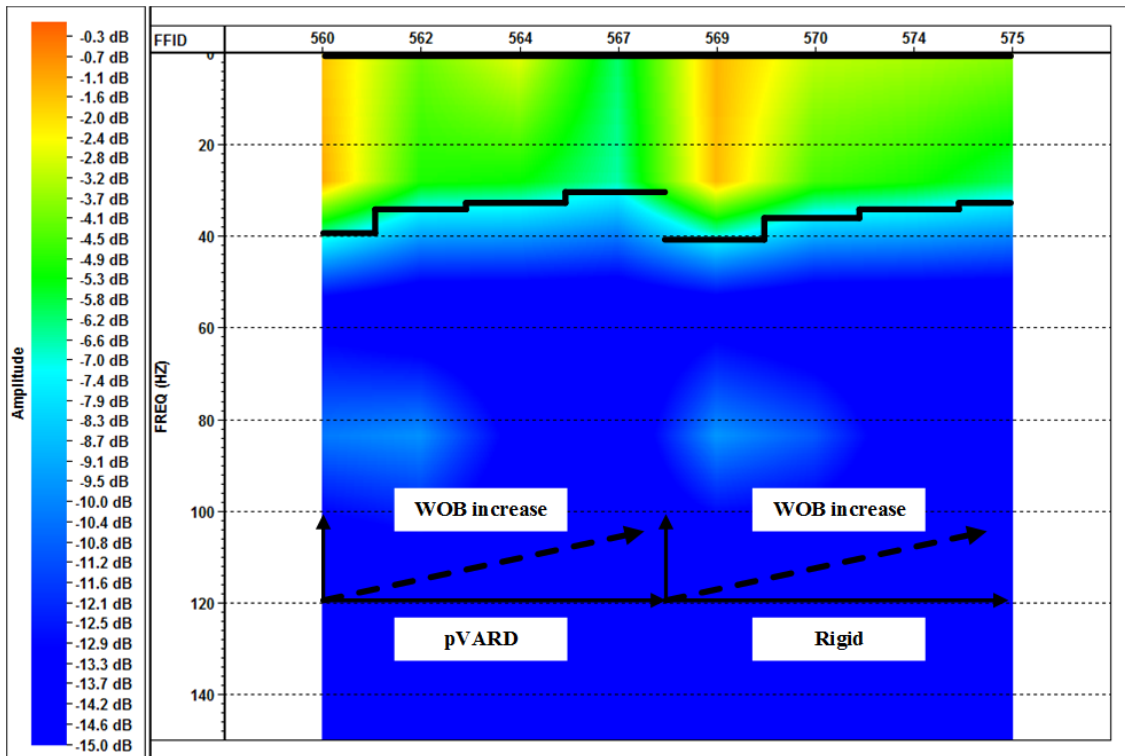


Figure 4.28: Four frequency bandwidths corresponded four WOBs for the pVARD tool and rigid drillings from channel #13, when grey shale was drilled from 54.5 to 60.0 m in borehole 3

## 4.8 Discussion and Conclusions

- 1) Bit motion closely correlated with WOB and seismic signal properties. With the increase of WOB, ROP increased. While bit natural vibration levels in axial and lateral directions decreased. This change was due to increased WOB in longitudinal direction. The rig-ground interaction was weakened both in magnitude and frequency content.
- 2) With the increase of WOB, the frequency bandwidth and energy magnitude of surface wave decreased for both the pVARD tool and conventional rotary drilling. A reasonable

presumption was proposed, i.e. less drill bit energy was partitioned to generate surface wave while more energy was used in bit penetration, when WOB was increased.

3) On higher strength rock, the pVARD tool improved drilling performance. This was largely attributed from the drill string compliance brought by the pVARD tool. More bit energy was partitioned into bit penetration and ROP was increased by enhancement of drill bit-rock interaction, i.e. bit-rock contact time was increased per revolution of rotation by imposing compliance on drill bit. This mechanism of pVARD tool has been verified in laboratory tests [5,6]. This resulted in intensified rig-ground interaction and corresponding higher magnitude of surface wave.

4) On lower strength shale, the pVARD tool hindered effective drilling. The pVARD tool drilling results of ROP and properties (frequency bandwidth and energy) of surface waves generated by rig-ground motion indicated more drill bit energy partition to the drill string and less rig-ground motion. Drill bit-rock interaction was hindered by this setting of springs and lower strength grey shale. This indicated that more researches should be conducted on the compliance setting of this pVARD tool for specific drilling conditions.

5) Surface wave was utilized to characterize drill bit-rock interaction and drilling performance by indirect means of identifying rig-ground interaction, which closely related to drill bit motion and drilling energy partition.

6) Only surface wave was available for PDC bit drilling on shale formations. This probably resulted from the properties of weak shale. An improvement on using direct wave as SWD source could be conducting tests on stronger rocks which could improve data quality for PDC bit.

#### **4.9 Acknowledgements**

The work was supported by Atlantic Canada Opportunity Agency (grant numbers: 781-2636-1920044), involving Husky Energy, Suncor Energy and Research and Development Corporation (RDC) of Newfoundland and Labrador.

Some of the seismic analysis was carried out using ProMAX and we acknowledge the support of Halliburton software and services. The authors also give appreciation to Dr. Sharon Deemer for help in seismic data processing.

#### **4.10 References**

1. Rana PS et al; *September 2014 Drilling Field Trial Report*. Drilling Technology Laboratory, St. John's, Canada: Memorial University of Newfoundland; 2015.
2. Guarin PL, Arnold HE, Harpst WE, Davis EE. Rotary percussion drilling. Paper presented at: Twenty-ninth API Annual Meeting; November 1949; Chicago, IL.

3. Volk BW, McLellan GW, Moak DJ, Lerch RE, Thompson KM, Barrow JC. ResonantSonic drilling: history, progress, and advances in environmental restoration programs. International Atomic Energy Agency. [http://www.iaea.org/inis/collection/NCLCollectionStore/\\_Public/25/040/25040388.pdf](http://www.iaea.org/inis/collection/NCLCollectionStore/_Public/25/040/25040388.pdf).
4. Babapour S, Butt SD. Investigation of enhancing drill cuttings cleaning and penetration rate using cavitating pressure pulses. Paper presented at: The 48th U.S. Rock Mechanics/Geomechanics Symposium; June 1-4, 2014; Minneapolis, MN.
5. Rana PS, Abugharara AN, Butt SD, Molgaard J. Experimental evaluation of passive-Vibration Assisted Rotary Drilling (p-VARD) tool to enhance drilling performance. Paper presented at: The 49th U.S. Rock Mechanics/Geomechanics Symposium; June 28-July 1, 2015; San Francisco, CA.
6. Xiao Y, Zhong J, Hurich C, Butt SD. Micro-seismic monitoring of PDC bit drilling performance during vibration assisted rotational drilling. Paper presented at: The 49th U.S. Rock Mechanics/Geomechanics Symposium; June 28-July 1, 2015; San Francisco, CA.
7. Biggs MD, Cheatham JB. Theoretical forces for prescribed motion of a roller bit. *Soc Petrol Eng J.* 1969;9(04):473-481. doi:10.2118/2391-PA
8. Sheppard MC, Lesage M. The forces at the teeth of a drilling rollercone bit: theory and experiment. Paper presented at: SPE Annual Technical Conference and Exhibition; October 2-5, 1988; Houston, TX.

9. Glowka DA. Use of single-cutter data in the analysis of PDC bit designs: part 1 - development of a PDC cutting force model. *J Petrol Technol.* 1989;41(8):797-849. doi:10.2118/15619-PA
10. Reyes R. *Bit-Rock Interaction in Rotary Drilling: Numerical and Experimental Study* [master's thesis]. St. John's, Canada: Memorial University of Newfoundland; 2017.
11. Richard T, Germy C, Detournay E. Self-excited stick-slip oscillations of drill bits. *C R Mecanique.* 2004;332(8):619-626. doi:10.1016/j.crme.2004.01.016
12. Gao Q. *Development of Laboratory and Field Drilling Tools to Measure Bit Operating Conditions and Drill String Motions* [master's thesis]. St. John's, Canada: Memorial University of Newfoundland; 2014.
13. Rahman R. *Development and Interpretation of Downhole Data from Downhole Vibration Monitoring Tool* [master's thesis]. St. John's, Canada: Memorial University of Newfoundland; 2015.
14. Hardage B. Seismic-while-drilling: techniques using the drill bit as the seismic source. AAPG Search and Discovery website. <http://www.searchanddiscovery.com/documents/2009/40411hardage/index.htm>.
15. Lutz J, Quichaud C, Raynaud M, Raynal J, Mucklero JA, Gstalder S. Instantaneous logging based on a dynamic theory of drilling. *J Petrol Technol.* 1972;24(06):750-758. doi:10.2118/3604-PA

16. Jardine SI, Lesage ML, McCann DP. Estimating tooth wear from roller cone bit vibration. Paper presented at: SPE/IADC Drilling Conference; February 27-March 2, 1990; Houston, TX.
17. Gradl C, Eustes AW, Thonhauser G. An analysis of noise characteristics of drill bits. Paper presented at: The 2008 SPE Annual Technical Conference and Exhibition; September 21-24, 2008; Denver, CO.
18. Yokota T, Onishi K, Karasawa H, Ohno T, Ota A, Kaneko T. Seismic while drilling: basic experiments using a percussion drill as an energy source. *Explor Geophys.* 2004;35(4):255-259. doi: 10.1071/EG04255
19. Sun B, Bóna A, Zhou B, van de Werken M. A comparison of radiated energy from diamond-impregnated coring and reverse-circulation percussion drilling methods in hard-rock environments. *Geophysics.* 2015;80(4):K13-K23. doi:10.1190/geo2014-0344.1
20. Poletto F, Magnani P, Gelmi R, et al. Seismic while drilling ( SWD) methodology in support to moon subsurface stratigraphy investigations. *Acta Astronaut.* 2015;110:99-114.
21. King AF. *Field Trip Guidebook: Trip A4, Late Precambrian Sedimentation and Related Orogenesis of the Avalon Peninsula, Eastern Avalon Zone.* St. John's, Canada: Geological Association of Canada; 1988.
22. Maurer WC. The perfect-cleaning theory of rotary drilling. *J Petrol Technol.* 1962;14(11):1270-1274. doi:10.2118/408-PA

23. Bourgoyne AT Jr, Millheim KK, Chenevert ME, Young FS Jr. *Applied Drilling Engineering*. Richardson, TX: Society of Petroleum Engineers; 1991.
24. Rector JW, Hardage BA. Radiation pattern and seismic waves generated by a working roller-cone drill bit. *Geophysics*. 1992;57(10):1319-1333. doi:10.1190/1.1443199
25. ASTM International. ASTM D5731, standard test method for determination of the point load strength index of rock and application to rock strength classifications.
26. ASTM International. ASTM D2845, standard test method for laboratory determination of pulse velocities and ultrasonic elastic constants of rock.
27. Jung SJ, Prisbrey K, Wu G. Prediction of rock hardness and drillability using acoustic emission signatures during indentation. *Int J Rock Mech Min Sci & Geomech Abstr*. 1994;31(5):561-567. doi:10.1016/0148-9062(94)90159-7

## **Chapter 5 Investigation of Active Vibration Drilling Using Acoustic Emissions and Cuttings Size Analysis**

Yingjian Xiao <sup>a</sup>, PhD candidate

Charles Hurich <sup>b</sup>, Associate Professor

John Molgaard <sup>a</sup>, Professor

Stephen D. Butt <sup>a</sup>, Professor

<sup>a</sup> Drilling Technology Laboratory, Memorial University of Newfoundland, St. John's, NL, Canada A1B 3X5

<sup>b</sup> Department of Earth Sciences, Memorial University of Newfoundland, St. John's, NL, Canada A1B 3X5

This chapter is based on the objective defined in section 1.3.4 and submitted to Journal of Rock Mechanics and Geotechnical Engineering which is now under review.

### **5.1 Co-authorship Statement**

The contributions of this collaborative work are described in the following four parts. 1) Identification of research topic and design of experiments are contributed by Yingjian Xiao, Dr. Hurich and Dr. Butt. 2) Yingjian Xiao is responsible of conducting drilling experiments.

3) Yingjian Xiao analyzes data and prepare the manuscript. 4) Dr. Hurich, Dr. Butt and Dr. Molgaard provide technical knowledge and review the manuscript.

## **5.2 Abstract**

This paper describes an investigation of active bit vibration on the penetration mechanisms and bit-rock interaction for drilling with a diamond impregnated coring bit. A series of drill-off tests (DOTs) was conducted where the drilling rate-of-penetration (ROP) was measured in a series of step-wise increasing static bit thrust or weight-on-bit (WOB). Two active DOTs were conducted by applying 60 Hz axial vibration at the bit-rock interface using an electromagnetic vibrating table mounted underneath the drilling samples, and a third passive DOT was conducted where the bit was allowed to vibrate naturally with a lower amplitude due to the compliance of the drilling sample mounting. During drilling, an acoustic emission (AE) system recorded the AE generated by the diamond cutter penetration and cuttings were collected for grain size analysis. The instrumented drilling system recorded the dynamic motions of the bit-rock interface using a laser displacement sensor, and a load cell and an LVDT recorded the dynamic WOB and the ROP, respectively. Calibration with the drilling system showed that rotary speed was approximately the same at any given WOB, facilitating comparison of results at the same WOB. Analysis of the experimental results shows that the ROP of the bit at any given WOB increased with a higher amplitude of axial bit-rock vibration, and drill cuttings increased in size with a higher ROP. Spectral analysis of the AE indicated that the higher ROP and larger cutting size correlated with a higher AE energy and a lower AE frequency, indicating

larger fractures were being created to generate the larger cutting size. Overall, these results indicate that a greater magnitude of axial bit-rock vibration produces larger fractures generating larger cuttings which, at the same rotary speed, results in a higher ROP.

**Keywords:** Active bit vibration; diamond coring drilling; drill-off test; acoustic emission; drilling performance; penetration mechanism; cutting size analysis.

### 5.3 Introduction

Two major types of drilling are used in the mineral, oil and gas, and construction industries. These are i) rotary drilling, where a static thrust or weight-on-bit (WOB) is applied to the bit, and ii) rotary-percussion drilling, where percussive hammer impacts are applied to the bit in addition to a static WOB. It is well known that rotary drilling performance, as measured by drilling rate-of-penetration (ROP) and the nature and rate of bit wear, is strongly influenced by bit motions and bit-rock interaction. This has been studied using roller cone and polycrystalline-diamond-compact (PDC) drag bits, which are widely used for oil and gas drilling. Theoretical models have been developed to study forces applied to roller cone bits as well as the correlation to ROP and drilling conditions [1,2]. Empirical relations have been proposed to correlate drag forces on a single-cutter PDC bit to rock type, depth-of-cut (DOC) and bit wear state [3]. Some researchers have reported on bit-rock interactions through measurement and evaluation of the three modes of drill string vibrations (i.e. axial, lateral and torsional) recognizing that these drill string vibrations are excited by bit-rock interactions [4,5].

At the Drilling Technology Laboratory at Memorial University of Newfoundland, several investigations have focused on using bit vibrations to improve rotary drilling performance. One study used compliant elastomers beneath rock specimens to enhance the oscillatory motions generated by bit-rock interaction while drilling with PDC bits, which resulted in improved cutting efficiency and overall drilling ROP [6]. Thereafter, this idea was further developed and incorporated into a drilling tool, called the passive Vibration-Assisted-Rotary-Drilling (pVARD) tool, which demonstrated improved ROP under both laboratory and field drilling conditions [7,8]. Another study investigated the influence of active vibration on drilling performance for diamond drilling with coring bits and full-face drag bits using an electromagnetic vibrating table to vibrate the rock specimen while drilling. These studies varied both the amplitude and frequency of the applied vibration, and demonstrated that ROP was generally increased at a rate proportional to the amplitude of vibration, regardless of the vibration frequency [9,10].

One major challenge for investigating rotary drilling is the difficulty to visualize the bit-rock interaction and bit penetration process. Cuttings analysis has been used to evaluate the penetration mechanisms by relating the size and shape of cuttings to the fracturing mechanisms [8,11], keeping in mind the potential influence of the mineral fabric of the rock [12]. Acoustic Emission (AE) technology provides an indirect way of studying these fracturing processes, in which AE signals are generated by the fracturing and remotely recorded. This technology has been abundantly reported in early studies on investigating micro-crack nucleation and crack propagation processes in core specimens under standard

strength tests in the laboratory [13]. In the drilling area, bit wear states were distinguished by studying frequency contents of AE signals using carbide rotary bits [14] and a single-cutter bit [15,16], and by studying the amplitude using twist drill bits [17]. Energy related parameters of AE signals were commonly used to study bit penetration mechanisms such as the root mean square (RMS) of amplitude and the AE event energy. Some researchers have reported that the RMS of an AE signal is an effective measure of its magnitude [18]. For the drilling with an impregnated diamond bit, the dominant bit action consisted of cutting and friction processes [19], and the processes were investigated by monitoring AE signals. In a diamond coring bit drilling, a variation of RMS levels in AE signals was correlated with varying DOC [20]. In a PDC bit drilling, an average AE energy was calculated to investigate bit penetration mechanisms and drilling performance [8]. Related studies at the seismic scale [21-23] have related the frequency content of seismic waves to the length of the generated fractures, with longer fractures generating lower seismic frequencies and vice versa.

Diamond core drilling is the primary form of rotary drilling used for mineral exploration and ore body evaluation. The paper outlines an investigation using AE and drill cuttings characterization to evaluate the penetration mechanisms for drilling with impregnated diamond coring bits while applying passive and active bit vibration. The experiments comprise a series of drill-off-tests where the WOB is increased in a step-wise manner while maintaining a constant bit vibration condition as provided by compliant specimen mountings and an external vibrating table. These drilling vibration experiments were carried out at the same vibration frequency but with incrementally increasing vibration

displacements. AE data was recorded for all of the DOTs to provide information about bit-rock interaction during the DOTs. Based on previous studies, we expected to observe an increase in ROP with the addition of active vibration, however, these experiments provided further data on the effect of the bit-rock interactions and penetration mechanisms that influence the ROP.

## **5.4 Methodology**

### **5.4.1 Experimental method**

Figure 5.1 shows the schematic diagram of the experiment setup for conducting DOTs and monitoring of AEs. A small drilling simulator (SDS) was used to conduct DOTs. With the SDS, a suspended mass provides a known WOB [24]. A Husqvarna coring bit with the outer diameter of 25.4 mm was mounted to the rig swivel. A constant flow rate and pressure of tap water flushed cuttings between bit and rock away to create space for a new round of penetration. The rotary speed was nominally set as 300 revolutions-per-minute (RPM) for all DOTs, but this measurement slightly decreased with increasing friction and torque from the increase of WOB [8]. However, a detailed calibration of the drilling system showed that the rotary speed was approximately constant for any given value of WOB up to the drilling founder point, where the drilling motor had insufficient torque to turn the bit [5]. All DOTs conducted for this investigation were at WOBs less than the founder point. A linear variable differential transformer (LVDT) was used to monitor bit-penetration depths that the drill bit actually penetrated and were measured by mm or m. Cylindrical drilling samples

measuring approximately 100 mm in both diameter and length were made from a fine-grained concrete cast using fine aggregate, water and Portland cement. Previous studies conducted using this fine grained concrete material confirmed that it behaves similar for drilling to the low permeability sedimentary rock with the same unconfined compressive strength (UCS) [25]. Table 5.1 lists the geotechnical properties of this material measured using a standard ASTM strength test [26] and a standard ASTM ultrasonic test [27].

Table 5.1: Geomechanics and ultrasonic properties of the drilling sample material [7]

Rock	UCS (MPa)	Young's modulus (GPa)	P-wave velocity (m/s)	S-wave velocity (m/s)
Concrete	51	34	4423	2448

Active bit vibration was indirectly provided by one external electromagnetic vibrating table for the purpose of studying the effect on ROP (Figure 5.1). The vibration was configured to be 60 Hz with two varying amplitudes: 0.044 mm and 0.055 mm at the lowest WOB, referred to be L1 and L2 respectively. A rock cylinder was firmly mounted to the vibrating table surface, thus they vibrated axially under controlled settings. Figure 5.2 is a schematic diagram showing the penetration process of a six-segment diamond coring bit [20] along with the laboratory two-segment diamond coring bit. Drilling parameters include WOB and angular velocity  $\Omega$  or rotary speed. The drill bit penetrates downwards perpendicular to X-X' in plot (a) and a segment moves rightwards from applied torque-on-bit (TOB) in plot (b). Depth-of-cut (DOC) is defined as the penetration depth of drill bit per revolution (mm/rev). Plot (c) shows the two-segment diamond coring bit used in this research with an outer diameter of 25.4 mm. The resultant WOB is then comprised of a combination of a

static one and a varying weight due to periodical vibrations. Vibration displacements of the rock cylinder were measured by a laser sensor, which was attached to the stationary rig frame of the SDS (Figure 5.3).

In all of the tests, four Panametrics P-wave sensors were placed symmetrically around a rock cylinder to monitor AEs. Locations of these sensors were set identical in reference to the top surface of this cylinder and the location of the sensors was the same for all of the tests to ensure a confident comparison of AE signals between varying WOBs as well as different drilling settings. These sensors were calibrated with a central frequency of 1.14 MHz, and a working bandwidth range from 0.65 to 1.63 MHz at -6 dB attenuation. Four preamplifiers, manufactured by Physical Acoustics Corporation, were used to amplify AE signals at a 20 dB gain. A GaGe CompuScope 8280 A/D board sampled these analogue signals at a sampling frequency of 10 MHz. The measurement of AE signals was synchronized to the drilling test.

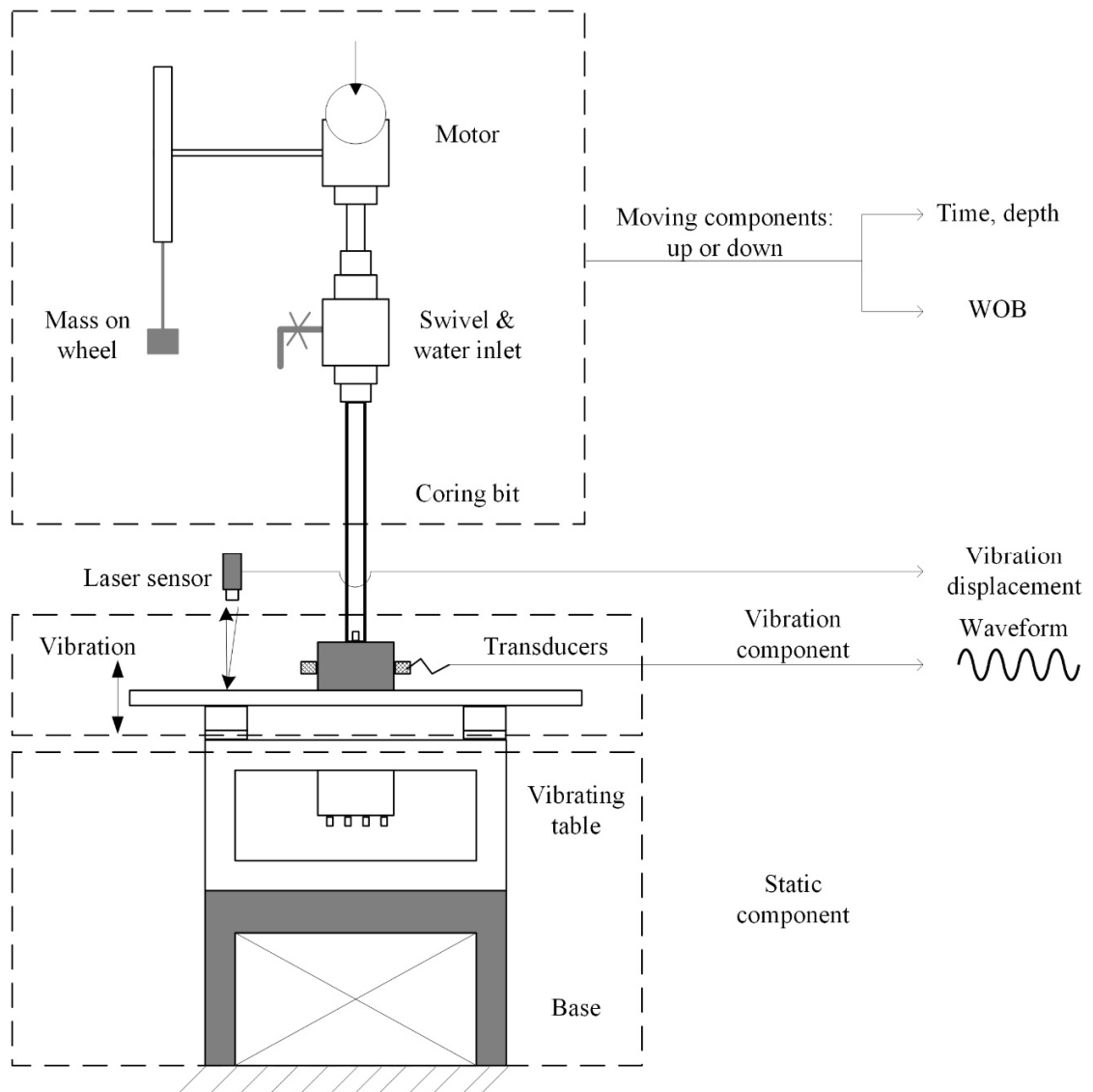


Figure 5.1: Schematic diagram for conducting DOTs using a small drilling simulator at the Memorial University of Newfoundland. A DOT is conducted on a concrete cylinder, which is firmly mounted to the vibration table

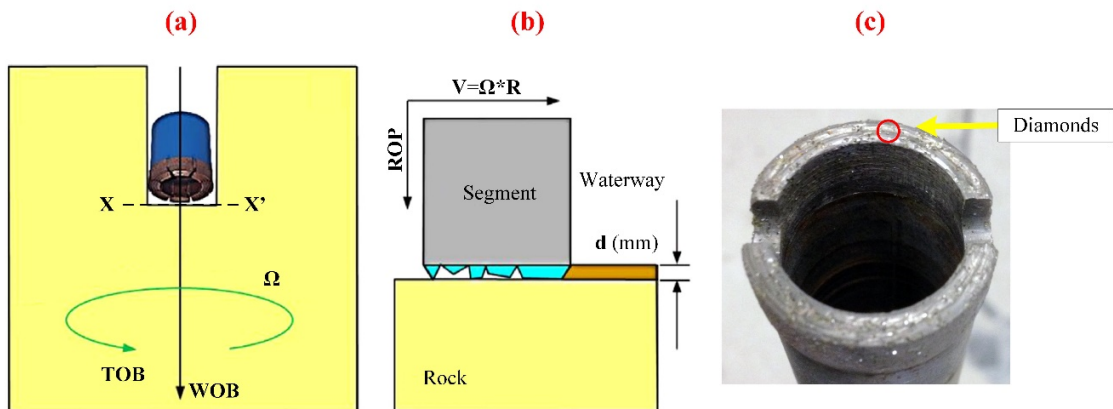


Figure 5.2: Schematic view of a diamond coring bit drilling: (a) drilling parameters for a six-segment diamond bit; (b) penetration process of a single segment; (c) two-segment diamond bit used in this paper. This is modified after Karakus and Perez [20]

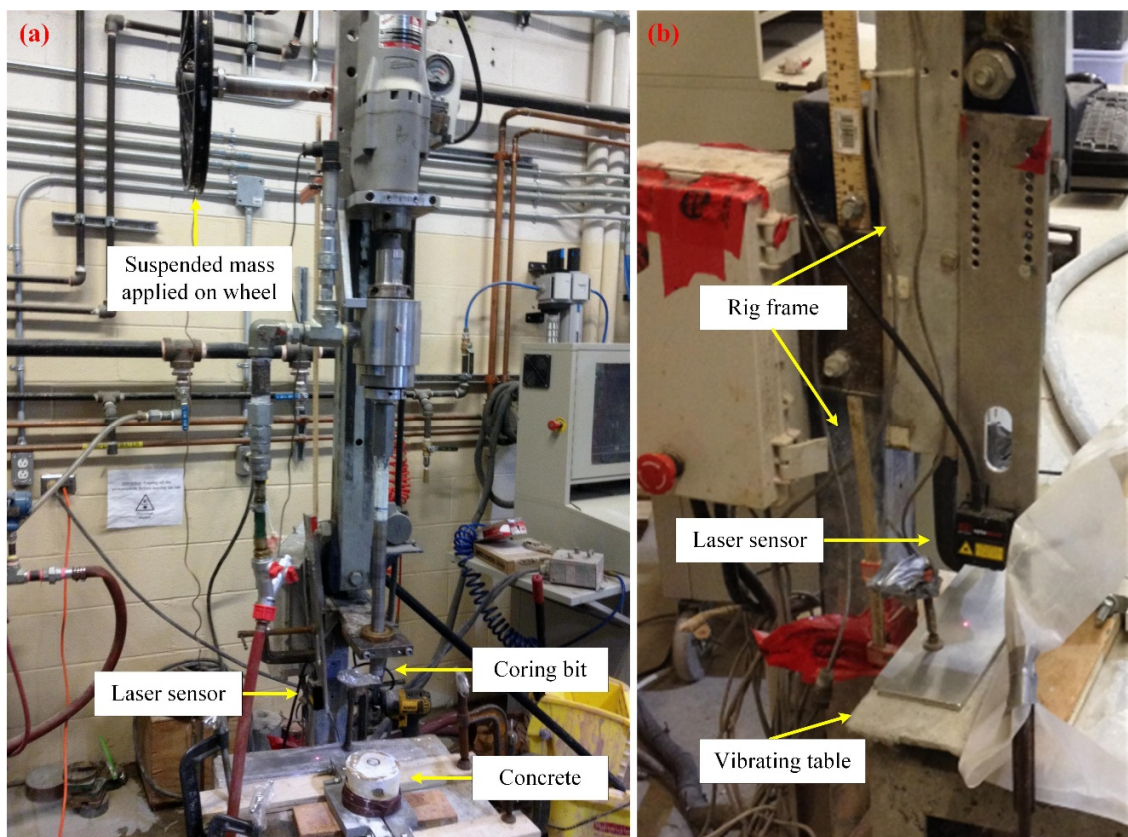


Figure 5.3: Overview of the DOT setup (a) with a concrete cylinder for mounting AE transducers; (b) the laser sensor attached to the stationary rig frame

### 5.4.2 Testing plan

For the DOT experiments, a water flow rate of 3.78 l/min and a total of bit-penetration depth of approximately 15 mm were confirmed at each WOB. A group of four increasing WOBs were confirmed: 84.1 kg, 95.3 kg, 106.5 kg and 117.7 kg. In each DOT, the four increasing WOBs were applied on a rock cylinder, and a drilling vibration setting was assigned to this test. Those rock cylinders were casted with the same proportions of materials and their geomechanics properties are shown in Table 5.1.

Table 5.2 lists the inputs for monitoring AE signals. These configurations were used for the following DOTs.

Table 5.2: Inputs for monitoring acoustic emission

Sampling frequency (Hz)	P-wave sensor #	Gain (dB)	Peak-peak input (V)	Trigger level (V)
10 Mega	4	20	10	0.05

The first series of DOTs was conducted without active vibration for a range of increasing WOB. Simultaneously, AE signals were monitored and cuttings were collected, providing data for frequency content and event energy analysis and a particle size distribution analysis. The second phase of the experiment consisted of two series of active vibration drillings. All other drilling parameters remained the same with the exception of vibration displacement. The two axial displacement settings had been previously described as: L1 and L2 ( $L1 < L2$ ).

## 5.5 Data Acquisition and Processing

For each DOT, drilling related data are obtained, i.e. WOB, bit-penetration depth - time, and vibration displacement - time. Synchronized AE signals are recorded as well.

Figure 5.4 shows an example of the analysis processes for ROP based on bit-penetration depth - time, and of bit vibration from vibration displacement - time. The bit-penetration depth was measured to be approximately 10 mm when the vibration setting of L1 and the WOB of 95.3 kg were chosen. The bit-penetration depth is determined by a moving average of the time-depth data resulting in a smooth average depth curve. This curve is quasi-linear and the slope of this curve was then taken as the ROP. Bit vibration data was first processed by removing trends of original vibration displacement. Spectral analysis using a fast Fourier transform (FFT) method was used to study a window of vibration displacement (the black square), indicating a dominant frequency of 60 Hz which is consistent with the working frequency of the vibrating table. The magnitude of vibration displacement, within the linear portion of the bit-penetration depth - time curve, was studied by the RMS method (Equation 1), which was an effective parameter of evaluating the vibration magnitude as reported by other researchers [20]. The above data processing was facilitated by a routine in MATLAB.

$$V_{RMS} = \sqrt{\frac{1}{T} \int_0^T V_i^2 dt} \quad (1)$$

Where

$V_{RMS}$  = RMS level of data;

$T$  = period of waveform;

$V_i$  = instantaneous value.

Figure 5.5 shows a sample AE signal with 16384 points at a sampling frequency of 10 MHz. By an FFT analysis on the whole signal, the resultant frequency spectrum shows an outstanding peak frequency of 133 kHz. Figure 5.6 shows four waveforms of a single AE event recorded at four sensors. For the four waveform characteristics, peak frequencies and spectral centroids remain approximately the same. While, the waveform energy is obviously different for the four channels due to distance to AE sources and coupling issue. In this way, one channel of signals are selected for further analysis. With this method, multiple AE signals were analyzed and similar frequency peaks were found. In this manner, this peak frequency was picked as a means of characterizing the AE signal. In each DOT, fifteen AE signals were randomly selected for spectral analysis and corresponding peak frequencies were further characterized by the arithmetic average peak frequency and the standard deviation. In addition, the spectral centroid of 264 kHz was obtained based on the frequency spectrum at a frequency range of 0 to 1 MHz. This range was chosen to filter out most of the high frequency noise. The arithmetic average and standard deviation of spectral centroids were calculated from over eighty consecutive AE signals.

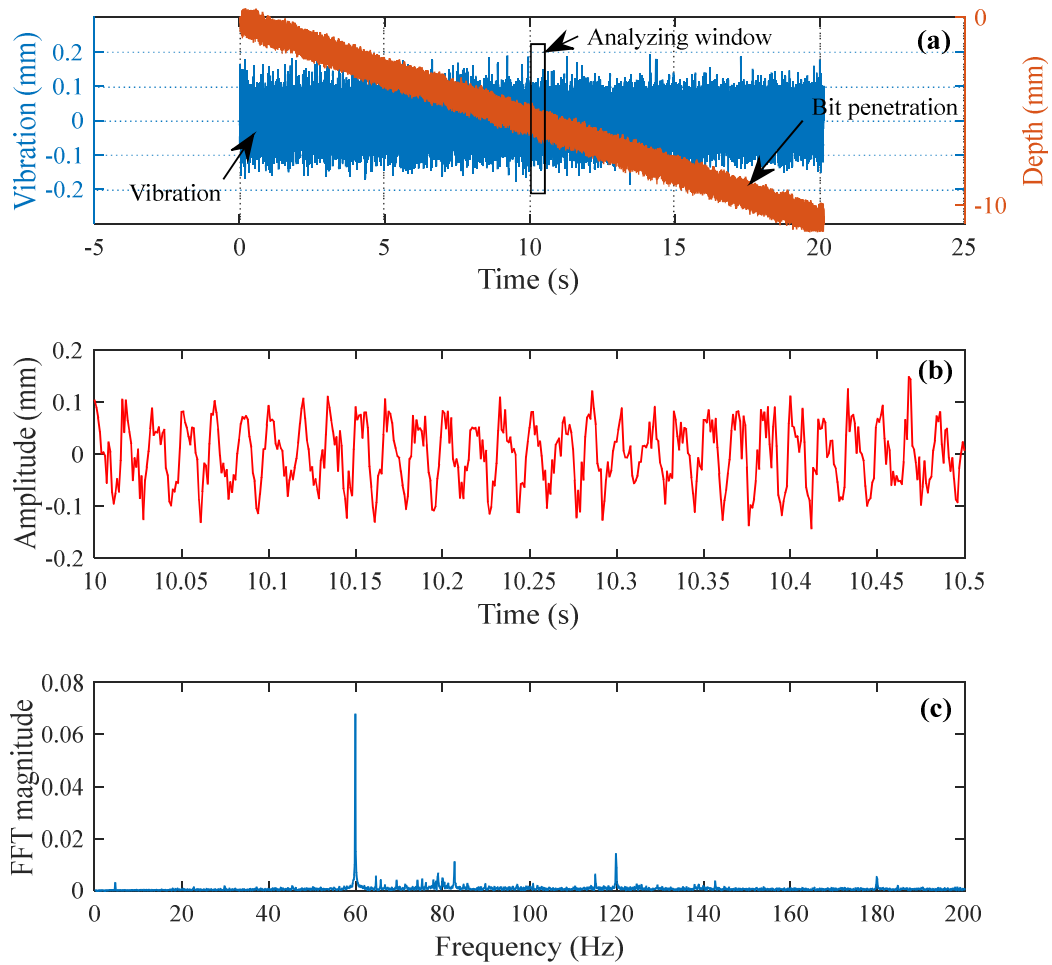


Figure 5.4: A sample DOT is synchronized with the displacement of the vibrating table (a) at vibration L1 and WOB=95.3 kg, from which an analysis window of vibration (b) and the corresponding frequency spectrum (c) are obtained. The peak frequency of 60 Hz represents the working frequency of the vibrating table

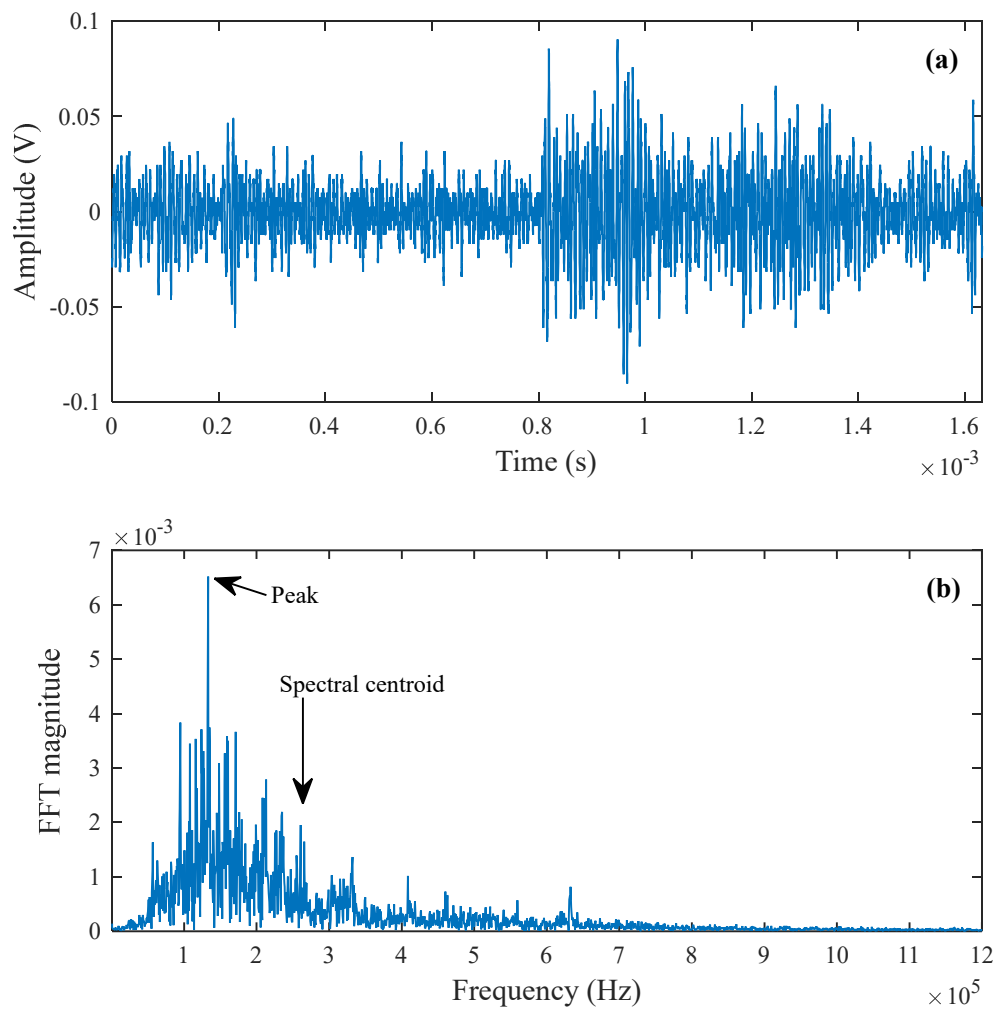


Figure 5.5: A sample AE signal (a) with its frequency spectrum (b) indicating a peak frequency of 133 kHz and a spectral centroid of 264 kHz at vibration L1 and WOB=95.3 kg. The spectral centroid is calculated based on a frequency range of 0 and 1 MHz

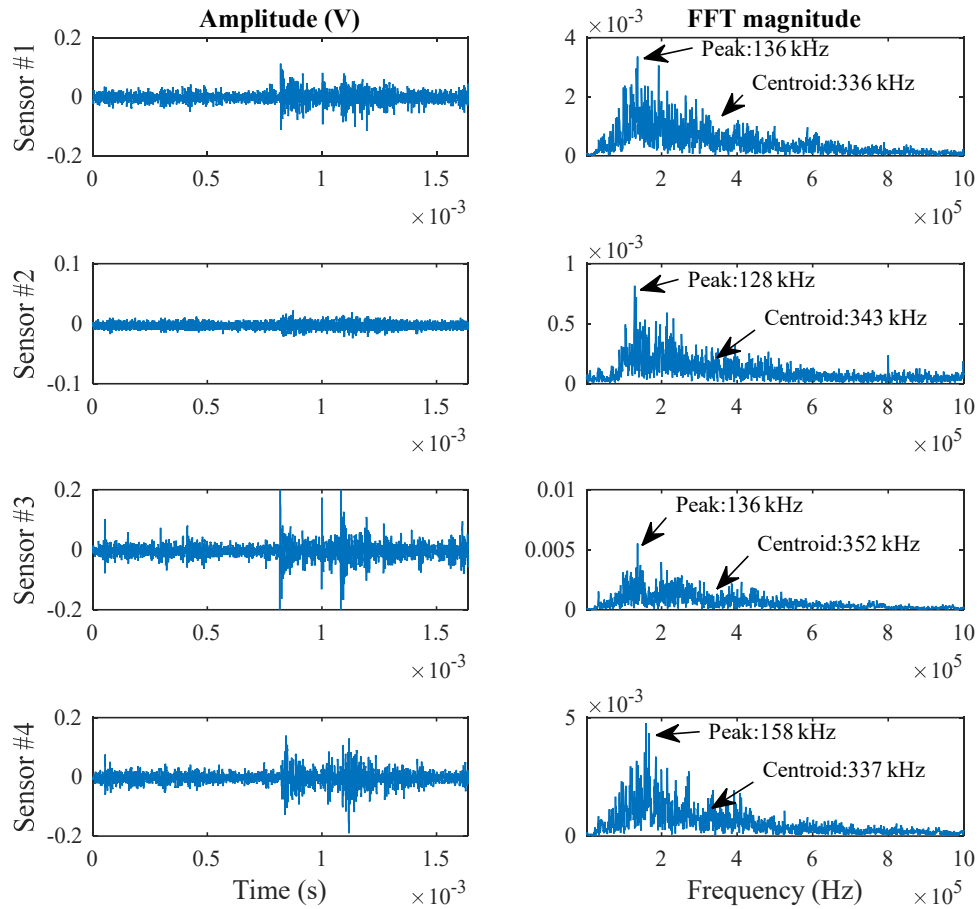


Figure 5.6: Four waveforms of a single event are recorded by four AE sensors from passive drilling at WOB=106.5 Kg. Each waveform is shown in left panel and peak frequency and spectral centroid are shown in right panel

Figure 5.7 shows the event count and the average event energy of AEs, which were recorded during a DOT. Every AE signal was grouped by its triggered time and synchronized with the drilling test. Multiple AE signals were continuously triggered and they were recorded at every two seconds according to the DAQ system. In this plot, an effective drilling penetration process was marked within the time range of 0 and 20 seconds and corresponding AE signals were included for further analysis. By integration of a rectified AE waveform, the event energy was obtained on the time domain based on the

method developed by other researchers [28]. It's approximately the same as the area under waveform FFT. At a specific time, an average event energy was then calculated by an arithmetic mean method on multiple AE event energies. In an effective drilling time window, e.g. from 0 to 20 seconds here, the average event energy was then calculated and taken as the AE energy level for this DOT.

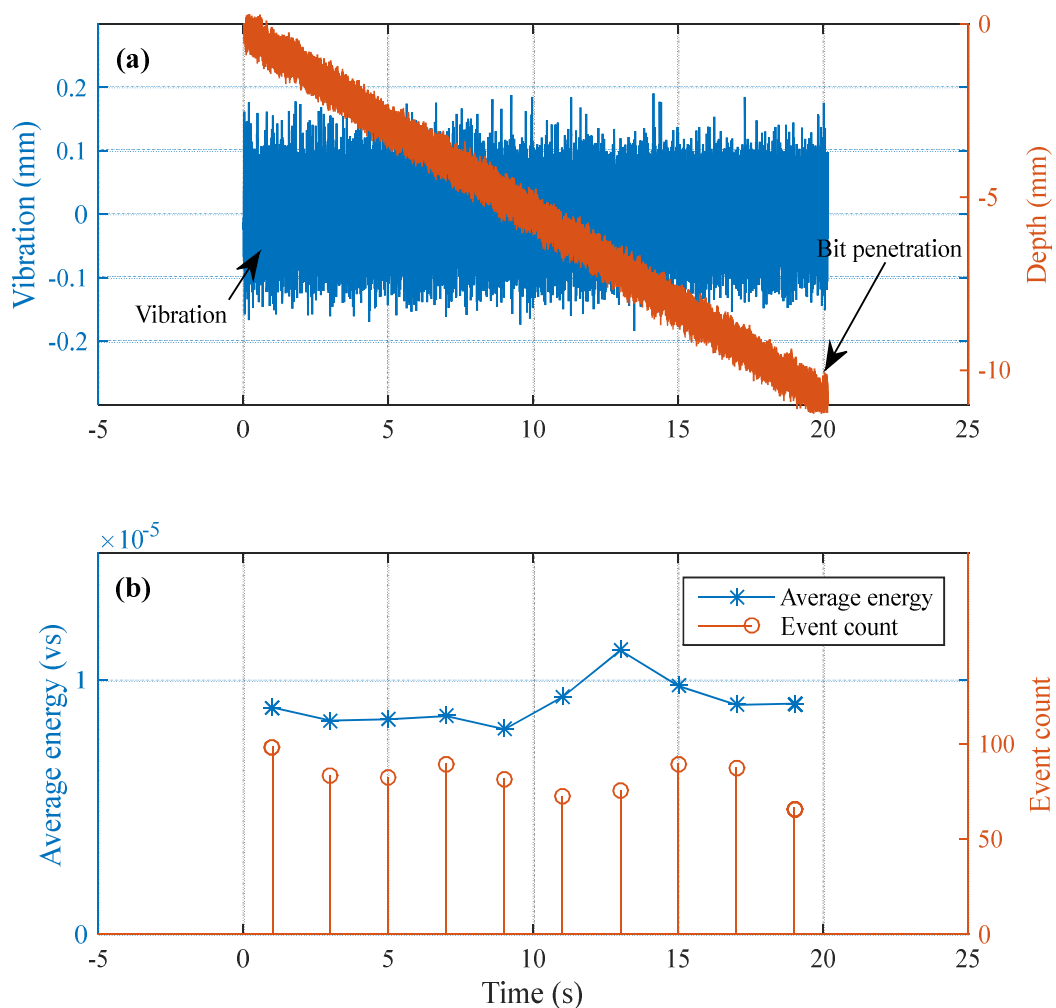


Figure 5.7: A sample DOT with synchronized vibration (a) and synchronized AE count and average energy (b) at vibration L1 and WOB=95.3 kg. The time at 0 second shows the start of the DOT

## 5.6 Data Analysis and Interpretation

### 5.6.1 Drilling performance and vibration

Figure 5.8 shows the experimental results demonstrating the relationship between ROP and the corresponding vibration level with respect to WOB for the three drilling settings.

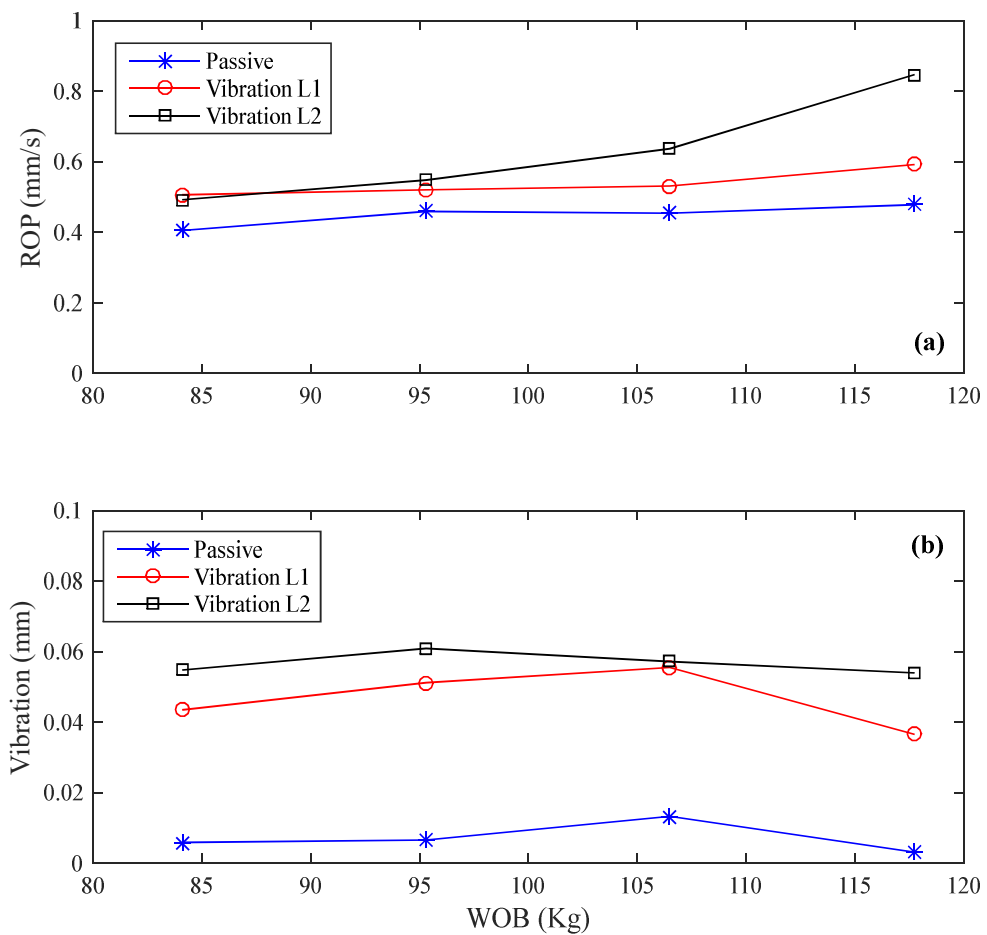


Figure 5.8: An assembly of both ROP (a) and the corresponding vibration level (b) are in correlation to WOB. ROP is positively correlated with WOB

In plot (a), the results show an increase in ROP with increasing WOB. At the same WOB, ROP is positively correlated with vibration level. In particular, under a higher WOB, the differences in ROP between three vibration settings are greater than that under a lower WOB. This indicates that active vibration increases ROP more at a high level of WOB than that in a lower level of WOB, compared to passive drilling.

In plot (b), the vibration levels for both vibration settings increase at beginning. This is due to the decrease of vibrating system compliance with increasing WOB. In this way, the vibrating system vibrates more effectively at the rated vibration setting. Then, the vibration levels decrease slightly with increasing WOB due to depression of vibration from high WOBs, confirming the results of this system reported by other researchers [29]. At different WOB, vibration displacements vary and variations of 10% and 14% are shown for vibration drilling setting L1 and L2, respectively. This indicates a relatively stable change of vibration displacement with respect to WOB. The passive vibrations are not zero due to the existence of compliance of the vibration table. The two active vibration levels are provided here as the first stage of evaluating the drilling performance with respect to the active vibration levels.

### **5.6.2 Acoustic emission analysis**

Figure 5.9 and Figure 5.10 show the frequency distributions in correlation to WOB for the three drilling settings. For every DOT, Figure 5.9 shows the peak frequency calculated by the arithmetic average method based on the fifteen peak frequencies. While Figure 5.10

show the spectral centroid with respect to WOB. The results show that peak frequency decreases with increasing WOB. Research in seismology has shown a reverse relation between a corner frequency to a crack size [21-23]. In this manner, the decrease in peak frequency here indicates an increase in the crack size from a diamond bit penetration process, when WOBs are increased. In addition, under the same WOB, a decrease in peak frequency is found, which indicates an increase in the crack size with the increasing vibration level. This decrease is more apparent at a higher WOB than in a lower WOB, which confirms that bit vibration functions more efficiently at a higher WOB.

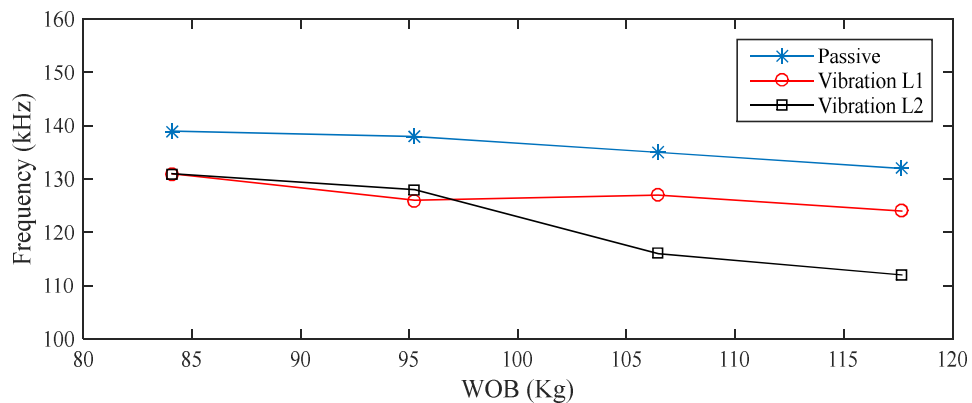


Figure 5.9: Peak frequency distribution is in correlation to WOB at drilling with settings of passive, vibrations L1 and L2. An arithmetic average of peak frequencies is obtained based on fifteen events at each WOB. Peak frequency is found to decrease with increasing WOB

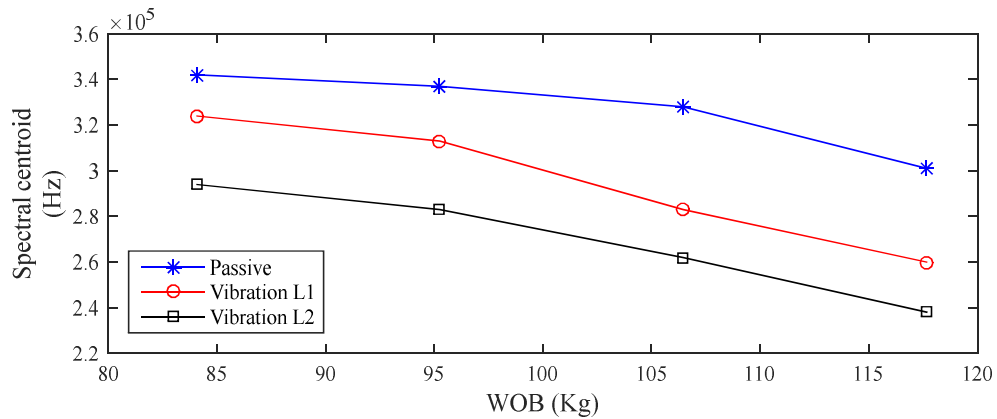


Figure 5.10: Spectral centroid varies with respect to WOB for the three drilling settings. Spectral centroids decrease with increasing WOB

Figure 5.11 plots the average energy with respect to WOB and ROP. In plot (a), the average energy of AE is elevated with the increase in WOB, when the corresponding ROP increases. Under the same WOB, the average energy is greater with a higher level of vibration ( $L2 > L1 > \text{Passive}$ ). These results indicate that AE average energy is positively correlated to ROP which is shown in plot (b). This phenomenon is consistent with the results obtained by previous research, i.e. the higher RMS of an AE signal correlates to a higher DOC [20], or a higher AE energy comes from a higher ROP [8]. In summary, diamonds cut more aggressively with a higher level of ROP, resulting in a greater magnitude of AE energy from rock cracking.

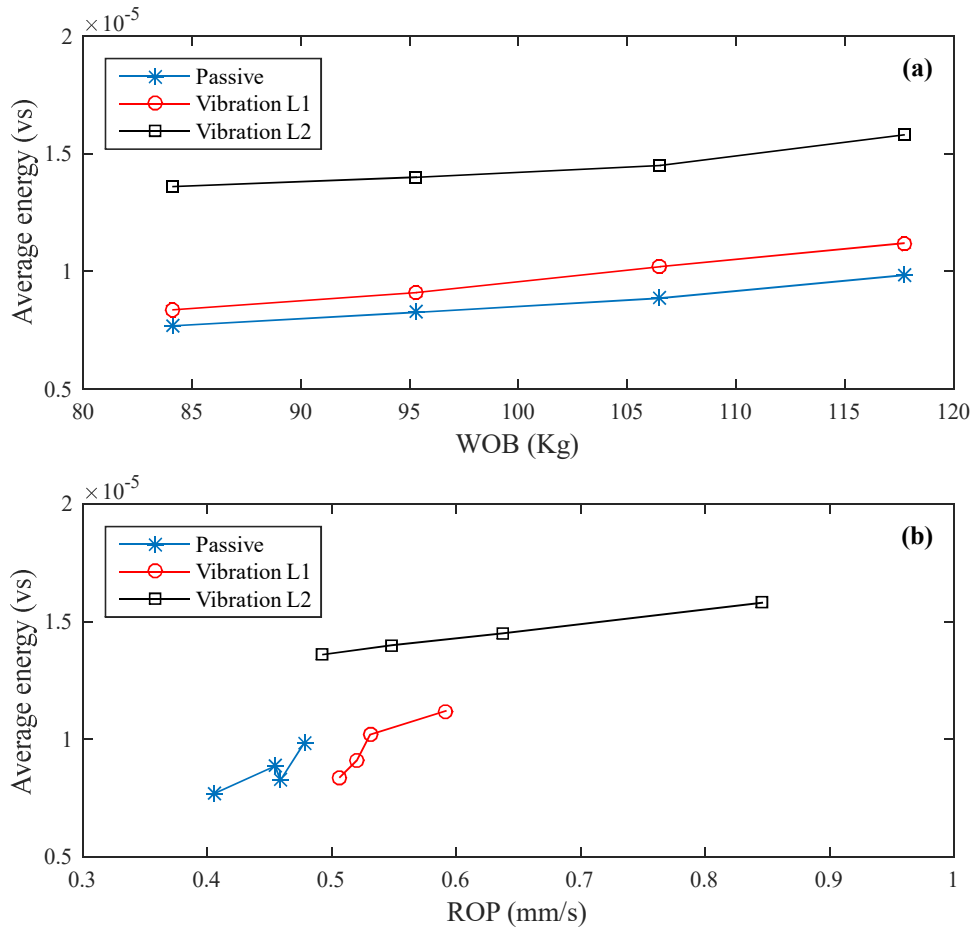


Figure 5.11: Average energy of AEs is in positive correlation to (a) WOB and (b) ROP for all DOTs using three settings of passive, vibrations L1 and L2. Bit vibration enhances the AE average energy

From the previous analyses, a summary is given here based on AE parameters (peak frequency and average energy) in response to WOB. An increase in WOB causes the increase in the size of crack and corresponding average energy of AE signals recorded from the diamond bit penetration process. In this way, an elevation of ROP is obtained from increasing WOB. In addition, an increase in vibration levels functions similarly. As a result, bit vibration improves the bit-rock interaction conditions thereafter enhances diamond bit penetration.

### **5.6.3 Cutting size distribution**

#### ***5.6.3.1 Particle size distribution (PSD)***

The analysis of cutting particle size distribution was conducted using two standard particle size analysis methods: sieving analysis for grain sizes greater than 75  $\mu\text{m}$  and hydrometer analysis for smaller particles. The sieving analysis involved using different size of meshes to retain cutting particles, and weight percentages of each size of particles were assembled according to the ASTM standard D6913 [30]. The hydrometer analysis involved quantitative determination of particle size distribution by sedimentation process using a floating hydrometer following the ASTM standard D422 [31]. Based on all particle size and corresponding passed weight percentage, the cumulative passed weight percentage - mesh size curve is plotted in normal - logarithmic coordinates, i.e. the particle size distribution (PSD) chart.

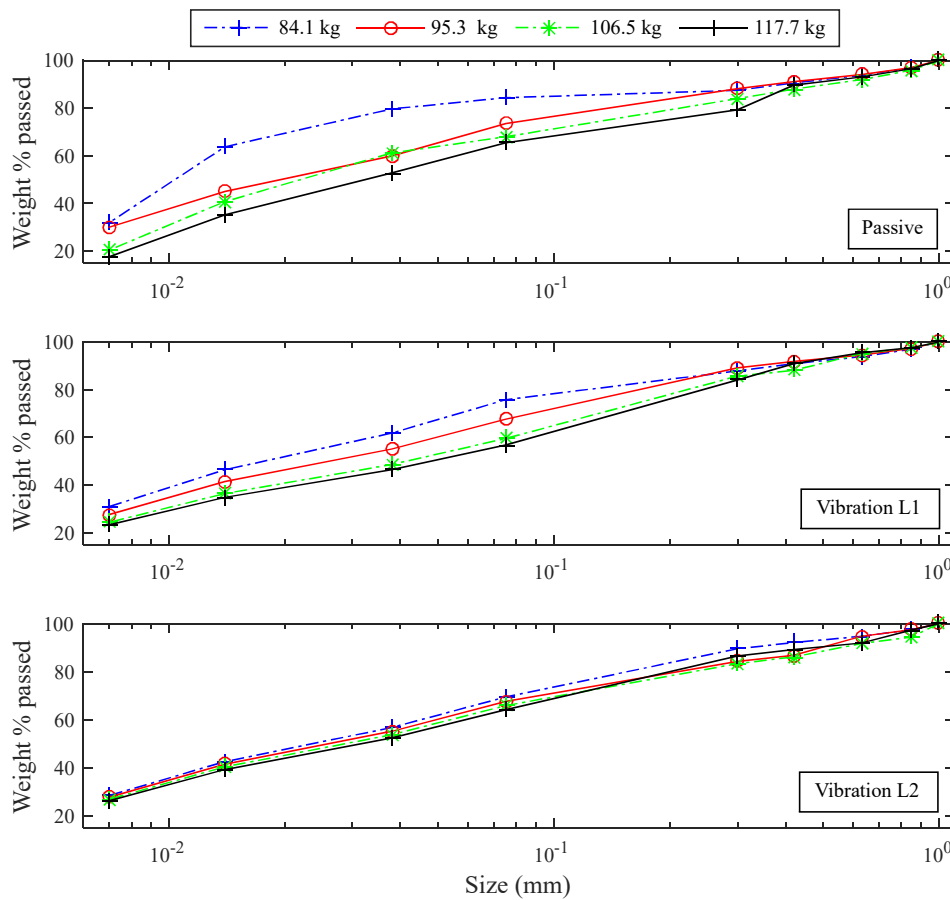


Figure 5.12: PSD charts for all DOTs using the three settings, i.e. passive, vibrations L1 and L2. Cutting is coarser when the PSD curve shifts to the right for each drilling setting

Figure 5.12 shows the PSD charts for drilling using three settings. A PSD curve corresponds to an analysis of cuttings from a drill-off test. The charts show that the maximum particle size from the three drillings is less than 1 mm. When a single PSD curve shifts to the right for each drilling setting, the particle size tends to be bigger with the increase in WOB which is also correlated with increase ROP. This phenomenon has been reported by other researchers, i.e. a higher DOC causes a higher percentage of coarser cuttings [15]. PSD curves are barely distinguishable when the mesh size is over 0.4 mm.

This is because a minor portion of cuttings (size over 0.4 mm) were obtained from the overall cuttings for each DOT.

### **5.6.3.2 Mean particle size**

Mean particle size is commonly used to quantitatively characterize the particle size distribution. In 1933, a particle size distribution (PSD) function was first proposed from a sieving analysis on powdered coal, known as the Rosin-Rammler (RR) model [32], or Rosin-Rammler-Sperling-Bennett (RRSB) model [33]. Later, this model was widely used to describe the PSD of powders of various types and sizes, and was specifically suited to representing powders from operations such as grinding, milling, and crushing [34]. This two-parameter function is described in Equation 2, from which the mean particle size can be obtained.

$$R(d) = 100 \exp[-(d/d_m)]^n \quad (2)$$

Where

$R(d)$  = retained weight fraction or cumulative weight percentage (%);

$d$  = particle size or mesh size ( $\mu\text{m}$ );

$d_m$  = mean particle size ( $\mu\text{m}$ );

$n$  = measure of the spread of particle sizes distribution parameter.

Both mean particle size  $d_m$  and distribution parameter  $n$  can be estimated by equation fitting on experimental data. Calculations of the two parameters are commonly done by linear regression of data represented as  $\{ \log[ -\log(\text{cumulative weight percentage}) ] \}$  versus  $[ \log(\text{retaining powder sieve size}) ]$ . In this method, 36.79% of the cumulative weight percentage corresponds to the theoretical mean particle size which is calculated using a MATLAB routine [35]. Figure 5.13 shows three samples of particle size distribution and corresponding linear regression fittings using this routine. Mean particle sizes for the three incremental WOBs are found to be 0.026, 0.049 and 0.069 mm respectively.

Figure 5.14 shows mean particle sizes for DOTs using the three settings. Mean particle sizes increases with increasing WOB, which corresponds to the visual understanding from the previous PSD charts. Under the same WOB, mean particle size is increased when the vibration level is elevated. Based on the positive correlation of ROP to the bit vibration level previously reported, this confirms that a higher level of vibration helps the diamond bit cut in a deeper depth per revolution and coarser cuttings are obtained.

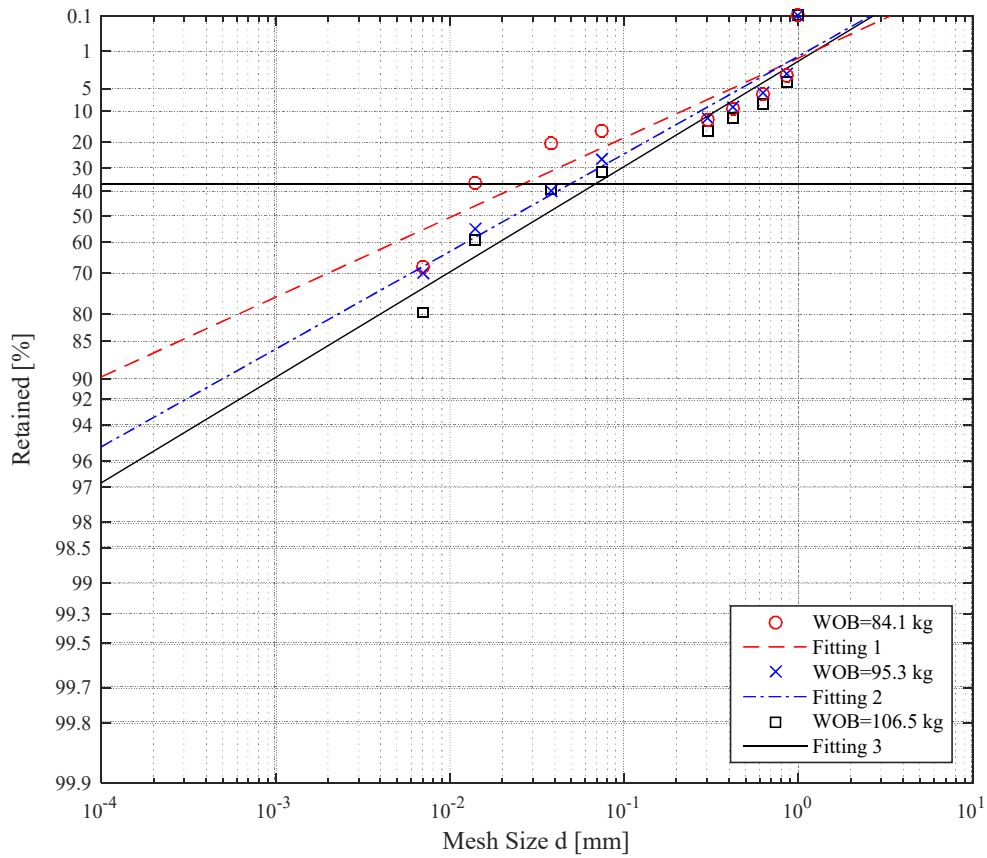


Figure 5.13: Demonstration of mean particle sizes for three increasing WOBs using the RR diagram, modified from Brezani and Zelenak [35]. Mean particle size is obtained as the mesh size at 36.79% retained

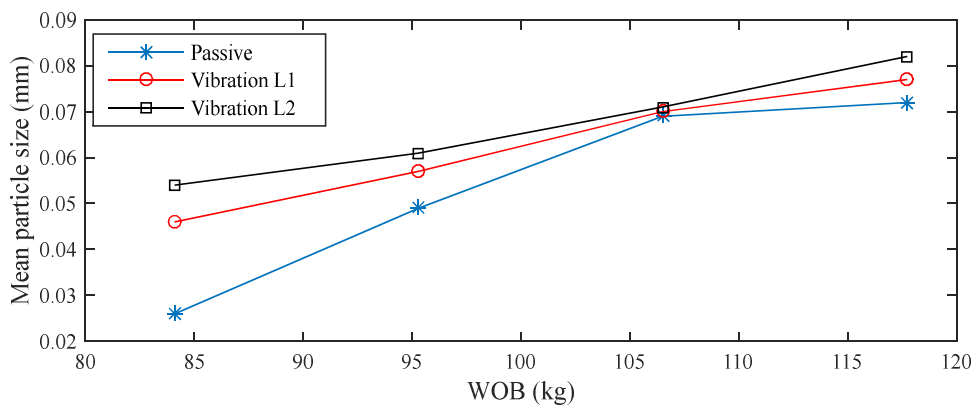


Figure 5.14: Mean particle size is positively correlated to WOB for DOTs using the three settings. Coarser cutting is obtained with the increase in WOB

#### **5.6.4 Correlation of ROP to AE energy and cutting size**

The response of cutting size distribution or mean particle size to WOB can be related to the previously described AE parameters. The average energy of AEs shows a positive correlation to the crack size, in terms of ROP, which is positively correlated to cutting size. In this manner, the increase in ROP comes from the increase in the average energy of AEs resulting from bigger cracks during the diamond bit penetration process, causing coarser cuttings.

### **5.7 Discussion and Conclusion**

- 1) For an increase in WOB and also an increase in vibration level, ROP is in a positive correlation to AE energy, crack size, cutting size distribution and mean particle size.
  
- 2) Diamond bit penetration mechanism is indirectly characterized by AE parameters, i.e. peak frequency, spectral centroid and average energy. They are successfully correlated to crack size confirming the results reported by other researchers.
  
- 3) A higher level of bit vibration improves diamond bit-rock interaction, thus helps a diamond bit cut more aggressively, resulting in better drilling performance.

### **5.8 Acknowledgements**

The research was conducted at the Drilling Technology Laboratory of Memorial University of Newfoundland and funded by Atlantic Canada Opportunity Agency (AIF contract number: 781-2636-1920044), involving Husky Energy, Suncor Energy and Research and Development Corporation (RDC) of Newfoundland and Labrador.

## 5.9 Abbreviations

AE	Acoustic emission
DOC	Depth-of-cut
DOT	Drill-off test
FFT	Fast Fourier transform
PDC	Polycrystalline-diamond-compact
PSD	Particle size distribution
pVARD	passive Vibration-Assisted-Rotary-Drilling
RMS	Root mean square
ROP	Rate-of-penetration
RPM	Revolution-per-minute
RR	Rosin-Rammer
SDS	Small drilling simulator
UCS	Unconfined compressive strength
WOB	Weight-on-bit

## 5.10 References

1. Biggs MD, Cheatham JB. Theoretical forces for prescribed motion of a roller bit. *Soc Petrol Eng J.* 1969;9(04):473-481. doi:10.2118/2391-PA
2. Sheppard MC, Lesage M. The forces at the teeth of a drilling rollercone bit: theory and experiment. Paper presented at: SPE Annual Technical Conference and Exhibition; October 2-5, 1988; Houston, TX.
3. Glowka DA. Use of single-cutter data in the analysis of PDC bit designs: part 1 - development of a PDC cutting force model. *J Petrol Technol.* 1989;41(8): 797-849. doi:10.2118/15619-PA
4. Richard T, Germain C, Detournay E. Self-excited stick-slip oscillations of drill bits. *C R Mecanique.* 2004;332(8):619-626. doi:10.1016/j.crme.2004.01.016
5. Reyes R. *Bit-Rock Interaction in Rotary Drilling: Numerical and Experimental Study* [master's thesis]. St. John's, Canada: Memorial University of Newfoundland; 2017.
6. Babapour S, Butt SD. Investigation of enhancing drill cuttings cleaning and penetration rate using cavitating pressure pulses. Paper presented at: The 48th U.S. Rock Mechanics/Geomechanics Symposium; June 1-4, 2014; Minneapolis, MN.
7. Rana PS, Abugharara AN, Butt SD, Molgaard J. Experimental evaluation of passive-Vibration Assisted Rotary Drilling (p-VARD) tool to enhance drilling performance. Paper

presented at: The 49th U.S. Rock Mechanics/Geomechanics Symposium; June 28-July 1, 2015; San Francisco, CA.

8. Xiao Y, Zhong J, Hurich C, Butt SD. Micro-seismic monitoring of PDC bit drilling performance during vibration assisted rotational drilling. Paper presented at: The 49th U.S. Rock Mechanics/Geomechanics Symposium; June 28-July 1, 2015; San Francisco, CA.

9. Babatunde Y, Butt S, Molgaard J, Arvani F. Investigation of the effects of vibration frequency on rotary drilling penetration rate using diamond drag bit. Paper presented at: 45th U.S. Rock Mechanics / Geomechanics Symposium; June 26-29, 2011; San Francisco, CA.

10. Li H, Butt SD, Munaswamy K, Arvani F. Experimental investigation of bit vibration on rotary drilling penetration rate. Paper presented at: 44th U.S. Rock Mechanics Symposium and 5th U.S.-Canada Rock Mechanics Symposium; June 27-30, 2010; Salt Lake City, UT.

11. Reyes R, Kyzym I, Rana PS, Butt SD, Molgaard J. Cuttings analysis for rotary drilling penetration mechanisms and performance evaluation. Paper presented at: The 49th U.S. Rock Mechanics/Geomechanics Symposium; June 28-July 1, 2015; San Francisco, CA.

12. Abugharara AN, Alwaar MA, Hurich C, Butt SD. Laboratory investigation on directional drilling performance in isotropic and anisotropic rocks. Paper presented at: 50th US Rock Mechanics / Geomechanics Symposium; June 26-29, 2016; Houston, TX.

13. Lockner D. The role of acoustic-emission in the study of rock fracture. *Int J Rock Mech Min Sci.* 1993;30(7):883-899. doi:10.1016/0148-9062(93)90041-B
14. Sun X. A study of acoustic emission in drilling applications. Paper presented at: The 37th U.S. Symposium on Rock Mechanics; June 7-9, 1999; Vail, CO.
15. Hardy HR, Shen HW, Kimble EJ. Laboratory studies of acoustic emission during coal cutting. Paper presented at: The 13th International Modal Analysis Conference; February 13-16, 1995; Nashville, TN.
16. Shen HW, Hardy HR, Khair AW. Laboratory study of acoustic emission and particle size distribution during rotary cutting. *Int J Rock Mech Min Sci.* 1997;34(3-4):121.e1-121.e16. doi:10.1016/S1365-1609(97)00247-5
17. Ferrari G, Gómez MP. Correlation between acoustic emission, thrust and tool wear in drilling. *Procedia Mater Sci.* 2015;8:693-701. doi:10.1016/j.mspro.2015.04.126
18. Jung SJ, Prisbrey K, Wu G. Prediction of rock hardness and drillability using acoustic emission signatures during indentation. *Int J Rock Mech Min Sci & Geomech Abstr.* 1994;31(5):561-567. doi:10.1016/0148-9062(94)90159-7
19. Mostofi M. *Drilling Response of Impregnated Diamond Bits: Modelling and Experimental Investigations* [dissertation]. Perth, Australia: Curtin University; 2014.

20. Karakus M, Perez S. Acoustic emission analysis for rock-bit interactions in impregnated diamond core drilling. *Int J Rock Mech Min Sci.* 2014;68(2014):36-43. doi:10.1016/j.ijrmms.2014.02.009
21. Brune JN. Tectonic stress and the spectra of seismic shear waves from earthquakes. *J Geophys Res.* 1970;75(26):4997-5009. doi:10.1029/JB075i026p04997
22. Madariaga R. Dynamics of an expanding circular fault. *Bull Seismol Soc Am.* 1976;66(3):639-666.
23. Haddon RAW. Earthquake source spectra in eastern North America. *Bull Seismol Soc Am.* 1996;86(5):1300-1313.
24. Khorshidian H, Butt SD, Arvani F. Influence of high velocity jet on drilling performance of PDC bit under pressurized condition. Paper presented at: 48th U.S. Rock Mechanics/Geomechanics Symposium; June 1-4, 2014; Minneapolis, MN.
25. Zhang Z. *Development and Characterization of Synthetic Rock-Like Materials for Drilling and Geomechanics Experiments* [master's thesis]. St. John's, Canada: Memorial University of Newfoundland; 2017.
26. ASTM International. ASTM D7012, standard test method for compressive strength and elastic moduli of intact rock core specimens under varying states of stress and temperatures.
27. ASTM International. ASTM D2845, standard test method for laboratory determination of pulse velocities and ultrasonic elastic constants of rock.

28. Butt SD, Calder PN. Experimental procedures to measure volumetric changes and microseismic activity during triaxial compression tests. *Int J Rock Mech Min Sci & Geomech Abstr.* 1998;35(2):249-254. doi:10.1016/S0148-9062(97)00325-2
29. Li H. *Experimental Investigation of the Rate of Penetration of Vibration Assisted Rotary Drilling* [master's thesis]. St. John's, Canada: Memorial University of Newfoundland; 2011.
30. ASTM International. ASTM D6913, standard test methods for particle-size distribution (gradation) of soils using sieve analysis.
31. ASTM International. ASTM D422, standard test method for particle-size analysis of soils.
32. Rosin P, Rammler E. The laws governing the fineness of powdered coal. *J Inst Fuel.* 1933;7:29-36.
33. Merkus HG. *Particle Size Measurements: Fundamentals, Practice, Quality.* Dordrecht, Netherlands: Springer; 2009.
34. Djamarani KM, Clark IM. Characterization of particle size based on fine and coarse fractions. *Powder Technol.* 1997;93(2):101-108. doi:10.1016/S0032-5910(97)03233-6
35. Brezani I, Zelenak F. Improving the effectivity of work with rosin-rammler diagram by using MATLAB GUI tool. *Acta Montan Slovaca.* 2010;15(2):152-157.

## **Chapter 6 Characterization of Rotary-Percussion Drilling as a Seismic While Drilling Source**

Yingjian Xiao <sup>a</sup>, PhD candidate

Charles Hurich <sup>b</sup>, Associate Professor

Stephen D. Butt <sup>a</sup>, Professor

<sup>a</sup> Drilling Technology Laboratory, Memorial University of Newfoundland, St. John's,  
NL, Canada A1B 3X5

<sup>b</sup> Department of Earth Sciences, Memorial University of Newfoundland, St. John's, NL,  
Canada A1B 3X5

This chapter is based on the objective defined in section 1.3.5 and was submitted as a research paper to Journal of Applied Geophysics and is now accepted.

### **6.1 Co-authorship Statement**

The contributions of this collaborative work are described in the following four parts. 1) Identification of research topic and design of experiments are contributed by Yingjian Xiao, Dr. Hurich and Dr. Butt. 2) Dr. Hurich is in charge of the field seismic survey and Yingjian Xiao is one of the three members. 3) Yingjian Xiao analyzes data and prepare the

manuscript under supervision of Dr. Hurich. 4) Dr. Hurich and Dr. Butt provide technical knowledge and review the manuscript.

## **6.2 Abstract**

This paper focuses on an evaluation of rotary-percussion drilling as a seismic source. Two field experiments were conducted aiming to characterize seismic sources from different rocks with different strengths, i.e. weak shales and hard arkose. Characterization of rotary-percussion drilling sources consist of spectral analysis and mean power study, along with field measurements of the source radiation patterns. Spectral analysis shows that increase of rock strength increases peak frequency and widens bandwidth, which makes harder rock more viable for seismic while drilling purpose. Mean power analysis infers higher magnitude of body waves in rotary-percussion drilling than in conventional drillings. Within the horizontal plane, the observed P-wave energy radiation pattern partially confirm the theoretical radiation pattern under a single vertical bit vibration. However a horizontal lobe of energy is observed close to orthogonal to axial bit vibration. From analysis, this lobe is attributed to lateral bit vibration, which is not documented elsewhere during rotary-percussion drilling. Within the horizontal plane, the observed radiation pattern of P-wave is generally consistent with a spherically-symmetric distribution of energy. In addition, polarization analysis is conducted on P-waves recorded at surface geophones for understanding the particle motions. P-wave particle motions are predominately in vertical direction showing the interference of free-surface.

**Keywords:** Rotary percussion drilling; seismic while drilling; source radiation pattern; polarization analysis; frequency spectrum; mean power.

### 6.3 Introduction

Rotary-percussion drilling (RPD) is widely used for drilling blast holes for the exploitation of mineral resources. It has also shown potential for seismic while drilling (SWD) purposes. For example, percussion drilling was first proposed as a seismic source, from which drill-bit position can be monitored [1]. Rotary-percussion drilling has been successfully developed for characterizing drilling conditions [2], estimating rock strength [3,4], and discriminating rock types [5]. Rotary-percussion drilling produces stronger- and wider-band sources than most standard active sources, which makes rotary-percussion drilling ideal for SWD [6]. The basic principles of SWD were reviewed by Poletto and Miranda [7]. In the past, theoretical studies have been used to characterize the seismic source radiation patterns from vertical and rotational motions of drill bits. Limited research has been done on characterizing the field radiation pattern of rotary-percussion drilling source.

In this paper, field experiments using rotary-percussion drilling were conducted with the purpose of measuring the radiation pattern of the seismic waves emanating from the drill bit. In addition to energy levels, particle motion directions and polarization angles are computed. The field measurements are done for drilling in two different rock types: weak shales and hard arkose. Measurements are divided into three parts: characterization of the rotary-percussion drilling source by frequency spectrum and mean power, radiation

patterns (in cross-hole survey and in horizontal plane), and particle motion properties. Measurements are subdivided into three parts.

1) The frequency spectra of rotary-percussion drilling are studied in response to different strengths of rocks; the mean power of rotary-percussion drilling is compared to conventional drilling sources, such as polycrystalline diamond compact (PDC) bit and roller-cone bit.

2) Drill-bit source energy radiation patterns are measured using cross-hole survey hydrophones and surface 3C geophones.

3) Particle motions are calculated from 3C geophones.

Elastic waves emanating from drilling originate in the interaction of drill bit with rock. Understanding this interaction is essential for characterizing rotary-percussion drilling as a seismic source. Theoretical studies of the forces involved in the interaction of drill bit with rock have been conducted to describe the cutting actions of drill bits, such as polycrystalline diamond compact and roller-cone bits. For example, an analytical model of a two-dimensional roller-cone bit is established to describe the gouging action of that bit. Forces on teeth are predicted when it rolls, given the depth-of-cut, torque, and the translational and rotational velocities [8]. The lobed pattern of the roller-cone bit has additionally been included in a theoretical model, from which the axial force on the bit is modulated for this periodic creation and destruction effect [9]. The interaction of polycrystalline diamond

compact bit with rock has also been studied by a numerical modeling to describe the drag and friction actions. Simulation results of drilling parameters, i.e. weight-on-bit, torque-on-bit (TOB) and rotary speed, demonstrate the bit vibrations in axial and torsional directions [10]. Experimental studies of the interaction of drill bit with rock have been done. For example, the vertical and horizontal forces on a single tooth of one roller-cone bit are experimentally correlated to the depth-of-cut [11]. The interaction of roller-cone bit with rock is reflected in recorded seismic signals. For instance, the low frequency content of the seismic signal is correlated with the forces of the lobed pattern effect [9].

Characterization of the radiation pattern of drill-bit seismic sources is of high interest for the geotechnical and engineering communities. In the simplified situation of homogeneous and isotropic media, source radiation has been theoretically studied from a single force. A mathematical model of radiation is proposed when three types of stresses are applied on a cylindrical hole embedded in an infinite solid medium. Radiated waves are interpreted as P-wave, S-waves (vertically polarized SV, and horizontally polarized SH). In the particular situation under a normal stress, P-wave amplitude maximizes parallel to the stress direction and minimizes perpendicular to the stress direction [12]. The radiation patterns of the P-wave and SV wave are similar to those for a theoretical radiation model, in which a harmonic vertical force is applied in an infinite homogeneous isotropic medium [13,14]. In realistic situations, inhomogeneity and anisotropy of the medium significantly complicate the radiation mechanism. A theoretical model proposed to study source radiation from finely stratified media with randomly distributed elastic parameters indicates radiation

patterns are significantly different from those calculated for isotropic homogeneous medium [15].

Field measurements of radiation patterns from drilling have shown good agreement with the theoretical radiation patterns. In one roller-cone bit drilling, measurements of P-wave amplitudes decrease with increasing angles relative to the direction of axial drill-tooth impact and SV wave amplitude is higher than for SH wave, which confirm the theoretical radiation patterns [16,17]. In one field cross-hole survey, SV wave amplitudes are measured on different depths of tricone bit drilling, and measurements show analogies with the theoretical SV wave radiation pattern [18].

Spectral analysis of the seismic waves radiated from drill-bit source is a frequently used method for characterization of the source radiation. Based on an accelerometer attached at top of the Kelly, tricone bits show peak frequencies that are correlated with formation hardness [19] and bit wear state [20]. Peak frequencies are related to bit geometries for both coring and roller-cone bits [21]. Frequency bandwidths of rotary-percussion drilling sources are sensitive to the relationship between drilling conditions [2], bit types [6] and rock types [5].

## **6.4 Methodology**

We have carried out two field experiments designed to characterize rotary-percussion drilling as a seismic source. The first (Red Bridge Road) experiment is a preliminary

experiment designed to characterize rotary-percussion drilling in low strength grey shale (unconfined compressive strength 32.3 MPa) and moderate strength red shale (unconfined compressive strength 56.0 MPa). The second (Collier Point) experiment is designed specifically to characterize the radiation pattern of the rotary-percussion drilling source while drilling in hard sandstone (unconfined compressive strength 163.0 MPa). The two experiments provide a field calibration of theoretical models.

#### **6.4.1 Field experiments**

Rotary-percussion drilling is carried out at two different sites representing rocks of different strengths to characterize the seismic signals generated by the drilling. At the Red Bridge Road quarry, a 1C geophone array is used to study drill-bit source spectral characteristics and mean power in low strength shales. For reference we also compare data from a polycrystalline diamond compact bit and a roller-cone bit. In the Collier Point barite mine, 3C geophones are used to study the source energy radiation pattern within the horizontal plane and particle motion properties in high strength arkose. A vertical hydrophone array is used to study the source energy radiation pattern within the vertical plane. Geomechanics and ultrasonic properties of rocks from the two experimental sites are listed in Table 6.1. The unconfined compressive strength is measured by the point load index method [22] and ultrasonic velocities are measured by the ultrasonic testing method [23] using standardized techniques.

Table 6.1: Geomechanics and ultrasonic properties of rocks, in which red shale properties are in reference to Rana et al. [24]

Rocks	Unconfined compressive strength (MPa)	Density (kg/m <sup>3</sup> )	P-wave velocity (m/s)	S-wave velocity (m/s)
Grey arkose	163.0	2692	5042	3059
Red shale	56.0	2760	5154	3767
Grey shale	32.3	2579	3394	2693

#### 6.4.2 Red Bridge Road quarry experiment

A linear array of 1C geophones (20) was spread adjacent to three boreholes (Figure 6.1). The lithology of underground formations by cross section A-A' are demonstrated in Figure 6.2. The quarry is composed of Manuels River Formation of the Harcourt Group which is black to dark grey shale with thin beds of grey limestone which we refer to as grey shale. This formation is underlain by the Chamberlain's Brook Formation of the Adeyton Group defined as green to grey shales with some red mudstones, which is locally red shale [25]. These lithologies are confirmed by drill cuttings circulated back to surface.

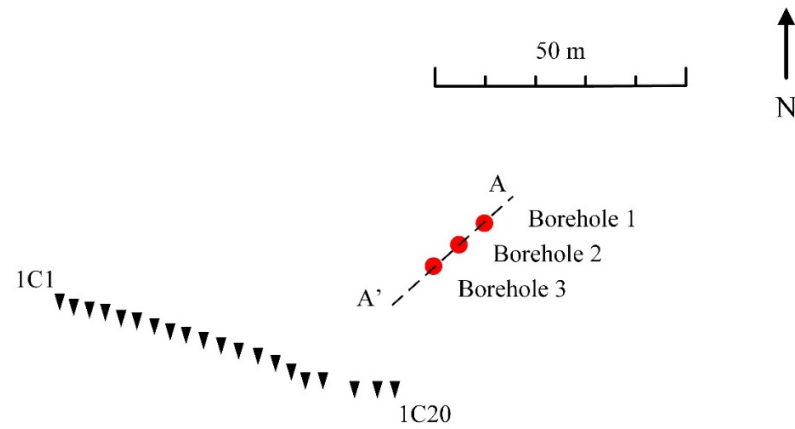


Figure 6.1: Spread of 1C geophones array (20) with three seismic source boreholes in Red Bridge Road quarry of eastern Newfoundland and Labrador of Canada



speed and weight-on-bits are applied on other two bits. During drill-off tests, seismic signals were continuously recorded for 30 s with sampling frequency of 1000 Hz.

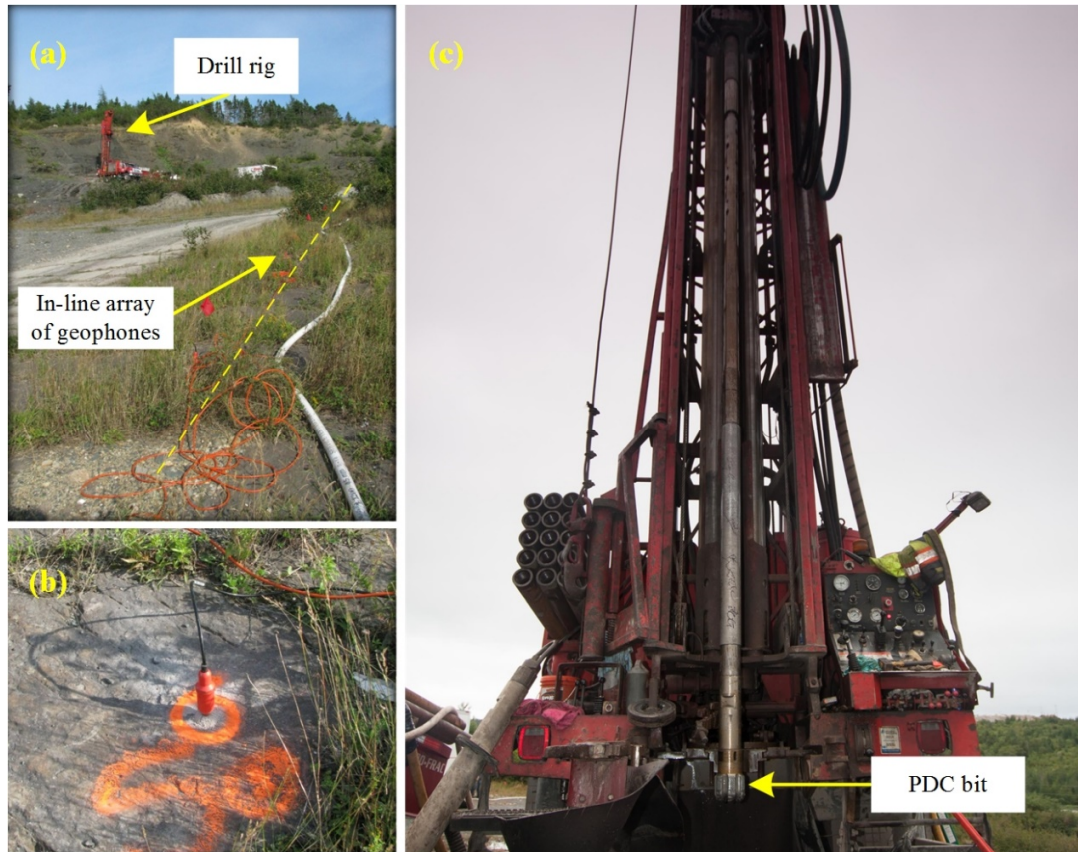


Figure 6.3: (a) Overview of drill site with in-line geometry of geophones; (b) 1C geophone; (c) Front view of the drill rig modified from Rana et al. [24]

In this experiment, characterization of rotary-percussion drilling source is achieved by evaluating:

- 1) Comparison of frequency spectra from the rotary-percussion drilling source from different rock types, i.e. grey and red shales.

- 2) Mean power comparison of rotary-percussion drilling signal and that from polycrystalline diamond compact and roller-cone bits. Seismic sources are compared on both grey and red shales.

### **6.4.3 Collier Point experiment**

In this experiment, the P-wave energy radiation pattern and wave particle motions are investigated on seismic sources generated by rotary-percussion drilling. An array of 3C geophones (12) was stiffly coupled into bedrock surrounding two source boreholes (Figure 6.4). The lithology of the site is shown in cross section B-B' (Figure 6.5). The host rock consists of green-grey volcanic sedimentary arkose with red arkose at top [26]. Cuttings show that the majority of rocks are grey arkose with red spots in few depths, which indicates high homogeneity through all the formation.

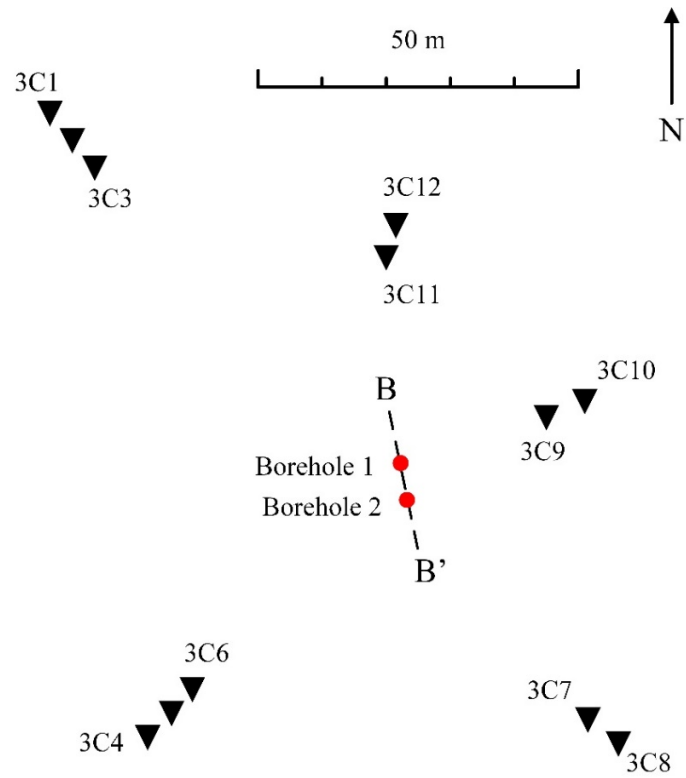


Figure 6.4: Top view of 3C geophones (12) spread around two source boreholes in Collier Point barite mine at eastern Newfoundland and Labrador of Canada

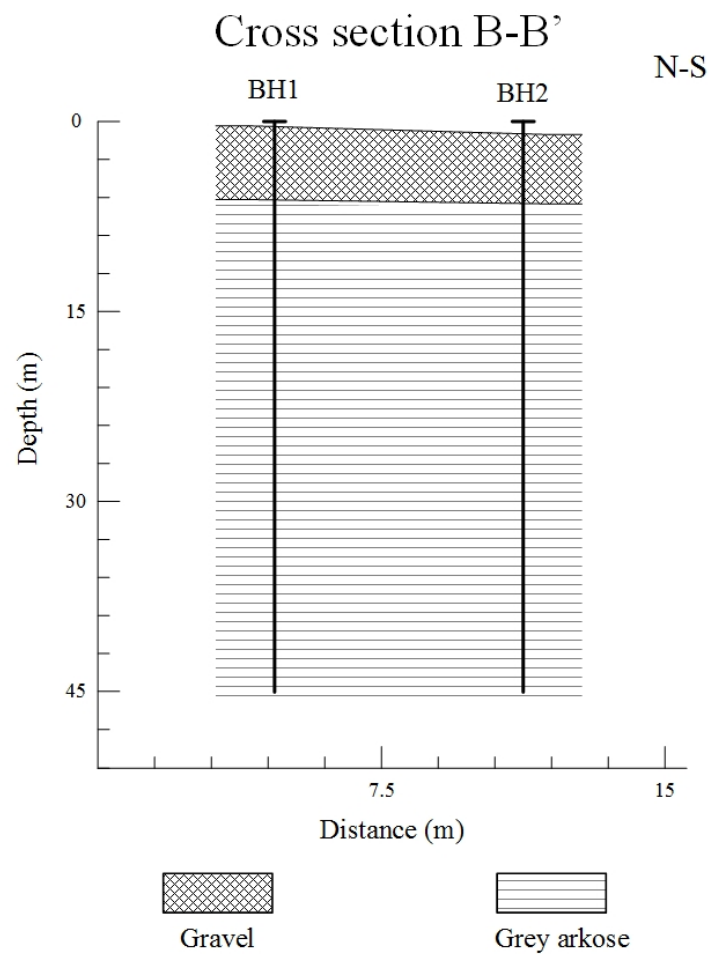


Figure 6.5: Cross section of B-B' showing the rock formation penetrated based on analysis of cuttings

The experimental drilling was carried out with an Atlas rotary-percussion rig with a 155 mm hammer bit (Figure 6.6). The drilling parameters remain constant with weight-on-bit of 3.45 MPa feed pressure and rotary speed as 58 revolutions-per-minute (RPM). Borehole 1 and 2 were both drilled to depths of 46 m. During drilling, seismic signals are continuously recorded for 30 s with sampling frequency of 1000 Hz.

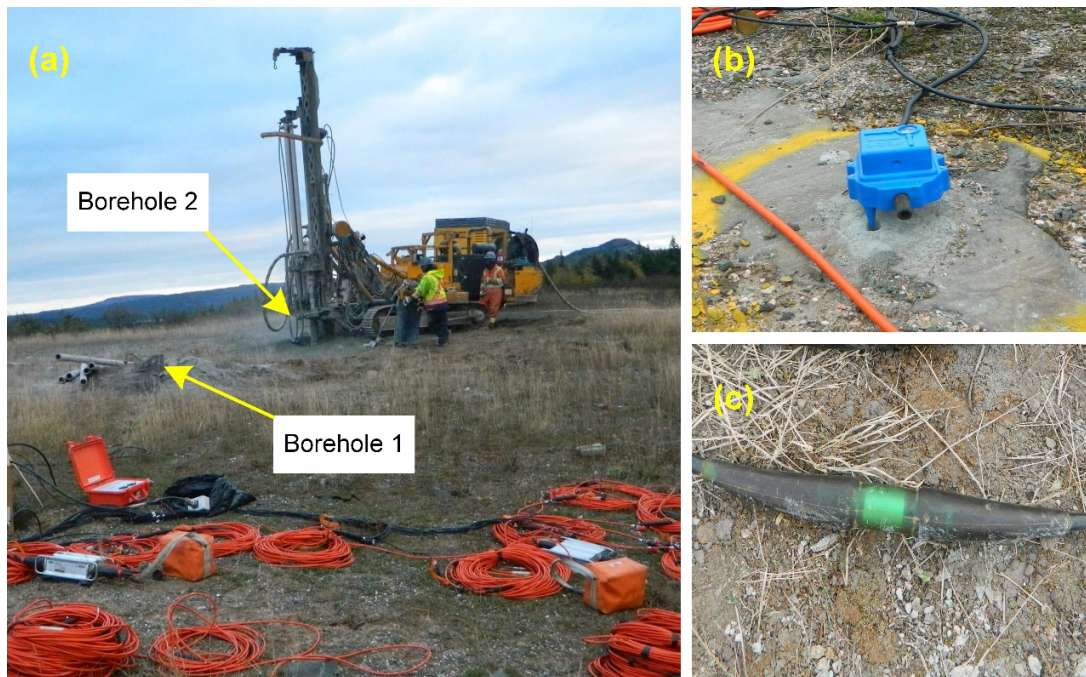


Figure 6.6: (a) Onsite seismic while drilling (facing south); (b) 3C geophone with horizontal in-line component facing borehole 2; (c) hydrophone

In this experiment, two objectives were achieved when rotary-percussion drilling is conducted at borehole 2 (Figure 6.4) by the following plans:

- 1) Frequency spectra of rotary-percussion drilling signal are obtained from hard arkose. This supplements the study of spectral characteristics of rotary-percussion drilling source on weak rock.
  
- 2) Wave energy radiation and polarization analysis within the horizontal plane. 3C geophones (12) are arranged in 2- or 3-geophone lines oriented radially from borehole 2 (Figure 6.4).

3) Wave energy radiation within the vertical plane. An array of hydrophones (21) was placed in water-filled borehole 1 for measuring seismic source from drilling in borehole 2 (Figure 6.6).

## **6.5 Data Processing**

### **6.5.1 Seismic data from the Red Bridge Road experiment**

For the Red Bridge Road quarry experiment, the raw seismic data are processed following a workflow that sequentially includes notch filtering, spiking deconvolution and cross-correlation with the reference channel #20. Notch filtering aims at removing 60 Hz noise. Channel #20 is selected as the reference channel because it is the closest geophone to drill-bit source. In Figure 6.7, a sample of cross-correlated seismic data are shown from borehole 2. The zero-lag of the cross-correlation is placed at 100 ms. Twenty traces are grouped as one drill-bit source and the apparent difference of amplitudes are shown between rotary-percussion drilling and drilling with the polycrystalline diamond compact bit.

Figure 6.8 shows an example of SV and surface waves determined in rotary-percussion drilling and polycrystalline diamond compact bit drilling. SV wave is identified only in rotary-percussion drilling and P-wave is not identified in this experiment because of the weakness of the grey and red shales. SV wave is selected as the target for spectral analysis for both grey and red shales.

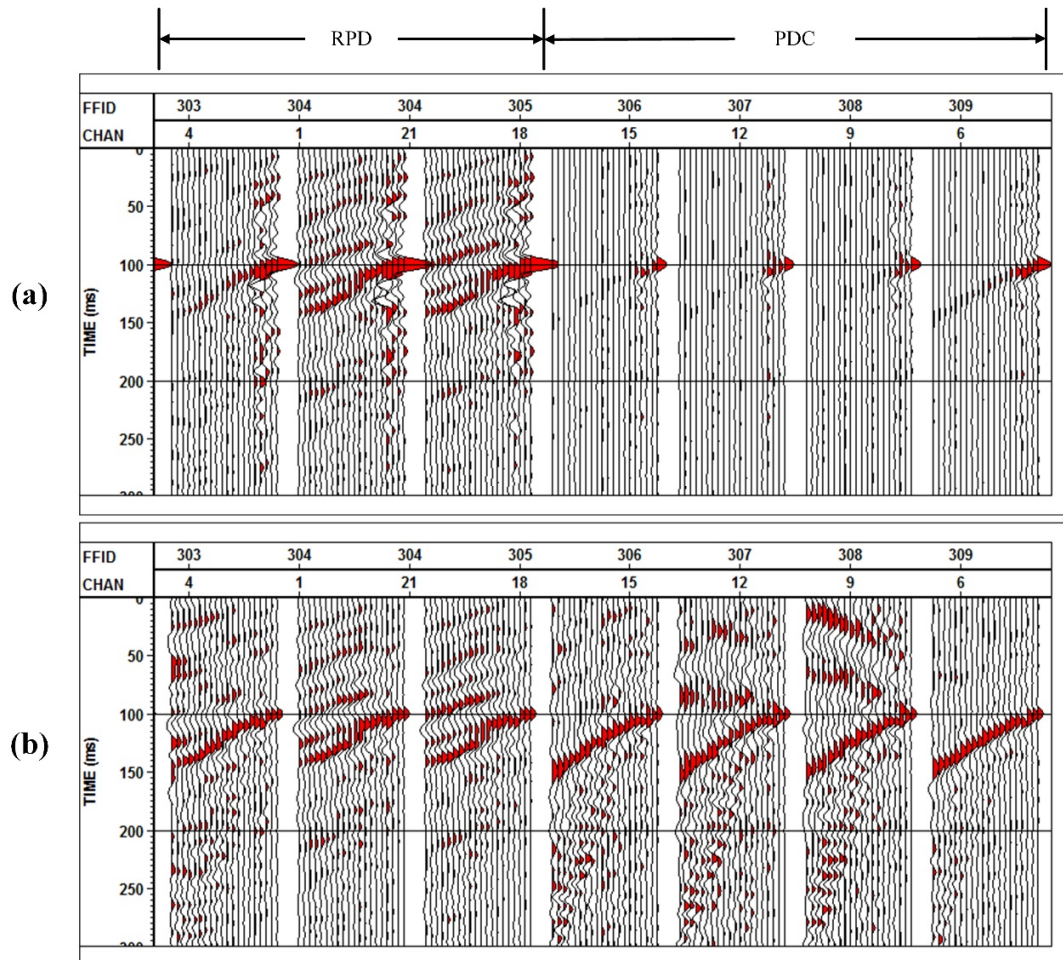


Figure 6.7: Sample seismic data cross-correlated on channel #20. No scaling (a) is compared with scaling at individual peak amplitude (b). In borehole 2 from 79.2 to 85.3 m depth, seismic sources are obtained from one rotary-percussion drilling (RPD) and one conventional drilling with a polycrystalline diamond compact (PDC) bit. Every twenty traces are assembled in one group recorded by 20 geophones

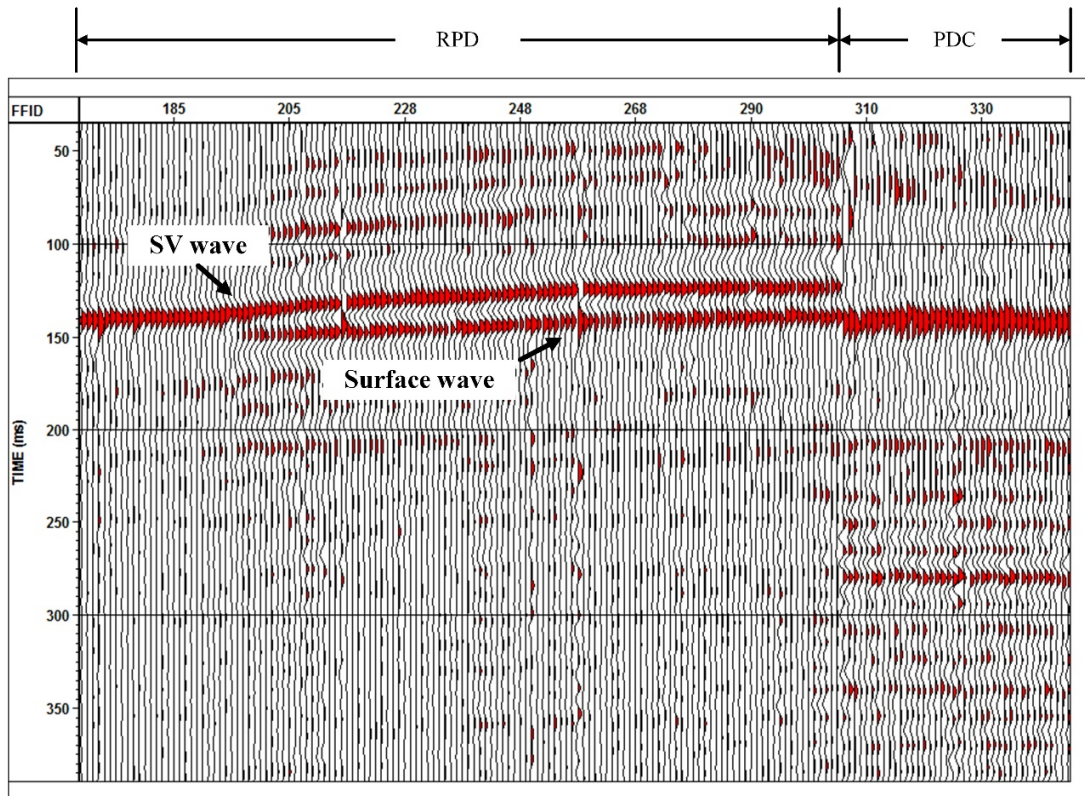


Figure 6.8: Cross-correlated records from channel #3 in borehole 2. One rotary-percussion drilling starts from surface and is followed by one conventional drilling with a polycrystalline diamond compact bit to 91.4 m depth. Trace is individually scaled at its peak amplitude

Rector and Hardage [17] demonstrate that surface waves observed in SWD experiments can be a combination of surface waves generated by drilling rig operations and longitudinal waves that propagate up the drill pipe, couple with the drill rig and are re-radiated as surface waves. The energy of the surface wave generated by rig operations and drilling can be used to characterize rock-bit interaction during drilling. We use this characteristic of the surface waves to characterize drilling with three different types of drill bits.

### 6.5.2 Seismic data from the Collier Point experiment

### 6.5.2.1 *Hydrophone data for cross-hole survey*

For the Collier Point experiment, seismic data are simultaneously recorded in 3C surface geophones and hydrophones in an adjacent borehole. The geometry for the hydrophones is shown in Figure 6.9. Rotary-percussion drilling in borehole 2 was monitored by in-line hydrophones (21) with 2 m spacing in borehole 1, covering depths from 6 to 46 m.

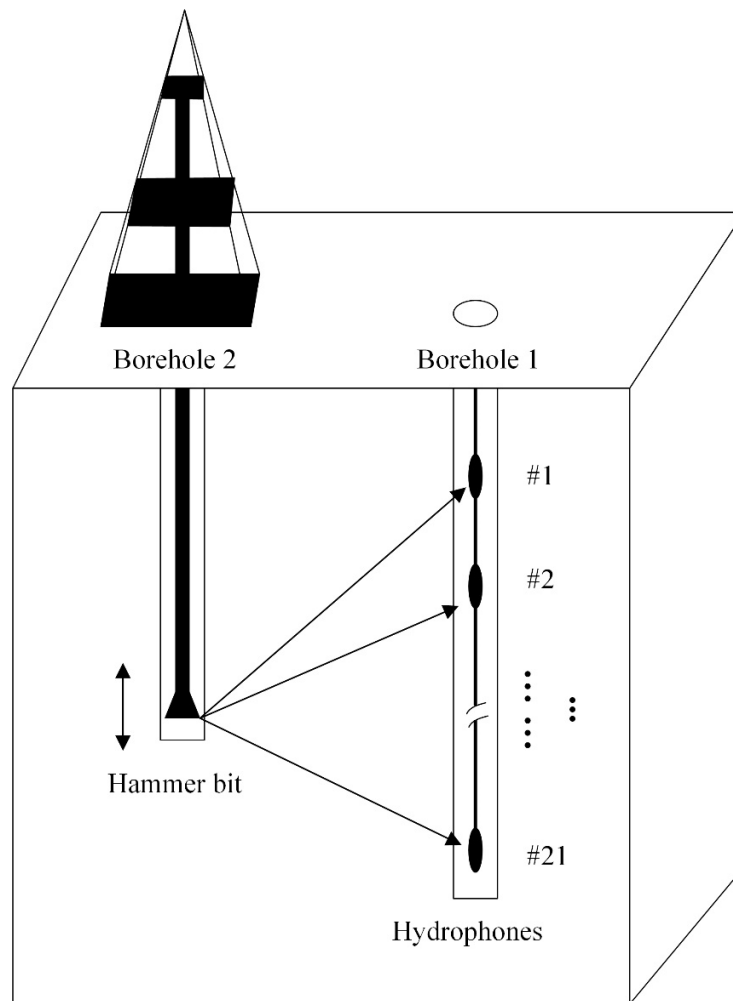


Figure 6.9: Illustration of cross-hole survey on hammer bit source with in-line spread of hydrophones

A standard workflow is used to process the raw seismic data. This workflow sequentially includes AGC (30 s window), notch filtering, spiking deconvolution and then cross-correlation. Cross-correlation is conducted using the hydrophone at the same depth as the drill-bit source. This takes the advantage of high S/N of hydrophone data. Figure 6.10 shows an example of a processed hydrophone record. The P-wave occurs as the first arrival and is selected as the target for analyzing cross-hole energy radiation. There is a notable polarity change indicating reverse travel direction of seismic wave from the source, and trace polarities from hydrophones #11 to #21 have been reversed for consistency. In this example the rotary-percussion drilling source is located between hydrophones #10 and #11 by depth.

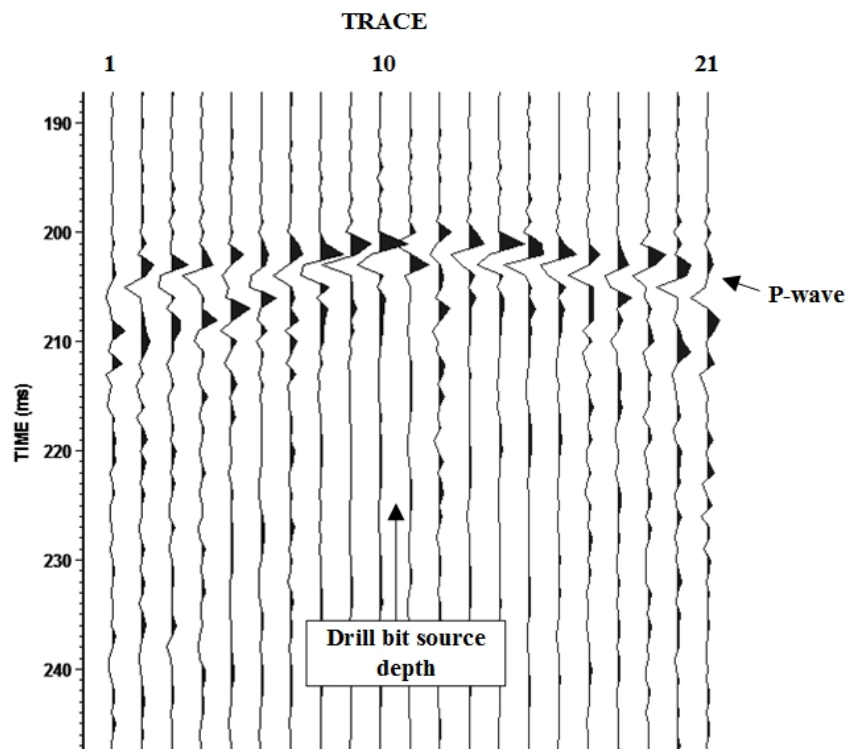


Figure 6.10: Sample seismogram of P-waves received by hydrophones. The polarities have been reversed from trace #11 to #21 for consistency. The drill-bit source depth is apparently located between trace #10 and #11

The P-wave from multiple sources is then picked from cross-correlated seismic data and those amplitudes from each source are normalized to its maximum. In homogeneous media without attenuation, wavefronts emanating from a single source are spherical and the amplitude decays due to geometric divergence of the wavefront. To compensate for this, a divergence gain function is applied following Newman [27] and Yilmaz [28]. The compensated P-wave amplitudes for each source-receiver pair are calculated by multiplying the normalized amplitude by the corresponding normalized gain function.

#### ***6.5.2.2 The 3C geophone seismic data***

Processing the 3C seismic data follows the same work flow described previously. Figure 6.11 shows an example of the response of the seismic source recorded on vertical component of all geophones at single source depth. The P-wave is identified as the first arrival according to the travel time. The vertical component of the P-wave is chosen as the estimator of the P-wave radiation pattern.

The vertical component of amplitudes emanating from a specific drill-bit depth is picked for the twelve geophones at five receiver locations. Geophones at the same locations are grouped to provide multiple measurements at the same azimuths with reference to borehole 2. To compensate for the effect from different angles of emergence ( $\phi$ ), vertical amplitudes are rotated to the source-receiver linear path (Figure 6.16), followed by amplitude normalization. Amplitude decay by geometric spreading is compensated by multiplying

normalized amplitude by the normalized gain function [27,28]. Amplitudes were measured by taking the maximum positive values of P-waves within vertical component traces.

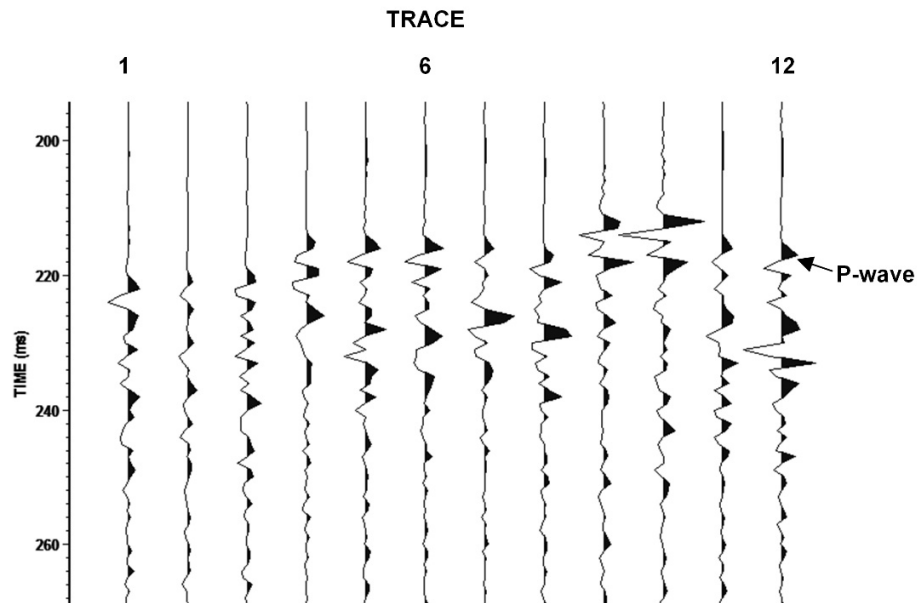


Figure 6.11: Seismogram received on vertical component of 3C geophones. Varying arrival times and amplitudes result from varying source-receiver distance and the geometric divergence

## 6.6 Data Analysis and Interpretation

### 6.6.1 Characterization of the rotary-percussion drilling source

Characterization of the rotary-percussion drilling source is carried out in the following two steps. First, frequency spectra of rotary-percussion drilling sources are studied on different rock strengths, i.e. grey shale and red shale from the Red Bridge Road experiment and arkose from the Collier Point experiment. Spectral analysis is conducted on rotary-percussion drilling sources for equal source-receiver distances. Second, the mean power of rotary-percussion drilling sources is compared to conventional sources by selecting surface

waves from the Red Bridge Road experiment. Autocorrelation is conducted on windowed surface waves. The zero-lag of the autocorrelation is then extracted as the mean power for surface wave [29]. The details for the mean power study are listed in Table 6.2.

Table 6.2: Seismic sources generated by rotary-percussion drilling and other bit sources

Rock	Source type	Drilling depth (m)	Seismic event (FFID)	Borehole #
Red shale	Polycrystalline diamond compact	81.6-93.8	86-99	1
	Roller-cone	93.8-99.9	100-109	1
	Hammer	79.2-82.3	290-305	2
Grey shale	Hammer	44.2-53.3	519-528	3
	Polycrystalline diamond compact	57.5-60.6	569-577	3

In Figure 6.12, frequency spectra of rotary-percussion drilling sources from different rock strengths are compared at the same source-receiver distance of 79 m. SV waves are selected from both Red Bridge Road and Collier Point experiments. Peak frequency increases with increasing rock strength, i.e. 55 Hz for grey shale, 83 Hz for red shale and 166 Hz for arkose. From the frequency spectra of SV waves, the difference of the range of frequency contents is used to characterize the frequency bandwidth. The spectra recorded in stronger arkose are significantly broader and peak at higher frequencies. The results show that increase of rock strength increases the peak frequency and widens the frequency bandwidth of seismic sources, which makes harder rock more viable for SWD purpose.

In Figure 6.13, autocorrelation mean powers of seismic sources generated by rotary-percussion drilling are compared to conventional drill bits, i.e. roller-cone bit and polycrystalline diamond compact bit from the Red Bridge Road experiment. In this experiment, body waves are not identified for conventional drillings because of the weakness of shales (Figure 6.8). The surface wave is then selected for the mean power analysis from the three drillings, which is generated by rig-ground motions comprised of original drill rig operation and new rig-ground motion coupled with longitudinal waves radiated from the interaction of drill bit with rock. The magnitude of sources from rotary-percussion drilling is higher than polycrystalline diamond compact bit by three orders in grey shale and is higher than polycrystalline diamond compact and roller-cone bits by two orders in red shale. These results demonstrate that rotary-percussion drilling releases significantly higher magnitude surface waves than conventional drilling sources. The difference in energy indicated by surface waves suggest that it will occur in body waves. This is demonstrated in Figure 6.8 that shows SV wave in rotary-percussion drilling but not in polycrystalline diamond compact bit drilling. The source mean power from polycrystalline diamond compact bit is much smaller than that for roller-cone bit. This demonstrates decreased axial vibration of polycrystalline diamond compact bit compared to that for the roller-cone bit which is documented in literature [7].

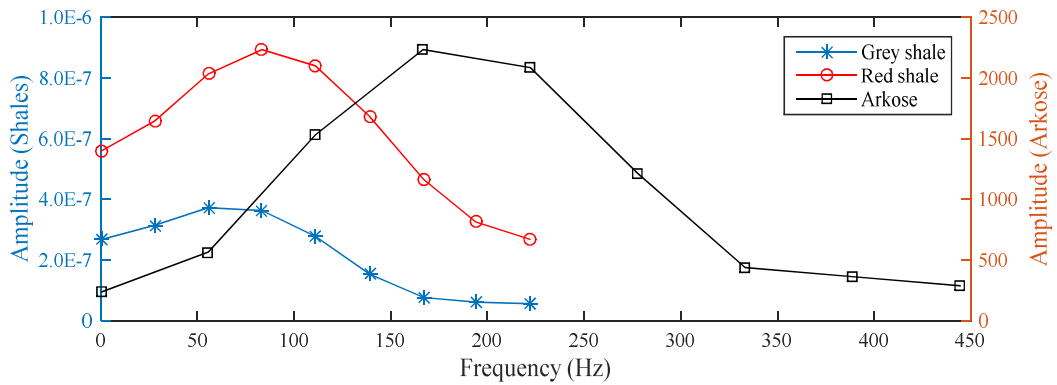


Figure 6.12: Frequency spectra of rotary-percussion drilling SV waves vary with different rock strengths: i.e. grey and red shales from the Red Bridge Road experiment, and arkose from the Collier Point experiment. Source-receiver distance for three rotary-percussion drilling sources is 79 m. Increase of rock strength increases peak frequency and widens bandwidth

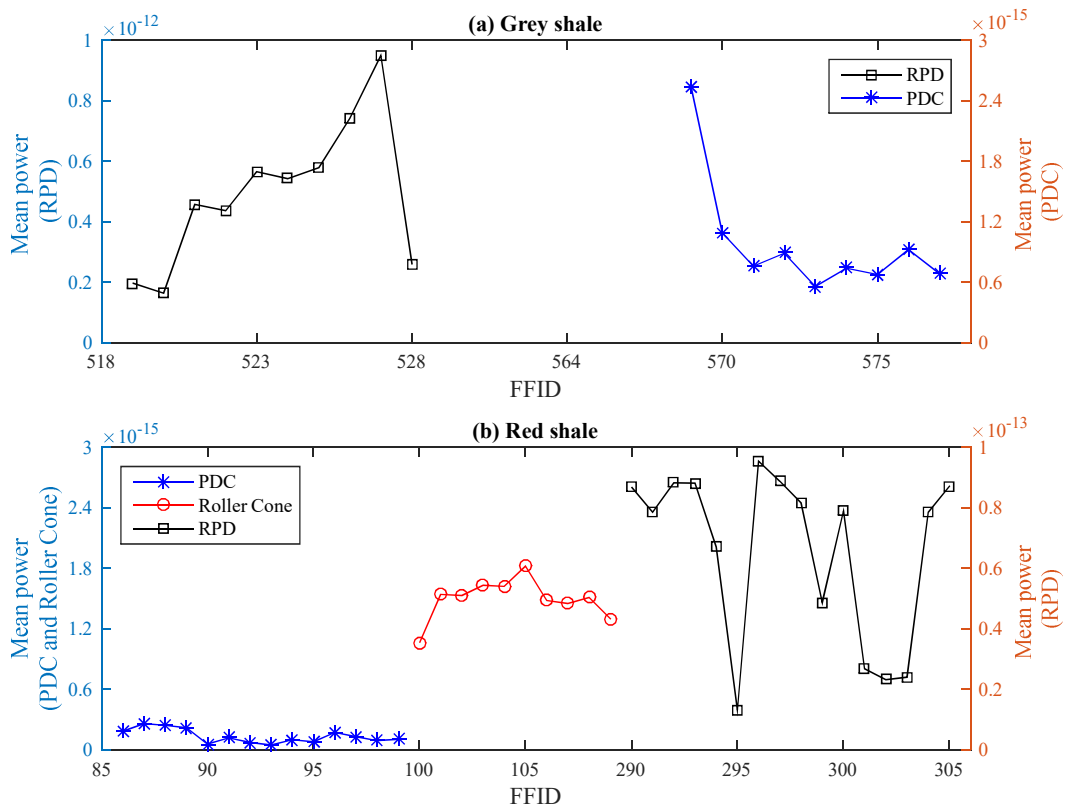


Figure 6.13: Mean power of rotary-percussion drilling and conventional drillings, i.e. roller-cone bit and polycrystalline diamond compact bit, in terms of surface waves from

(a) grey shale and (b) red shale. The magnitude of sources from rotary-percussion drilling is higher than polycrystalline diamond compact bit in three orders in grey shale, and is higher than polycrystalline diamond compact and roller-cone bits in two orders in red shale

## 6.6.2 Radiation pattern of drill-bit source

### 6.6.2.1 Energy radiation within vertical plane

The energy radiation pattern within the vertical direction plane is obtained from the cross-hole survey (Figure 6.9). For a single seismic source depth, the P-wave amplitude is compensated to remove the divergence effect by multiplying by a P-wave gain function. To obtain more reliable and stable amplitude distribution, amplitude correction is repeated in five sources from 17.1 to 45.3 m depth.

For purpose of analysis, the corrected amplitudes from all sources are classified into five degree bins based on the angle of incidence referred to the horizontal plane on the hydrophones. The arithmetic mean amplitude is taken from each group, and normalized and plotted along with the moving average smoothing curve in polar coordinates. Figure 6.14 shows the measured amplitude distribution of P-waves within the vertical plane when measurements are only conducted on the right side of the borehole 2. The P-wave energy radiations from theoretical axial bit vibration (a) and lateral bit vibration (b) are demonstrated [12,17] and they are symmetrical about the borehole 2. For theoretical radiations, the angle of emergence ( $\phi$ ) is referenced from the horizontal plane to the linear path intersecting the polar center and the length represents energy level.

For rays travelling downwards, the measured radiation of P-wave amplitudes increase with increasing angle of emergence to  $80^\circ$ . In plot (a), the measured amplitude distribution of P-waves generally confirms the theoretical radiation pattern under a single axial bit vibration [12,17] when rays travel downwards, i.e. emanating P-wave amplitudes increase with the increasing angle of emergence to the maximum in the bit vibration direction. There are no measured amplitudes for angles of emergence from  $80^\circ$  to  $90^\circ$  because of experimental limitations.

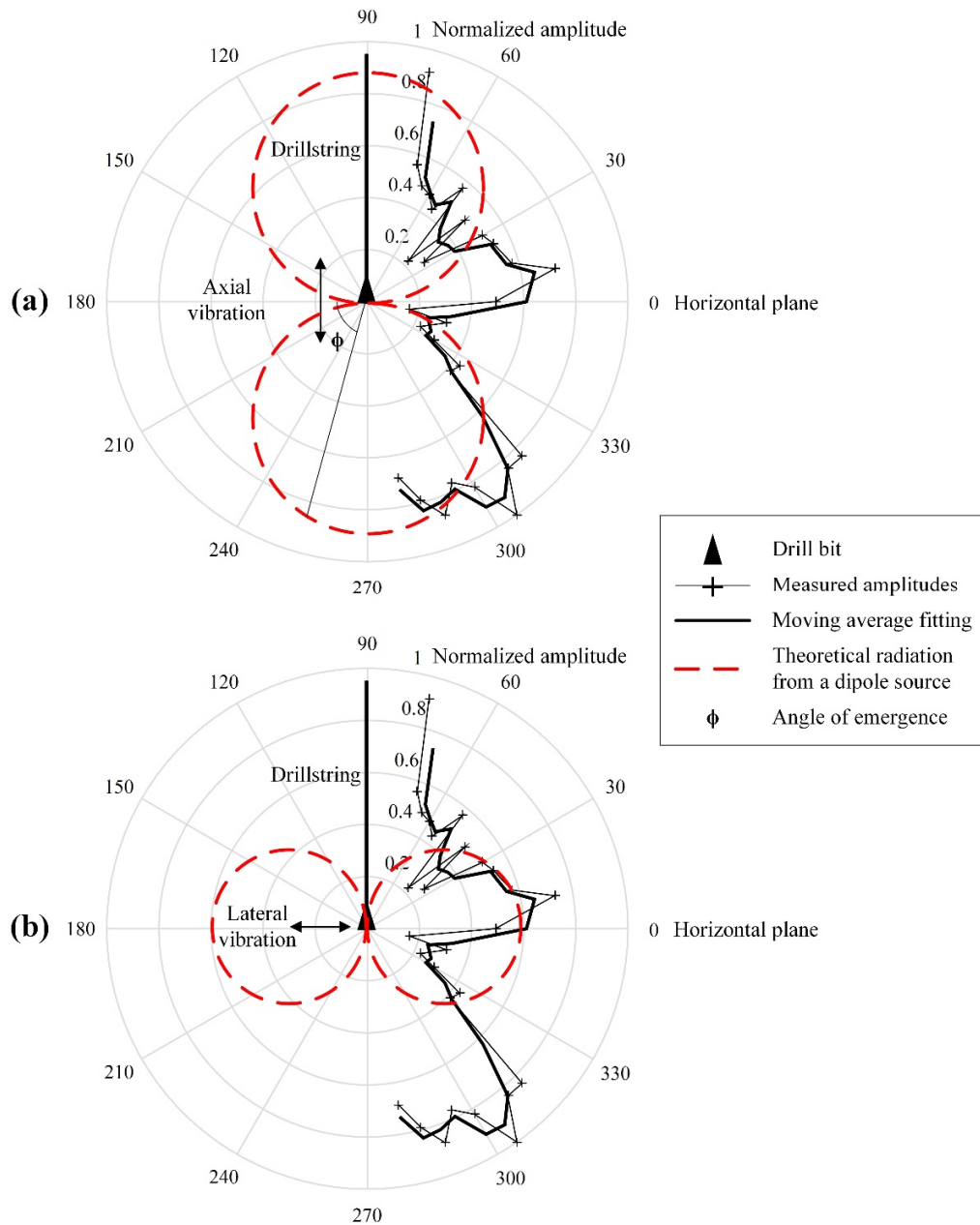


Figure 6.14: Measured amplitude distribution of P-waves within the vertical plane along with energy radiations from theoretical (a) axial bit vibration and (b) lateral bit vibration. Measured amplitude distribution partially confirms the theoretical prediction for axial bit vibration. An additional lateral vibration is indicated by the new horizontal energy lobe (b)

For rays travelling upwards, a horizontal lobe of amplitude is found when the angle of emergence is located between  $0^\circ$  and  $30^\circ$ , and then measured amplitudes increase until the angle of emergence reaches the measurement limit of  $75^\circ$ . The additional horizontal lobe of amplitude is observed close to orthogonal to axial bit vibration. In fact, the smallest geometric correction is made in this direction where significantly higher corrected amplitudes are not possible. This strongly indicates that the lobe of amplitude is authentic which is attributed to an additional horizontal vibration source. In plot (b), the observed horizontal lobe of amplitude is consistent with the theoretical radiation pattern of P-wave under a single lateral vibration source [12,17] for rays travelling upwards. An additional lateral vibration is indicated by the new horizontal energy lobe during rotary-percussion drilling which is not documented elsewhere. This lateral bit vibration has been measured by downhole accelerometers during the Red Bridge Road experiment with a polycrystalline diamond compact bit in addition to axial and torsional bit vibrations [30]. From the above analysis, a combination of axial and lateral vibrations have been demonstrated during rotary-percussion drilling from field measurements of radiation patterns.

#### ***6.6.2.2 Energy radiation within horizontal plane***

The energy radiation pattern within the horizontal plane is determined from P-waves recorded by 3C geophones. Data processing includes angle rotation and geometric compensation which have been previously demonstrated. This procedure is repeated on nine sources from 24.9 to 45.3 m depth. The corrected amplitudes from those sources are then averaged on common geophones of each groups (Figure 6.4), where geophones are taken into one group based on the proximity of its azimuth with reference to borehole 2.

The azimuth is the counter-clockwise angle measured from the north direction through borehole 2. The arithmetic average amplitude taken from every group of measurements is plotted in polar plot showing errors between the average value and limit measurements.

Figure 6.15 shows the distribution of measured amplitudes recorded from borehole 2 within the horizontal plane. Measured amplitudes are evenly distributed except for geophones at the azimuth of  $33^\circ$  where amplitude levels are much higher in geophone #1 and #3 than the rest. This largely results from extraordinarily high recordings from the two geophones. The observed pattern is generally consistent with a spherically-symmetric distribution of energy [17].

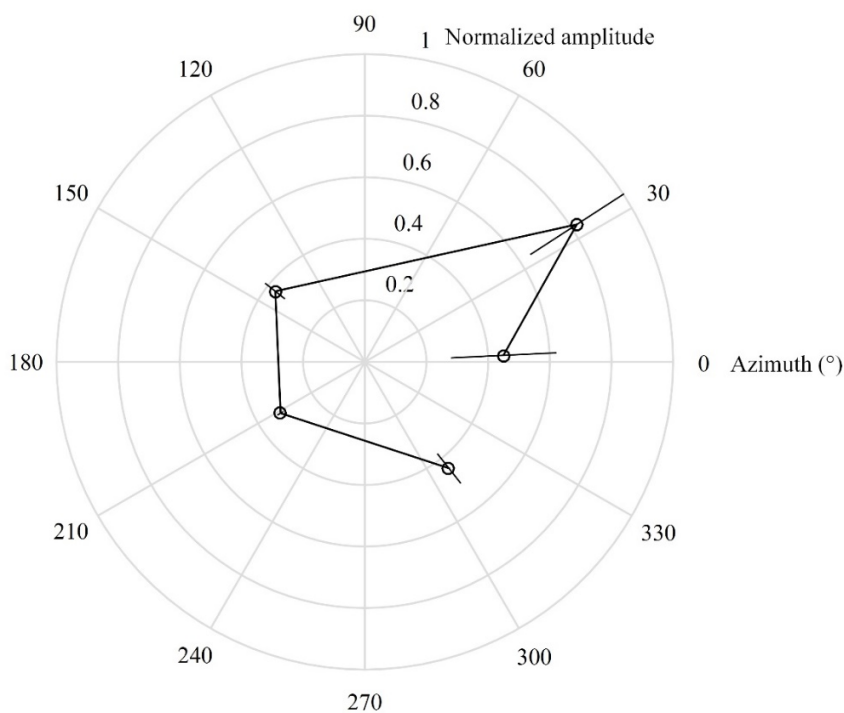


Figure 6.15: Measured amplitude distribution of P-waves within the horizontal plane. Five groups of geophones are distributed as even as possible around borehole #2 (polar center), with redundant measurements for every group showing an arithmetic average (cycle) and errors

### 6.6.3 Polarization analysis

The purpose of polarization analysis is to determine the actual particle motion (displacement) direction so that the true wave motion is understood at the surface geophones. The hodogram is used to visually show the trajectory of particle motion. A hodogram is defined as the curve described by displacement of two components over a specific time window [31]. Particle motion direction is calculated by the following procedures. First, the original hodogram components are projected to a new coordinate system which has been rotated within that plane. Second, the power of projected components is calculated. Third, the maximum power is found from all rotated coordinates and the angle of rotation is taken as the polarization angle and corresponding direction is the particle motion direction [32].

Figure 6.16 shows the orientation of a 3C geophone, including three orthogonal components, i.e. vertical (V) component, horizontal in-line (H-I) or radial component, and horizontal out-of-line (H-O) or transverse component. Positive values are obtained from H-I component when the H-I orientation is consistent with the source-receiver azimuth as demonstrated, and vertical and transverse components then maintain the same polarity as H-I component. The angle of emergence ( $\phi$ ) is referenced to the horizontal plane. . Polarization analysis is conducted on the first arrivals of P-wave which is easily distinguished and not mixed with other phases. The time window of P-wave remains the same for plotting hodograms of components V and H-I, and components H-O and H-I

recorded at a single depth of source. Polarization analysis is conducted on the first 11 geophones due to a loss of component on the 12<sup>th</sup> geophone.

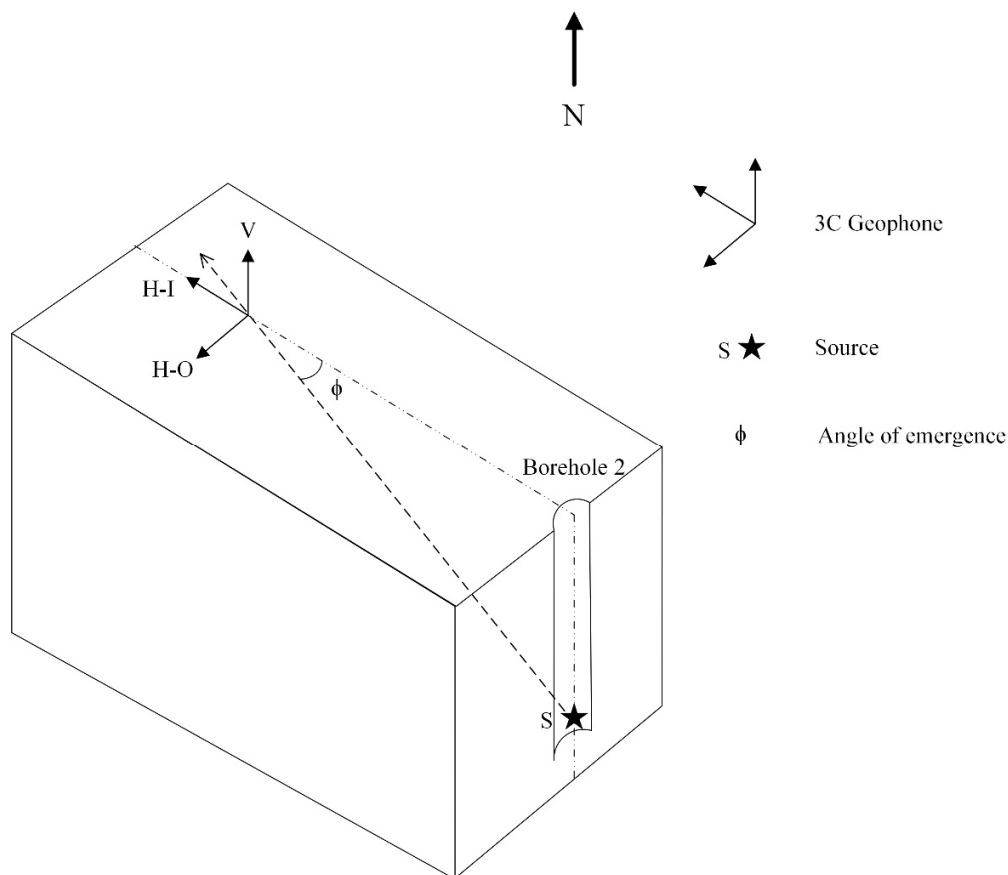


Figure 6.16: Orientation of 3C geophone showing three orthogonal components. The orientation of H-I component follows the source-receiver azimuth

Figure 6.17 shows an example of hodograms for P-waves recorded at the azimuth of  $32.8^\circ$  (geophone #2) with six sources of depths from 17.1 to 45.3 m. The azimuth is the counterclockwise angle measured from the north direction with reference to borehole 2. For every event, a specific time window is taken on P-waves resulting in two hodograms listed in a row. This time window is rigorously defined to pick P-waves, which are hard to separate due to the short distance from source to receiver. For each hodogram, a black arrow

shows the vector of the interpreted particle motion direction along with an angle, which is rotated counterclockwise from the H-I orientation and referred to as the polarization angle. In column (a), polarization angles are within the range of  $86.2^\circ$  and  $89.7^\circ$  showing particle motions are almost parallel to the direction of component V for the whole range of depths of the source. This results indicates that despite high angles of emergence, the free-surface effect dominates the response of the surface geophones as has been reported by other researchers [33]. In column (b), particle motions is dominantly in the H-I orientation and all the polarization angles are smaller than  $45^\circ$ . This shows that P-wave particle motions deviate from the H-I orientation indicating the H-I components of geophones are not in exact consistence with the source-receiver azimuths.

Figure 6.18 shows an example of hodograms for P-waves recorded at five different azimuths of geophones (#11, #2, #5, #7 and #9 from top to bottom) from a common source depth of 17.1 m. In column (a), polarization angles are within the range of  $58.1^\circ$  and  $107.6^\circ$  showing particle motions are predominately in the vertical direction. In column (b), polarization angles are smaller than  $45^\circ$  showing particle motions predominates in the H-I orientation, with an exception of  $116.4^\circ$ . This results also show that P-wave particle motions deviate the H-I orientation indicating the H-I orientations of geophones are not in exact consistence with the source-receiver azimuths.

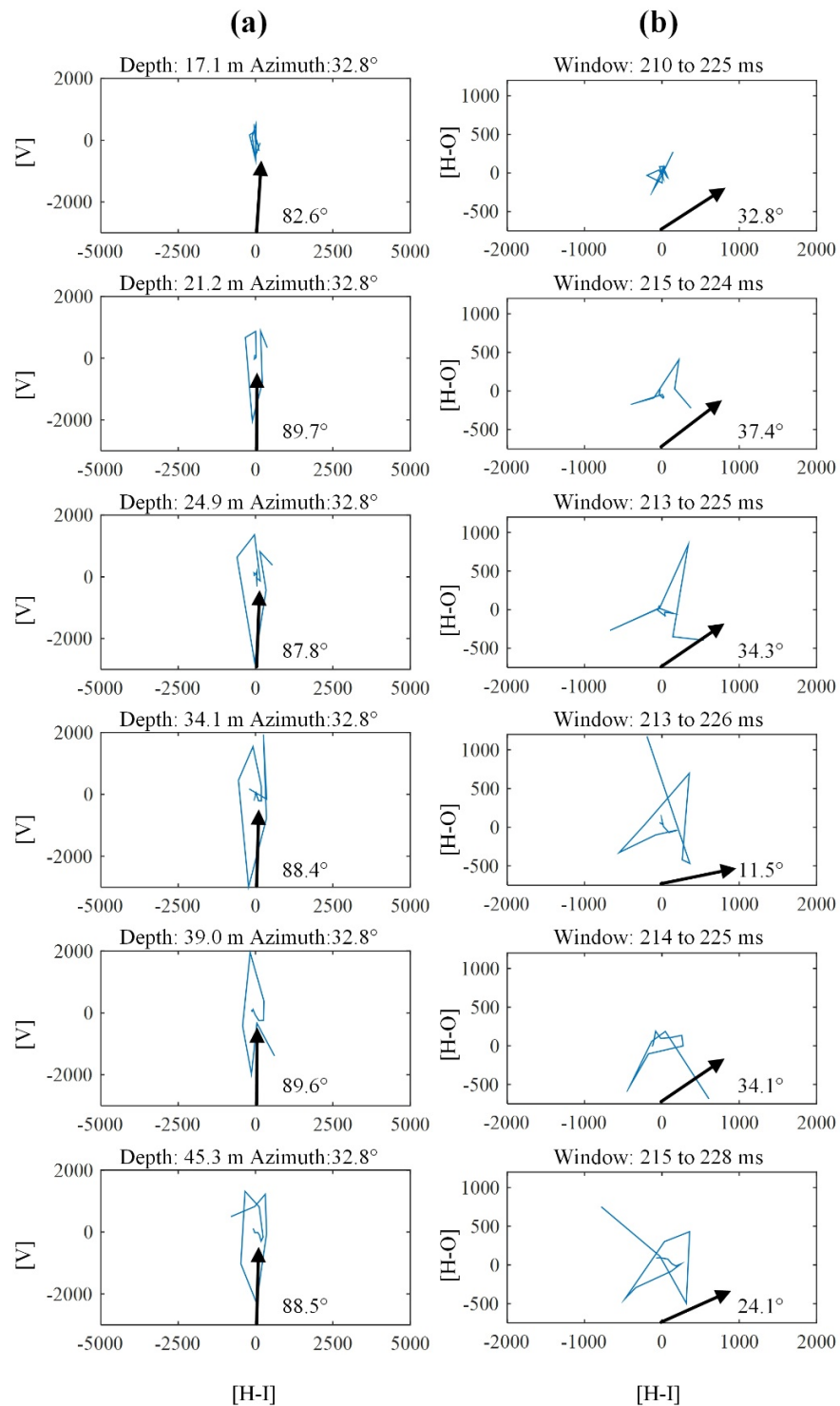


Figure 6.17: Hodograms for P-waves recorded at the azimuth of  $32.8^\circ$  from multiple depths of sources. The azimuths are relative to the direction away from the source. Each

row refers to an event covering two hodograms in column (a) and (b). Blue lines show hodograms of P-waves at specific time windows. Black arrows show the vectors for particle motion directions

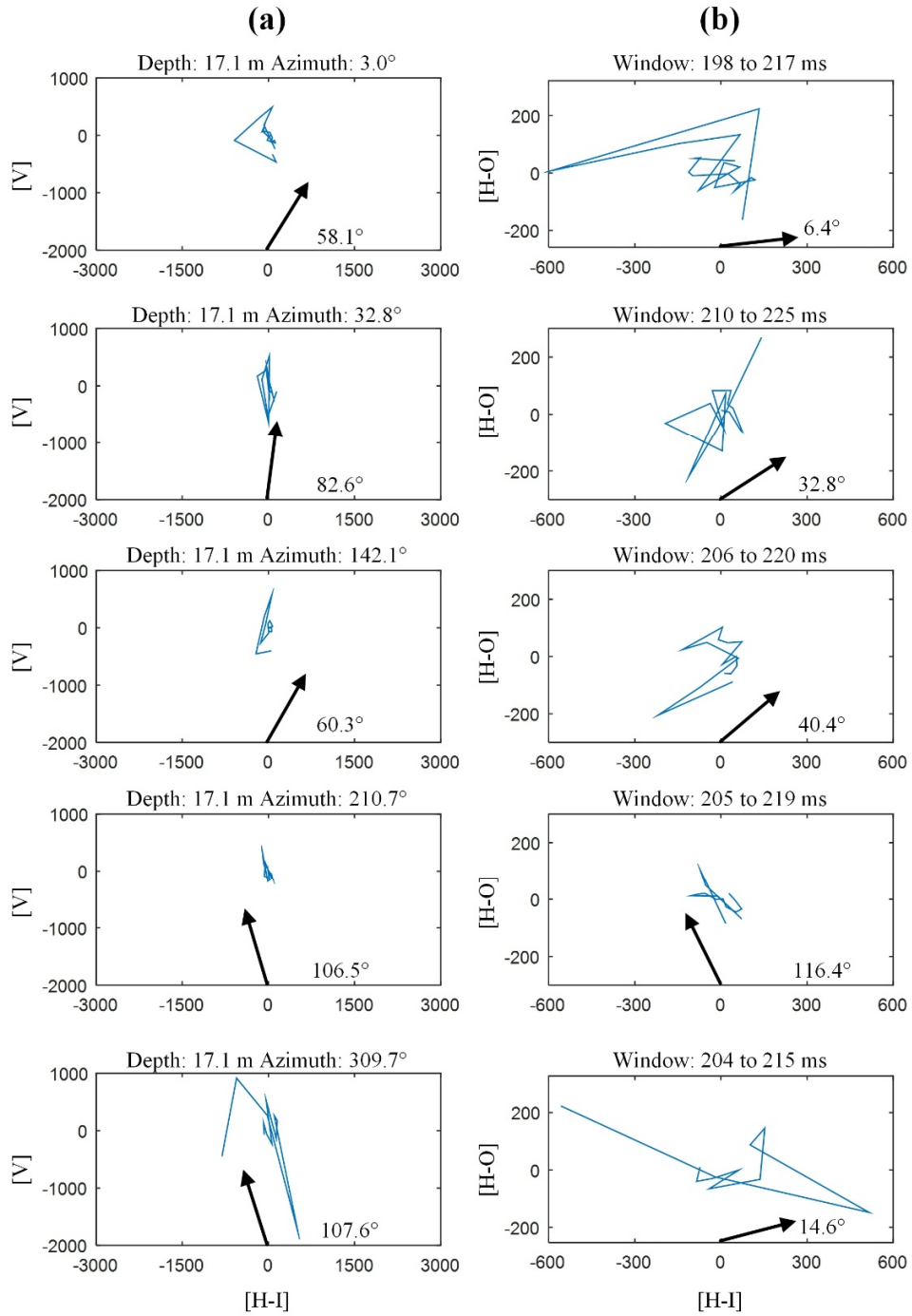


Figure 6.18: Hodograms for P-waves recorded at varying azimuths of geophones from a common source depth of 17.1 m. The azimuths are relative to the direction away from the source. Each row refers to an event covering two hodograms in column (a) and (b). Blue lines show hodograms of P-waves at specific time windows. Black arrows show the vectors for particle motion directions

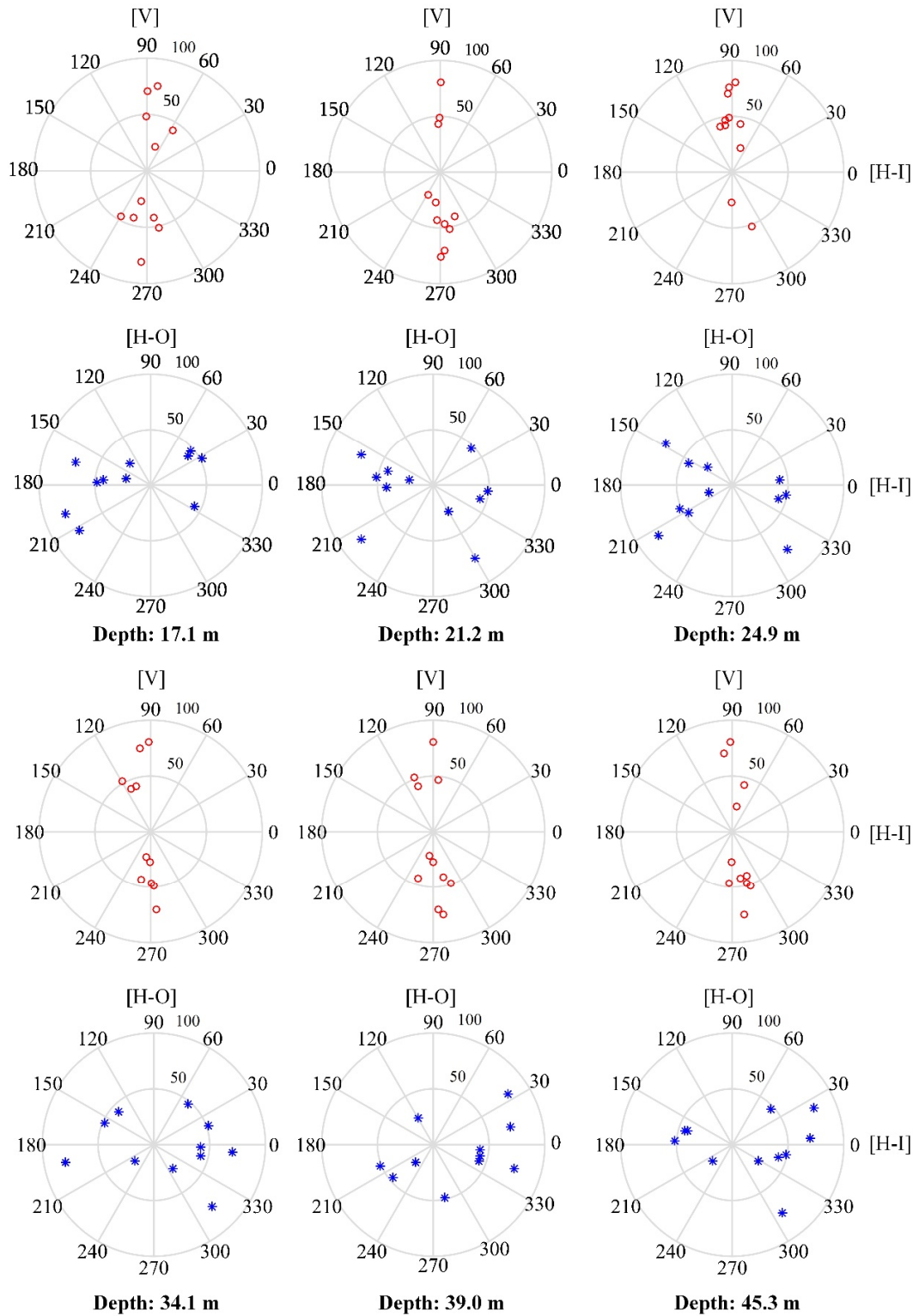


Figure 6.19: Calculated polarization angles from hodograms of P-waves recorded at 11 geophones (except geophone #12) from the six depths of sources. Polarization angles are rotated counterclockwise from the H-I orientations. Radii represent planar distance of source-geophone in meters

Figure 6.19 shows the calculated polarization angles from hodograms of P-waves recorded at 11 geophones from the six depths of sources as previously described. Following the previous convention, polarization angles are rotated counterclockwise from the H-I orientation. Radii are the planar distances from the sources to geophones. In hodograms for components V and H-I, polarization angles are predominately located closer to the vertical component orientation. The assembly results show the interference of free-surface on P-wave particle motion which is deflected to near vertical [33]. In hodograms for components H-O and H-I, polarization angles distribute closer to the H-I direction, i.e. most of them are within  $45^\circ$  of the H-I orientation. This shows similar results as previously described, i.e. P-wave particle motions deviate the H-I orientations indicating the H-I orientations of geophones are not in exact consistence with the source-receiver azimuths.

#### **6.6.4 Deviation of horizontal components of P-wave polarizations from source-receiver azimuths**

Deviation of H-I orientation from the source-receiver azimuth is further studied for each geophone. Figure 6.20 shows the polarization angles from six sources of depths from 17.1 to 45.3 m recorded by a single geophone. Take geophone #1 as an example, polarization angles are predominately in the azimuth of  $30^\circ$  or  $210^\circ$  from six different depths of sources, indicating the systematic deviation of H-I orientation away from the source-receiver

azimuth. In other words, the H-I orientation is inconsistent with the source-receiver azimuth. For most of geophones (#3, #4, #5, #6, #7, #8 and #11), deviation angles are predominately less than  $15^\circ$ . This shows the confidence of geophone orientations and recorded data. For the rest of geophones, deviation angles vary moderately and are mostly over  $30^\circ$ . In experiments, geophones were set approximately in orientations of source-receiver azimuths. These orientations are not measurely precisely. We just report these deviation angles which are possibly due to the deviation of geophone orientation from source-receiver azimuth or anisotropy associated with vertical fractures.

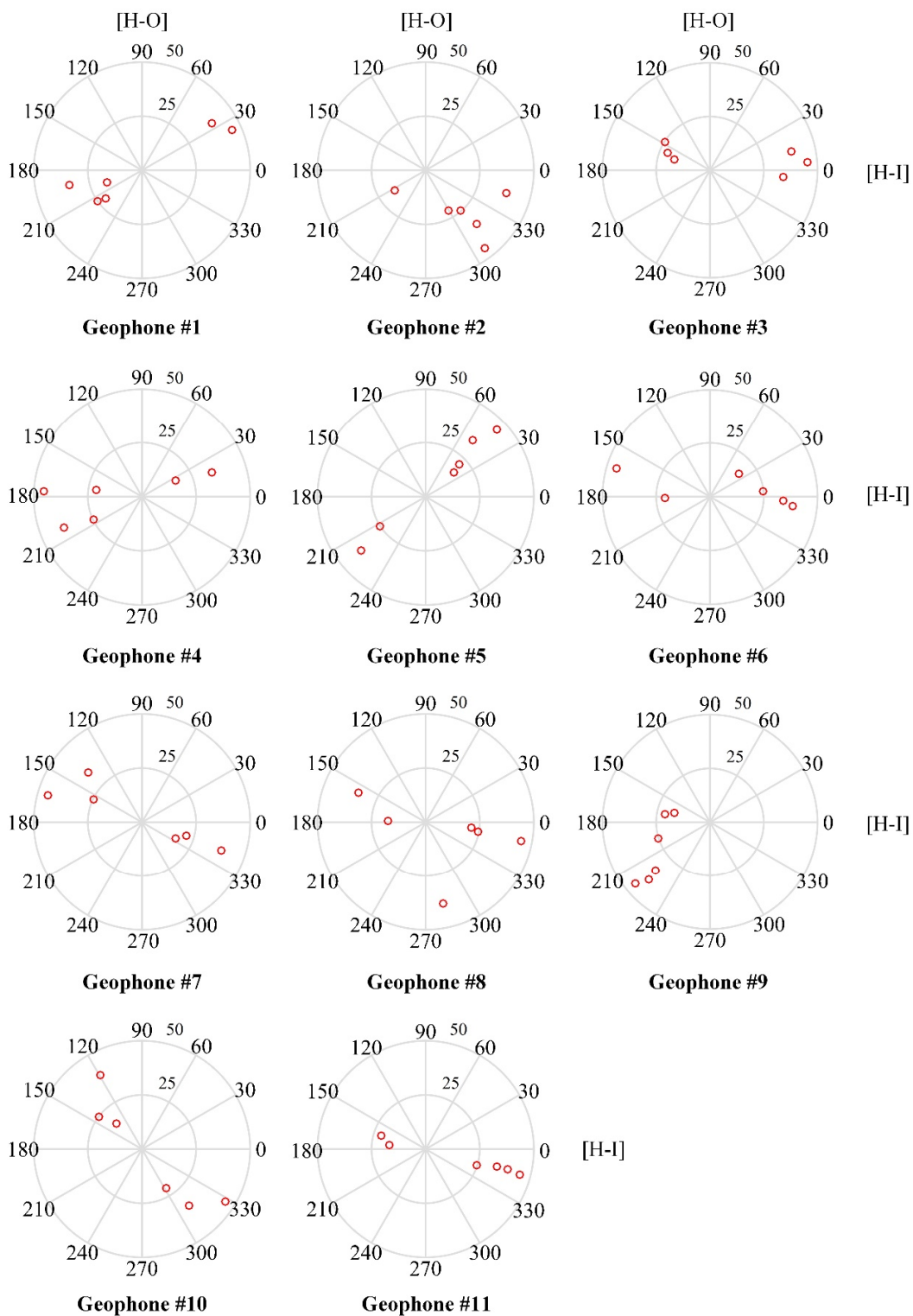


Figure 6.20: Polarization angles from six sources of depths from 17.1 to 45.3 m recorded by a single geophone. Particle motions deviate the H-I orientations showing the H-I components are not in exact consistence with the source-receiver azimuths. Radii represent planar distance of source-geophone in meters

## 6.7 Conclusions

In this research, rotary-percussion drilling source properties are comprehensively studied. Sources in weak shales and hard arkose are studied. Some essential points are discussed below.

1) Characterization of rotary-percussion drilling sources consists of spectral analysis and mean power study. Spectral analysis shows that an increase of rock strength increases peak frequency and widens the corresponding frequency bandwidth, which makes harder rock more viable for SWD purpose. Mean power analysis shows that rotary-percussion drilling releases a significantly higher magnitude of surface waves than conventional polycrystalline diamond compact and roller-cone bit drillings. The difference in energy indicated by surface waves suggests that this will also occur in body waves. The smaller magnitude of mean power from polycrystalline diamond compact bit than roller-cone bit demonstrates decreased axial vibration of polycrystalline diamond compact bit compared to that for the roller-cone bit which is documented in literature.

2) Field measurements of the P-wave energy radiation pattern within the vertical plane partially is consistent with the theoretical energy radiation pattern under a single vertical

bit vibration. However, an additional horizontal lobe of energy is observed close to orthogonal to axial bit vibration.

3) The measured radiation pattern within the horizontal plane is generally consistent with a spherically-symmetric distribution of energy.

4) Polarization analysis of P-wave is conducted to determine the actual particle motion direction so that the true wave motion is understood at geophones. The P-wave motion is shown to be near-vertical which confirms the interference of free-surface. P-wave particle motions deviate the H-I orientations indicating the H-I orientations of geophones are inconsistent with the source-receiver azimuths. Deviation angles are predominately less than  $15^\circ$  for most of geophones, showing the confidence of geophone orientation and data recording.

## **6.8 Acknowledgements**

The work was supported by Atlantic Canada Opportunity Agency (grant numbers: 781-2636-1920044), involving Husky Energy, Suncor Energy and Research and Development Corporation (RDC) of Newfoundland and Labrador.

## 6.9 References

1. Weatherby BB, inventor; Geophysical Res Corp, assignee. Method of making subsurface determinations. US patent 2,062,151. November 24, 1936.
2. Yokota T, Onishi K, Karasawa H, Ohno T, Ota A, Kaneko T. Seismic while drilling: basic experiments using a percussion drill as an energy source. *Explor Geophys.* 2004;35(4):255-259. doi: 10.1071/EG04255
3. Chitty DE, Blouin SE, Zimmer VL, Thompson PH, Tremba EL. Rotary percussion sounding system for in situ rock mass characterization. Paper presented at: The 40th U.S. Symposium on Rock Mechanics; June 25-29, 2005; Anchorage, AK.
4. Reppert PM. Seismic while drilling (SWD) with a rotary percussive sounding system (RPSS). *J Environ Eng Geophys.* 2013;18(3):169-182. doi:10.2113/JEEG18.3.169
5. Poletto F, Magnani P, Gelmi R, et al. Seismic while drilling (SWD) methodology in support to moon subsurface stratigraphy investigations. *Acta Astronaut.* 2015;110:99-114. doi:10.1016/j.actaastro.2015.01.013
6. Sun B, Bóna A, Zhou B, van de Werken M. A comparison of radiated energy from diamond-impregnated coring and reverse-circulation percussion drilling methods in hard-rock environments. *Geophysics.* 2015;80(4):K13-K23. doi:10.1190/geo2014-0344.1

7. Poletto FB, Miranda F. *Seismic While Drilling: Fundamentals of Drill-Bit Seismic for Exploration*. Oxford, UK: Elsevier Ltd; 2004.
8. Biggs MD, Cheatham JB. Theoretical forces for prescribed motion of a roller bit. *Soc Petrol Eng J*. 1969;9(04):473-481. doi:10.2118/2391-PA
9. Poletto F. Energy balance of a drill-bit seismic source, part 2: drill-bit versus conventional seismic sources. *Geophysics*. 2005;70(2):T29-T44. doi:10.1190/1.1897039
10. Richard T, Germy C, Detournay E. Self-excited stick-slip oscillations of drill bits. *C R Mecanique*. 2004;332(8):619-626. doi:10.1016/j.crme.2004.01.016
11. Sheppard MC, Lesage M. The forces at the teeth of a drilling roller cone bit: theory and experiment. Paper presented at: SPE Annual Technical Conference and Exhibition; October 2-5, 1988; Houston, TX.
12. Heelan PA. Radiation from cylindrical source of finite length. *Geophysics*. 1953;18(3):685-696. doi:10.1190/1.1437923
13. Gangi A. *A Theoretical Study of the Radiation Patterns of a Tunnel-Boring Machine (Infinite Medium)*. Vicksburg, MS: U.S. Army Engineer Waterways Experiment Station; 1987. Technical Report GL-87-20.
14. Poletto F. Energy balance of a drill-bit seismic source, part 1: rotary energy and radiation properties. *Geophysics*. 2005;70(2):T13-28. doi:10.1190/1.1897038

15. Carcione JM, Carrion PM. 3-D radiation pattern of the drilling bit source in finely stratified media. *Geophys Res Lett*. 1992;19(7):717-720. doi:10.1029/92GL00543
16. Rector JW. *Utilization of Drill Bit Vibrations as a Downhole Seismic Source* [dissertation]. Stanford, CA: Stanford University; 1990.
17. Rector JW, Hardage BA. Radiation pattern and seismic waves generated by a working roller-cone drill bit. *Geophysics*. 1992;57(10):1319-1333. doi:10.1190/1.9781560801580
18. Aleotti L, Poletto F, Miranda F, Corubolo P, Abramo F, Craglietto A. Seismic while-drilling technology: use and analysis of the drill-bit seismic source in a cross-hole survey. *Geophys Prospect*. 1999;47(1):25-39. doi:10.1046/j.1365-2478.1999.00113.x
19. Lutz J, Quichaud C, Raynaud M, Raynal J, Mucklero JA, Gstalder S. Instantaneous logging based on a dynamic theory of drilling. *J Petrol Technol*. 1972;24(06):750-758. doi:10.2118/3604-PA
20. Jardine SI, Lesage ML, McCann DP. Estimating tooth wear from roller cone bit vibration. Paper presented at: SPE/IADC Drilling Conference; February 27-March 2, 1990; Houston, TX.
21. Gradl C, Eustes AW, Thonhauser G. An analysis of noise characteristics of drill bits. Paper presented at: The 2008 SPE Annual Technical Conference and Exhibition; September 21-24, 2008; Denver, CO.

22. ASTM International. ASTM D5731, standard test method for determination of the point load strength index of rock and application to rock strength classifications.
23. ASTM International. ASTM D2845, standard test method for laboratory determination of pulse velocities and ultrasonic elastic constants of rock.
24. Rana PS, Abugharara AN, Butt SD, Molgaard J. Experimental evaluation of passive-Vibration Assisted Rotary Drilling (p-VARD) tool to enhance drilling performance. Paper presented at: The 49th U.S. Rock Mechanics/Geomechanics Symposium; June 28-July 1, 2015; San Francisco, CA.
25. King AF. *Field Trip Guidebook: Trip A4, Late Precambrian Sedimentation and Related Orogenesis of the Avalon Peninsula, Eastern Avalon Zone*. St. John's, Canada: Geological Association of Canada; 1988.
26. White J. Fourth year assessment report on licence 11964M, and first year assessment report on license 15683M of geochemistry, prospecting and trenching on the Collier Point property, NTS 1N/12 long cove, Newfoundland. Government of Newfoundland and Labrador. [http://gis.geosurv.gov.nl.ca/geofilePDFS/Batch2014/001N\\_0879.pdf](http://gis.geosurv.gov.nl.ca/geofilePDFS/Batch2014/001N_0879.pdf).
27. Newman P. Divergence effects in a layered earth. *Geophysics*. 1973;38(3):481-488. doi:10.1190/1.1440353
28. Yilmaz Ö. *Seismic Data Analysis: Processing, Inversion, and Interpretation of Seismic Data*. 2nd ed. Tulsa, OK: Society of Exploration Geophysicists; 2001.

29. Kanasewich ER. *Time Sequence Analysis in Geophysics*. 3rd ed. Edmonton, Canada: University of Alberta Press; 1981.
30. Rana PS et al; *September 2014 Drilling Field Trial Report*. Drilling Technology Laboratory, St. John's, Canada: Memorial University of Newfoundland; 2015.
31. Guevara SE, Stewart RR. *Multicomponent Seismic Polarization Analysis*. Calgary, Canada: CREWES; 1998. CREWES Research Report Volume 10.
32. DiSiena JP, Gaiser JE, Corrigan D. Horizontal components and shear wave analysis of three-component VSP data. In: Toksoz, N, Stewart RR, eds. *Vertical Seismic Profiling - Part B: Advanced Concepts*. London, UK: Geophysical Press; 1984:177-188.
33. Shearer, P.M., Orcutt, J.A. Surface and near-surface effects on seismic waves-theory and borehole seismometer results. *Bull. Seismol. Soc. Am.* 1987;77(4), 1168–1196.

## **Chapter 7 Concluding Remarks**

### **7.1 Summary**

In the work for this dissertation, the mechanism of improving drilling performance was studied for three typical drilling methods: rotary, rotary-percussion, and the newly developed pVARD technology. In terms of the fundamental differences in drill-bit motions, the objectives were addressed by an indirect means of studying drill-bit seismic sources and the corresponding drilling performances in the test drillings using SWD or AE technologies. DOTs were planned and grouped for comparison of different types of drilling such as rotary drilling and pVARD drilling, rotary drilling and RPD. The processed SWD and AE signals showed good correlations of waveform energy and frequency to ROP, WOB, rotary speed, bit vibration, drill cutting size distribution, and rock type. This study is a comprehensive examination of SWD and AE to the three drilling methods, and shows some promise for the application of SWD and AE technologies in studying drilling in the oil and gas industry, and in the mining area.

The details of five research areas in this study are provided in Chapters 2, 3, 4, 5 and 6. These research will be commented on as follows.

### **7.2 Concluding Remarks**

Chapter 2 reports on a study of the geomechanical deformation of specimens of synthetic rock or concrete using the AE technique in standard CCS tests. This research aimed to provide a comparison of synthetic rock to natural rock in terms of deformation properties. This research provides support for the use of AE in conjunction with DOTs on synthetic rock. From the analysis on AE signals, internal crack locations were plotted showing the progress of deformation and failure during tests, and showing the failure mechanism of shearing as observed and illustrated by previous test results.

Chapter 3 reports on a comparison of rotary drilling and pVARD drilling using AE technique in the laboratory. DOTs were conducted with the same materials and variable WOB. For every test, AE signals were monitored and drilling cuttings were collected, resulting in AE energy and cutting size distributions. For an increase of WOB, ROP is in positive correlation to AE energy and the cutting size distribution. For two drillings under the same WOB, ROP from pVARD drilling is higher than that from rotary drilling, i.e. pVARD compliance increases bit-rock contact time per revolution resulting in a higher number of AE events and coarser cuttings than rotary drilling.

Chapter 4 reports on a comparison of rotary drilling and pVARD drilling through the use of SWD technique in the field. DOTs were conducted. The drilling parameters were not identical in each run, but they were controlled to be closely comparable. Seismic surface waves were recorded for every test, resulting in seismic parameters of energy and frequency bandwidth. Surface waves were verified to be radiated from the rig-ground interaction as reported by some other researchers. Seismic wave parameters were in good correlation to

bit vibration and ROP. For an increase of WOB, ROP increased while measured bit vibration levels decreased due to compression from WOB, and the corresponding seismic energy and frequency bandwidth decreased. For the comparison of rotary drilling and pVARD drilling, results varied with the variation of rock strength. In stronger rock, both ROP and seismic wave energy from pVARD drilling were higher than that from rotary drilling. This was explained as follows. Greater drill string compliance with this tool caused more bit energy to go into bit penetration and increased ROP by increasing bit-rock interaction time per revolution, which also intensified the rig-ground interaction resulting in a higher magnitude of surface wave. In weaker rock, both ROP and seismic wave energy from pVARD drilling were lower than that from rotary drilling. This was also explained as follows. The pVARD tool drilling results, in terms of ROP and the seismic properties (frequency bandwidth and energy) of surface waves generated by the rig-ground interaction indicated greater partition of drill-bit energy to a drill string and less rig-ground interaction. Bit-rock interaction was reduced by the chosen setting of springs inside the pVARD tool and the softer shale. In summary, the drilling mechanism and bit vibration were indirectly characterized using the SWD technique by means of recording rig-ground interaction which was correlated to bit vibration. This pVARD tool was less favorable in some rock types and the inner spring settings need to be modified for better results.

Chapter 5 reports a study of an active vibration drilling. Axial bit vibration was produced by mounting rock samples on an electromagnetic vibrating table. DOTs were conducted with a diamond coring bit on synthetic rock, with varying WOB and vibration amplitude. For every test, AE signals were monitored and drilling cuttings were collected, providing

AE energy and cutting size distributions. For an increase of WOB and also an increase in vibration level, ROP was in a positive correlation to AE energy, crack size, cutting size distribution and mean particle size. Spectral analysis of the AE indicated that the higher ROP and larger cutting size were correlated with a higher AE energy and a lower AE frequency, indicating larger fractures were being created to generate the larger cutting size. Diamonds cut more aggressively with a higher level of ROP, resulting in a greater magnitude of AE energy from micro cracking.

Chapter 6 is a study of RPD in the field using the SWD technique. The characterization of RPD sources consisted of spectral analysis and mean power study, along with field measurements of the seismic source radiation patterns. The spectral analysis showed that increase of rock strength increased peak frequency and widened bandwidth of seismic waves. This indicated that harder rock was more viable for SWD purposes. The mean power analysis inferred a higher magnitude of body waves in RPD than that in rotary drilling. Within the horizontal plane, the observed P-wave energy radiation pattern partially confirmed the theoretical radiation pattern under a single vertical bit vibration. However, a horizontal lobe of energy was observed close to orthogonal to axial bit vibration. From analysis, this lobe was attributed to a lateral bit vibration, which was not documented elsewhere during RPD. Within the horizontal plane, the observed radiation pattern of P-wave is generally consistent with a spherically-symmetric distribution of energy. In addition, polarization analysis is conducted on P-waves recorded at surface geophones for understanding the particle motions. P-wave particle motions are predominately in vertical direction showing the interference of the free-surface. Analysis of seismic waves showed

that P-wave was recognizable while S-wave was mixed with P-wave. This is due to a short distance from source to receiver and a larger distance can separate body waves. Field drilling studies of this type should be conducted with greater distance of receivers from the drill bit source than was the case in this work.

### **7.3 Dissertation Highlights and Contributions**

#### **7.3.1 Rock failure mechanisms and acoustic emission**

AE event energy increases with increased core deformation and is found inversely related to dominant frequency. Dominant frequency has been proven to be in an inverse relation to crack size. In this way, larger cracks are generated when cracks nucleate and propagate in the process of core deformation. For the same shearing mechanism in PDC bit drilling, bigger cracks have been anticipated and confirmed from passive and active drillings with larger crack sizes causing larger cuttings. It is anticipated to be different in cracking mechanism using roller cone and hammer bits.

#### **7.3.2 Characterization of bit vibration and bit-rock interaction**

1) Natural bit vibration is measured by a downhole sensor sub as three types of accelerations. In particular, the axial vibration acceleration decreases with increasing WOB.

2) The passive drilling using pVARD setting of 12,000 pounds for the tool springs at quarter deflection have shown the potential to significantly improve drilling performance in higher strength of red shale. Under the same setting, drilling performance is not improved in the weaker grey shale. It is anticipated to obtain a better drilling performance using this setting of passive drilling in harder rock.

3) Active vibration drilling has shown the potential to improve bit-rock interaction compared to rotary drilling. This is based on the improved drilling performance active vibration drilling.

4) Characteristics of rig-generated surface waves (energy and frequency bandwidth) decrease with decreasing natural bit vibration levels.

5) A higher energy of surface waves in pVARD is obtained in stronger shale while a lower one for weaker shale, compared to rotary drilling. The contradictory results show the influence of rock strength on drilling performance of pVARD.

6) Measurement of P-wave amplitude shows an additional lateral vibration in rotary-percussion drilling that is not initially observed.

7) Energy of seismic source from rotary-percussion drilling is higher than that of rotary drilling by 2 to 3 orders of measurements.

### **7.3.3 Evaluation of drilling performance and penetration mechanisms**

1) Dominant frequency and spectral centroid of AE signals are inversely related to ROP. From the inverse relation between dominant frequency and crack size, higher ROP will result in lower dominant frequency and spectral centroid.

2) Mean energy of AE signals and mean particle size of cuttings are both positively correlated to ROP.

3) ROP is increased from rotary drilling for both pVARD and rotary-percussion drilling, in which natural bit vibration is passively utilized and active bit vibration is applied, respectively.

### **7.4 Recommendations for Future Work**

Based on the current research on drilling performance and penetration mechanisms for all three drilling types, some recommendations can be offered.

1) For commercial use of this pVARD technique, variation of number and setting of springs and dampening rubbers can result in different outcomes. Limited compliance settings have been tested in field using this tool. In addition, limited rock type has been tested, i.e. shale. It is recommended to conduct further study on drilling performance from variation of compliance settings numerically and physically.

2) It is highly recommend to conduct more research on pressurized drill-off tests with monitoring AE. In this way, a real-time investigation method on drill bit vibration and drilling mechanisms can be more feasible based on laboratory tests. A real-time AE monitoring tool is expected to be developed.

3) Last but not the least, numerical simulations on seismic radiation and AE during drilling are recommended.

## Appendix 1 Processing of AE Signals Using Matlab® Codes

### A1.1 Main Function

```

clear all

clc

srcFolder_CH4 = [uigetdir('','Select Channel #4 Folder to Open') '\']; % Source Directory
sig_files_CH4 = dir(fullfile(srcFolder_CH4,'*.sig'));

srcFolder_CH6 = [uigetdir('','Select Channel #6 Folder to Open') '\']; % Source Directory
sig_files_CH6 = dir(fullfile(srcFolder_CH6,'*.sig'));

TimeNum0=*; % Start time of experiment converted to seconds

Vp=*; % P velocity in specimen (mm/s)

D_specimen=*; % Specimen diameter (mm)

L_specimen=*; % Specimen length (mm)

L_steel=*; % Length from top sensor to bottom of steel platen (mm)

xls_name_in='*.xls'; % Stress data input name

xls_name_out='*.xls'; % All results saved name

%Stress-strain

[Stress, text_data, all_data]=xlsread('*'); % [Time Extension Load Strain% Stress]

[Row_num,Column_num]=size(Stress);

for j=1:Row_num

```

```

Stress(j,4)=abs(Stress(j,2))/L_specimen;

Stress(j,5)=abs(Stress(j,3))/(pi*D_specimen*D_specimen/4);

end

TriggerTime4=[0 0 0 0 0 0 0]; % [Elapsedtime DF Energy PekAmp PekAmpSamp
%ArrivalSample RA_value] RA_value=rise time/PekAmp

TriggerTime6=[0 0 0 0 0 0 0]; % [Elapsedtime DF Energy PekAmp PekAmpSamp
%ArrivalSample RA_value]

for fle = 1:length(sig_files_CH4)

    clc;display([num2str(fix(1000*fle/length(sig_files_CH4))/10) '% converted' ])

    [Vlt4 Tme4 Hdr4] = readSignal(srcFolder_CH4,sig_files_CH4(fle,1).name); % Input file
    %path & file name with extention

    [Vlt6 Tme6 Hdr6] = readSignal(srcFolder_CH6,sig_files_CH6(fle,1).name); % Input file
    %path & file name with extention

    [ElaspeTime DF Energy PekAmp PekAmpSamp ArriSamp RA_value] =
processSignal(Tme4,Vlt4,Hdr4,TimeNum0);

    TriggerTime4(fle+1,:)= [ElaspeTime DF Energy PekAmp PekAmpSamp ArriSamp
RA_value];

    [ElaspeTime DF Energy PekAmp PekAmpSamp ArriSamp RA_value] =
processSignal(Tme6,Vlt6,Hdr6,TimeNum0);

```

```

    TriggerTime6(fle+1,:)=[ElaspeTime DF Energy PekAmp PekAmpSamp ArriSamp
RA_value];
end

TriggerTime=[TriggerTime4 TriggerTime6];

% AE source location
Yloc=[0,0];
for i=2:size(TriggerTime(:,1))
    delta=(TriggerTime(i,6)-TriggerTime(i,13))/10^7;
    Yloc=[Yloc;0.5*(L_specimen+2*L_steel-Vp*delta),(TriggerTime(i,6)-
TriggerTime(i,13))];
end
TriggerTime=[TriggerTime Yloc];
Results_orig=TriggerTime;

%Filter out source without the range of bottom and top of specimen
inx=2;
for i=2:size(TriggerTime(:,1))
    if TriggerTime(i,15)>=L_steel & TriggerTime(i,15)<=L_steel+L_specimen;
        TriggerTime(inx,:)=TriggerTime(i,:);
        inx=inx+1;
    end
end

```

```

end

Source=TriggerTime(1:inx-1,:);

% Average repeated AE results within the same second
averageSource =averageSignal(Source);

% Save all results to xls_name_out
xlswrite(xls_name_out,Results_orig,'Results_orig');
xlswrite(xls_name_out,Source,'Location_Filter'); % filtered out
xlswrite(xls_name_out,averageSource,'average_filter_Signal');
xlswrite(xls_name_out,Stress,'Stress_Strain');

```

## A1.2 Function “readSignal”

```

function [Vlt Tme Hdr] = readSignal(PathName,FileName)

if nargin == 0

[FileName,PathName] = uigetfile({'*.sig';*.SIG'}, 'Select Data File'); %fileSelect dialog

end

if FileName~=0

fid = fopen(strcat(PathName,FileName), 'r');

if fid == -1

sprintf('%s', 'Can not open file');

else

```

end

end

```
%fid = fopen('AS_CH04-00001.sig', 'r');  
  
fseek(fid, 0, 'bof') ;Hdr.file_version = char(fread(fid, [1 14], 'char'));  
  
fseek(fid, 16, 'bof') ; Hdr.name = char(fread(fid, [1 9], 'char'));  
  
fseek(fid, 27, 'bof') ; Hdr.comment = char(fread(fid, [1 256], 'char'));  
  
fseek(fid, 287, 'bof') ;Hdr.sample_rate_index = (fread(fid,[1 1], 'int16'));  
  
fseek(fid, 289, 'bof') ;Hdr.operation_mode = (fread(fid, [1 1], 'int16'));  
  
fseek(fid, 291, 'bof') ;Hdr.trigger_depth =fread(fid, [1 1], 'int32');  
  
fseek(fid, 295, 'bof') ; Hdr.trigger_slope =fread(fid, [1 1], 'int16');  
  
fseek(fid, 297, 'bof') ;Hdr.trigger_source =fread(fid, [1 1], 'int16');  
  
fseek(fid, 299, 'bof') ;Hdr.trigger_level =fread(fid, [1 1], 'int16');  
  
fseek(fid, 301, 'bof') ;Hdr.sample_depth =fread(fid, [1 1], 'int32');  
  
fseek(fid, 305, 'bof') ;Hdr.captured_gain =fread(fid, [1 1], 'int16');  
  
fseek(fid, 307, 'bof') ;Hdr.captured_coupling =fread(fid, [1 1], 'int16');  
  
fseek(fid, 309, 'bof') ;Hdr.current_mem_ptr =fread(fid, [1 1], 'int32');  
  
fseek(fid, 313, 'bof') ;Hdr.starting_address =fread(fid, [1 1], 'int32');  
  
fseek(fid, 317, 'bof') ;Hdr.trigger_address =fread(fid, [1 1], 'int32');  
  
fseek(fid, 321, 'bof') ;Hdr.ending_address =fread(fid, [1 1], 'int32');  
  
fseek(fid, 325, 'bof') ;Hdr.trigger_time =fread(fid, [1 1], 'uint16');  
  
fseek(fid, 327, 'bof') ;Hdr.trigger_date =fread(fid, [1 1], 'uint16');  
  
fseek(fid, 329, 'bof') ;Hdr.trigger_coupling =fread(fid, [1 1], 'int16');
```

```
fseek(fid, 331, 'bof');Hdr.trigger_gain =fread(fid, [1 1], 'int16');
fseek(fid, 333, 'bof');Hdr.probe =fread(fid, [1 1], 'int16');
fseek(fid, 335, 'bof');Hdr.inverted_data =fread(fid, [1 1], 'int16');
fseek(fid, 337, 'bof');Hdr.board_type =fread(fid, [1 1], 'uint16');
fseek(fid, 339, 'bof');Hdr.resolution_12_bits =fread(fid, [1 1], 'int16');
fseek(fid, 341, 'bof');Hdr.multiple_record =fread(fid, [1 1], 'int16');
fseek(fid, 343, 'bof');Hdr.trigger_probe =fread(fid, [1 1], 'int16');
fseek(fid, 345, 'bof');Hdr.sample_offset =fread(fid, [1 1], 'int16');
fseek(fid, 347, 'bof');Hdr.sample_resolution =fread(fid, [1 1], 'int16');
fseek(fid, 349, 'bof');Hdr.sample_bits =fread(fid, [1 1], 'int16');
fseek(fid, 351, 'bof');Hdr.extended_trigger_time =fread(fid, [1 1], 'uint32');
fseek(fid, 355, 'bof');Hdr.imped_a =fread(fid, [1 1], 'int16');
fseek(fid, 357, 'bof');Hdr.imped_b =fread(fid, [1 1], 'int16');
fseek(fid, 359, 'bof');Hdr.external_tbs =fread(fid, [1 1], 'float');
fseek(fid, 363, 'bof');Hdr.external_clock_rate=fread(fid, [1 1], 'float');
fseek(fid, 367, 'bof');Hdr.file_options=fread(fid, [1 1], 'int32');
fseek(fid, 371, 'bof');Hdr.version =fread(fid, [1 1], 'uint16');
fseek(fid, 373, 'bof');Hdr.eeprom_options =fread(fid, [1 1], 'uint32');
fseek(fid, 377, 'bof');Hdr.trigger_hardware =fread(fid, [1 1], 'uint32');
fseek(fid, 381, 'bof');Hdr.record_depth =fread(fid, [1 1], 'uint32');
fseek(fid, 385, 'bof');Hdr.sample_offset_32 =fread(fid, [1 1], 'int32');
fseek(fid, 389, 'bof');Hdr.sample_resolution_32 =fread(fid, [1 1], 'int32');
fseek(fid, 393, 'bof');Hdr.multiple_record_count =fread(fid, [1 1], 'uint32');
```

```

fseek(fid, 397, 'bof') ; Hdr.dc_offset =fread(fid, [1 1], 'int16');
fseek(fid, 401, 'bof') ; Hdr.padding =fread(fid, [1 1], 'uint8');
inputRangeTable=[10 5 2 1 .5 .2 .1];
sample_rate_index_Table= [1 2 5 10 20 50 100 200 500 ...
    [1 2 5 10 20 50 100 200 500]*10^3 ...
    [1 2 2.5 5 10 12.5 20 25 30 40 50 60 ...
    65 80 100 120 125 130 150 200 250 300 500]*10^6 ...
    [1 2 4 5 8 10]*10^9] ;

if (Hdr.resolution_12_bits)
    fseek(fid, 512, 'bof') ; ADC = fread(fid,'int16') ;
else
    fseek(fid, 512, 'bof') ; ADC = fread(fid,'uint8') ;
end

sample_rate = sample_rate_index_Table(Hdr.sample_rate_index+1);
Tme = (-Hdr.trigger_depth+(0:Hdr.record_depth-1))/sample_rate; % 16384x1 double
Vlt = ((-1-
ADC)*inputRangeTable(Hdr.captured_gain+1)/Hdr.sample_resolution_32+Hdr.dc_offset
); % 16384x1 double

fclose(fid);

end

```

### A1.3 Function “averageSignal”

```

function [out]=averageSignal(TriggerTime)

TmInd = 1;cum =-1;

out=[];          % Counting repeated events within one second
while(TmInd <=size(TriggerTime,1))

    ind = find(TriggerTime(:,1)==TriggerTime(TmInd,1));

    cum = cum+length(ind);

    out = [out;TriggerTime(TmInd,1)    sum(TriggerTime(ind,2))/length(ind)
sum(TriggerTime(ind,3))/length(ind) sum(TriggerTime(ind,4))/length(ind) ...
    sum(TriggerTime(ind,5))/length(ind)    sum(TriggerTime(ind,6))/length(ind)
sum(TriggerTime(ind,7))/length(ind) sum(TriggerTime(ind,8))/length(ind) ...
    sum(TriggerTime(ind,9))/length(ind)    sum(TriggerTime(ind,10))/length(ind)
sum(TriggerTime(ind,11))/length(ind) sum(TriggerTime(ind,12))/length(ind) ...
    sum(TriggerTime(ind,13))/length(ind)    sum(TriggerTime(ind,14))/length(ind)
sum(TriggerTime(ind,15))/length(ind) sum(TriggerTime(ind,16))/length(ind) length(ind)
cum];

    TmInd=TmInd+length(ind);

end

end

```

### A1.4 Function “processSignal”

```

function [ElaspeTime DF Energy PekAmp ArriSamp] = processSignal(Tme,Vlt,Hdr)

    SampleRate=10^7; Trigger=0.1;

    n=14; SampleNum=2^n;

    DF=0;Energy=0;

    c=struct2cell(Hdr);% Returns structure values

    Bin_result=de2bi(cell2mat(c(17)),16);% Integer of trigger time

    Sec=bi2de(Bin_result(1:5))*2;

    Min=bi2de(Bin_result(6:11));

    Hr=bi2de(Bin_result(12:16));TimeNum0=14*3600+25*60+21.6;% Initial trigger time
in seconds

    ElaspeTime=Hr*3600+Min*60+Sec-TimeNum0;% Event elapsed time in seconds

    Element=[Tme Vlt]; % [Time Amp DemeanAmp RectifiedAmp]

    % 1 DC Offset calculation

    sum=0.0;

    for i=1:1:SampleNum

        sum=sum+Element(i,2);

    end

    DCOffset=sum/SampleNum;

    % 2 Demeaning operation

    for i=1:1:SampleNum

```

```
Demean(i)=Element(i,2)-DCoffset;
end
Element=[Element Demean'];
%plot(Element(:,1),Element(:,3));
%title('Demeaning Amplitude');xlabel('Time(Second)');ylabel('Amplitude(Volt)');
%xlswrite('AS_CH04-00001',Element(:,3),'sheet1','c1:c16384')

%3 Rectification operation
for i=1:1:SampleNum
    Rectify(i)=abs(Demean(i));
end
Element=[Element Rectify'];
%xlswrite('AS_CH04-00001',Element(:,4),'sheet1','d1:d16384');

% 4 Maximum amp and its index
PekAmp=max(Element(:,4));

% 5 Arrival sample or time
for i=1:1:SampleNum
    if Element(i,2)>=Trigger
        break;
    end
end
end
```

```
if i<SampleNum
    ArriSamp=i;
else
    ArriSamp=0;                % No waveform detected
end

% Calculation of waveform parameters
if ArriSamp~=0
    % 7 Total energy in time domain / Some issue about selected window
    sum=0.0;
    for i=ArriSamp:1:SampleNum
        sum=sum+Element(i,4);
    end
    Energy=sum/SampleRate;

% 6 Dominant frequency and FFT
ZeroCross=0;FstNum=ArriSamp;LstNum=ArriSamp+1023;
if LstNum>SampleNum
    LstNum=SampleNum;
end
if FstNum==1
    FstNum=2;
```

```
end  
  
for i=FstNum:1:LstNum  
    if Element(i-1,3)/Element(i,3)<0      % Dominant frequency  
        ZeroCross=ZeroCross+1;  
    end  
end  
  
DF=(ZeroCross-1)/2/((LstNum-FstNum+1)/SampleRate);  
  
end  
  
end
```

## Appendix 2 Calculation of Bit Vibrations from Sensor Sub Data

### A2.1 Methodology

Bit accelerations, i.e. axial, lateral and torsional, are calculated from the three accelerometers using Equations (A2.1) to (A2.3) [1], respectively. Geometry of accelerometers are available in Chapter 4.

$$\begin{cases} a1x' = a1x + 1 \\ a2x' = a2x - 1 \\ a3z' = a3z + 1 \\ A_{axial} = \frac{a1x' + a2x'}{2} \\ A_{shock} = -a3z' \end{cases} \quad (A2.1)$$

$$\begin{cases} alx = \frac{-a1z - a2z + a2y - a1y}{2} \\ aly = \frac{-a1z - a2z - a2y + a1y}{2} \\ A_{lateral} = \sqrt{Alx^2 + Aly^2} \end{cases} \quad (A2.2)$$

$$A_{torsional} = \frac{-a1z - a2z - a2y + a1y}{2} \quad (A2.3)$$

$A_{axial}$ ,  $A_{lateral}$ , and  $A_{torsional}$  are the axial, lateral and torsional accelerations from sensor sub geometry.  $a1x$  and  $a1y$  are the accelerations recorded from accelerometer #1;  $a2x$  and  $a2y$  are the accelerations recorded from accelerometer #2;  $a3z$  is the acceleration recorded from accelerometer #3.  $A_{shock}$  is used to replace  $A_{axial}$  when any acceleration from accelerometers #1 and #2 exceeds the limit of 4 g, where g is the gravity of earth.

## A2.2 References

1. Gao Q. *Development of Laboratory and Field Drilling Tools to Measure Bit Operating Conditions and Drill String Motions* [master's thesis]. St. John's, Canada: Memorial University of Newfoundland; 2014.